UTS UNIVERSITY OF TECHNOLOGY SYDNEY

Assessment of Residual Load Capacity of ASR Affected Prestressed Concrete Structures

by Mehdi Habibagahi

Thesis submitted in fulfilment of the requirements for the degree of

Doctor of Philosophy

under the supervision of

Principal Supervisor: A/Prof Shami Nejadi
Co-Supervisor: Prof Vute Sirivivatnanon

University of Technology Sydney
Faculty of Engineering and Information Technology

November 2023

Certificate of Original Authorship

I, *Mohammadmehdi Habibagahi*, declare that this thesis is submitted in fulfilment of the requirements for the award of Doctor of Philosophy in the School of Civil and Environmental Engineering, Faculty of Engineering and Information Technology, at the University of Technology Sydney.

This thesis is wholly my own work unless otherwise referenced or acknowledged. In addition, I certify that all information sources and literature used are indicated in the thesis.

This document has not been submitted for qualifications at any other academic institution.

This research is supported by the Australian Government Research Training Program.

Signature: Production Note:
Signature removed prior to publication.

Date: 01/11/2023

Acknowledgements

The research presented in this PhD thesis was undertaken in the School of Civil and Environmental Engineering at the University of Technology, Sydney (UTS).

I wish to express my sincerest gratitude to my principal supervisor, A/Professor Shami Nejadi for his patience, outstanding guidance, knowledge, motivation and caring support provided throughout my thesis. His exceptional personality and positive attitude became a source of inspiration and a role model for my professional and personal development. Utmost gratitude is also forwarded to my co-supervisor, Professor Vute Sirivivatnanon for his guidance, motivation and support throughout my study. I am heartily thankful to Professor Hadi Khabbaz for his encouragement, guidance and unfailing assistance throughout this study.

The assistance from the SRG Global company for the post-tensioning operation has been very important in completing the experimental tests included in the thesis. I would like to thank all working staff in those laboratories, especially Mr. Mulugheta Hailu, Ms Ann Yan and Mr. Peter Brown, Mr. Peter Winnacott and Mr. Scott Graham. Working in the lab would never have been easy without the assistance provided by all these people.

I would like to express my deepest gratitude to my family for their love, support and encouragement while I was thousands of miles away from home. My special thanks also go to my friends for their support and motivation. I offer my regards and blessings to all of those who supported me in any respect during the completion of this study.

Table of Contents

List of Figures

List of Tables

Abstract

Alkali silica reaction (ASR) is a major cause of degradation in concrete structures globally, affecting their durability and functionality. Despite some recent research on ASR's impact on reinforced concrete beams and other components, the influence of prestressed loads on the expansion and behaviour of structures affected by ASR is not well known.

The objective of this research program is to assess the residual load capacity of prestressed concrete beams impacted by ASR. A laboratory investigation was conducted to examine the impact of ASR-induced expansion and cracking on the mechanical properties and structural behaviour of concrete structures. To accomplish this, six full-scale prestressed concrete beams and two reinforced beams were constructed using both reactive and non-reactive aggregates. Accompanying cylinders were tested at various stages to determine their compressive strength, splitting tensile strength, and dynamic modulus. The length expansion of the plain concrete prisms and the strain in the reinforcing and prestressing bars of the beams were continuously measured during the accelerated ASR conditioning period. Following nine months of accelerated conditioning, the reinforced and prestressed beams were subjected to flexural and shear loading tests. The results showed that the compressive strength, splitting tensile strength, and dynamic modulus of the cylinders were significantly reduced after ASR cracking. However, the flexural load-carrying capacity of the reactive prestressed beams was largely unchanged compared to the corresponding non-reactive beams.

In addition, an artificial intelligence model using the artificial neural network (ANN) was proposed to provide an accurate estimation for predicting the elastic modulus of damaged concrete, since ASR affects the modulus of elasticity more drastically than concrete's compressive and tensile strength. Also, alkali/silica concentration in a mixture, aggregate size, externally applied stress, and ambient temperature on ASR expansion, a constitutive model was proposed and verified with the experimental results due to the lack of proper models that can account for the effects of relative humidity.

Finally, a nonlinear analysis of prestressed concrete structures affected by ASR was presented based on the fracture-plastic model. The results of the three-dimensional FEM model were successfully validated with the experimental results of ASR-affected real-size prestressed and reinforced members conducted in the UTS Tech Lab laboratory.

Chapter 1: INTRODUCTION

1.1 BACKGROUND

Numerous technical developments over the past few decades have increased the varieties of construction materials and types of concrete currently used. In one form or another, concrete is now a required and common building material in the modern world. Portland cement concrete, which includes 60 to 75% aggregate, 10 to 15% Portland cement, supplementary admixtures, and water, is the most extensively used building material in the construction industry.

With the evolution of technology, a comprehensive understanding of the nature of these materials and the possibility of structural problems, some of which might lead to their early degradation and failure, has been established. One of these phenomena is the reaction between some reactive aggregate materials with an unstable crystal structure and hydroxyl ions in concrete pore solution. This problem might be driven by the inappropriate materials and cement used in the concrete mix design. Although at first, concrete may have all the qualities of strength and durability, after several years, the concrete starts to expand and fracture, necessitating costly reconstruction or retrofitting replacement procedures.

The term "Alkali-Aggregate Reaction" (AAR) primarily refers to a chemical reaction occurring in concrete over time between the non-crystalline silicon dioxide in many common aggregates and the highly alkaline cement paste.

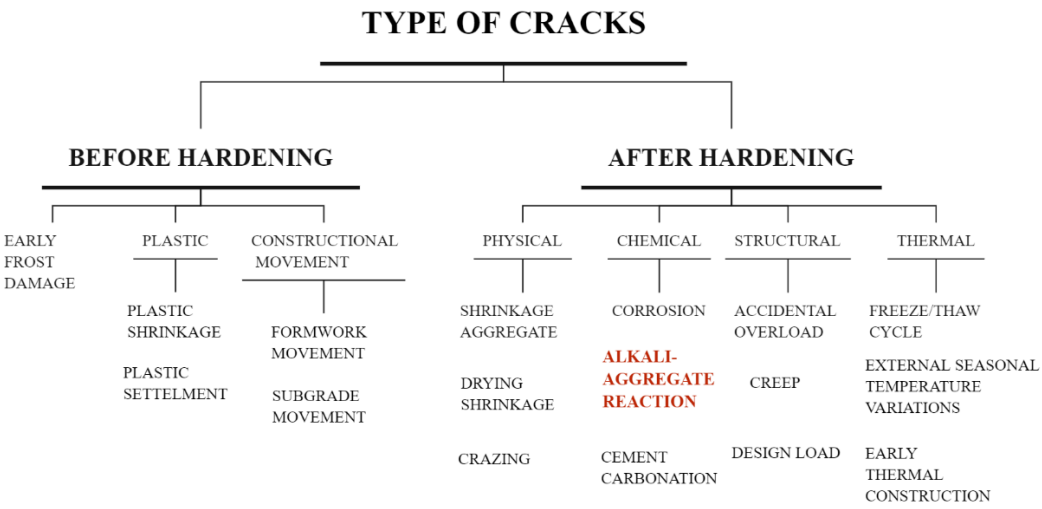

Figure 1.1 Type of cracks in concrete structures (Courtesy of concrete Society, 2010).

AAR is a primary issue with concrete's durability that severely damages buildings, paved surfaces, bridges, dams, and other concrete constructions worldwide.

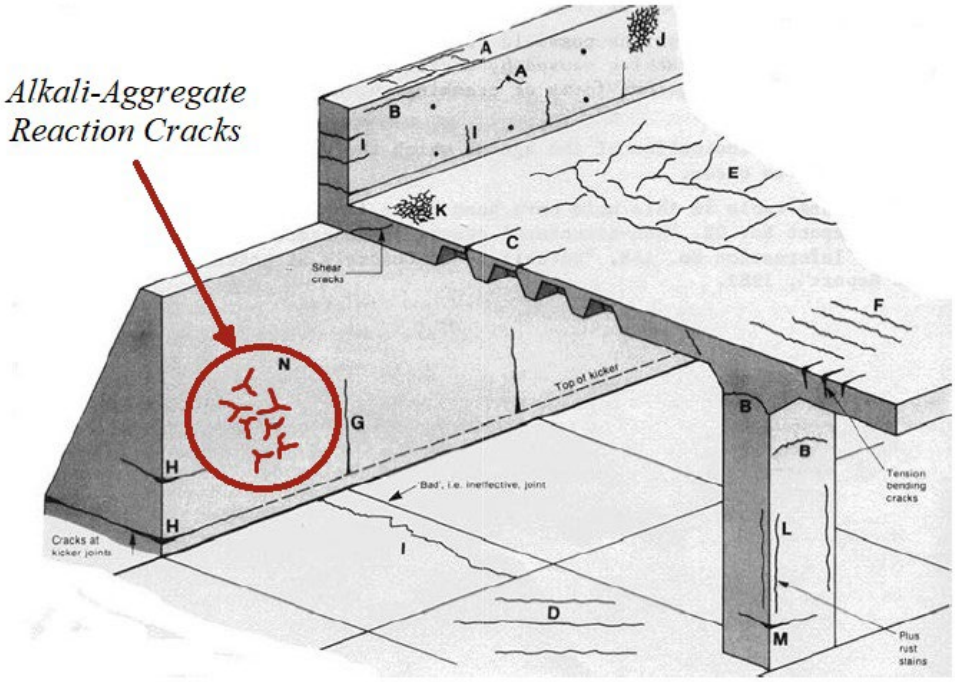

Figure 1.2 Typical cracks in reinforced concrete. (Courtesy of Beeby, 1983).

Generally, AAR can be divided into two reactions: Alkali-Carbonate Reaction (ACR), formed by the dolomite or carbonate in specific aggregates, and Alkali-Silica Reaction (ASR), which is caused by active silica minerals present in aggregates. As

most rocks have a high proportion of silica content, ASR is the most prevalent type of AAR.

Figure 1.3 Multiple cracks on the surface of road over-pass pier. (Blight, 2011).

ASR impacted many concrete buildings in the United States in the late 1930s. Stanton (1942) first observed and reported it in North America. Additionally, he released the first comprehensive body of scientific data explaining the reaction and its consequences in December 1940. Stanton investigated the expansion of concrete pavement and the failure of concrete pavement in several projects. Further research by (Stanton 2008) demonstrated that this problem only appeared when a particular type of mineral was present in the aggregates and the alkalinity of the cement exceeded a set threshold level. His research not only provided extensive information regarding the nature of the reaction and its relevance, but it also included early iterations of test procedures that would eventually become standard methods, as well as strategies for preventing or reducing the reaction's negative impacts.

Stanton began the research in the early stages, and various researchers have since conducted further investigations worldwide. The number of studies concentrating on ASR significantly increased, making ASR a widespread durability issue in concrete structures. Some concrete buildings are severely damaged by ASR, which includes gel formation, considerable concrete expansion, cracking, particles pull-off through the concrete, and destructive unsightly white deposits on the concrete's surface. As Diamond (1992) noted, ASR is causing widespread, continuous, and relatively slow concrete deterioration. A hygroscopic alkali-silica gel is produced due to this interaction over time. This gel reacts with the active alkalis in cement and generates swelling in the concrete, which causes internal force and reduces the lifespan and functionality of the structure. Concrete structures suffer severe damage due to ASR-related distress, eventually leading to structural failure.

Despite previous research, structural issues brought on by ASR have lately been reported in Seabrook nuclear power plant by Hayman (2010) in America, and the same problem has been observed in the Mactaquac dam by Beaver et al. (2013) in Canada. Such issues point to the need for more study and analysis of ASR and contemporary developments.

1.2 STATEMENT OF PROBLEM

Chemical degradation of concrete in the form of ASR is a steadily developing mechanism leading to concrete expansion and cracking. This internal swelling causes damage to the material properties, leading to the weakening of the concrete's structural properties and the structure's stability. Since the early 1940s, ASR has been the subject of intensive research. However, most have focused more on the scientific aspect of ASR, such as chemistry, the characteristics of different reactions, exposed materials,

chemical kinetics, variables impacting them, and anticipating their reactivity rather than on structural aspects. To address this problem, researchers initially used a phenomenological approach to suggest models for explaining the role of ASR in concrete mechanical deterioration. Other models, such as the chemo-mechanical or hydro-thermo-chemo-mechanical models, have also been proposed to model the mechanical distress and evolution of the chemical extent of ASR reaction. These systematic investigations are crucial for improving our comprehension of the ASR phenomena. Additionally, it has aided in removing potential aggravating factors for ASR and enhancing the performance of concrete, cement, and related materials.

In recent years, a few studies have been performed on reinforced concrete beams and other structural components influenced by ASR. However, the effect of prestressing load on the expansion and the structural behaviour of the prestressed concrete members that ASR deteriorates is not well understood and investigated yet. An example of longitudinal cracking of a prestressed jetty structure and a schematic of cracking of a prestressed member due to ASR are provided in Figures 1.4 and 1.5, respectively.

Figure 1.4 Longitudinal cracking of Prestressed jetty structure in Western Australia due to ASR (Cherry and Green 2021).

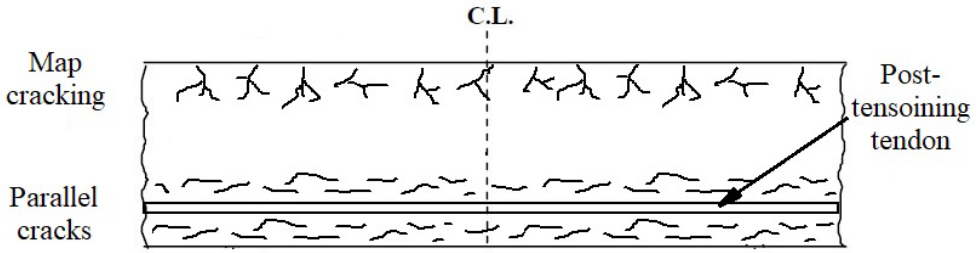

Figure 1.5 Schematic of ASR cracking in prestressed concrete beam.

This work focuses on the structural assessment of ASR impacts on concrete structures, particularly prestressed concrete structures. In some research, ASR addresses considerable flexural strength loss, while a series of experiments show that the failure of the structure occurs at a higher load. This phenomenon of cracking delay is caused by the chemical prestress in concrete caused by ASR swelling in the direction of the reinforcing bar. Furthermore, the performance of concrete structures is reduced, and distasteful surface cracks are produced, which is one of the minimal primary impacts of ASR. One of the major issues for owners and operators of concrete structures impacted by ASR is assessing the detrimental impacts of ASR in terms of technical performance. ASR damage varies in different structures, locations, and individual members depending on the environmental and confinement conditions.

The lack of adequate methods to assess the load-carrying capacity of ASR-affected structures inevitably leads to using estimates and assumptions in the design procedure. Therefore, a technique that provides a practical assessment of the load-carrying performance of the ASR-affected structures is essential. The mechanical qualities of the concrete, the reinforcing bars, the bond connection between the bars and the concrete, or the amount of compressive force in prestressed structures all affect how well concrete structures operate structurally due to ASR.

It must be acknowledged that at the end of the day, civil or structural engineers will have to evaluate, fix, and manage issues brought on by ASR. Therefore, it is

necessary to conduct a precise and reliable investigation of the mechanisms through which ASR damages concrete and the impacts of this damage on the structural performance of concrete buildings.

1.3 OBJECTIVES AND SCOPE OF THE THESIS

This research program aims to evaluate the residual load-carrying capacity of prestressed concrete beams affected by ASR. It is first necessary to assess the level of concrete's mechanical property degradation before evaluating its structural performance. Also, finite element analysis is proposed as a computational investigation of the structural performance of ASR-affected prestressed concrete beams to verify the experimental results and predict the residual strength of the prestressed concrete members affected by ASR.

In this study, prestressed and reinforced concrete beams with reactive and non-reactive aggregates were exposed to the accelerated ASR conditions at 38 degrees and 100% relative humidity. Then, four-point loading tests were conducted to evaluate their residual flexural and shear carrying capacity due to ASR. Concurrently, control samples were also made and tested.

It is known that ASR is a prolonged chemical reaction; in some cases, it takes tens of years; therefore, the samples were placed in an accelerated environment to boost the reaction and shorten the testing period. Additionally, a constitutive law model has been presented and validated to simulate the impact of ASR on concrete structures and predict the structural behaviour of prestressed concrete structures affected by ASR.

The primary objective of this research can be expressed as assessing the residual load-carrying capacity of ASR-affected prestressed concrete structures. Therefore, there is a need to predict the structural behaviour of prestressed concrete structures.

Thus, experimental tests and numerical models have been proposed in this thesis. In summary, this research can be defined as follows:

- To assess the effect of ASR on the residual load-carrying capacity of the prestressed concrete beams over time.
- To propose numerical models for calculating and predicting the load-carrying capacity of prestressed concrete elements affected by ASR.

The objective and scope of the thesis are summarized in Figure 1.6.

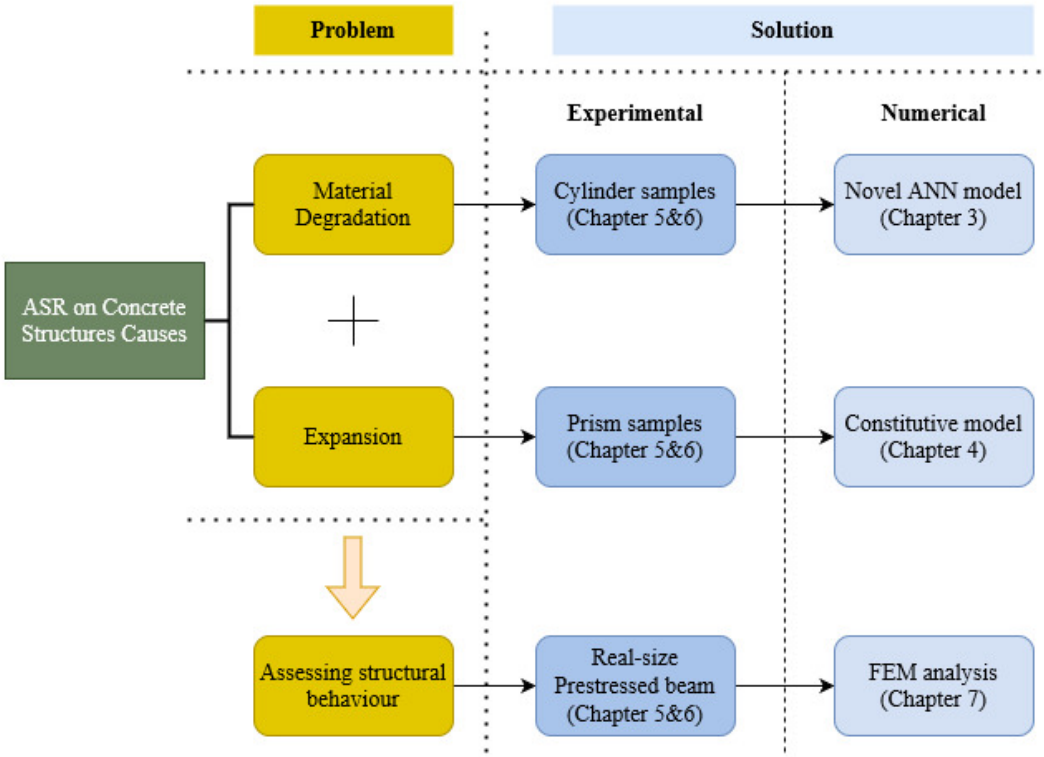

Figure 1.6 Summary of objectives and scope of the thesis.

The lack of satisfactory methods to assess the load-carrying capacity of ASR-affected structures inevitably leads to using estimates and assumptions in the design procedure. Therefore, a practical technique that evaluates the load-carrying performance of ASR-affected concrete structures is still required. The research

includes the following to develop a method of estimating the load-carrying capacity of prestressed concrete beams:

- ✓ Long-term experimental tests using companion specimens to determine the degree of ASR deterioration and expansion.
- ✓ Load testing to determine the ASR-affected real-size prestressed beam's behaviour under both normal and anticipated peak load conditions.
- ✓ A novel numerical model to predict the mechanical properties of ASR-affected concrete samples, using the artificial neural network (ANN) concept.
- ✓ A precise constitutive model to predict the ASR-induced expansion.
- ✓ Analytical evaluation of the load-carrying ASR-affected prestressed concrete beams by utilizing nonlinear Finite Element (FE) method..

This study tested eight beams after one year of ASR accelerated condition, and the structural behaviour of ASR-deteriorated prestressed concrete beams, both experimentally and numerically, was monitored and investigated.

1.4 LAYOUT OF THE THESIS

This thesis is presented in seven chapters. Chapter 2 of the thesis reviews the previous study related to the history of ASR, its mechanism, causes, contributing factors, diagnostic procedures methods, the expansion in free and constrained conditions, the mechanical properties of concrete affected by ASR, the concept of prestressed concrete, and effects of ASR on the engineering performance of concrete structures.

Chapter 3 proposes a state-of-the-art numerical model based on Artificial Neural Networks (ANNs) to predict the mechanical properties of concrete affected by ASR.

Chapter 4 presents a state-of-the-art comprehensive constitutive modelling and its equations to estimate the expansion caused by ASR. The verification of the suggested model has also been evaluated at the chapter's conclusion by comparing the numerical and experimental data available in previous studies.

Chapter 5 describes an experimental program for flexural and shear tests. It entails material preparation, sensor and data logger installation, moulding, rebar placement, concreting, the creation of an accelerated ASR environment, and prestressing procedures.

Chapter 6 provides the results of conducted tests at the laboratory, including the mechanical properties of concrete, the expansion of concrete samples, the stress in rebars and the amount of prestress loss in prestressing rods, the amount of longitudinal and transverse expansion of beams, and four-point loading tests. Finally, a discussion of the flexural and shear behaviours of the tested prestressed and reinforced beams is presented.

Chapter 7 evaluates the finite element models defined in the ATENA programme. After expressing the generated model and its equations, three conventional reinforced concrete beams which were experimentally tested in the lab were modelled. Then the numerical results were compared with the experimental data. In addition, beams were created and developed to fail in a different failure mode to guarantee the proposed model's performance. The findings of numerical modelling were compared and discussed with the outcomes of the experimental test results for prestressed and reinforced beams in Chapter 6.

Chapter 8 concludes with a summary and findings derived from this research and makes suggestions for future studies.

Chapter 2: LITERATURE REVIEW

2.1 HISTORY

Stanton (1940) reported a failure of a section of concrete pavement after two years of service in 1938. The concrete mix for this pavement used a similar coarse aggregate, while the fine aggregates were chosen from two separate sources. Initial studies revealed that the failure only happened in regions where a specific aggregate known as Oro Fino was used. Several other failures of concrete pavements were reported in that region, such as King City Bridge piers and the Southern Pacific Main Line Bridge over the Santa Clara River. Finally, it was discovered that all projects with expansion issues used the same type of fine aggregates.

This problem became more complicated because failure due to expansion wasn't a problem in some other projects that used the same aggregate. Therefore, a laboratory study was initiated utilizing imported Coyote fine aggregates and Oro Fino fine aggregates with different coarse aggregates. The aggregates were subjected to various environmental factors, with some test samples continuously wet, some always dry, and others intermittently damp and dry.

Contrary to predictions, even after more than a year, no excessive expansion was observed in these samples, except for the sample where the tested coarse aggregate was entirely made of claystone, which was caused by the claystone's physical expansion and not by any other reaction. Quite by accident, blotches fringed with a white efflorescence (which eventually turned into sodium carbonate) were seen in a mortar cylinder sample that had been sealed and kept for a year. And after a short while, fractures started to appear on its surface. Further investigation using this technique

revealed that the same reaction occurs after a few months in concrete mixtures made with Oro Fino fine aggregate and the same cement mixture. Studies using the same cement mixture and imported aggregates showed a slight expansion over 1.5 years. Further investigation revealed a link between cement and specific aggregates. Claystone and chert aggregates, sodium and potassium oxides, impure limestones, and other alkali compounds found in cement are all found in sedimentary deposits from the higher Miocene.

Additionally, it was discovered through additional research that silica gel, a kind of sodium silicate, leaks through holes or fractures on the surface of concrete constructions when aggregates and similar cement were used. The same gel's existence in the pores and concrete pieces of collapsed buildings and pavements was also confirmed.

Figure 2.1 A bridge parapet wall with signs of Alkali-Silica Reaction damage captured by Stanton. (Adopted from Thomas and Fournier et al. 2013).

Many observations by Stanton were the foundation for subsequent investigations by other researchers, which led to the current understanding of this field. His extensive study of this reaction problem established a new area of research in connection with the durability of concretes. Additionally, he covered the composition of the reaction products, potential reactive minerals, the impact of pozzolanic materials on the reaction, and two possible chemical reactions that may have occurred. One of these instances was the interaction of magnesium and sodium hydroxide, which resulted in carbonate formation in siliceous magnesium limestone. The reaction of alkalis and silica in the aggregate was another one.

Finally, he presented the first evidence of a chemical interaction between minerals in specific aggregates and alkalis in cement in 1940. Besides, the "Mortar Bar Test" was suggested in his early research to determine whether this reaction would occur. Following then, several initiatives of a similar nature were reported by various researchers. The report of his study explained the failure of many structures in different parts of the country and started an intensive investigation into the possible mechanism of the reaction, the reactivity of various rocks and minerals, corrective measures, and multiple tests designed to accelerate the reaction. As a result, many test procedures for reactivity during the initial phases of identification were suggested by several researchers.

2.2 NATURE OF THE ALKALI-SILICA REACTION AND MECHANISM

In the past decades, the ASR mechanism has been widely discussed and investigated since it was identified as a destructive chemical reaction for concrete. (Diamond 1975, Diamond 1976, Chatterji, Thaulow et al. 1988, Garcia-Diaz, Riche et al. 2006). ASR is a chemical reaction between alkali cations, hydroxyl ions in pore

solution, and unstable silica in concrete materials. As explained by Rajabipour and Giannini et al. (2015), the mechanism of ASR was introduced as the result of several consecutive reactions, including Silica dissolution, a sol, ASR gel formation, and finally, swelling of the gel. (Figure 2.2)

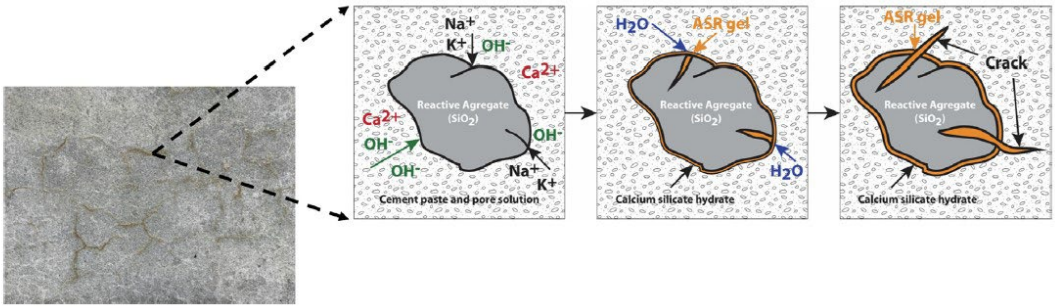

Figure 2.2 The ASR's concrete mechanism is depicted schematically. Adopted from (Du and Tan, 2014).

In some aggregates, due to unstable silica in their structure, active silica reacts with the alkali present in concrete. As Ichikawa and Miura (2007) described, this chemical reaction leads to the production of hygroscopic ASR gel. However, this gel alone does not have a destructive effect on the concrete; it can absorb the surrounding moisture. As a result, this gel expands by absorbing moisture, which is aggravated by different weather conditions. Some factors, such as temperature and an alkaline environment, accelerate this reaction. As a result, it creates cracks on the concrete surface.

The details of gel swelling behaviour based on osmotic pressure were described by Diamond (1992). Accordingly, gel swelling depends on two factors: moisture availability and mass transfer properties of concrete. Therefore, the amount of concrete destruction due to ASR is less in dry and dense concrete.

Based on Multon's (2003) study, gel swelling includes two main phases: gel hydration and gel volume increase. The potential chemical difference between the ASR

gel solution and the pore solution, during the hydration of the alkaline ASR gel, causes more water to be absorbed. Consequently, the ASR gel expands. As illustrated in Figure 2.3, X-ray tomographic images of a specimen are provided at distinct time intervals during the commencement of the ASR acceleration at 30, 85, 145, and 250 days, respectively.

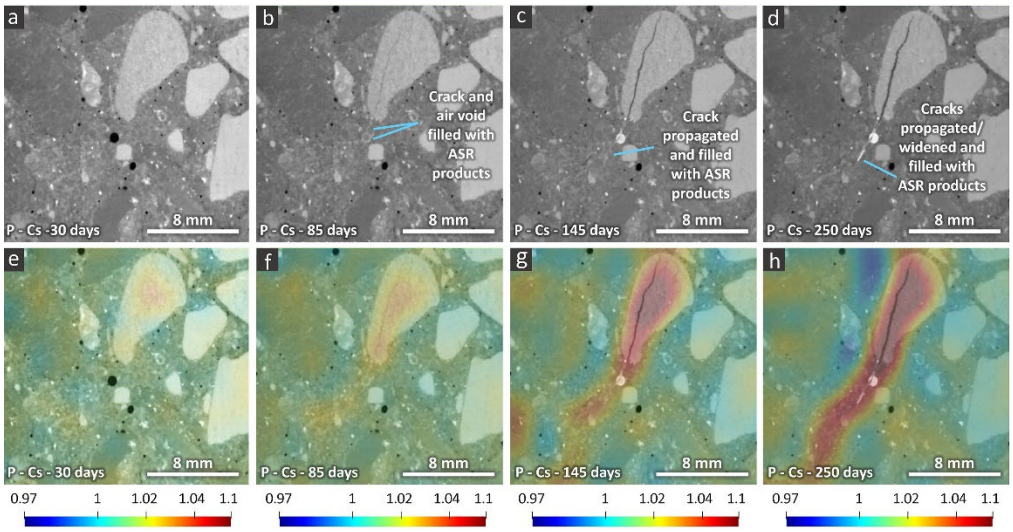

Figure 2.3 An X-ray tomogram of the ASR-affected specimen (Shakoorioskooie, Griffa et al. 2021).

The pore solution contains (Na+), (K+), and (OH-) ions create an alkaline environment with high pH. Unstable silicas react in this alkaline environment, which leads to the production of hydrous ASR gel. As Hou and Struble et al. (2004) discussed, silica is composed of silicon groups in some materials. In these materials, like quartz, the structure of silica is well-crystallized or dense. In this case, Ichikawa and Miura (2007) assumed that the aggregates are chemically non-reactive, as the attack of alkaline hydroxides occurs only on their surface. However, Thomas and Fournier's (2012) investigations revealed that the irregularity of the salicyl surface increases water absorption. Then the silicas are dissolved in concentrated hydroxyl ions. In the meantime, it neutralises the silanol and siloxane groups (≡Si-OH and ≡Si-O-Si≡). In

the first stage, high pH pore solution interacts with (≡Si-O-Si≡) bonds to create silanol bonds. Thus, four-coordinate silicon with one coordination site already occupied by OH is abbreviated as Si-OH, and in the second step, it interacts with additional hydroxyls:

$$\equiv Si\text{-}OH + OH^{-}\ Si\text{-}O^{-} + H_2O$$

$$\equiv Si\text{-}O\text{-}Si\equiv + 2OH^{-}\ 2Si\text{-}O\text{-} + H_2O \qquad (2.1)$$

The kinetics of this silica attack depends on the concentration of alkali ions in the concrete. During the gradual breaking of the (≡Si-OH, ≡Si-O-Si≡) structures, the alkaline solution absorbs hydroxyl as NaOH and KOH. Calcium hydroxide is released from cement hydration and adds to the pore solution's hydroxyl ions. The primary product of the reaction between siloxane groups (≡Si-O-Si≡) and hydroxyl ions is an alkaline silicate solution. Eqs. (2.1 and 2.2). Then Si-OH reacts with OH and more alkali metals. As a result, water and alkaline silicate hydrate are formed (Swamy 1992, Bažant and Steffens 2000, Ichikawa and Miura 2007, Godart, de Rooij et al. 2013).

$$\equiv Si\text{-}O\text{-}Si\equiv + OH^{-} + R^{+}\ (Na\ or\ K) \equiv Si\text{-}O\text{-}Na + H\text{-}O\text{-}Si\equiv$$

$$\equiv Si\text{-}OH + OH^{-} + Na+ \equiv Si\text{-}O\text{-}Na + H_2O$$

$$\equiv Si\text{-}O\text{-}Na + nH_20 \equiv Si\text{-}O^{-}\ (H_2O)_n + Na^{+} \qquad (2.2)$$

Dron and Brivot (1992) stated this alkaline silicate gel diffuses into the concrete paste from inside the aggregates and reacts with calcium ions, leading to the calcium silicate alkaline gel (Figure 2.4). If there is moisture in the surrounding environment, this gel expands. Excessive expansion in the surface between aggregates and cement paste causes internal stress and cracks in the concrete surface. The penetration rate of alkaline hydroxide into the crystal structure of quartz is low. But in quartz with a

cryptocrystalline structure, this rate increases due to the increase in surface area (Broekmans 2004). The same behaviour can be seen in the coarser quartz grains, which means that no silica aggregate can be considered entirely non-reactive (Bérubé and Fournier 1993, Broekmans 2004, Šachlová, Kuchařová et al. 2017).

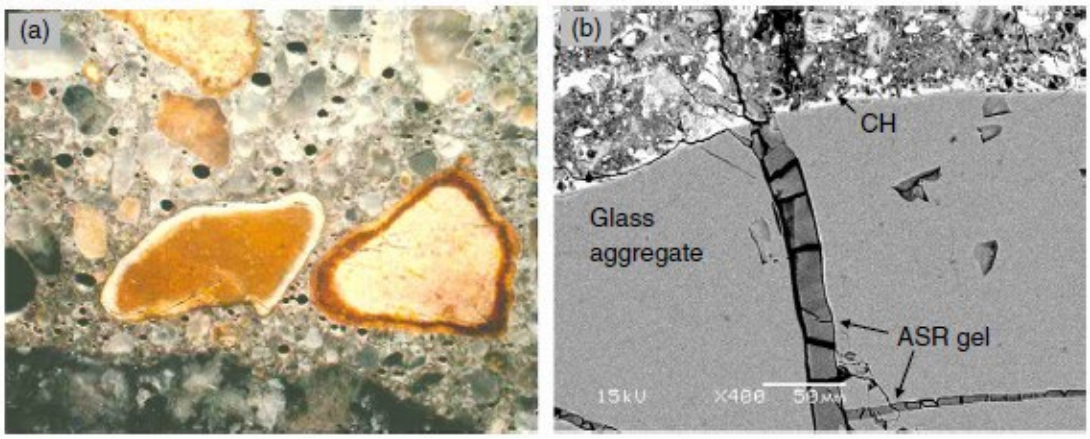

Figure 2.4 (a) ASR for granite gneiss and chert particles at the aggregate surface (Lane 1994), (b) Soda-lime glass particles' homogeneous composition. (Rajabipour, Maraghechi et al. 2012).

Since the ASR phenomenon in concrete is very complex, its different aspects have been investigated and studied separately for simplification. Briefly, in the ASR reaction, two types of gels are formed in concrete. A non-swelling agent of alkaline calcium silicate, the formation itself does not damage the concrete. The problem begins when the alkaline chemical composition of silicate hydrate in concrete forms the swelling gel.

In the first stage, activated silica reacts with water and ions in the pore solution and leads to depolymerization, dissolution, and swelling of the aggregate. Non-swelling gels are formed by releasing alkali and calcium ions by swelling gels. Then the pore solution penetrates the aggregates through these non-swelling gels. This swelling gel tends to absorb water, which causes volume expansion and local tension.

When these stresses become greater than the tensile strength of concrete, cracks appear on the concrete surface.

2.3 ESSENTIAL CONDITION FOR ASR

Generally, ASR gel alone does not cause strain or internal force in concrete structures. This gel absorbs moisture from its surroundings and causes swelling in the concrete, resulting in internal pressure applied to the concrete skeleton. If this internal pressure exceeds the tensile strength of concrete, it will cause gradual cracking and destruction of concrete. The three factors of silica which are found in some aggregates, a sufficient amount of alkali in the cement mixture and moisture, are some of the foremost influential factors in ASR reaction. (Figure 2.5)

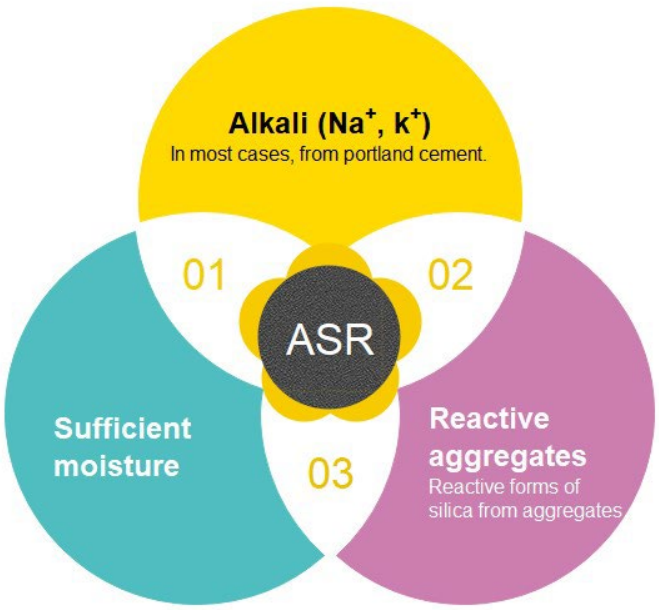

Figure 2.5 Factors that contribute to the development of ASR in concrete.

2.3.1 Reactive Aggregate

Since about 65 to 75% of the volume of concrete is made of aggregates, the quality of aggregates and the amount of unstable silica in their structure play a very determining role in causing ASR reactions and the durability of concrete against

chemical reactions. Therefore, aggregates are one of the most influential factors in developing chemical reactions such as ASR. Based on Léger and Côté et al. (1996) investigations, different aggregates show different behaviour based on the type of structure, chemical composition and solubility in alkaline solution. According to Thomas and Fournier's (2011) report, many materials, including unstable silica, are prone to react in alkaline conditions. As a result, any silica-containing aggregate can participate in ASR. Besides, Zapała-Sławeta and Owsiak (2016) indicated that mineral composition, texture, and geological origin affect aggregate alkali reactivity. Bérubé and Fournier (1993) cited cristobalite, tridymite, opal, chalcedony, and acid volcanic glass as a few examples of strained and cryptocrystalline quartz that react quickly with sodium and potassium hydroxides. Moreover, chert, opal, tridymite, cristobalite, acid volcanic glass, siliceous rocks, basalt glass, and dacite as the other reactive aggregates. However, Kurtis and Monteiro (2003) found that ACR expansion is more likely to occur in limestone, rocky dolomite, chalcedony, strained quartz, and cryptocrystalline quartz than ASR.

The proportion of reactive aggregates in the concrete mix is another critical factor. Numerous research (Ichikawa 2009, Garcia-Diaz, Bulteel et al. 2010, Gao, Multon et al. 2013) studied the impact of reactive aggregates on ASR reaction in quantity and structure over the past few decades.

In the early studies, Stanton and Thomas (1942) introduced a specific percentage as the maximum reaction rate for reactive aggregates. The effect of the size of aggregate particles, such as the amount of pessimum, has been the subject of many studies in the past decades (Ramyar, Topal et al. 2005, Dunant and Scrivener 2012, Du and Tan 2014). The expansion process due to ASR has been increasing up to this pessimum

level. After that, adding reactive materials reduces the expansion, so an amount lower or higher than the pessimum limit causes a decrease in expansion due to ASR.

According to Multon and Cyr et al.'s (2010) report, expansion does not occur in particles smaller than 0.08 mm. In contrast, the maximum expansion for particles is between 0.63 mm and 1.25 mm. Based on this study, the increase of aggregates smaller than 0.08 mm has reduced expansion. On the other hand, since finer grains have more surface area than coarser grains, they are more likely to be attacked by alkali. Therefore, increasing the level of aggregates increases the amount of expansion due to ASR. Poyet and Sellier's (2006) results have also shown a decrease in expansion with the increase of fine aggregates.

Thomas and Fournier et al. (2007) mentioned the effect of porosity in aggregates which was another influential factor in ASR reaction. Thus, the ASR rate increases with the increase of porosity in aggregates. The presence of porosity in the structure of aggregates provides easy access for moisture absorption. Similarly, according to Haha, Gallucci et al. (2007) report, increasing the porosity of the aggregates enhances the ASR reaction.

2.3.2 Alkali Content

Bérubé and Fournier's (1993) investigations revealed that in cementitious materials, Portland cement is the principal source of accessible alkali. Moreover, cementitious supplementary materials, such as fly ash or natural pozzolans, or external sources, such as chemical compounds of salt water, can also be other sources for the amount of alkali in the concrete mixture. Alkalinity is another influential factor in ASR reaction. Hobbs's (1998) studies have shown that concrete with a pH of more than 13.5

to 13.9 has a high alkaline content. In contrast, concrete with a pH between 12.7 and 13.1 has low alkalinity.

Marfil et al. (2010) observed in addition to the available alkali in cement; some alkali was also presented in the reactive particles. Further research by Lindgård and Andiç-Çakır et al. (2012) indicated that sodium and potassium ions also play an active role in concrete properties degradation. Equation 2.3 illustrates how to determine equivalent Na_2O from K_2O.

$$Na_2O_{eq} = Na_2O + 0.658\ K_2O \text{ (in percentage)} \quad (2.3)$$

According to Diamond (1983), ions attack reactive aggregates at a substantial rate when the concentration of hydroxide ions in the pore solution is between 0.2 and 0.25 molar.

Recently, Du and Tan's (2014) experimental tests showed that calcium hydroxide also plays a very active role as a source of calcium ions, causing the formation of ASR gels around the aggregates. The produced calcium, which is released during the hydration stages of cement, causes the alkaline ASR gel to form around the aggregates. Over time, these gels absorb the surrounding moisture and cause expansion.

2.3.3 Moisture

In the presence of two other factors, the amount of moisture has a double effect in creating cracks caused by ASR. Humidity is essential in two ways. It initiates the reaction and acts as a transport agent for the reaction components. A decrease in humidity can slow or even stop the operation. Although Woolf (1952) found out that the minimum relative humidity for the reaction is 80%, Raupach and Schiessl (1997) observed that some samples stored in drier conditions are still susceptible to silica dissolution and ASR gel formation. As discussed by several pieces of literature

(Ramyar, Topal et al. 2005, Ichikawa 2009, Garcia-Diaz, Bulteel et al. 2010, Gao, Multon et al. 2013), water plays a crucial role in the spread of ASR in concrete because it transports alkali ions into the matrix of cement paste.

Ramyar and Topal et al. (2005) pointed out that in addition to mixing water, water from the outside may also be absorbed into the concrete. As Du and Tan (2014) discussed, water seems to have a dual effect on ASR, serving as a reactive agent (affecting the expansion rate as reaction products are created) and a transporter for different reactive species. The interfacial transition zone of the aggregates experiences increased expansion and breaking over time due to the gel absorbing water from the surroundings. As a consequence, reducing water exposure may be able to slow or halt the reaction and ASR progression.

2.4 EVALUATION OF ALKALI-SILICA REACTION

More than 70 years ago, ASR was identified as a weakening factor for concrete strength and durability by Stanton (2008). Since then, various test methods have been presented to analyze and evaluate concrete samples affected by ASR. The diagnostic approach is an effective method to identify whether the concrete is degraded or not.

In addition, the stage of development of ASR-affected concrete is also vital to examine the potential ASR damage. Therefore, a practical and accurate method was needed to evaluate and understand the effects of ASR. A constant attempt has been made to accelerate and improve the technique of previous tests. The main methods of tests to evaluate ASR are summarized in Figure 2.6.

With the advent of more reliable methods, such as ASTM C295, ASTM C1260, and ASTM C1293 and new technique, such as MCPT, some methods, including ASTM

C289, ASTM C85 and ASTM C227, have become obsolete in recent years (ASTM 2018, Mukhopadhyay and Shi 2019). Details of the methods are given in Figure 2.6.

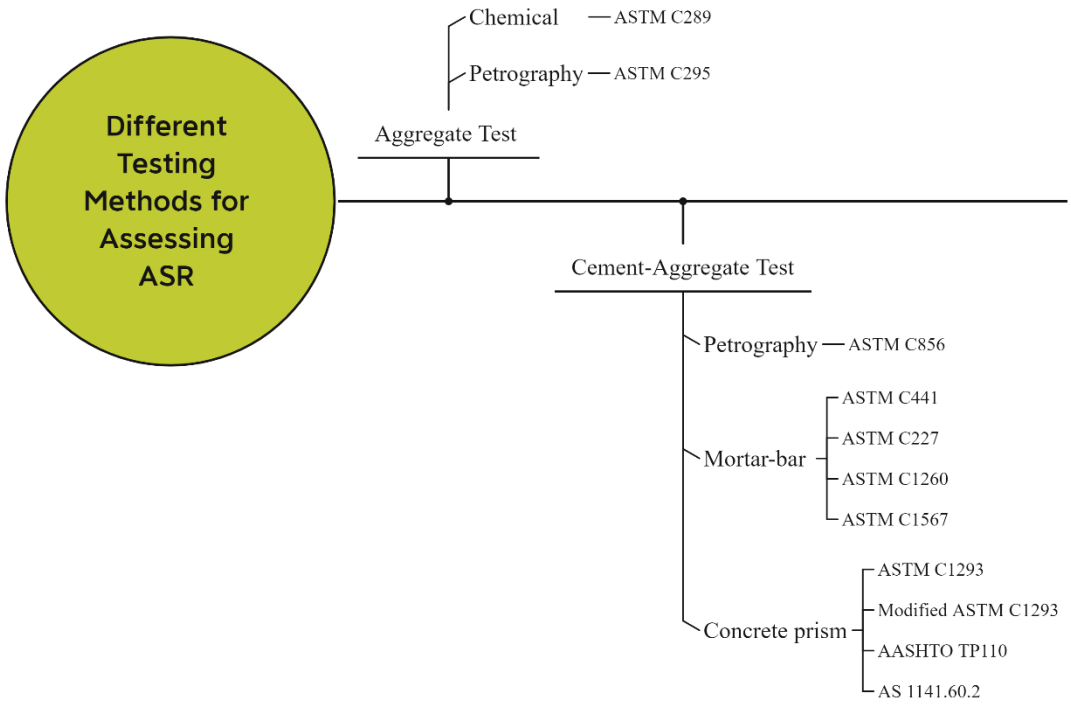

Figure 2.6 Various test methods used for assessing ASR.

2.4.1 Aggregate Petrographic Examination - ASTM C1295

This method was initially presented by Mather (1950) and later modified in ASTM (2003). Initially, this method was developed to identify aggregates' chemical and physical properties. A very thin part of the aggregate is carefully examined using a sieve analysis or an optical microscope (Figure 2.7).

However, this method has weaknesses and limitations, including the inability to describe the level of reactivity of aggregate, and the need for a skilled expert to evaluate. In addition, it is consider as a time-consuming test (Touma, Fowler et al. 2001). Another chemical method was the ASTM C289, which was obsolete in 2016. In this method, to determine the reactivity of aggregates using ground aggregates, the

amount of silica dissolved in sodium hydroxide at 80 degrees is measured for 24 hours, and the decrease in the alkalinity of the solution is estimated.

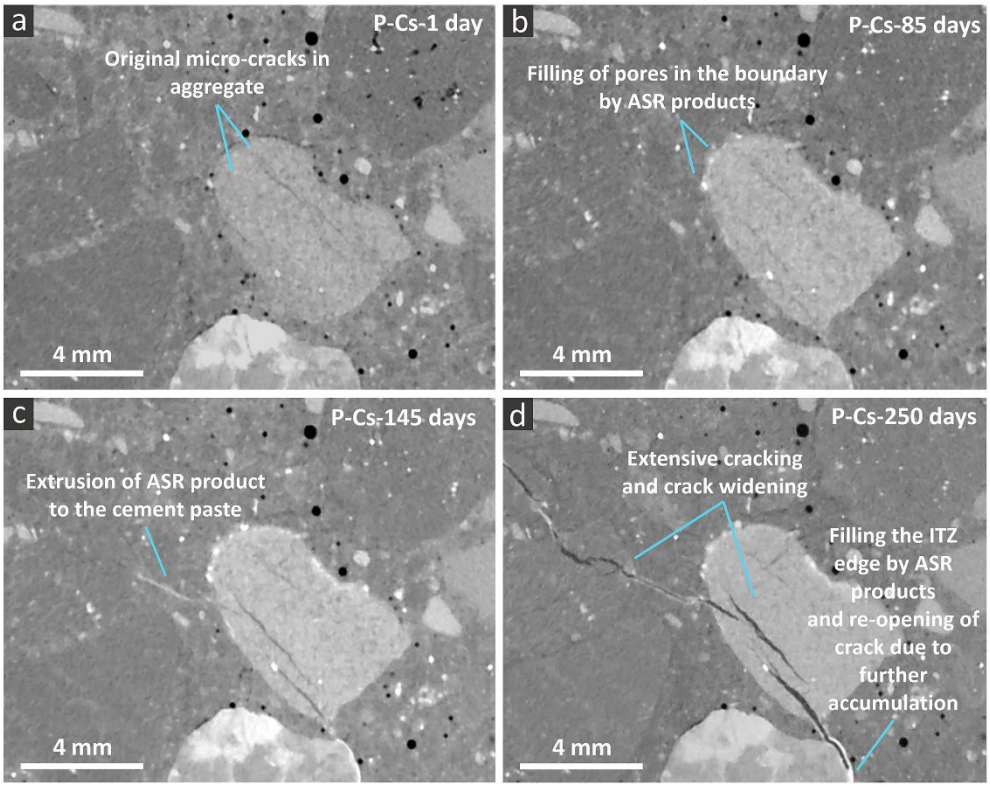

Figure 2.7 Scanning electron microscopy method (Shakoorioskooie, Griffa et al. 2021).

2.4.2 Accelerated Mortar Bar Test (AMBT) - ASTM C1260

The accelerated mortar bar test is an ASR detection and evaluation method that was first invented by National Building Research Institute (NBRI); in 2007, it was revised and approved. One of the characteristics of this test is its short duration. The samples are poured in dimensions of 285 mm × 25 mm × 25 mm and placed in one molar concentration of sodium hydroxide solution at 80 degrees for two weeks. And its results can be measured from the sixteenth day. Based on Folliard and Barborak et al. (2006) studies, this method considers inactive aggregates with less than 0.1% expansion. In these categories, an expansion greater than 0.1% means aggregate reactivity. If the expansion of the aggregates is greater than 0.1% and less than 0.2%,

the aggregates are classified as slow reactive aggregates, which requires a CPT test to determine their reactivity.

Although this method has shortcomings, Folliard and Barborak et al. (2006) and Gillerman and Weppner's (2014) experimental tests detected the aggregates as non-reactive using this method, while in the additional tests by the CPT method, aggregates were categorized as reactive. In another example, Ideker, East et al. (2010) experienced different results from this method and other methods; because the samples were placed in a very harsh environment compared to the normal state. Since the expansion of more than 0.1% is not enough to determine the reactivity of the aggregates, (Hooton 1991) proposed the same test with a slight modification for 28 and 56 days. In the case of 28 and 56 days, the expansion limit for reactive aggregates has increased to 0.28 and 0.48%, respectively.

Contrary to Hooton's (1991) result, which was mentioned earlier, others considered the 14-day period sufficient for this test. For example, Shi et al. (2015) found a 16-day trial to be adequate. And Fernandez-Jimenez and García-Lodeiro et al. (2007) also supported their results and confirmed that some special aggregates, such as xenolith, show more expansion even before 14 days. It can be noted that another weakness of this method is the crushing of aggregates, which can affect their expansion.

2.4.3 Concrete Prism Test (CPT) - ASTM C1293

One-Year CPT

CPT is recognized as the standard method for determining expansion for concrete prism samples. This method is often used to calibrate other methods. Swenson and Gillott developed CPT in Canada in the early 1950s. The limitations of this method are less than the previous methods. In this test, the samples are made with dimensions of 285 mm × 75 mm × 75 mm and placed in sodium hydroxide solution at 38 degrees for

one year. Sodium hydroxide is added to the solution in the amount of 1.25 in proportion to the weight of the cement. According to this test, if the expansion after one year is less than 0.04%, that aggregate is considered non-reactive. Unlike the AMBT method, there is no need to crush the aggregates, and both fine-grained and coarse-grained materials can be tested. This method is one of the most reliable known methods among the various techniques presented by researchers (Thomas, Fournier et al. 2006, Lu, Fournier et al. 2008, Ideker, East et al. 2010) to identify the reactivity of materials.

One of the disadvantages of this method is its duration. A period of at least one year is required to perform this method, in contrast to the AMBT method, which was only 14 days. Therefore, it cannot be used in short-term projects. Another disadvantage of this method is the amount of alkali leaching in concrete samples. About 20% of alkali leaching has been reported by (Rivard, Bérubé et al. 2003, Rivard, Bérubé et al. 2007, and Thomas, Fournier et al. 2012) after only three months from the beginning of the experiment. These limitations made (Thomas, Fournier et al. 2006, Ideker, East et al. 2010) suggest a 13- or 26-week period for this experiment. Therefore, a new test called Accelerated CPT was introduced.

Six-month CPT (Accelerated)

Ranc and Debray (1992) introduced the Six-month CPT method, which is a modification of the ASTM C1293 method to overcome the shortcomings of the previous methods. The purpose of changing the test was to reduce the time duration from one year to half, i.e., six months. In this method, sodium hydroxide is added to the solution by 1.25% weight of the cement. Also, the size of the samples is the same as the CPT samples (285 mm × 75 mm × 75 mm). The temperature of the solution was raised from 38 degrees to 60 degrees to shorten the test's duration. Also, the reports of

Thomas and Fournier et al. (2006) showed that the results of this test had a good correlation with the results of the CPT test.

On the other hand, based on Ideker and East et al. (2010) reports, it was found that reactive aggregates had a significant decrease in expansion in 6 months compared to one-year CPT. The inconsistency of the experiment's results, on the one hand, and the relatively long duration of the experiment, on the other, led to the presentation of another model of experiments known as MCTP.

2.4.4 Miniature Concrete Prism Test (MCPT) – AASHTO TP 110

The MCPT method was developed by Latifee and Rangaraju (2015). This method was presented to overcome the weaknesses of the previous methods, including ASTM C 1260 and ASTM C1293. The results revealed a good correlation between MCPT and ASTM C1293 results. The shortcomings in the AMBT method, such as aggregate crushing, high storage temperatures, and sample size, were evaluated and revised in this method. Similarly, the weaknesses of the CPT method, such as long duration and alkali leaching, were corrected.

In this method, samples are kept at 60 degrees for 56 days in a sodium hydroxide solution with a concentration of 1 N. Unlike the AMBT method, the temperature of 60 degrees reduces the possibility of false results in this method. Also, the reduction in test duration from one year to 56 days compared to the CPT test significantly reduces the chance of alkali leaching. However, increasing the temperature from 38 to 60 degrees might still affect the ASR reaction. The temperature effects on the kinetics of ASR have been presented by (Maraghechi, Rajabipour et al. 2016, Kleib, Aouad et al. 2018). This method uses samples with dimensions of 285 mm × 50 mm × 50 mm. An

expansion of less than 0.04% indicates that aggregates are non-reactive. Moreover, an additional time (28 days) has been considered to ensure slow reactive aggregates.

Though few studies have been done on it, the effectiveness of MCPT for field performance has not yet been established. In general, the adaptability of this test needs more experimental studies. Two methods were presented based on the new Australian standard for ASR in 2014. They used the test methods defined in ASTM C1260 and C1293, respectively. The accuracy of these methods was evaluated by (Sirivivatnanon, Mohammadi et al. 2016). According to the results, AS 1141.60.1 was assessed as an accurate and appropriate test for reactive and slow reactive aggregates. However, compared to the ASTM C1260 test, it had weaker results than non-reactive aggregates. As expected, both AS1141.60.2 and ASTM C1293 were more reliable than the AS1141.60.1 method.

2.5 MECHANICAL DEGRADATION INDUCED BY ASR

Compressive strength, tensile strength, and modulus of elasticity are critical parameters in the assessment of concrete structures. Therefore, the relationships between concrete expansion and concrete mechanical properties are crucial to evaluate the behaviour of ASR-affected concrete structures. This section discussed the relationship between the mechanical degradation of concrete properties and ASR expansion.

The serviceability and durability of concrete structures may be threatened by the harmful, degrading process known as ASR. The structural effects of ASR-induced concrete expansion at various scales have been studied in several investigations on concrete structures and members down to the microscopic level. Even though studies have found a strong link between concrete swelling and the deterioration of mechanical

characteristics, there has never been a single, universally accepted conclusion due to the findings.

2.5.1 Experimental Database

The experimental data from the literature have been collected to examine how ASR degrades the mechanical characteristics of concrete due to ASR. During the last three decades, several authors have investigated the loss of mechanical characteristics related to ASR in concrete samples under free expansion circumstances. The conclusions of (Swamy and Al-Asali 1988), (Larive 1997), (Ahmed, Burley et al. 2003), (Monette 1998), (Multon 2003), (Ben Haha 2006), (Giaccio, Zerbino et al. 2008), (Sargolzahi, Kodjo et al. 2010), (Giannini and Folliard 2012), and (Lindgrd (Sanchez, Fournier et al. 2014), and (Esposito, Anaç et al. 2016) were presented and discussed in this section. The data obtained from the tested concrete samples in free expansion conditions with different concrete mixes were collected. In addition, the comprehensive statistical analysis proposed by Esposito has also been provided to ascertain the process of concrete deterioration due to ASR. Table 2.1 summarizes the relevant ASR-affected concrete deterioration from the literature—the interpolated values for the expansion of 500 microstrains as a reference value.

In the collected data set, the water-to-cement ratio range was between 0.3 and 0.61, and the corresponding alkali content was between 0.40 and 2.25% of cement weight. Most samples were either directly submerged in water or held at 38 degrees Celsius with a two-degree variation and high relative humidity.

As the reaction process could be impacted by temperature and relative humidity changes, the guidelines and requirements of existing standards, such as ASTM C1293 and the RILEM recommendation, served as the basis for the maintenance requirements.

Furthermore, half of the researchers left the samples in the fog room for a day at 20 degrees in the initial phase.

Most studies focused on the effects of ASR on elastic modulus E_{st} and compressive strength f_c of concrete. Some researchers also investigated tensile behaviour, represented by the splitting tensile strength, the modulus of rupture MOR, and the direct tensile strength. Non-destructive testing has also been employed in several pieces of research to figure out the dynamic elastic modulus. The samples were given names based on the first author. The number in front of each sample denotes its test number, the letters a, b, and c denote its testing environment, and i, ii, and iii indicate the author's mixing of various concrete mixes.

Based on the asymptotic expansion value obtained, the concrete mixes were categorized to examine the effects of ASR on mechanical properties from the test results. Concrete mixes with expansion between 500 and 1000 microstrains were classified as possibly reactive, between 1000 and 5000 microstrains were considered reactive, and expansion greater than 5000 microstrains was categorized as extremely reactive. For expansion lower than 500 microstrains, concrete mixtures were categorized as non-reactive and excluded from the analysis.

Figures 2.8 and 2.9 provide detail of degradation in mechanical characteristics resulting from concrete expansion due to ASR. Except for Swamy's experiments, which only examined two samples at each step, the data in Figure 2.8 represents the average outcome of testing three samples. The results of the tests revealed that the elastic modulus deteriorated significantly in all samples.

Table 2.1 Experimental data sets of collected ASR-affected concrete samples from literature. (Esposito, Anaç et al. 2016)

Author	*Data set*	*Time (day)*	*Expansion*	E_{st} *(GPa)*	E_{dyn} *(GPa)*	f_c *(MPa)*	$f_{t,sp}$ *(MPa)*	*MOR (MPa)*	$f_{t,dir}$ *(MPa)*
Swamy	*ER1*	*365*	*0.62*		*39.0*	*52.23*	*3.24*	*4.08*	
	ER2	*365*	*1.64*		*34.3*	*43.08*			
Larive	*RR*	*365*	*0.21*	*33.9*		*52.64*	*3.93*		
Monette	*RR*	*147*	*0.35*	*18.8*	*38.2*	*27.51*		*5.87*	
Ahmad	*RR*	*365*	*0.15*	*32.7*		*51.15*	*4.74*	*5.37*	*4.80*
	ER1	*365*	*0.73*	*36.3*		*50.30*	*5.05*	*6.76*	*2.60*
	ER2	*365*	*2.70*	*22.1*		*41.22*	*3.57*	*5.26*	*1.42*
Multon	*PR*	*365*	*0.10*	*32.6*		*42.01*	*3.14*		
Ben Haha	*PR1ia*	*365*	*0.05*	*24.8*		*63.86*	*4.35*		
	PR1iia	*365*	*0.07*	*24.8*		*51.43*	*3.81*		
	PR1iiia	*365*	*0.08*	*25.2*		*53.62*	*4.05*		
	PR1ib	*365*	*0.05*	*21.8*		*51.09*	*4.39*		
	PR1iib	*365*	*0.12*	*26.8*		*48.27*	*4.27*		
	PR1iiib	*365*	*0.14*	*25.00*		*46.15*	*4.25*		
	PR1iic	*365*	*0.14*	*25.00*		*46.15*	*4.25*		
	PR1iiic	*365*	*0.16*	*26.50*		*47.53*	*4.36*		
	PR2ia	*365*	*0.05*	*26.4*		*34.26*	*4.25*		
	PR2iia	*365*	*0.07*	*25.7*		*55.72*	*3.81*		
	PR2iiia	*365*	*0.07*	*24.9*		*54.73*	*3.93*		
	PR2ib	*365*	*0.12*	*26.7*		*50.47*	*4.22*		
	PR2iib	*365*	*0.14*	*26.0*		*48.98*	*4.33*		
	PR2iiib	*365*	*0.14*	*25.8*		*47.93*	*4.25*		
	PR2iic	*365*	*0.14*	*25.5*		*49.21*	*4,37*		
	PR2iiic	*365*	*0.16*	*26.2*		*47.47*	*4.37*		
Giaccio	*PR*	*365*	*0.08*	*38.1*		*36.50*			
	RR1	*365*	*0.21*	*24.1*		*30.20*			
	RR2	*365*	*0.28*	*32.0*		*27.80*			
Sargolzahi	*PR*	*365*	*0.08*	*32.5*	*20.9*	*43.02*			
Giannini	*RR1*	*120*	*0.14*	*25.5*		*36.82*			
	RR2	*270*	*0.42*	*25.4*		*34.52*			
Lindgard	*PR1a*	*365*	*0.05*		*44.7*				
	PR2a	*365*	*0.08*		*51.6*				
	RR1a	*365*	*0.21*		*36.5*				
	RR2a	*365*	*0.26*		*42.1*				
	PR1b	*273*	*0.14*		*43.2*				
	PR2b	*273*	*0.17*		*47.6*				
	RR1b	*273*	*0.18*		*34.7*				
	RR2b	*273*	*0.23*		*38.7*				
	PR1c	*273*	*0.04*		*40.3*				
	PR2c	*273*	*0.06*		*49.1*				
	RR1c	*273*	*0.28*		*37.8*				
	RR2c	*365*	*0.27*		*42.7*				
Sanchez	*RR1i*	*63*	*0.30*		*21.0*				
	RR1ii	*63*	*0.30*		*29.5*				
	RR1iii	*63*	*0.30*		*28.0*				
	RR2i	*182*	*0.20*		*23.2*				
	RR2ii	*182*	*0.20*		*30.9*				
	RR2iii	*182*	*0.20*		*29.3*				
Esposito	*RR1*	*365*	*0.11*	*39.5*		*60.11*	*3.76*		
	RR2	*365*	*0.18*	*26.1*		*61.23*	*3.85*		

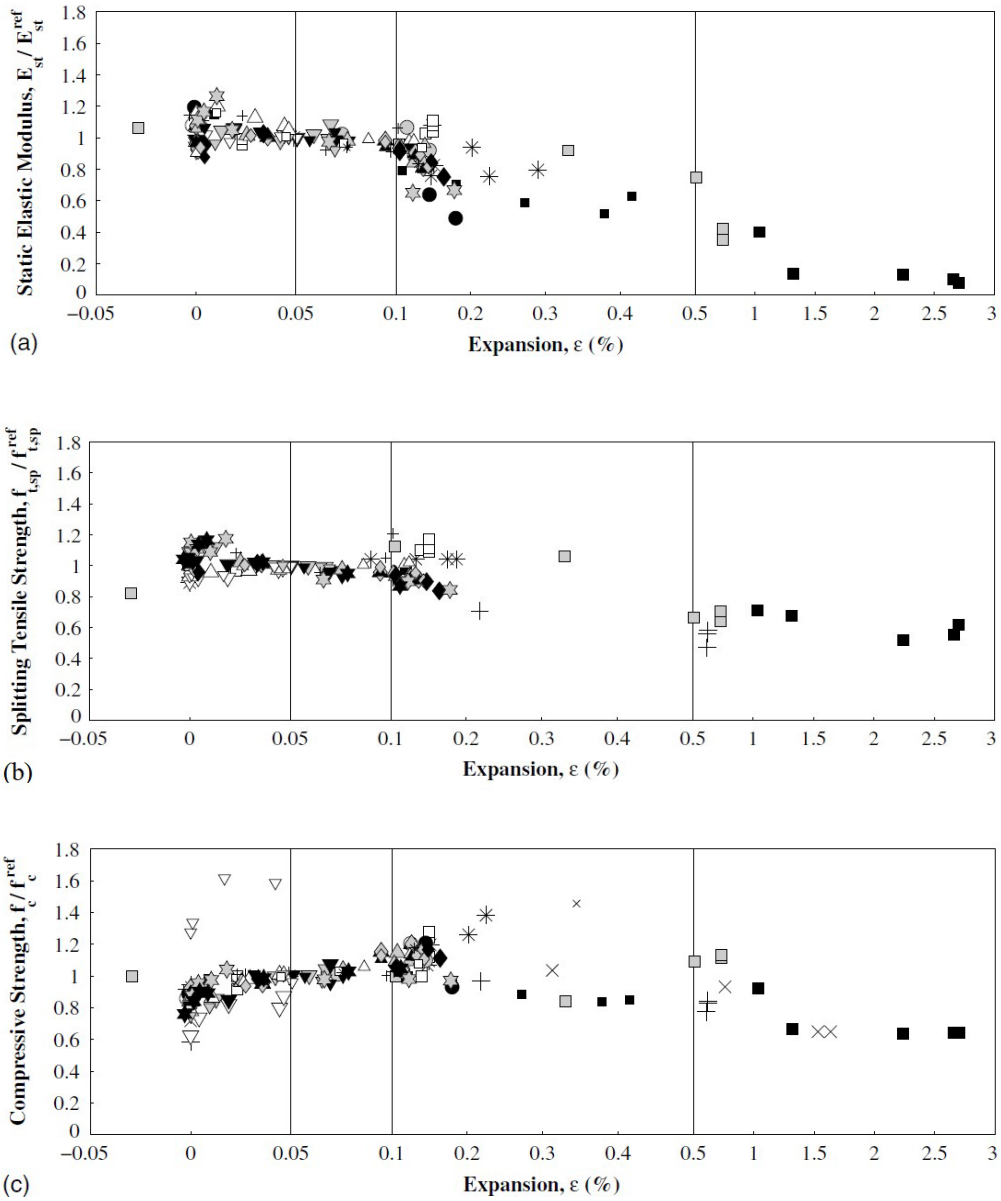

Figure 2.8 Literature-based experimental data: (a) static elastic modulus; (b) splitting tensile strength; (c) compressive strength (Esposito, Anaç et al. 2016).

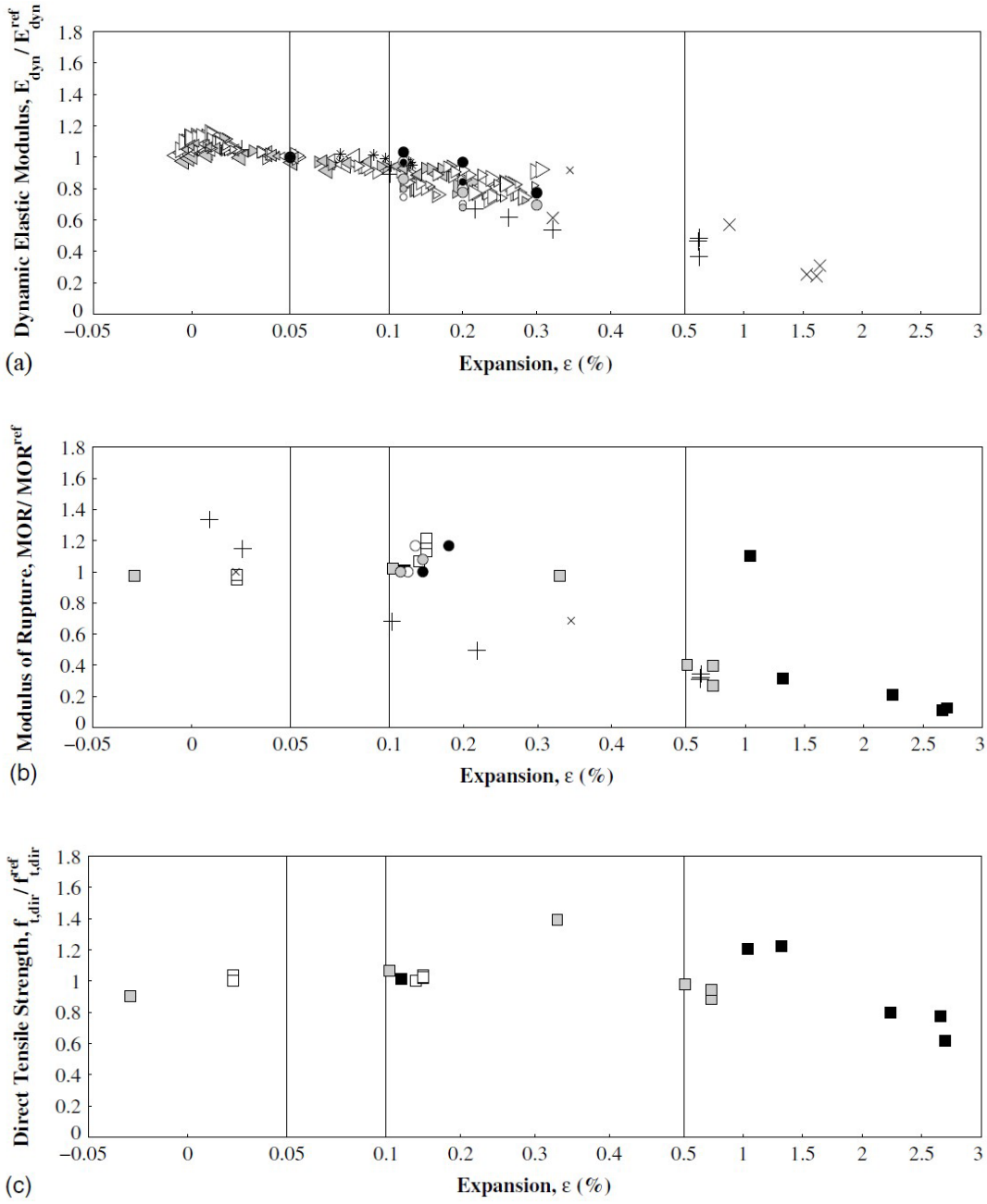

Figure 2.9 Literature-based experimental data: (a) dynamic elastic modulus; (b) Modulus of rupture; (c) direct tensile strength (Esposito, Anaç et al. 2016).

The normalization approach has been utilized to compare the experimental outcomes. In general, four zones were introduced: the low expansion zone (expansion less than or equal to 0.05%), the medium expansion zone (0.05%–0.10%), the high expansion zone (0.10%–0.50%), and the extremely high expansion zone (0.50%).

Modulus of Elasticity (MOE)

The effect of ASR on the elastic modulus is summarized in Figures 2.8 and 2.9. The static and dynamic elastic modules have marginally increased for expansion values up to 0.03%. Although there is a little decline in regions of low and medium expansion, the average values of changes in these zones still hover around one. Since the stiffness qualities reduced as samples expanded further, both stiffness properties declined at the same rate for expansions more significant than 0.1%. The region of severe expansion, where the static and dynamic modulus of elasticity has fallen by 92% and 86%, respectively, has experienced the most degradation.

Tensile Strength (TS)

It was found that, like the tensile behaviour of unaffected concrete, the tensile behaviour of ASR-affected concrete was highly dependent on the test method. The normalized values for tensile strength in all three methods were almost equal to one in the low-expansion zones. While the splitting and flexural tests showed a remarkable decrease in tensile strength for the values of the high-expansion zones, this decreasing trend was lower for the direct tensile strength of the ASR-affected sample.

The direct tensile strength degraded significantly only in zones of severe expansion. However, only three concrete mixtures were evaluated for direct tensile strength by Ahmed et al (2003). Extreme-expansion zones exhibited the greatest deterioration in tensile strength. Compared to unaffected samples, the rates of splitting tensile strength, the modulus of rupture, and direct tensile strength were lowered by 53%, 89%, and 38%, respectively. (Figures 2.10 and 2.11)

Compressive Strength (CS)

Extensive research has been conducted into the compressive strength of specimens, even though it is a poor predictor of the beginning or advancement of ASR, according to the findings of Swamy's investigations. Figure 2.10(c) depicts this pattern. The normalized compressive strength value ranged from 0.59 to 1.62, with an average of 0.92 in the region with modest expansion. The sample that included the least amount of alkali content and was maintained at a temperature of 20 degrees experienced the least reduction in compressive strength. Given the low alkali content and storage circumstances, it might be concluded that ASR did not significantly cause concrete to expand. The increase in strength may be attributable to the concrete's hydration process. As a result, the highest normalized value in the region of low expansion was decreased to 1.04 by deleting this data from the data set. Data density is low and compressive strength has a normalized value of 1.28 in the region of medium expansion. The compressive strength of most concrete mixes has decreased for expansion values larger than 0.15%. Nevertheless, the results indicated a sizable number of exceptions. The most significant compressive strength degradation in the region of intense expansion was 46%.

The splitting test findings appeared to capture the tensile behaviour accurately. In the high-expansion zone, tensile strength and elastic modulus decline at about the same rates. Its value is 46% of the reference tensile strength. When the elastic modulus approached 85% of its initial value, the rate of deterioration of compressive and tensile strength decreased at a similar rate but still more slowly than that of the elastic modulus. The compressive strength was drastically reduced to a normalized elastic modulus value of 0.20%.

2.5.2 Statistical Analysis

The data sets were divided into four categories: non-reactive, potentially reactive, reactive, and highly reactive. An S-shaped and piecewise linear curves were defined by considering the statistical analysis of two different fitting laws. The generated S-shaped curves and the experimental results are shown in Figure 2.10.

In addition, lists of the estimation errors and fitting coefficients in terms of standard deviation are summarized in Tables 2.2 and 2.3.

In terms of the elastic modulus, as seen in Figure 2.11(a), the curves show a slight difference only in the extreme-expansion zones. All data indicate stiffness degradation in ASR-affected concrete. The estimation error was calculated to be as small as 7%. In this case, latency time (ε_l) is minimal, which indicates fast stiffness degradation starting from the early stages. The normalized values for elastic modulus (minimum β_0 and maximum β_∞) were between 0.19 and 1.06. The elastic modulus was identified as the best indicator of ASR symptoms in concrete, indicating the corresponding degradation even at small expansion values. Degradation up to 90% was observed for the elastic modulus of concrete affected by ASR. Also, it showed that tests of the elastic modulus, both static and dynamic, can describe the residual stiffness of the material.

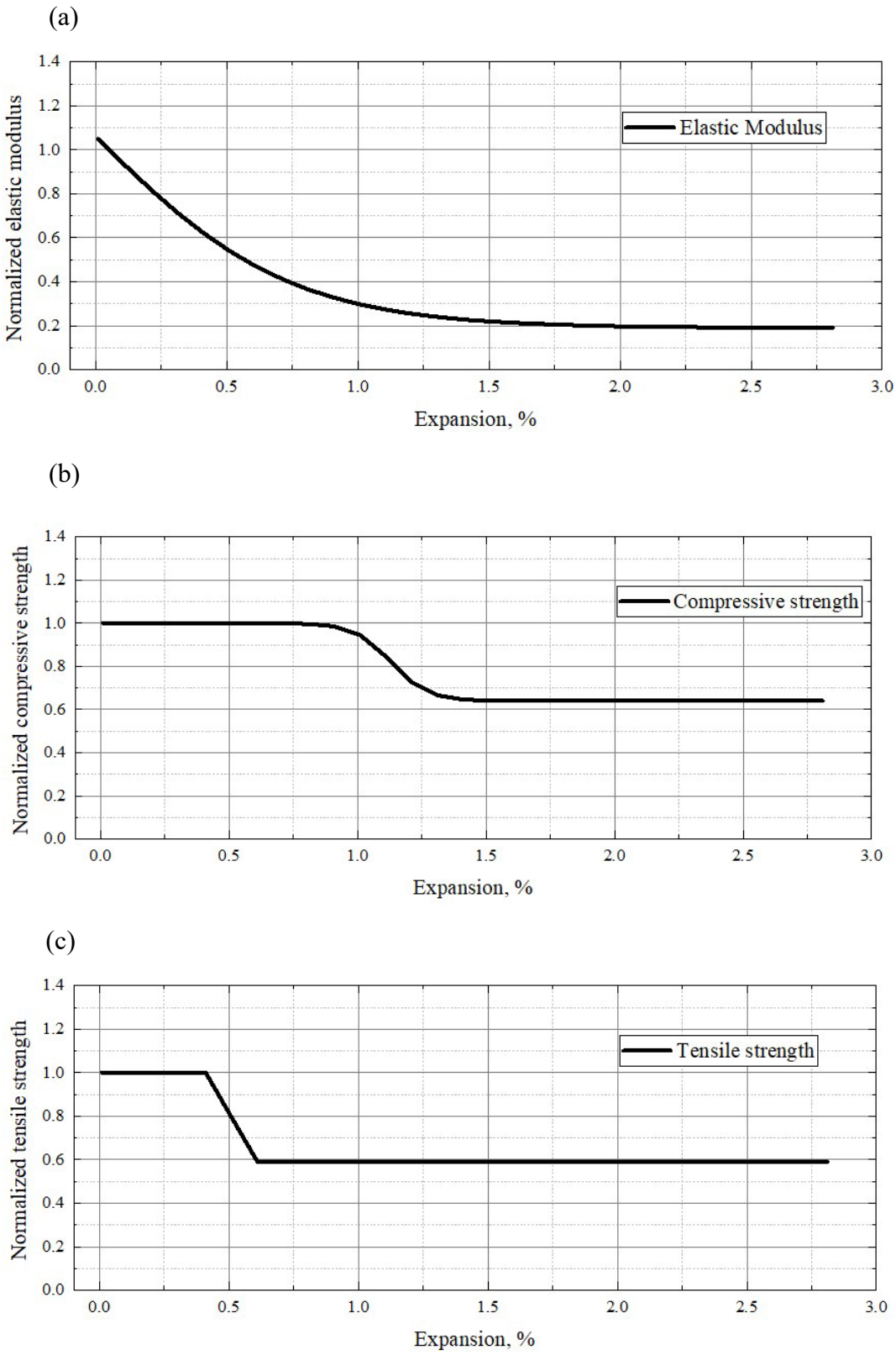

Figure 2.10 Utilizing an S-shaped curve: (a) modulus of elasticity; (b) compressive strength; (c) tensile strength.

The degradation process for compressive strength with an S-shape curve is provided in Figure 2.10(b). An initial increase in strength cannot be considered due to the nature of the formulation. The maximum normalized value of β_0 is 1.00, and the latency expansion ε_l is 0.51%. The S-shaped curve exhibits an asymptote at 0.64 with the 15% estimated error.

For the evaluation of the tensile strength, each test method should be considered separately due to the sensitivity of tensile strength results to the test type. The curve based on splitting tensile strength data with an 8% error provided the finest fitting. The range of normalized values is from 1.01 to 0.60. After a latency expansion of 0.35%, degradation is obvious. The modulus of rupture started to decrease almost at the same level. Maximum degradation for this procedure was estimated at 76%. The estimation error was 20%, which is significant. The direct tensile strength indicated a maximum deterioration of 30% with a latency expansion of 2.15%, and the estimation error was 12%.

Table 2.2 Standard deviation and fitting coefficients for S-Shape curve (Esposito, Anaç et al. 2016)

Data	$\mathcal{E}_c$ (%)	$\mathcal{E}_l$ (%)	β_0	β_∞	σ (%)
E	0.37	1.13×10^{-9}	1.06	0.19	7
E_{st}	0.42	2.27×10^{-14}	1.05	0.11	9
E_{dyn}	0.31	6.89×10^{-12}	1.07	0.29	6
f_c	0.07	1.13	1.00	0.64	15
f_t	5.24×10^{-4}	0.51	1.00	0.59	15
$f_{t,sp}$	0.11	0.35	1.01	0.60	8
MOR	0.07	0.37	1.05	0.34	20
f_{tdir}	0.10	2.15	1.05	0.70	12

Where β_0 and β_∞ are the maximum and the minimum normalized values of the elastic modulus and $\mathcal{E}_l$ and $\mathcal{E}_c$ are the values of the latency and characteristic expansion and σ is the estimation error.

Moreover, the piecewise linear curve was also proposed by Esposito to depict the behaviour of compressive strength. However, The S-shaped curve was chosen to describe other characteristics, including tensile strength and elasticity modulus.

Figure 2.11 illustrates the experimental data and the resulting piecewise linear curve. Table 2.3 displays the estimation errors and fitting coefficients in terms of standard deviation.

The piecewise linear curve accurately described the decrease in the elastic modulus as well. Comparable results are obtained by measuring the estimated error and degradation rate in the high-expansion zone and by fitting S-shaped curves. This formulation supplies the elastic modulus at unrealistically negative normalised values for more than 2.60 % expansion values. After this limit, the residual stiffness should be deemed to be zero.

The piecewise linear curve better described the compressive strength behaviour (Figure 2.11(b)), indicating an increase in the medium-expansion zone. This method's total estimation error reached 13%, slightly lower than the s-curve error. However, the estimation error decreased from 20 to 13%, only considering the medium-expansion zone. The piecewise linear curve showed a similar trend and the estimation error to the S-shaped curve for splitting tensile strength (Figure 2.11(c)).

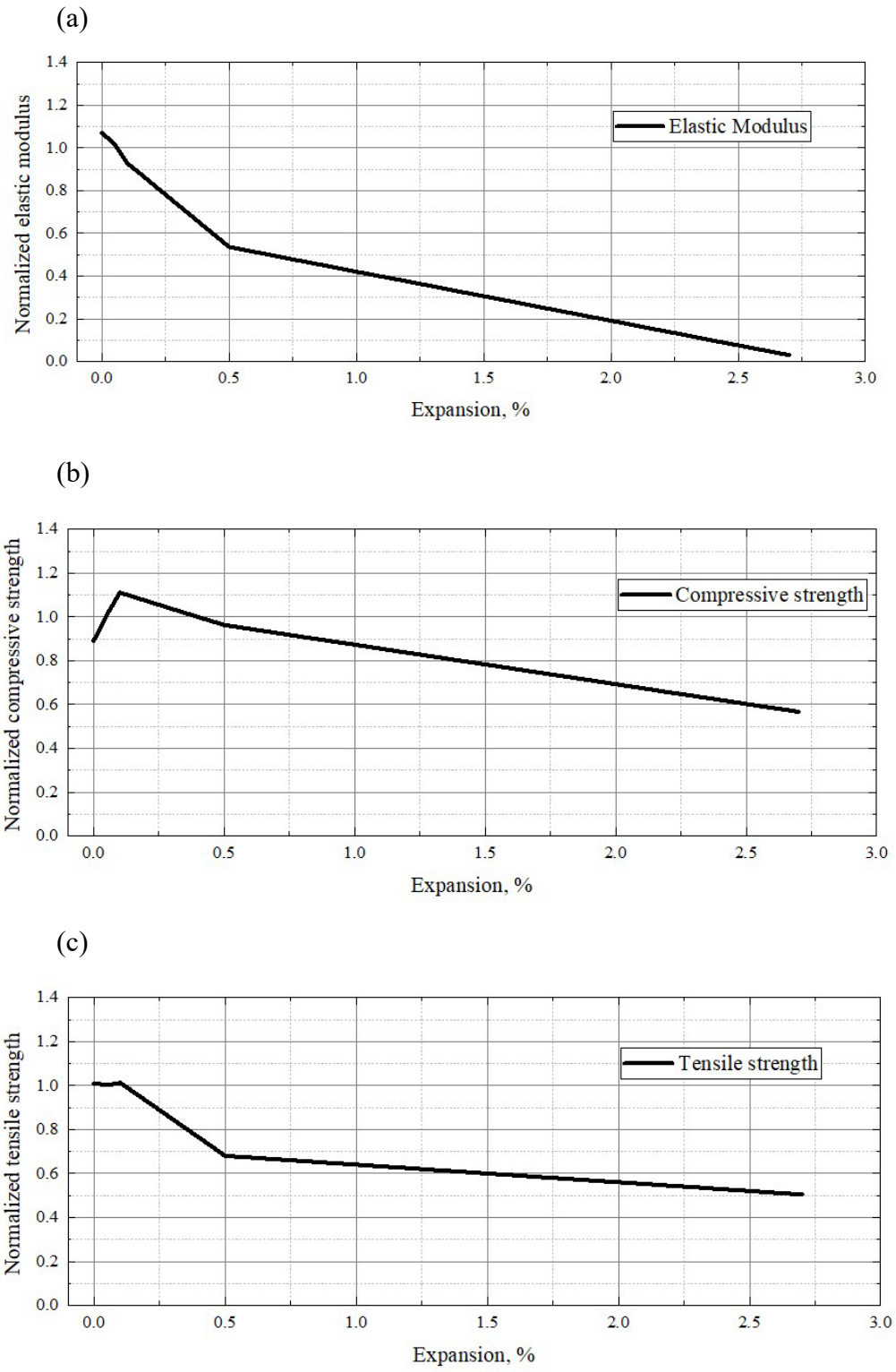

Figure 2.11 Adopting a piecewise linear fit curve: (a) modulus of elasticity; (b) compressive strength; (c) tensile strength.

Based on the linear fitting curve, the data show the degradation of elastic modulus at the beginning of the initial expansion. The residual stiffness is equal to 20% of the

reference value for high expansion (expansion greater than 2000 microstrains). On the contrary, the compressive strength trend experienced an initial increase of 15% and a maximum decrease of 46%, although the 13% estimation error is relatively high.

Table 2.3 Standard deviation and fitting coefficients for piecewise linear curve

Data	q_1	m_1	m_m	m_h	m_e	σ (%)
E	1.07	−1.06	−1.78	−0.98	−0.23	7
E_{st}	1.04	−0.46	−1.89	−1.08	−0.21	9
E_{dyn}	1.08	−1.43	−1.75	−0.91	−0.26	6
f_c	0.89	2.36	2.06	−0.37	−0.18	13
f_t	1.01	−0.15	0.20	−0.83	−0.08	15
$f_{t,sp}$	1.01	−0.25	−0.15	−0.86	−0.04	8
MOR	1.06	0.53	0.04	−1.54	−0.14	20
f_{tdir}	0.97	2.23	−0.68	0.20	−0.18	13

Where q and m are the linear coefficients for different zones.

2.6 ASR EXPANSION AND CRACKING

ASR reaction occurs in structures containing specific silica reactive aggregates and an alkaline environment. Engineers can identify this phenomenon pathology by the concrete structure cracks observation. ASR crack propagation mainly occurs in structures that bear significant loads or those restrained by external loading conditions, including bridge foundations, dams, etc. Restraint of expansion by rebars as well as prestressing in concrete structures causes tension during expansion. Many recent studies have been conducted on free expansion conditions. So that several models realistically predict the ASR-caused expansion; however, the ASR expansion under constraints is still not fully understood. This section aims to investigate the effect of applied stresses caused by rebar restraint or external restraint through limitations in boundary conditions on the expansion of ASR and anisotropic cracks based on previous experimental data. Some experimental studies on the effect of restraint on ASR

expansion have been collected and reviewed in the following sections to investigate the effect of stresses and cracks caused by the alkali-silica reaction.

Jones and Clark (1996) designed an array of laboratory tests to evaluate the effect of restrained expansion. Their experiments aimed to gain experimental data for expansion under different conditions, such as free expansion, rebar-restrained, and external stress. In their study, 120 short and 12 long specimens were conducted to assess the effect of ASR on the expansion of concrete samples in different conditions, such as reinforcement, free expansion, and externally applied stress. 100 × 200 cylindrical samples made of active aggregates were cast for experiments. Different-sized rebars were inserted into these specimens to assess the effect of rebars on specimens with 0, ¼, 1, 2, and 4% of steel ratios. In addition, some specimens were subjected to different external stresses of 0, 1, 2, and 4 MPa to determine the effect of external compressive and tensile stresses. It was reported that after 200 days, the free expansion was 5800 microstrain; however, the expansion was 4100, 3200, 2500, and 2100 microstrain for concrete specimens with 1, 2, 3, and 4% steel ratio, respectively. The results indicated that the expansion was 36, 43, 55, and 70% lower than the free expansion. After 200 days, the expansion was measured at 1600, 2500, and 950 microstrains for the specimens under 1, 2, and 4-MPa stress, respectively. In other words, the expansion was reduced by 16, 28, and 43%, respectively, due to external stress. The experimental results showed that ASR-induced expansion was reduced as the compressive stress and reinforcing rebars increased. If the compressive stress were higher than 2 MPa, a higher percentage of reinforcing rebars would not reduce the expansion. The results also indicated that compressive stress of 10 MPa is needed to prevent ASR expansion. The expansion rate did not significantly affect the relationship

between free and restrained expansion. The experiments also determined the correlation between free expansion and specimen size.

Similarly, Li and Tan's (2020) investigations revealed that the amount of stress state significantly affects the expansion and cracks caused by ASR. Stresses can be caused by an internal restraint such as rebar or an external restraint in boundary conditions. Thus, several experiments have been conducted on the restraint effect on ASR. Additionally, the effect of rebars in the expansion caused by ASR has been investigated. For this purpose, cubic concrete samples with reactive aggregates and various 12, 16 and 20 mm rebars have been used. Their study investigated the effect of internal rebars on expansion. This experiment used concrete with compressive strength of 40 MPa and reactive aggregate. Cubic samples of 150×150×150 were reinforced with 12-, 16- and 20-mm diameter rebars. The rebars were placed in the middle of the cube. For this experiment, the rebars' embedded length was considered $5\times ds$[1]. (To avoid underestimating and scattering its strength) (Okelo and Yuan 2005, Liu, Yang et al. 2017). After 28 days, the samples were placed in sodium hydroxide solution with one molar concentration and at a temperature of 80 degrees to accelerate the ASR reaction. Then, the samples were measured once every seven days for 170 days. However, it should be noted that according to the accelerated environment type, the ASR gel's viscosity obtained will be different from the actual conditions due to the different concentrations and temperatures. This test showed that after 170 days, the expansion for the first sample was equal to 0.448%, while the expansion rate for the sample with 12, 16, and 20 rebars was equal to 0.344, 0.324, and 0.277%, respectively.

[1] Diameter of the rebar

It should be noted that the samples' expansion was nearly identical until the first 90 days, after which a slight difference in expansion was identified.

Kagimoto, Yasuda et al. (2014) performed several experimental tests and examined the longitudinal and transverse expansion of concrete samples in the dimensions of 100×100 to study the effect of expansive pressure subjected to different degrees of restraint. According to their findings, the relationship between expansive pressure and degree of restraint was almost linear for different amounts of alkali. And the rate of expansion has decreased drastically from a degree of restraint. In addition, expansion was expanded in directions perpendicular to the restrained direction. The results also stated that the cracks spread along the restraining direction. Concrete samples of 100×100×400 were placed in an assembled machine using metal sheets, rebars and a load cell. Expansive pressure caused by ASR has been measured using a load cell. After 24 hours of concreting the samples, they were unmoulded and placed in this assembled machine. Also, an initial pressure of 0.2 MPa was applied to samples to stabilize them in place. The samples were placed in water at 40 degrees to speed up the ASR reaction. Also, rebars with different diameters of 44, 31, 18, 14, 8, 6, and 3 mm have been used to create different degrees of restraint. The restraint ratio was expressed as a relative percentage (A_s/A_c). A free expansion was measured from the average of three samples. The free expansion in these experiments has been checked for different amounts of alkali content. The samples have expanded continuously, almost after 28 days. After 100 to 130 days, the expansion reached a constant value for the samples. Also, the increase in pressure after this period, like the free expansion curves, was minimal. The maximum compressive strength of 4.9, 1.1 MPa has been measured for two beams. In this study, the amount of alkali was measured as 7 kg/m^3. Their experiment showed that the ultimate expansion pressure for the percentage of

reinforcement less than 1% was proportional to the percentage of reinforcement. In comparison, the rate was significantly reduced by 3.1% and higher. As in previous reports, it has been shown in this experiment that after a certain amount of alkali, adding it reduces expansion.

A series of laboratory tests were conducted to acquire the effect of restraint on ASR expansion by Mohammed and Hamada et al. (2003). Several experimental samples with a cross-sectional area of 250 × 250 mm and a length of 600 mm and different amounts of restraint were made and examined. In this series of experiments, the samples were placed at a temperature of 40 degrees to accelerate the ASR reaction. Also, sodium hydroxide was added to the concrete mixture to reach 6 kg/m^3. Eight samples with different designs were made and examined.

The first model is a non-ASR model that was made without using rebars for comparison. The remaining seven samples were cast with different design details and used reactive materials. The size of the rebars varied between 12.7 and 25 mm. And in samples 3, 6, 7 and 8, an end plate was also used. Case 1 was cast as a control case with nonreactive materials and without rebar. In this sample, the amount of strain was less than 200 microstrains. In contrast, case 2 was made using reactive materials and without rebar to measure the expansion rate as free expansion. In this expansion sample, after 197 days of exposure to the ASR environment, the strain in both longitudinal and transverse directions was measured to be approximately 600 microstrains. The expansion ratio of length to width was almost equal to one.

In the third sample, a rebar with a diameter of 13 mm was used in the centre of the sample. Also, the ends of the rebars were enclosed with end plates. A considerable difference was observed between the expansion in the longitudinal and transverse

directions. So that the strain in the longitudinal direction was equal to 400 microstrains compared to the strain in the transverse direction, which was approximately 7550 microstrains; in other words, the ratio of expansion in the transverse direction to the length was equal to 2. In the fourth example, this time, it was designed and made from a 13 mm rebar without an end plate. Removing the endplate in this sample caused the degree of restraint to decrease in these samples. Therefore, the longitudinal strain in this sample has increased compared to the previous state, with the decreased strain in the transverse direction. The ratio of expansion in the transverse to longitudinal direction was 1.3. (Versus 2 for sample number three). In sample number five, a 12.7 mm rebar was used in the centre, with the difference that deformed rebar was used instead of a smooth one. The level of restraint in these samples was estimated to be between the third and fourth. Therefore, the ratio of transverse to longitudinal expansion in these samples was 1.5. This amount was larger than sample 4 and smaller than sample 3.

Similar to sample 3, a rebar with a diameter of 25 was used in the centre of sample number 6 and was bounded by an end plate. But the steel ratio of this sample is 3.7 times that of the third sample. The transverse to longitudinal strain ratio was estimated as 1.9. The surface strain has not changed much compared to the third sample. In sample 7, four smooth round bars were used along with the end plate. The steel ratio in this sample was equal to sample number 6, with the difference that the rebars were distributed in the four corners of the sample. This change in the placement of the rebars has caused a significant reduction in the length strain compared to sample number 6. The ratio of transverse to longitudinal strain is higher than in other samples and almost equal to 3.6.

In the final sample, sample 8, five stirrups were used to restrain the strain in the transverse direction and 4 bars in the longitudinal direction. The results showed that stirrups did not have much effect on expansion, so the lateral-longitudinal ratio in these samples was almost 3.4. The results of this experiment showed that the expansion process could be divided into three parts: the first was a prolonged expansion rate period, the cracking period with the maximum expansion rate and the stabilized period with few changes in expansion. It has also been demonstrated that the bars' position significantly affected the samples' expansion in addition to the steel ratio. As a result, the amount of expansion for two samples with the same percentage of steel and only by changing the position of the steel has decreased significantly. Therefore, the closer the rebars are to the surface, the amount of strain on the surface also decreases while it increases the lateral strain. The overall results of the studies show that increasing the compressive stress can reduce the expansion caused by ASR.

2.7 EFFECT OF ASR ON STRUCTURAL BEHAVIOUR

There have been a significant number of tests on ASR beams. The literature is organized and examined according to the names of the researchers or investigating organizations.

Three series of reinforced concrete beams with various ratios of tensile steel were tested by Abe (1989) to find out the impact of ASR on yield strength and ultimate strength. The experimental tests consist of three sets of reinforced concrete beams with various longitudinal and transverse steel ratios of 0.75, 1.17, 1.75%, and 0.32%, respectively. Overall, 30 concrete beams with a 200 × 200 mm square cross-section and 2-meter length were tested to find out the effects of ASR on the structural behaviour of the reinforced concrete beam. The alkali content of the concrete was boosted to 8

kg/m^3 by adding 5.83 kg/m^3 of sodium hydroxide to the concrete mixture. After 192 days, the longitudinal expansion in series 1 to 3 was read as 1000, 600, and 500 microstrains and the transverse expansion of beams was 3600, 2800, and 2700, respectively. Under a 4-point loading test setup, the reactive and non-reactive beams exhibited similar behaviour in the elastic region. Then after, the stiffness of the ASR beams was higher than the non-ASR specimens. The first and the second series of non-reactive beams failed in the diagonal tension failure, whereas the failure mode for the third group was diagonal shear tension failure. However, the first and second series of beam failure modes were switched to flexural after ASR; a failure mode for the third set after ASR was horizontal slip failure. Their test findings indicate that although the ultimate strength of ASR for series 1 and 2 has remained constant, their yield strength has slightly dropped. Also, yield strength in series three has declined; but particular beams in series three experienced an increase in ultimate strength.

Similarly, six 1.7-meter beams with a cross-sectional of 200 × 200 mm were tested by Susumu Inoue (1989). Three levels of tensile reinforcement ratio, 0.77%, 1.20% and 1.74%, were selected in both ASR and non-ASR beams. All beams were provided with D6 stirrups at a web reinforcement ratio of 0.3%. The alkali was added to the concrete mixture to reach the total amount of 8 kg/m^3 of the weight of cement. The expansion was measured after 178 days of exposure to a temperature of 40 degrees and relative humidity of 100%. The expansion in the longitudinal and transverse directions was measured at 1384, 1075, and 917 microstrains and at 1729, 1607, and 1477 microstrains, respectively.

The test findings revealed that ASR had lowered the cylinders' compressive strength, tensile strength, and elastic modulus by 64, 59, and 48%, respectively, but had increased the flexural cracking load for all beams. All of the beams failed in flexure

except the third series of the control beam, which failed in shear. It should be noted that in these experiments, the span-to-depth ratio was 2.5. Based on the results of this study, ASR beams have a stronger resistance to flexural cracking. There was a maximum 10% loss in yield strength and ultimate strength compared to non-reactive beams. First, second, and third series beams' yield strengths fell by 8, 13, and 14%, respectively. In the third series of the reactive beam, ultimate strength increased, whereas the first and second series beams' final strengths declined by around 5 and 6%, respectively. Additionally, it is noteworthy that the ultimate strength variation between reactive and non-reactive beams was lower than the change in yield strength.

Another research was carried out by S. Ohno (1989). They compared non-reactive and reactive ASR-affected reinforced concrete beams in two phases at 17 and 45 months. Six beams were evaluated throughout two periods of 17 and 45 months. The length of the rectangular reinforced concrete beams was 4 meters with a cross-section of 250 × 500 mm. The alkali content of the concrete was enhanced to 9.2 kg/m^3 by adding sodium hydroxide. All the beams were provided with stirrups at a web reinforcement ratio of 0.3%, whereas longitudinal tensile rebars were selected at 0.78%. After 17 and 45 months, the expansion in longitudinal bars was measured by 250 and 100 microstrains. Additionally, the transverse expansion measured between 1200 and 4500 microstrains.

Their findings revealed that after loading with a span-to-depth ratio of 3, both ASR and non-ASR beams failed in flexural mode. There was less than a 4% change in yield or ultimate strength for ASR beams. The findings demonstrated that when reinforced concrete beams are intended to collapse due to yielding steel, ASR has minimal impact on the bending behaviour of the beams. No significant impact on the

ultimate bending behaviour was also seen. However, stiffness often increases during loading, most likely due to the compressive stress produced by ASR.

At the University of Ottawa, Monette (2000) performed various laboratory tests. Eight reactive and seven non-reactive beams were tested. In reactive specimens, reactive materials were employed, while non-reactive materials were used in non-reactive samples. These experiments were conducted on 900 mm beams having a 120 × 90 mm cross-section. 8 mm tensile rebars were used to strengthen the beams, while 4.8 mm rebars were used for shear reinforcements at every 64 mm. After being exposed for 147 days to a solution of sodium hydroxide with a one-molar concentration at 38 degrees to speed up the reaction, the beams were tested for strength. Beams were subjected to various loading protocols; now, unloaded beams were scrutinized. Expansion at the bottom of the beam was about 900 microstrain; in the middle, there was about 2100 microstrain. Generally, expansion in the transverse direction is estimated to be 3400.

All reactive beams failed in flexural. The results of this test revealed that the ultimate strength in samples with and without ASR was almost identical. ASR did not lessen the beams' ultimate strength in these tests, and various loading scenarios did not affect the structure's bending performance. The research outcomes concerning the influence of ASR on structural behavior is presented in Table 2.4.

Table 2.4 Summary of experimental studies on the structural behaviour of ASR-affected reinforced beams.

	Steel compressive/ Tensile/shear	Age	Alkali Content	Expansion X/Y	Cracking	Failure Mode R	Failure Mode N	Yield Strength %	Ultimate Strength %
	0.75/0.75/0.34			1000/3600	-	Flexural	Diagonal Tension	Slightly lower	
Abe							Diagonal Tension	Slightly lower	
200*200* 2000	1.17/1.17/0.32	192	8	600/2700	-	Flexural	Diagonal Shear Tension	Slightly lower	Slightly higher
	1.76/1.76/0.32			500/2800	-	Horizontal Slip			
Inoue	0.77/0/0.3			1384/1729	Larger	Flexural	Flexural	8.258	4.93827
200*200* 1700	1.2 /0/0.3	178	8	1075/1607	Larger	Flexural	Flexural	13.221	6.329114
	1.74/0/0.3			917/1477	Larger	Flexural	Shear	14.181	-0.78788
	0.78/0.78/0.3	510	9.2	250/1200	-	Flexural	Flexural	0.843882	0.367647
S Ohno	0.78/0.78/0.3			-	-	Flexural	Flexural	-3.26531	-0.73529
250*500* 4000	0.78/0.78/0.3	1350		-	-	Flexural	Flexural	0	1.481481
	0.78/0.78/0.3			1000/4500		Flexural	Flexural	-0.85106	3.703704

Similarly, Fan (1998) conducted various laboratory tests at the University of Carolina. Six reinforced concrete beams with a length of 1.5 meters and a cross-section of 150 × 250 mm were tested. Three of them were reactive, while the others were non-reactive for comparison. 0.4 and 1% of the steel in the longitudinal direction, and 5D stirrups were employed for shear. The samples were immersed in a solution with a concentration of 0.5 M of sodium hydroxide that was created in this experiment to boost the process by adding 10 grams of sodium hydroxide, 14 grams of potassium hydroxide, and 0.1 grams of calcium oxide per litre of tap water. For 0.4 and 1% of the steel ratio, the expansion in the longitudinal direction after 365 days was 820 and 750 microstrains, respectively. Expansion in the transverse direction has also been detected in 1100 and 1200 microstrains.

The cracking load for the ASR beams of the first series decreased by 3%, while it increased by 1.5% for the second series. While the yield strength of the second beam did not vary, that of the first beam changed by 2.5%. The first series beams' ultimate strength has dropped by over 5% due to ASR, while the second series has fallen by less than 3%.

In another set of tests, reactive and non-reactive concrete were poured by Kyoto (1986) onto 1.7-meter beams with a 200 × 200 mm square cross-section. The concrete mixture included 6 kg of alkali per m^3 of cement weight. The steel ratio for compression bars was 0.43 and 1.2%, shear bars were 0.2 and 0.3%, and tensile bars were 0.77 and 1.77%. After two weeks in the accelerating ASR condition, the first cracks appeared at 40 degrees and with tension in the longitudinal bars of 200 microstrains. For beams with 0.43% and 1.7%, the stress in longitudinal bars was 1400 microstrains and 650 microstrains, respectively. Then, the expansion stayed unchanged after 100 days. For bars of 0.2 and 0.3%, the transverse expansion was equivalent to 1800 and 1300,

respectively. Compressive and tensile strength and elastic modulus for cylinders were 59.51 and 34% of non-ASR samples, respectively. The beams were tested under a symmetrical 4-point loading test with a span-to-depth ratio of 2.5 after 150 days.

These tests' findings have led to the observation that ASR beams have fewer bending fractures. Furthermore, no shear fracture was produced. Two non-ASR beams failed in shear, but all the ASR beams failed in flexure. The ultimate strength ratio of ASR to non-ASR beams ranged from 0.95 to 1.1. ASR cracks did not impact the tensile strength or stiffness of concrete beams in this study.

In addition, twenty beams with a square cross-section of 200 × 200 mm were tested by Kyoto (1986) in a different series to determine if their flexural strength was affected by ASR. The beams ranged between 1.4 and 1.7 meters, and 0.77 to 1.2% tensile steel and 0.17% compression steel were employed. The alkali content of the concrete was increased to 8 kg/m^3 by adding sodium chloride to the mixture. The compressive strength of concrete cylinders has reduced to 42%, and the elastic modulus of ASR samples has decreased to 26% after 140 days of immersion in an alkali solution. The span-to-depth ratio of beams was between 1.5, 2, and 2.5 under symmetrical loads. The test's findings demonstrate that the beams' stiffness was comparable, and the ASR beams' strength decrease was limited to 10%. Seven beams failed in flexure, three after ASR failed in shear, and none of the non-ASR beams was damaged.

Takenaka (1987) Investigations were conducted on three 4-meter-long beams having a cross-sectional of 250 × 500 mm. Two reactive and one non-reactive beams were chosen to compare the effects of ASR on the structural behaviour of reinforced beams. The total alkalinity was 9.2 kg/m^3, and longitudinal rebars were 0.89% in tension and compression. The longitudinal bars' ASR-induced stress has been

calculated to be between 6 and 3 MPa. The symmetrical loading on the beams had a 3.3 span-to-depth ratio. The findings indicated that the failure load was increased (9.5 tons against 6.5 tons for non-ASR beams). Every beam failed in flexure. ASR beams had 27.8- and 28-ton failure loads, while non-ASR beams failed by 27.8 tons.

The findings of this investigation further demonstrate that ASR had no impact on the strength or stiffness of the beams. Another test had 27 beams with varying lengths between 1.4 and 3.15 meters and an identical square cross-section of 500×500 mm. The fifteens reactive beams were cast reactive while the remainder were cast with non-reactive aggregate. Shear rebars were between 0 and 0.36%, whereas tensile and compressive rebars were between 0.25 and 0.4%. The curing conditions in this investigation are not specified in detail. The test data analysis was done in two stages over 200 and 337 days. The findings indicate that ASR beams were more complex than standard beams. Additionally, after 200 days, the failure load ratio for ASR beams was the same as 0.94 for conventional beams. The failure load ratio for ASR beams ranged between 0.93 and 1.47 to normal beams in the second stage and after 337 days.

Kobayashi and Inoue et al. (1988) conducted several tests on ten ASR and non-ASR prestressed beams. The 100×200 mm rectangular cross-section and 1.6 meters length reinforced beam were chosen. The prestressing force was applied at around 4.9 MPa and 9.8 MPa, with an 11 mm and 15 mm bar, respectively. The shear steel ratio was 0.58% with a 6 mm diameter. The stirrups were made using 46 mm long bars as well. The prestress force was applied to the beams after 28 days when the concrete had reached its maximum strength. Three distinct concrete mixtures were employed in this investigation. Normal materials were used only in the first series of beams, reactive materials were used in the second mixture, and reactive and non-reactive materials were used equally in the third mixture. The mixes included 6, 8 and 2.8 kg/m^3 of total alkali,

respectively. After applying the prestress force, the beams were immersed in the accelerated ASR water tank. The following outcomes were attained after 284 days of ASR. The beams were tested for flexural and shear tests under loading with a span-to-depth ratio of 2.5 and 4.

All the beams were cracked during bending, and the flexural crack in the first set of beams grew somewhat, but not in the second series. Additionally, the ultimate strength of the beams due to ASR was changed by less than 10% as compared to the non-reactive ones.

Several reinforced concrete beams were recently tested by Multon (2021) to determine the impact of ASR on structural behaviour. From a mechanical perspective, these alterations were seen positively due to the ASR chemical prestress produced in the direction of tensile bars. The issues, though, might become significant over time when fractures grow parallel to the bars. According to their experiments, ASR did not impact the flexural behaviour of beams, resulting in minor deformation for the same loading in the reinforced concrete beams. It is of interest to note that the cracking load has increased.

2.8 PRESTRESSED CONCRETE

2.8.1 Overview

In 1872, Jackson obtained a patent for post-tensioning. A design of tie rods and individual blocks for arched beams was presented. In continuation of his efforts, in 1988, Doehring obtained a patent for prestressing slabs using metal wires.

The concept of prestressing is similar to the idea used in wooden barrels. In wooden barrels, the metal strips were tightened under tensile stress so that they

compressed the wooden staves to resist the internal pressure of the liquid as shown in Figure 2.12.

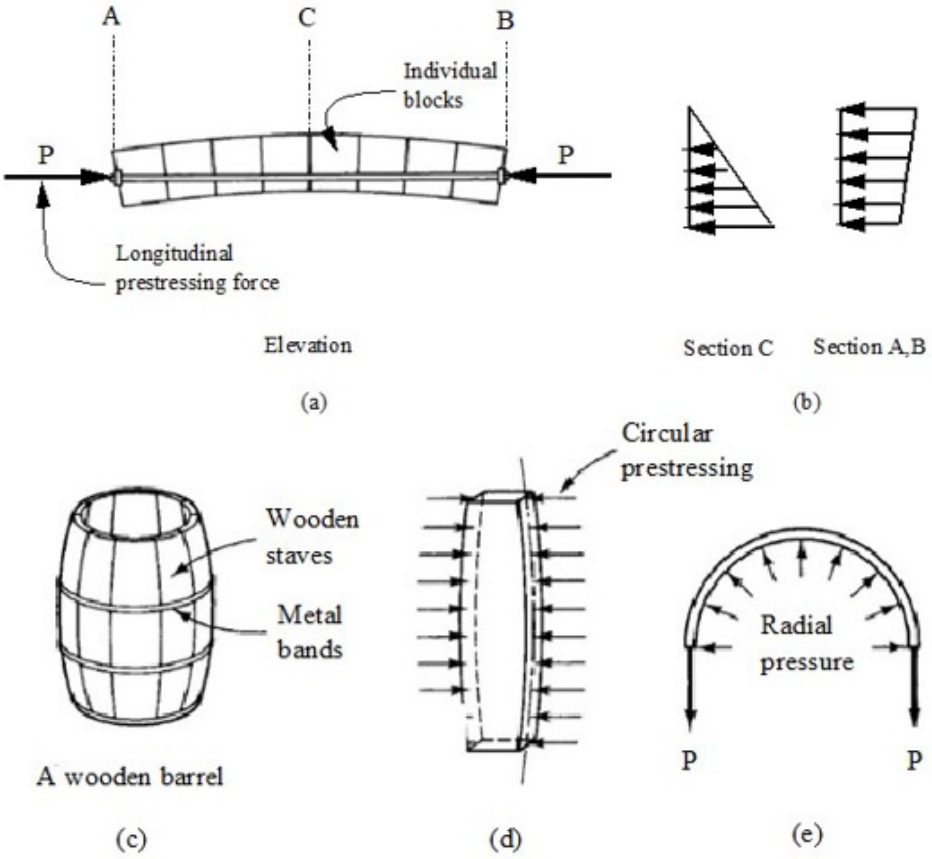

Figure 2.12 Concept of prestressing with wooden barrel and slaves.

Early steels' relatively low yield stress at that time prevented them from achieving particular success. Meanwhile, low initial jacking and high creep shrinkage of concrete caused much prestressing force to be lost in the initial stages. The drastic increase in progress in prestressing strands was the first critical milestone for the realization of the idea of prestressing. Between 1926 and 1928, Freysiinet succeeded in making prestressed members by using new high-strength steels, considering the losses caused in the long term.

In 1940, the well-known Eugene Freyssinet system was introduced by him for the first time. Advances in the production of high-strength steel and the development

of prestressing hardware were essential steps that made prestressing operations practical. Although at that time, less attention was paid to post-tensioning. In the early 1950s, with the introduction of lift slab construction in the U.S., prestressing was considered and revised to eliminate cracks and reduce deflection. Lin (1963) presented the primary design tool and utilized load-balancing techniques. The load balancing method enabled engineers to consider the effects of prestressing as a reduction in the dead load of the slab (Figure 2.13).

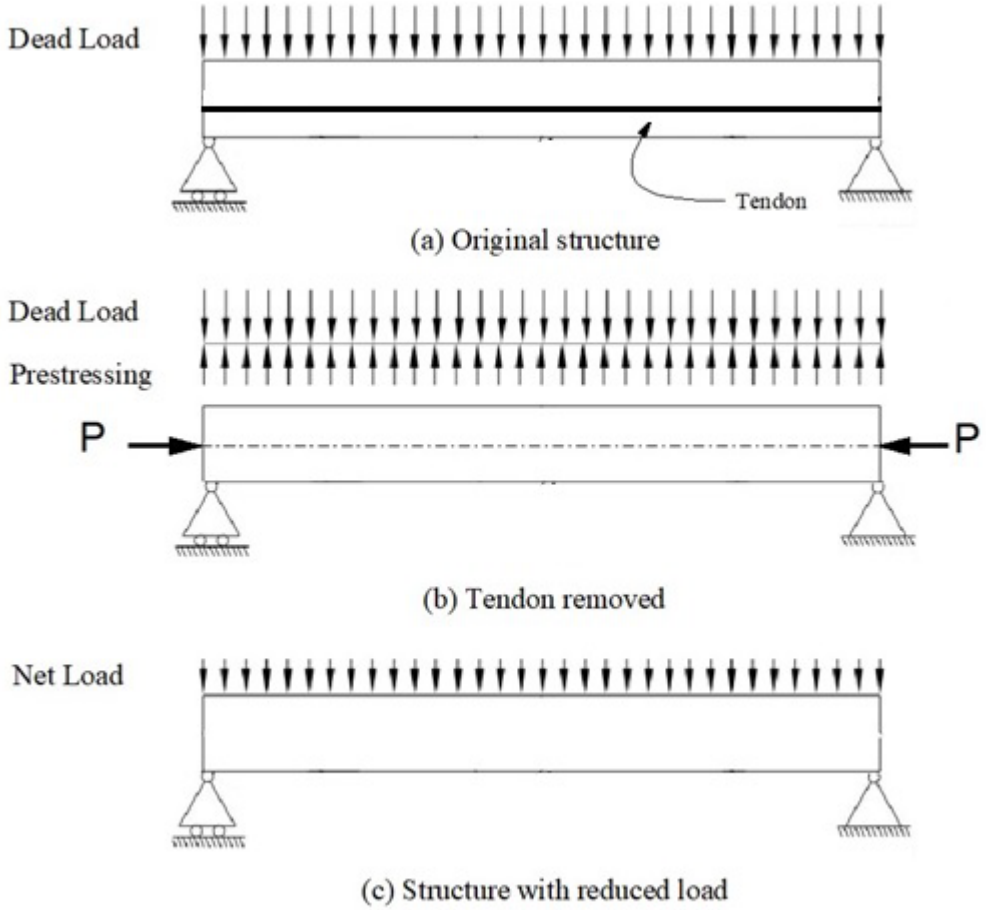

Figure 2.13 Simple load balancing method of prestressing. (a) Original structure. (b) Tendon removed. (c) Structure with reduced load.

Assuming that the axial force and bending effects caused by prestressing tendon can be separated, the prestressing force is constant throughout the length of the tendon, and the member centroid height is also fixed, load-balancing is defined as follows.

A) The structure with the same thickness is subjected to applied dead load with one tendon post-tensioning.

b) Assuming the effect of post-tensioning is applied with the equivalent load method, the reduced net load is used for design and traditional load combination.

2.8.2 Principles of Prestressed Concrete

Reinforced concrete is the most used structural material in constructing evolution's infrastructure. Concrete sections may experience tensile stresses due to loads, deformations, or load-independent factors such as temperature changes and shrinkage. Internal steel bars are used in concrete to carry tensile forces since the tensile strength of concrete is relatively low (Figure 2.14).

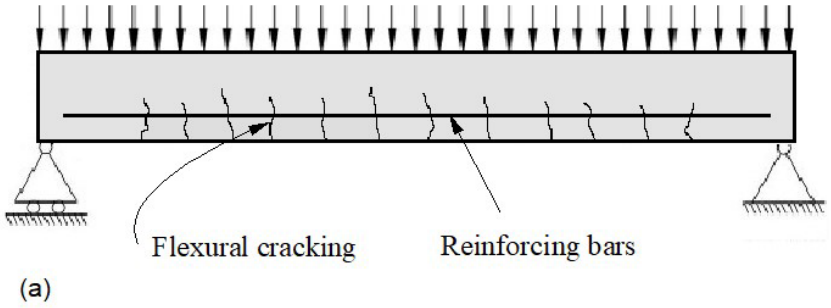

(a)

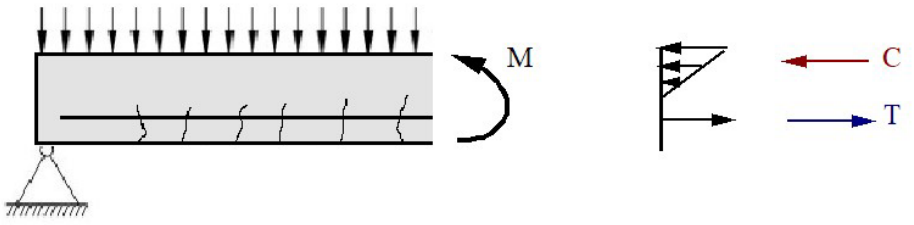

(b)

Figure 2.14 (a) elevation and section of the cracked reinforced concrete beam. (b) free-body diagram, stress distribution and resultant forces of reinforced beam.

External loads place stress on the bottom web, which results in cracks in the bottom section of the beam. Conventional reinforced concrete beams usually crack under regular service loads. Due to the applied bending moment M, the tension is resisted in the bonded reinforcing steel, and the compressive stress is resisted in the uncracked cross-section of the concrete beam.

Although the use of steel reinforcement helps the bending resistance of the beam in tension, it cannot prevent concrete cracking and thus avoid loss of stiffness when cracking occurs. The width of a crack is roughly inversely proportional to the reinforcement's stress and consequent strain. Therefore, steel stresses must be appropriately limited to avoid excessively wide cracks under in-service conditions.

Furthermore, the enormous strain in steel rebars generates a large curve in the beam, thereby increasing deflection. Therefore, there is little to be gained from utilizing stronger steel or concrete because the extra capacity provided by stronger steel cannot be used to satisfy serviceability criteria.

2.8.3 METHODS OF PRESTRESSING

Prestressing is usually applied to a concrete member by high-tensile steel reinforcement. The hydraulic jacks are generally utilized to tension the high-strength prestressing steel. Prestressed members are classified into two categories, pre-tensioned or post-tensioned, depending on whether the tensioning operation is done before or after concrete casting.

Pretensioned

Using fixed abutments and anchored, the prestressing tendons are initially tensioned. After setting up the formwork, the concrete is poured around the highly

stressed steel tendons and left to cure. The wires are cut or released from the abutments after the concrete reaches its required strength. Figure 2.15 illustrates the procedure for pre-tensioning a concrete member. Concrete restrains the high-pressure steel as it tries to contract, which causes the concrete also to compress. The steel and concrete bond introduces prestressing force into the concrete member. The prestressing is often transferred to the concrete within 24 hours of casting. However, steam curing can also be used to facilitate the rapid increase in the strength of concrete to reduce construction cycle time. The relatively large shortening of concrete over time and creep in concrete causes a significant reduction in the tensile strain in the bonded prestressing steel. This causes a relatively high loss of prestressing, which should be considered in the initial design.

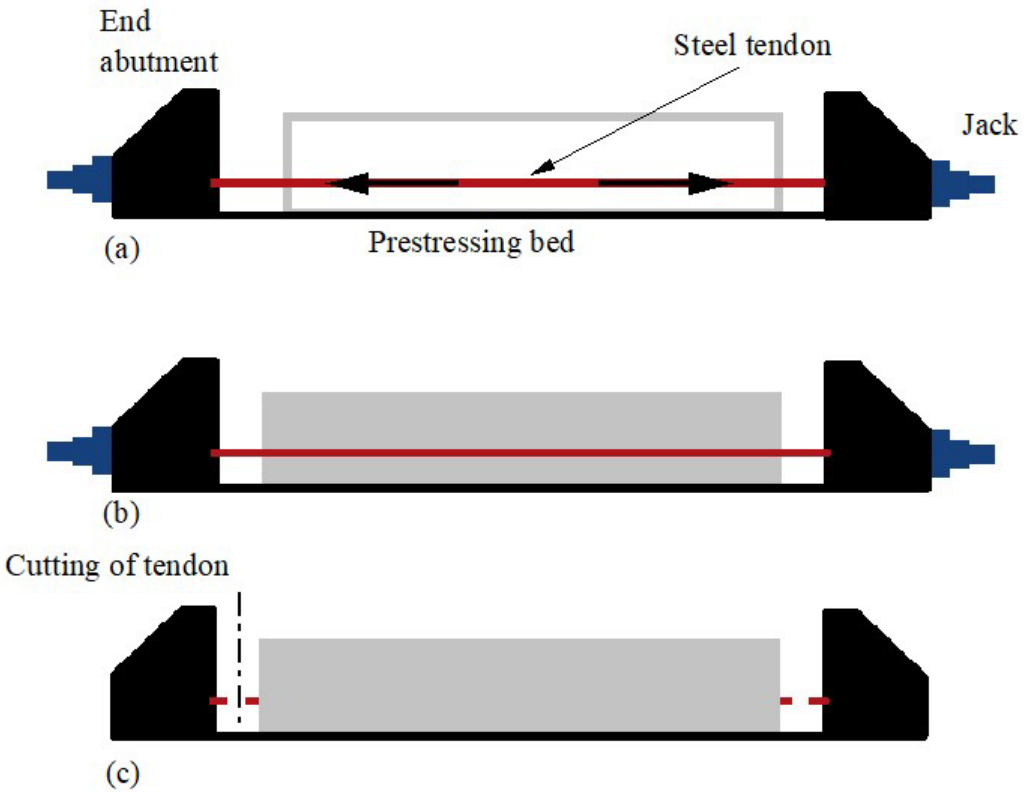

Figure 2.15 Simple diagram of a pre-tensioned concrete. (a) Applying tension to tendons (b) Casting of concrete (c) Transferring of prestress.

Post-tensioned

The procedure for post-tensioning a concrete member is shown in Figure 2.16. After setting up the formwork, concrete is poured around hollow ducts that can be attached to any desired profile. Stress-free steel tendons are placed in the ducts during concreting. The tendons are tensioned once the concrete has acquired the necessary strength. Tendons can either be stressed from both ends and one end while the other is anchored.

At each stressed end, the tendons are then anchored. The tension operation causes the concrete to be compressed. After anchoring the tendons, the prestress load is maintained by bearing the end anchor plates on the concrete. Wherever the direction of the cable changes, transverse force is also applied to the member by the post-tensioned tendons. Once the tendons are anchored, the ducts of the tendons are filled with grout. This bond between the tendons and concrete provides better cracks and final strength control with greater efficiency. It also reduces the possibility of corrosion or safety problems.

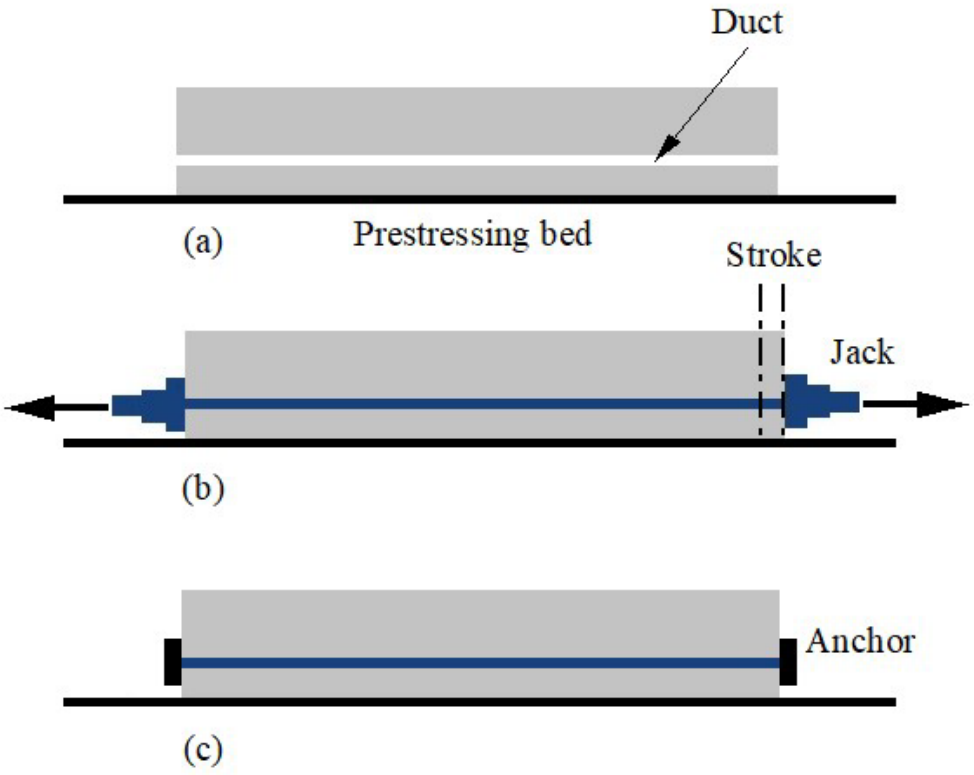

Figure 2.16 post-tensioning concrete procedure. (a) The casting of concrete with duct placed. (b) Tensioning the tendons in the duct. (c) Anchoring the tendons at the stretching ends.

Tendons may occasionally not be injected for financial reasons and be left permanently unbounded, especially in North America and Europe. However, according to AS3600, except for slabs on the ground, unbonded tendons are not permitted in Australia. Post-tensioning is most common in in-situ prestressed concrete. The relatively uncomplicated use of lightweight and portable hydraulic jacks has made on-site tensioning more popular among other methods. Large-span bridge girders are segmentally built using post-tensioning as well.

Other methods of prestressing

Prestressing can also be applied to new or existing parts using flat jacks or other equipment, such as external tendons. Although these systems may be helpful for temporary prestressing operations, they are subject to high time-dependent stress losses over time.

2.8.4 Advantages of Prestressed Concrete

One of the critical benefits of prestressed buildings is the potential to prevent irreversible cracks. In addition, the increased durability of reinforced concrete is advantageous for marine structures and members exposed to corrosive environments or harsh ground conditions. Additionally, prestressing may apply internal forces that counteract external loads and lessen or eliminate deflection. Its advantages are evident in the construction of pipes and tanks containing liquid.

In addition, since the weight of high-strength prestressing steel is a fraction of the weight of the reinforcements, much less steel is used. Also, the cross-sectional area of the member can be smaller because the entire cross-sectional area of the concrete is under pressure. And finally, beams show significant resistance against shear and bending cracks compared to reinforced concrete beams. It also allows for designing spans or cantilevers with a longer length and comparatively shallow and slender cross-sections. Without reducing the structure's final strength, a structure can become more rigid or flexible by controlling the prestressing force. Under seismic and dynamic situations, the performance of a flexible system will be enhanced because it may absorb large amounts of energy before failing due to impact.

According to Ganz (2008), the use of prestressing concrete technology can reduce the consumption of concrete materials by approximately 25% and 65% of steel consumption in the structure.

2.8.5 Material Properties

In general, three main forms of high-strength steel are used for tensioning tendons:

i. Wires (as shown in Figure 2.17)

ii. Multi-wire strings (strands)

iii. High-strength alloy rods

Based on the AS/NZS 4672 standard of Australia and New Zealand, the specifications of steel prestressing materials are presented. Important design information of AS 3600 and some essential characteristic properties of prestressing steel are summarized below in Table 2.5.

Table 2.5 Typical material data for prestressing steels (AS 4672.1).

Type of tendon	Dia. (mm)	Area (mm^2)	E_P (GPa)	f_{pb} (MPa)	P_u (kN)	A_{gt}
Stress relieved wire	5.0	19.9	205	1700	33.8	0.035
	7.0	38.5	205	1670	64.3	0.035
7-wire strand ordinary	12.7	98.6	195	1870	184	0.035
	15.2	143.0	195	1790	250	0.035
7-wire strand compact	15.2	165.0	195	1820	300	0.035
	18.0	223.0	195	1700	380	0.035
High strength alloy bar	26.0	562.0	200	1030	579	0.060
	32.0	840.0	200	1030	865	0.060
	40.0	1232.0	200	1030	1269	0.060
	56.0	2428.0	200	1030	2501	0.060

Prestressing wires

Wires are produced by cold drawing using medium to high-carbon steel. In order to improve the mechanical properties of wires, such as ductility, hard-drawn wire is usually stress-relieved by straightening and heat treatment at low temperatures. Also, the stretching process and simultaneous heat treatment are used to improve steel's stress-relaxation properties. Steel prestressing wires can be crimped or indented to

strengthen the bond and anchorage properties. The diameter of wires ranges from 2mm to 8mm, but 5mm and 7mm wires are more commonly used in Australia.

Prestressing strand

Pre-tensioning wires are used as multi-wire strands to provide the high pre-tensioning forces required in many structural works. Both 7-wire and 19-wire strings are manufactured in Australia. In the more common 7-wire strand, the outer six wires are spirally twisted around a single-core wire. In order to improve the mechanical properties of strands, the stress is usually relieved. The prestressed strand has a slightly lower elastic modulus than a wire.

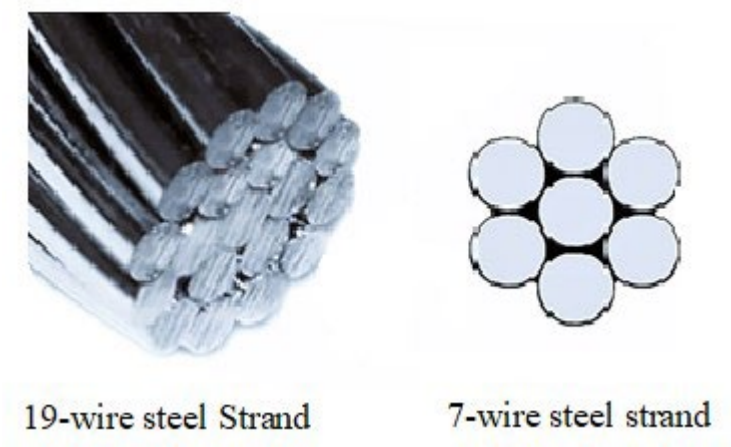

Figure 2.17 Typical multistrand sections of post-tensioning strands.

High-strength alloy bars

Hot rolling is typically used for high-strength alloy steel bars. According to AS 3600, rebars of all diameters must have a minimum breaking strength of 1030 MPa. Ribs are sometimes made by rolling them to increase their bond behaviour. The yield stress is equal to 0.1% proof stress for super-grade and ribbed bars, or 0.81 and 0.89 f_{pb}, respectively.

Strength properties of concrete

Concrete with a higher strength—more than 40 MPa—is typically used to design concrete in prestressed concrete structures. For concrete to obtain high strength in the early stages, additives and low-pressure steam curing are used to achieve early transfer of prestress to concrete in the prestressing process.

2.8.6 Anchorage Systems

A hydraulic jack stretches the cable after it has been anchored at one end of the member. The cable is anchored at both ends once it has been stretched. Some of the most common anchorage systems are described below.

Freyssinet system

The first method introduced was the Freyssinet system, which a French engineer developed. It consists of a cable with a coil spring inside high-strength steel wires, including 8, 12, 16 or 24 individual wires. As shown in Figure 2.18, in this system, a spring is used to maintain the proper distance of the wire. This device is made of a concrete cylinder with a concentric conical hole and surface waves.

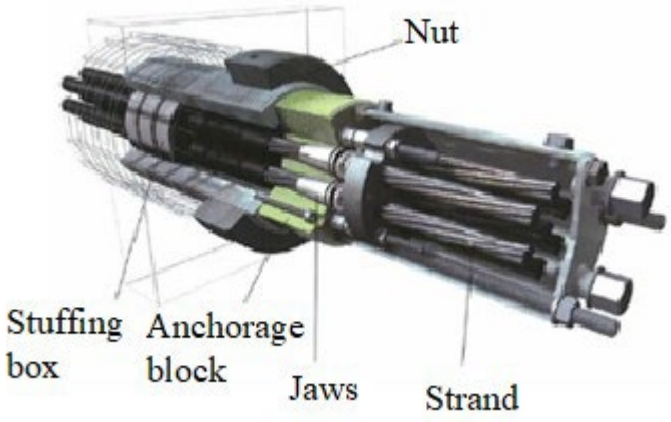

Figure 2.18 Freyssinet anchorage system.

Magnel Blaton system

In the Freyssinet system, several wires are drawn simultaneously, while in the Magnel Blaton system, only two wires are drawn. The structure of this anchorage device system consists of a sandwich plate with grooves to hold the wires and wedges that are also grooved. Each plate consists of eight wires. In order to pull two wires at the same time, the jack is specially designed and anchors them.

Gifford-Udall system

Unlike previous systems, this is a single-wire system. Each wire is independently stressed using a double-action jack. There is a tube unit, a steel component with a thrust plate, and a steel tube with a spiral around it. This unit is attached to the end shutters and forms an efficient casting component of the anchor.

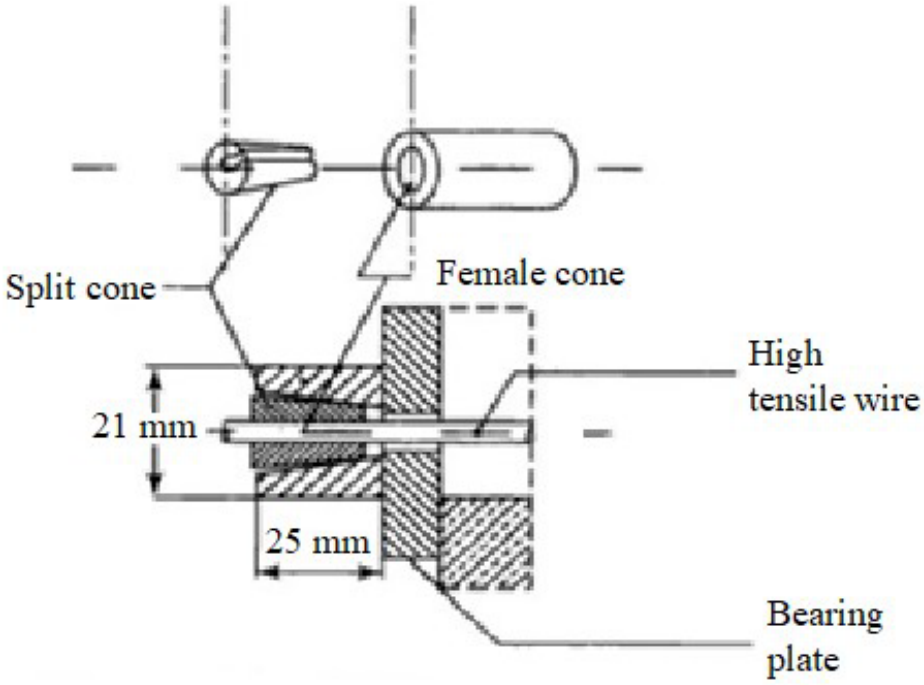

Figure 2.19 Schematic of Gifford Udall anchorage systems.

Lee-McCall system

This method is used for the post-tensioning process. Rods with threads at the end are placed in the steel duct. After stretching the rods to the required length, they are tightened using nuts against the bearing plates placed at both ends of the member.

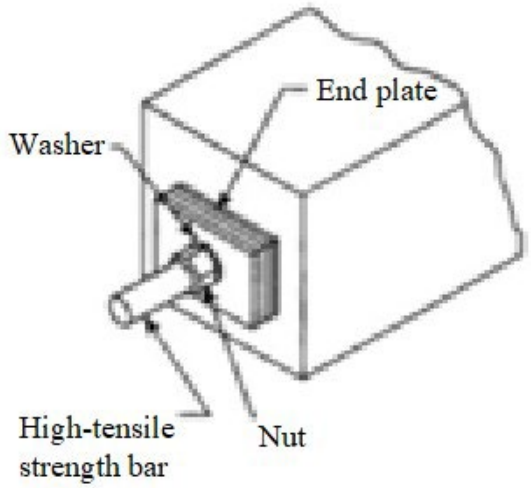

Figure 2.20. Shematic of Lee- McCall anchorage systems.

2.8.7 Prestress Losses

Several factors cause the force in the prestressed tendons to drop from the initial value given to them by the jack system. Some losses occur immediately after the prestressing force is transferred to the concrete member, while deferred losses occur after the prestressing operation is complete.

Elastic Shortening of Concrete

As soon as the tendons are cut, and the pre-tensioning force is delivered to the pre-tensioned part, the concrete quickly shortens subjected to the pre-tensioning force. Simultaneously, the tendon relaxes, leading to stress reduction. The post-tensioned part retains the applied stress after being elastically shortened. When more than one tendon is stretched sequentially, a tendon is lost during the successive stretching of the other

tendons. In the case of a single tendon, the loss of elasticity is minor. The definition of prestress loss owing to the elastic shortening of concrete is as follows.

$$\sigma_e = m\sigma_c \tag{2.4}$$

Where m is the modular ratio, and σ_c presents stress in the concrete at the level of the tendon.

Steel relaxation

Steel relaxation is defined as a reduction in stress over time when under constant tension; as a result, the tendon's pressure gradually decreases. The types of steel, the initial pressure, and the temperature all affect the stress loss that results from relaxation. According to the observation, pre-tensioned members experience a 2% loss in stress, whereas post-tensioned members experience a 3% loss in stress.

Shrinkage of Concrete

As a result of concrete shrinkage in prestressed members, tensioned wires shorten, which leads to stress loss. Moist curing is typically applied to pre-tensioned members to prevent shrinkage until they are transferred. As a result, the total residual shrinkage strain in pre-tensioned members following prestress transfer will be larger than in post-tensioned members, in which some shrinking will have already occurred at the time of stress transfer.

Creep of Concrete

Creep refers to the deformation that develops over time due to a constant force. Prestress is a constant force that creates compressive stress at the steel level in prestressed concrete. Both the pretension and post-tension member experience prestress loss as a result of concrete creep. For concretes with light aggregates, the effects of creep and shrinkage are more, and the modulus of elasticity is lower than the

values related to concretes with normal density. Therefore, the expected prestressing force drop will be larger. Prestress losses due to creep of concrete.

$$\sigma_{cr} = \theta m \sigma_c \tag{2.5}$$

Where m is the modular ratio, σ_c defines stress in the concrete at the level of the tendon, and θ is the creep coefficient.

Friction

In post-tensioned members, friction is formed at the interface of concrete and steel when the tendons are stretched. The size of this friction is predicated on the type of duct used and the type of existing tendon. Two primary mechanisms create this friction. One is the curvature of the tendons to reach the desired profile, whereas the other is the unavoidable deviation between the tendon's central line and the duct's axis.

Prestress losses due to friction.

$$\sigma_f = (P_0/A)(K_w X + \alpha\mu) \tag{2.6}$$

where K_w is the wobbles friction loss, X is equal to L: When jacking from one end, X is equal to L/2: when jacking from both ends, α presents the effect of the angle of the tendon, and μ is the coefficient of friction.

Anchor Slip

At both ends of the tendon, anchoring is provided to transfer the stressing force to the concrete. The tendons tend to loosen when the anchorage is moved from its original position, resulting in prestress loss. The primary function of anchorage after the stressing process is to transfer the stressing force to the concrete. Since the amount of indentation in the clamp depends only on the type of clamp used, its amount is constant, and its effect on short-prestressed concrete members is much greater than on longer-prestressed members. Generally, this slip is about 5 mm. Slippage of the wedges

can be reduced by making sure to push the wedges forward as far as possible before releasing the jack to hold the tendons firmly in place. In tendons with a screw surface that are secured in place by a nut, the amount of wear in the clamp is negligible. In pre-tensioned concrete, stress loss due to anchorage slip does not occur. When pre-tensioning, the tendons are firmly embedded in the concrete.

Prestress losses due to anchorage slip.

$$\sigma_a = \left(\frac{\Delta l}{l}\right) E_s \tag{2.7}$$

where Δl is anchorage slip, l is the Length of cable, and E_s is Young's modulus of steel.

2.9 SUMMARY AND GAP IDENTIFICATION

The effect of ASR on compressive strength has been extensively studied. Nevertheless, compressive strength assessment was determined as the worst indicator to evaluate the evolution of ASR in concrete. First, the compressive strength in low and medium expansion areas slightly increased. Then it decreased to 46% of the initial value. The piecewise linear curve showed the best fit for the compressive strength with an estimation error of less than 15%.

The splitting test demonstrated the influence of ASR on the tensile behaviour of concrete most effectively. In the early phases, there was a delay in the deterioration of the elastic modulus, but the rate of deterioration was comparable in the high expansion zone. In the end, the tensile strength of the splitting test was 46% lower than its starting value.

The best indicator of ASR symptoms in concrete was the elastic modulus, indicating the corresponding degradation even at small expansion values. Degradation

up to 90% was observed for the elastic modulus of concrete affected by ASR. The normalized values for elasticity were between 0.19 and 1.06.

Comparing the elastic modulus-related deterioration behaviour of compressive and splitting tensile strengths revealed a non-linear connection. Consequently, the known stiffness-strength formulation created for unaffected concrete cannot be used since ASR-affected concrete appears to be an entirely new material. It is necessary to thoroughly examine the linkage between mechanical deterioration and concrete expansion, which is crucial for assessing the concrete structures that ASR has impacted. Several factors can significantly influence this phenomenon, including sample size, storage conditions, aggregate type, and sample confinement. More experimental tests are needed to obtain statistically significant data sets.

In recent years, a few studies have been conducted on reinforced concrete beams and other structural components influenced by ASR regarding the structural behaviour of ASR-affected concrete members. In some of these studies, ASR resulted in considerable flexural strength loss, while a series of experiments show that the failure of the structure occurs at a higher load. The flexural cracking delay phenomenon happens due to the generated chemical prestress in the concrete induced by ASR swelling in the direction of the reinforcing bar.

However, the effect of prestressing load on the expansion and the structural behaviour of the prestressed concrete members that ASR deteriorates is not well understood and investigated yet.

Chapter 3: NUMERICAL EVALUATION OF MECHANICAL PROPERTIES OF ASR-AFFECTED CONCRETE

3.1 OVERVIEW

The alkali-silica reaction (ASR) is a major problem that remains yet to be fully comprehended. This chemical reaction can deteriorate the mechanical properties of concrete significantly. Consequently, it can cause premature distress in concrete structures and serviceability problems. ASR affects the modulus of elasticity more drastically than concrete's compressive and tensile strength. Therefore, The best indicator of ASR symptoms in concrete was the elastic modulus. Several empirical models have been developed to estimate the reduction of elastic modulus based on the ASR expansion only. As the deterioration of mechanical properties of concrete is generally expressed in terms of both expansion and expansion rate parameters, the results of these experiments do not directly express the performance of real concrete structures. In addition, Lindgård (2013) mentioned that mechanical properties degradation could significantly vary for different concrete mixes and environmental conditions.

In the most recent research, other factors such as reactive aggregate type, cement content, temperature and alkali content were considered too. Although the recently proposed model had significant improvements compared to the previous models, essential factors such as sample geometry and casting direction have not been considered so far. Furthermore, the expansion rate should be considered for a better

prediction. This component also enables us to use more inputs, such as data from ultra-accelerated ASR tests that result in a rapid and significant expansion. In this chapter, an artificial intelligence model using the artificial neural network (ANN) is proposed to provide an accurate estimation for predicting the elastic modulus of damaged concrete due to ASR by adding the sample size, casting direction, and expansion rate to the other variables.

3.2 REVIEW OF CURRENT EMPIRICAL MODELS

Esposito et al. (2016) used a complete statistical analysis method to show how mechanical properties degrade under free expansion conditions. The S-shaped curve is a modified version of the model for the deterioration of the mechanical properties of concrete by Saouma and Perotti (2006). The normalised data were fitted using four regions—from low to extreme expansion zones—to determine each data piece's weight. By employing a weighted least-squares fitting approach, data points were equally weighted within each zone.

$$\beta p = \frac{P}{P^{ref}} = \beta_0 - (\beta_0 - \beta_\infty) \frac{1-\exp\left(-\frac{\varepsilon}{\varepsilon_c}\right)}{1+\exp\left(-\frac{\varepsilon-\varepsilon_l}{\varepsilon_c}\right)} \tag{3.1}$$

The P and P_{ref} values are the characteristic values of the concrete in the current state and the reference value, respectively. β_0 and β_∞ , respectively show normalised property values in zero expansion and asymptotic expansion. Besides, latency and characteristic expansion values are defined by ε_l and ε_c, respectively.

Latency expansion ε_l defines the latency rate before mechanical degradation is observed. The lower this rate is, the earlier the degradation has occurred. The characteristic expansion ε_c is defined as the average between ε_l and $\varepsilon_l + 2\varepsilon_c$.

Esposito also proposed a continuous piecewise linear function, considering the rise in mechanical properties, such as that seen in compressive strength (Esposito, Anaç et al. 2016). The formulation is as follows:

$$\beta p = \frac{p}{p^{ref}} = \begin{cases} q_1 + m_1 \varepsilon & \varepsilon \leq 0.05\% \\ q_m + m_m \varepsilon & 0.05\% < \varepsilon \leq 0.1\% \\ q_h + m_h \varepsilon & 0.1\% < \varepsilon \leq 0.5\% \\ q_e + m_e \varepsilon & \varepsilon > 0.5\% \end{cases} \quad (3.2)$$

$q \; and \; m$ are the linear coefficients of each zone. As shown below, the three coefficients can be calculated.

$$q_m = q_1 + (m_1 - m_m)0.05;$$

$$q_h = q_m + (m_m - m_h)0.1;$$

$$q_e = q_h + (m_h - m_e)0.5 \quad (3.3)$$

Two alternative models were proposed by Kawabata et al. (2017) and Martin et al. (2017) with the same principle. In their fitting method, the chemical damage rule provided by Brunetaud et al. (2008) has been employed for assessing the reduction of elastic modulus of concrete affected by ASR. For simplification, the damage was assumed to be isotropic. Therefore, degraded elastic modulus E_c can be described as:

$$E = E_0(1 - d), \quad (3.4)$$

$$d = d_m.(1 - \exp(-\omega < \varepsilon_\infty.\xi(t) - \varepsilon_0 > +)) \quad (3.5)$$

In these expressions, E_0 is the original Young's modulus, ω is a material parameter, and d is the damage caused by ASR expansion, which varies from 0 (initial value) to its maximum value d_m. Also, ε_0 denotes the chemical expansion where cement paste begins to crack. According to this model, damage d depends on chemical strain (ε), not the extent of the reaction (ξ).

Based on the proposed model by Kawabata et al. (2017), d_m , ω, and ε_0 have been calibrated on laboratory tests and set as 0.74, 470 and 0%, respectively. While these parameters were assumed to be 1, 120 and 0% for Martin's (2017) model. According to their report, variations in model results may be related to aggregate types. Figure 3.1 compares three models predicting the normalized elasticity of modulus affected by ASR.

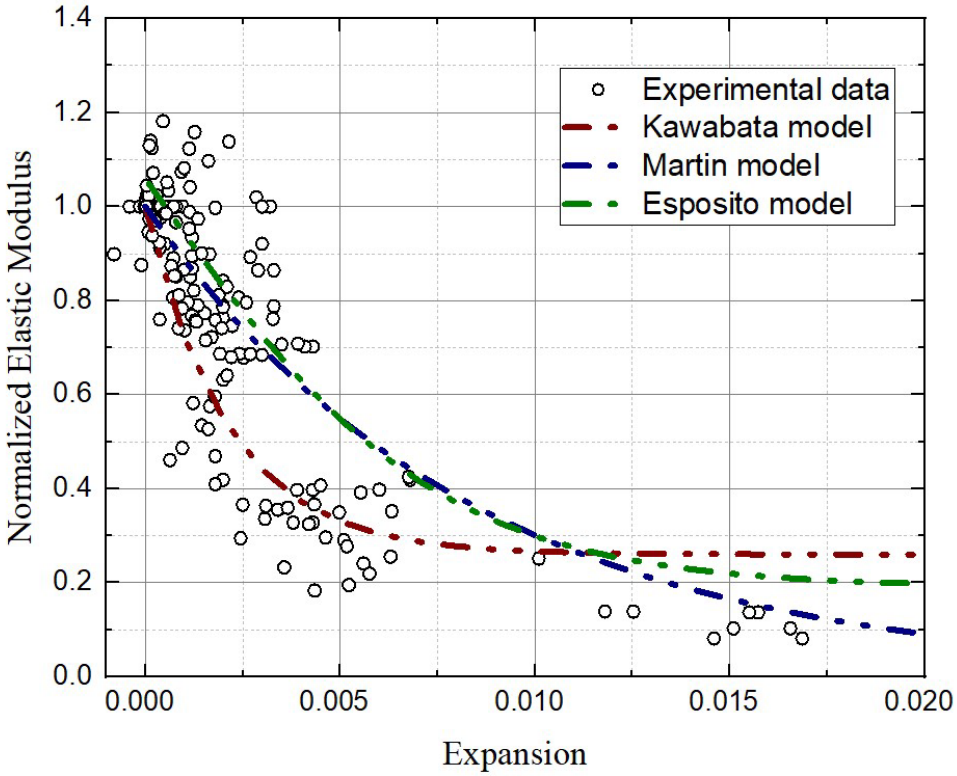

Figure 3.1 Comparison of three different models of predicting the normalized elastic modulus affected by ASR.

3.3 DATA COLLECTION AND PROCESSING

3.3.1 Data Collection

A highly accurate ANN model has been established to predict the elastic modulus of concrete using data from a database created using many experimental research studies. Data sets from 15 studies using 48 different concrete mixtures, including 191

experimental groups testing elastic modulus at various stages of ASR- expansion, were collected.

3.3.2 Model Input and Output Description

In addition to the ASR expansion, the effect of other factors that influence the mechanism of this reaction and the elastic modulus of concrete should be considered in the modelling. Therefore, it is necessary to choose the appropriate input variables to predict the elastic modulus accurately. In the suggested model, 12 additional influencing factors and expansion were taken into account as input variables for the artificial neural network model. These factors including the water-to-cement ratio, the proportion of reactive and non-reactive fine and coarse aggregates, exposure conditions, alkali content, casting direction, the geometry of samples, maximum measured expansion, and duration of the test. The specifics and significance of taking these factors into account are provided.

Mix proportions and types of aggregates

Reactive aggregates are considered the main supplier of non-crystalline reactive silica for the ASR in concrete. The type of aggregates and the amount of unstable silica in their structure play a very determining role in causing ASR reactions and the durability of concrete against chemical reactions. In most previous research, the mechanical properties degraded to various degrees in accordance with different reactive aggregate types and nature. (Gao et al. 2011; Giaccio et al. 2008; Sanchez et al. 2015; Smaoui et al. 2005). In addition, Sanchez et al. (2017) reported that Concrete mixtures containing reactive sands experience mechanical property reductions earlier than those containing reactive coarse aggregates.

Therefore, aggregates are one of the most influential factors in developing ASR. Based on Léger and Côté et al. (1996) investigations, different aggregates show

different behaviour based on the type of structure, chemical composition and solubility in alkaline solution. Additionally, the reactivity of aggregate is frequently assessed using the accelerated mortar bar test (AMBT) or concrete prism test (CPT) (AS-1141.60.1 2014; AS-1141.60.2 2014).

However, the use of reactive aggregate for experimental studies in the literature did not perform the same testing protocol for investigating the mechanical properties of ASR-affected concrete. In order to represent the variation in reactivity of the used reactive aggregate, the maximum ASR expansion was included as an input variable. The proportion of reactive aggregates in the concrete mix is another critical factor. Numerous research (Ichikawa 2009, Garcia-Diaz, Bulteel et al. 2010, Gao, Multon et al. 2013) studied the impact of reactive aggregates on ASR reaction in quantity and structure over the past few decades.

In the collected data set, natural aggregates have been employed in concrete mixes, except for Swamy and Ahmed, who have added synthetic elements to accelerate the reaction. Even though, according to Bazant, Zi et al. (2000) investigations, using artificial aggregates is sometimes criticized since it might lead to inaccurate findings, it is occasionally utilized to comprehend how ASR works in concrete.

In this study, cement content and aggregate proportion were chosen to consider the effects of mix proportion. Four distinct input variables—fine, coarse, reactive, and non-reactive aggregates—were considered to assess the impact of aggregate size and reactivity.

Alkali content

According to Bérubé et al. (2002), using cement with a high alkalis content, greater than 0.60% Na_2O_{eq}, was the primary contributing factor to the development of

ASR. Due to an increase in OH- concentration and consequently an increase in pH, the high concentration of alkalis optimises the appearance of ASR (Santos and Brito 2008).

Based on Hobb's (1998) report, the pH of high-alkali-content concrete is between 13.5 and 13.9, while this amount is between 12.7 and 13.1 for low-alkali-content concrete. Additionally, according to Vivian's (1950) research, adding alkali above a threshold (the pessimum content) inhibited free expansion.

The following equation can be used to express the risk assessment of ASR associated with alkali content in cement in terms of equivalents of sodium oxide (Na_2O_{eq}), taking into account the contribution of sodium and potassium. (Hobbs 1988)

$$Na_2O_{eq} = Na_2O + 0.658\,K_2O \tag{3.6}$$

The equivalent sodium oxide, including the alkali content of cement and adding boosted alkali to the concrete mixture, was considered input data in the proposed model.

Exposure condition

As the rate of alkali-silica reaction is generally slow, taking ten years or more to occur in field conditions. Therefore, such long-duration experimental research is not feasible. (Pan, Feng et al. 2012). Therefore, several attempts have been made to accelerate the reaction. The common accelerating variable to boost the reaction rate appears to be raising the temperature. With little impact on concrete's material properties, increasing the temperature by 12 degrees can reduce the duration of the test by one-third.

According to the concrete prism test method (CPT), which is known as the most reliable test method, the temperature at which ASR is most commonly accelerated on concrete specimens is 38 °C. However, the CPT takes 1-2 years to complete, and for

many purposes, it is seen as a slow test. Practical considerations have encouraged reducing the test duration by raising the temperature further (Ranc and Debray 1992, Fournier, Chevrier et al. 2004, and Thomas, Fournier et al. 2006)

A slight rise in temperature can accelerate the rate of reaction in two ways. First, increasing the temperature speeds up the dissolution of silica. Second, higher temperatures enhance the formation of reaction products (Ulm, Coussy et al. 2000).

The expansion rate roughly doubles when the temperature rises by 12 °C according to the formulas for the two-time constants (Ulm, Coussy et al. 2000). Similarly, based on the formulas suggested in a different experimental study by Haha (1998), raising the temperature from 38 to 50 °C can increase the rate of reaction at roughly 1.7 times.

Despite having the same ultimate expansion, a rise in temperature can cause more damage, according to a recent numerical study (Giorla, Scrivener et al. 2015). Therefore, the influence of temperature on concrete damage should be considered an input parameter.

The results of the reduction of modulus of elasticity at various temperatures were collected in this proposed model, which can account for the impact of temperature.

Specimen Geometry and Orientation of Casting Plane

Based on the literature's collected data, concrete samples have been cast using a rodding or vibrating table, either horizontally for prisms or vertically for cylinders and prisms. The elastic modulus of concrete due to ASR seems to be influenced by the geometry of the test specimens. As reported by several studies on the influence of the shape of the sample (Smaoui, Bérubé et al. 2004), (Multon, Seignol et al. 2005), (Latifee and Rangaraju 2015),(Piersanti 2015), the cylindrical specimens experienced

more expansion than prismatic specimens in the same condition. Clark and Ng (1989) demonstrated that the longitudinal expansion of cylinders (cast vertically) was about 1.7 times greater than prisms expansion (cast horizontally). Similarly, Larive et al. (2000) reported that the expansion of cylinders was two times greater than the expansion of prisms). The longitudinal expansion was generally more significant for cylinders than for prisms under the same curing conditions. The recent study by Diab and Soliman et al. (2021) indicated that the cylindrical specimens' expansion was about 9–40% greater than that of the prismatic specimens.

The direction of casting is an additional crucial differential between cylindrical and prismatic specimens that may influence expansion. In addition, the petrographic analysis demonstrated the impacts of heterogeneity (random variation within space) and anisotropy (variability dependent on direction) on ASR growth. In several laboratory studies, cylindrical specimens were cast vertically, whereas prisms were cast horizontally and then subjected to vertical expansion testing. The results indicate that the ASR expanded more perpendicular to the casting plane. Over time, vertically cast specimens grew by 3% to 9% more than horizontally cast specimens. In addition, the enlargement was mitigated by increasing the number of specimens. The bigger the short-term expansion, but the lesser the long-term expansion was attributed to the greater quantity of alkalis leached over time from the smaller specimens.

Therefore, the proposed numerical model takes into account the role of geometry (prisms or cylinders), the specimen’s size (area and length), and the casting direction (cast horizontally or vertically) in the reduction of the elastic modulus of concrete due to ASR.

ASR-induced expansion and expansion rate

Expansion is the most important factor in determining the elastic modulus of ASR-affected concrete. The major tool for measuring the physical progression of the reaction is the measurement of expansion. In general, the performance of concrete impacted by ASR is assessed in terms of expansion, which may vary significantly depending on the concrete mixture and climatic circumstances. (Larive 1997) (Lindgård, Andiç-Çakır et al. 2012)

Despite the fact that several experiments have been done under accelerated settings, it is possible that the findings do not adequately reflect the development of ASR and the consequent deterioration of field concretes. For a more realistic assessment of field concretes affected by ASR, it is necessary to further evaluate the influence of expansion rates as a factor affecting the elastic modulus of ASR-affected concrete.

The reduction of elastic modulus due to ASR is significantly affected by the rate of ASR expansion. Based on (Swamy and Al-Asali's 1988) study, the rate of ASR expansion has an effective role in the progress of ASR damage and, consequently, the degradation of concrete mechanical properties. The data collected from the literature shows that the expansion rate of ASR can significantly impact the elastic modulus of concrete. As a result, the trend towards a reduction in the elastic modulus of concrete due to ASR increases at the same level of expansion along with an increase in the expansion rate of ASR.

Statistical data from laboratory results show that for a specific volumetric expansion of 0.5%, a decrease in elastic modulus for very high-rate expansion has been reported up to 50%. In contrast, the elastic modulus has experienced a maximum

reduction of 20 to 25% for the same volumetric expansion at a slow rate. This change in elastic modulus reduction can be due to cement's continuous hydration and creep, which may reduce the degradation process of different concrete mixtures with a slower expansion rate.

As discussed by Ahmed, Burley et al. (2003), two time-dependent mechanisms occur simultaneously during the development of ASR. First, maturity development due to cement hydration and then concrete creep. Cement hydration can help offset ASR damage when the rate of ASR expansion is slow by allowing the concrete to become stronger and more mature before the effects of ASR become noticeable.

Giorla (2015) pointed out that the creep of the cement paste can also impact the progression of ASR damage. According to his study, creep can effectively relax the slowly developed stresses caused by ASR gel pressure, which reduces ASR damage. In other words, increasing the ASR rate can increase the damage caused by ASR.

The statistical results of previous studies demonstrate that the rate of ASR expansion and damage progression significantly impact the process of reducing the elastic modulus of concretes affected by ASR. According to Figure 3.2, the modulus of elasticity of concrete with a high expansion rate is reduced more than concrete with a lower ASR expansion rate at the same volume expansion. Figure 3.2 depicts how the volumetric expansion under various ASR expansion rates affects the degradation of elastic modulus for unconfined concretes.

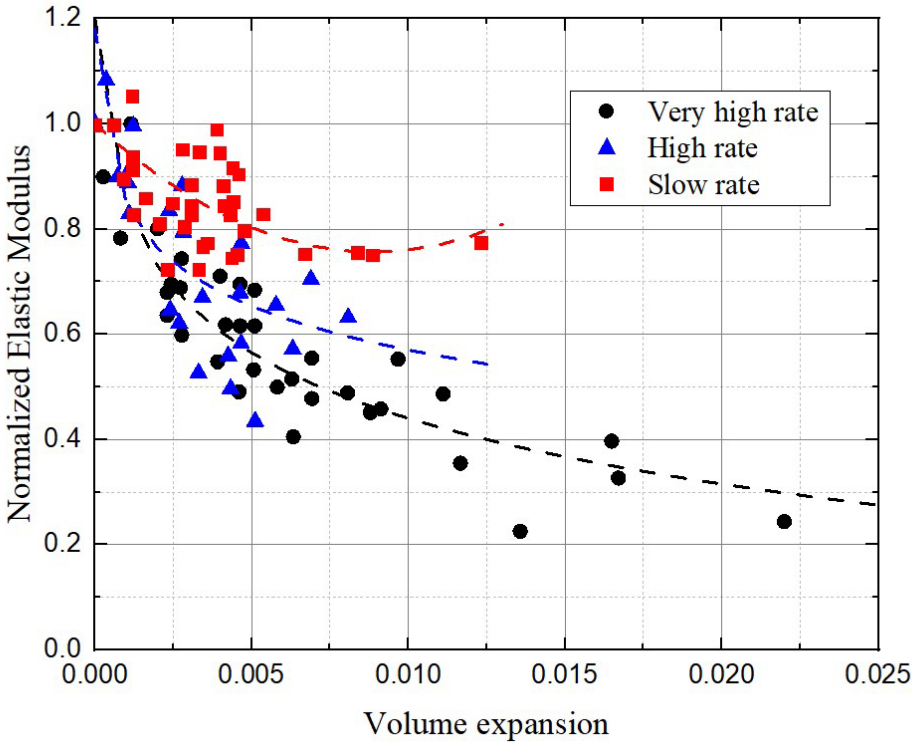

Figure 3.2 The effects of ASR expansion rates on elastic modulus reduction.

The test duration in the suggested model represented the impact of the rate of ASR expansion on the evaluation of the elastic modulus of ASR-affected concrete.

Output variable

Normalizing damaged elastic modulus to the original elastic modulus, denoted by the following formula, has been a common method of presenting the ASR-induced degradation on elastic modulus.

$$\beta_E = \frac{E_c}{E_{co}} \tag{3.7}$$

where E_c Is the elastic modulus of ASR-affected concrete and E_{co} is the original value. The normalised elastic modulus was used as the single output for this model.

After achieving high performance from the model, the impact of all input variables was also evaluated based on weighting factors. The range of all input and

output variables is given in Table 3.1. Further, the following table provides information on the chosen input variables.

Table 3.1 Variables used in the model and their ranges.

Type	*Model variable description*	*Symbol*	*Variation range [min, max]*
Input	Measured expansion (mm/mm)	ε	[-0.008, 0.01686]
	Casting direction	$\boldsymbol{PV}$	[0, 1]
	Exposure temperature (°C)	$\boldsymbol{T}$	[23, 70]
	Maximum measured expansion (mm/mm)	ε_{max}	[0.00015, 0.01686]
	The proportion of Alkali content	$\boldsymbol{Alkali}$	[0.096, 3.018]
	The proportion of fine reactive aggregates	$\boldsymbol{FR}$	[0, 3.03]
	The proportion of coarse reactive aggregates	$\boldsymbol{CR}$	[0, 3.36]
	The proportion of fine non-reactive aggregates	$\boldsymbol{FN}$	[0, 2.93]
	The proportion of coarse non-reactive aggregates	$\boldsymbol{CN}$	[0, 3.2]
	Water/ Cement ratio	$\boldsymbol{WCR}$	[0.4, 0.574]
	Area of sample's section (m^2)	$\boldsymbol{A}$	[0.001761, 0.0625]
	Length of the sample (m)	$\boldsymbol{L}$	[0.2, 0.6]
	Duration (day)	$\boldsymbol{t}$	[0, 745]
Output	Normalised elastic modulus	$\boldsymbol{\beta_E}$	[0.0814, 1.1816]

3.3.3 Artificial Neural Networks (ANNs)

This section proposed a pioneering method for evaluating the elastic modulus of ASR-affected concrete using a feed-forward ANN model. The number of neurons in the input and output layers was chosen based on the quantity of input and output

variables during the model structure design. Numerous neural networks were generated and assessed by loading various neurones into the ANN model's hidden layer and using various training techniques. R^2 and mean square error (MSE) was used as statistical indices to calculate the accuracy of the models in different phases. Based on the results then, the most accurate model was chosen. For modelling purposes, all data were separated into three groups. With portions of 70%, 15%, and 15%, the first section was used for training, validation, and testing. Four backpropagation training algorithms were employed to determine their accuracy, including Levenberg-Marquardt (trainlm), robust backpropagation (trainrp), scaled conjugate gradient (trainscg), and gradient descent with momentum (traindm) (traingdm). In the output and hidden layers, respectively, a tangent sigmoid transfer function (tansig) and a linear transfer function (purelin) were also used. The values of MSE were calculated using the MSE equation (Table 3.2). As illustrated in Figure 3.3, the different number of neurones in the hidden layer from 1 to 20 were studied to determine the most suitable number of layers to be applied. It is noteworthy to mention that, in order to reduce errors and improve prediction accuracy, this modelling was also carried out with ten replications in each of the three testing, validation, and training phases.

Table 3.2 Equations of error functions

Index	Equation
Determination coefficient	$R^2 = 1 - \frac{\sum_{i=1}^{N}(y_{prd,i} - y_{Act,i})}{\sum_{i=1}^{N}(y_{prd,i} - y_m)}$
Adjusted determination coefficient	$R^2 adjusted = 1 - \frac{(1-R^2)(N-1)}{N-p-1}$
Sum square error	$SSE = \sum_{i=1}^{N}(y_{prd,i} - y_{Act,i})^2$
Mean square error (MSE)	$MSE = \frac{1}{N}\sum_{i=1}^{N}(y_{prd,i} - y_{Act,i})^2$
Root mean square error (RMSE)	$RMSE = \sqrt{\frac{1}{N}\sum_{i=1}^{N}(y_{prd,i} - y_{Act,i})^2}$

$y_{Act,i}$ and $y_{prd,i}$ are the actual and predicted values of normalized elastic modulus, respectively; N is the total number of data points; and y_m is the mean of actual value of modulus of elasticity reduction.

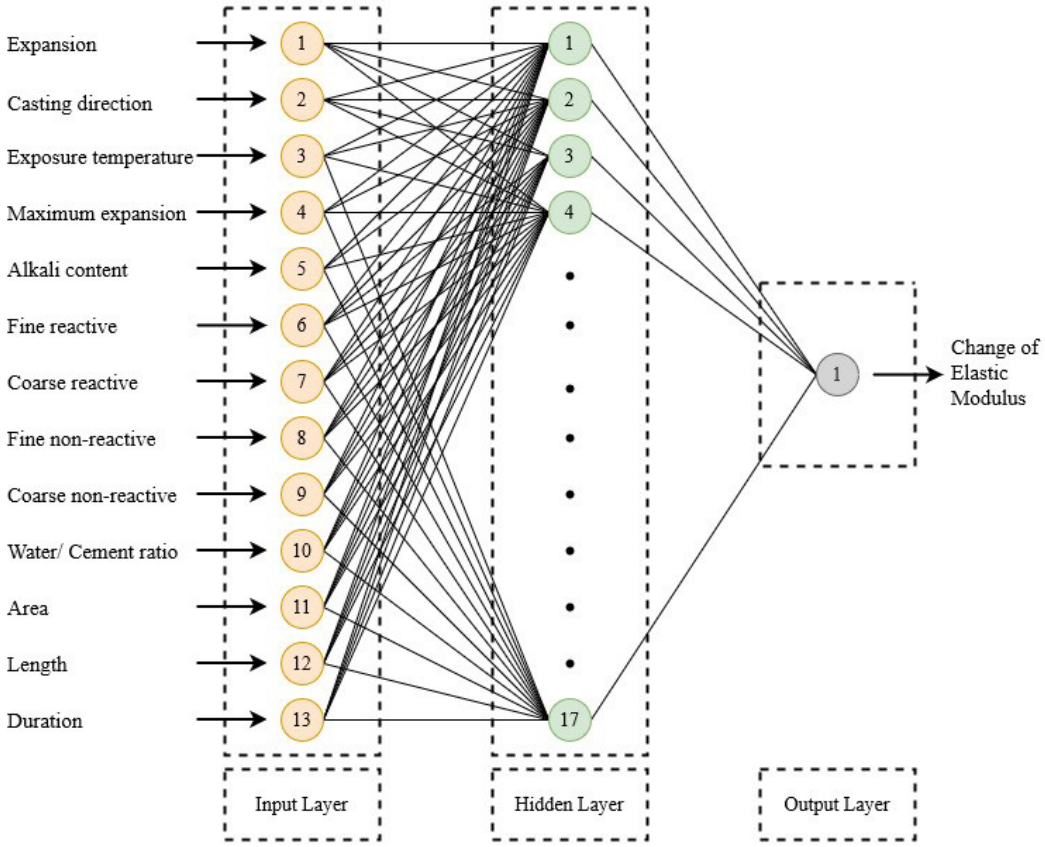

Figure 3.3 The neural network's architecture for estimating the elastic modulus reduction of ASR-affected concrete.

Analysis of the network weights for the relative input variable contribution

The significance of various parameters in evaluating the elastic modulus changes in concrete due to ASR was evaluated using ANN models. Sensitivity analysis was first introduced by Garson (1991) as an equation-based procedure (Eq.3.8) that is used to assess the effective influence of various inputs on output.

$$Ij = \frac{\sum_{m=1}^{m=Nh}\left(\left(\frac{|W_{jm}^{ih}|}{\sum_{k=1}^{Ni}|W_{km}^{ih}|}\right)\times|W_{mn}^{ho}|\right)}{\sum_{k=1}^{k=Ni}\left\{\sum_{m=1}^{m=Nh}\left(\frac{|W_{km}^{ih}|}{\sum_{k=1}^{Ni}|W_{km}^{ih}|}\right)\times|W_{mn}^{ho}|\right\}}\times 100 \qquad (3.8)$$

where W is the weight function, m, k, and n, which stand for the number of hidden neurones, the number of input factors, and the number of the output variable, respectively; and o, I and h are related to the hidden, output, and output layers of the model (Baziar et al., 2017).

3.4 RESULTS AND DISCUSSION

3.4.1 ANN Models for Evaluation of ASR-affected Concrete

Backpropagation training algorithm choice

The backward propagation of errors is referred to as backpropagation. It is a common technique for developing artificial neural networks. This technique aids in calculating a loss function's gradient concerning all network weights. This algorithm depends on the error rate recorded in the previous epoch (i.e., iteration) for adjusting a neural network's weights. The MSE value for each number of neurones in the various algorithms should be as low as possible to produce the optimum backpropagation training method. In this modelling, the trainlm was selected as the primary target for ANN models.

Optimization of neuron number

Seventeen neurones with the trainlm method exhibited the minimum MSE and, as a result, were picked as the best ones for our ANN model. Therefore, the optimum topologies for the ANN models of the normalised elastic modulus were 13-17-1, where 13 and 1 represent the respective numbers of neurones in the input and output layers (Figure 3.4).

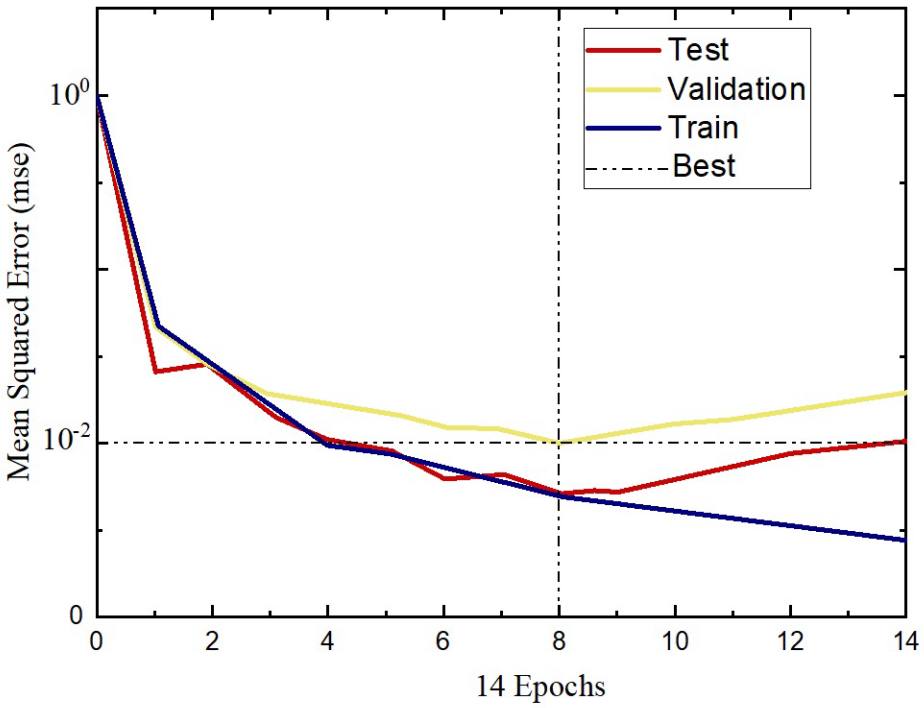

Figure 3.4 Best validation performance is 0.0118 at epoch 8.

Validation of the model

15% of each data were used in the test and validation phases. Eq. (3.9) was used to get the predicted normalised elastic modulus using the ANN model and actual normalised elastic modulus data. The resulting scatter plots compare the predicted and actual normalised elastic modulus values and the correlation coefficient of the model for all three stages and all data. R^2 values for the normalised elastic modulus for the three different phases were shown in Figures 3.5 to 3.7, 0.9705, 0.9225, and 0.9607, respectively. In addition, R^2 for the entire dataset was 0.9448. The ANN model for evaluation of the elastic modulus of ASR-affected concrete is summarized in Eq. (3.9):

$$ANNequation = Purelin\{W2 \times tansig\,(W1 \times [Input\ values] + b_1) + b_2\} \quad (3.9)$$

Based on the predicted results, the proposed model is able to accurately predict the percentages of reduction of elastic modulus values up to 94.5%. Notably, the MSE

proportions for the training, validation and testing phases for predicted elastic modulus reduction were 0.00516, 0.0118, and 0.00539 (Figure 3.8).

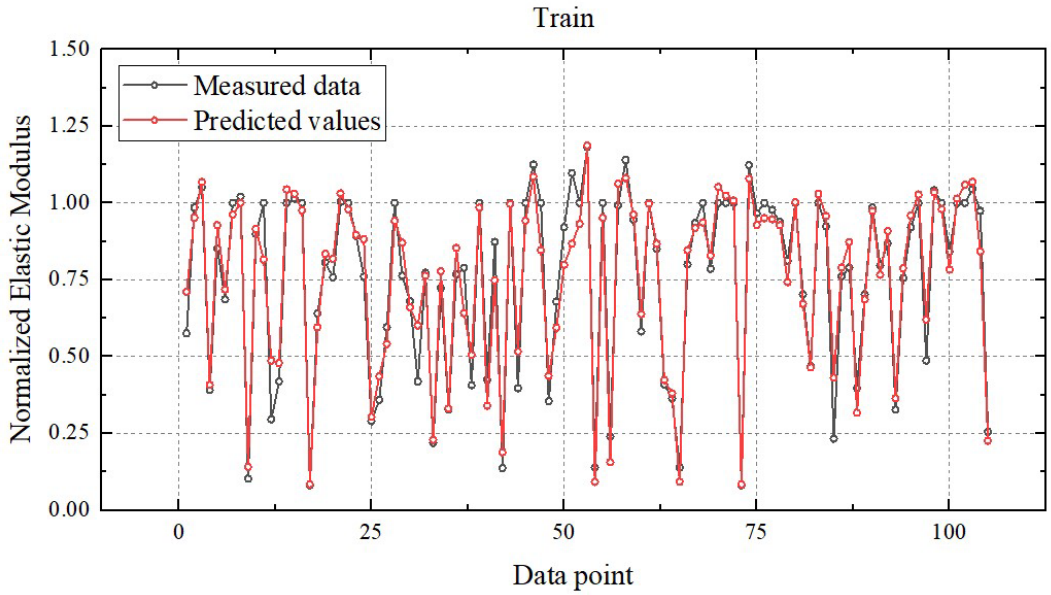

Figure 3.5 Scatter plots of predicted normalized elastic of modulus values for training data set.

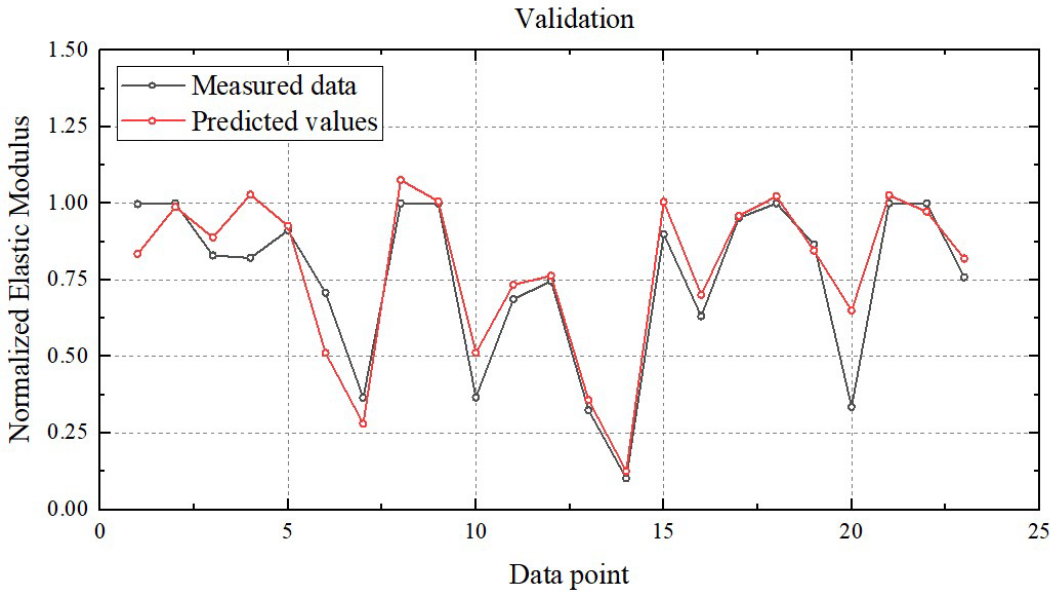

Figure 3.6 Scatter plots of predicted normalized elastic of modulus values for validation data set.

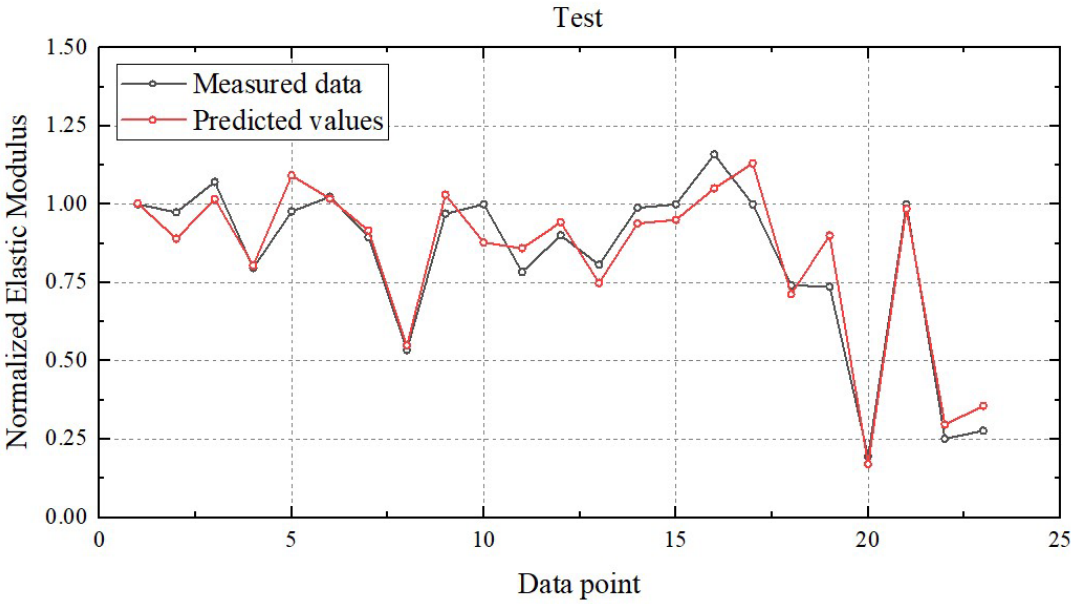

Figure 3.7 Scatter plots of predicted normalized elastic of modulus values for testing data set.

The followings are the equations for the best linear fit and R^2 for the generated ANN model for all data of change in concete elastic modulus:

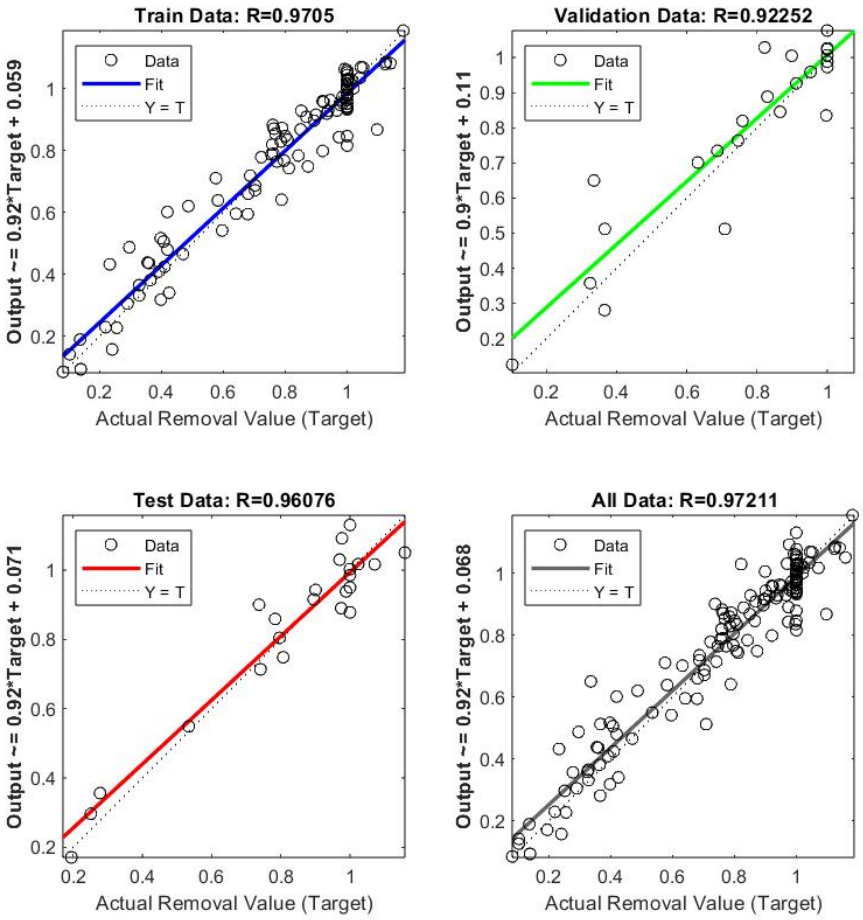

Figure 3.8 Scatter plots of predicted elastic of modulus reduction values versus the actual values.

An additional test was carried out to use ANN models to predict the reduction in elastic modulus due to ASR. Based on the results, the R^2 and MSE values for the normalized value of elastic modulus were 0.945 and 0.0044 (Figures 3.9). A comparisons of predicted and actual values of elastic modulus is depicted in Figure 3.10.

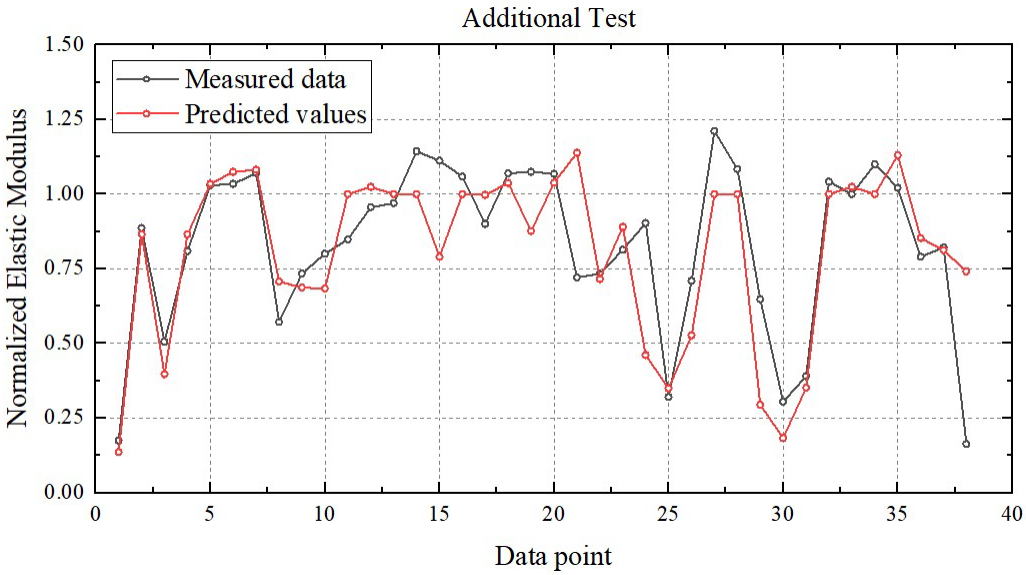

Figure 3.9 Scatter plots of predicted normalized elastic of modulus values for additional data set.

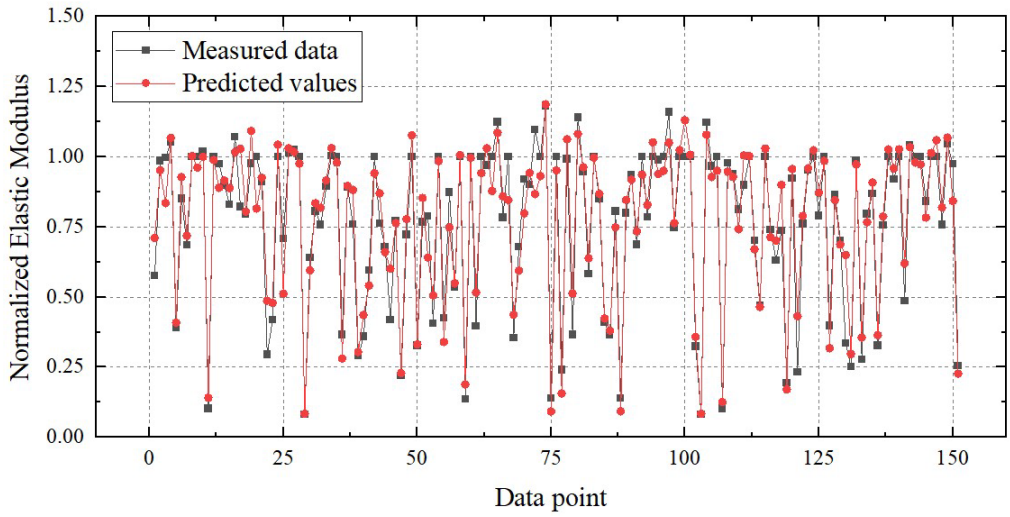

Figure 3.10 Elastic modulus historical comparisons of predicted and actual values.

3.4.2 Sensitivity Analysis of ANN Models

Sensitivity analysis was used to evaluate the significance of several influential independent variables, such as expansion, expansion rate, reactive aggregate, alkali content, temperature, and casting direction, in the ANN models of elastic modulus change on ASR-affected concrete. This method took advantage of the connection weights of the built-in models.

As illustrated in Figure 3.12, The elastic modulus is most significantly influenced by the expansion level, followed by expansion rate and maximum expansion. The output is also influenced to some extent by other input variables. The impact of expansion, expansion rate and maximum expansion on the modulus reduction are clearly obvious compared to the other factors.

In various empirical models, the only variable taken into account when estimating elastic modulus is expansion. As shown in Figure 3.11, the modelling results also confirm that expansion was the most important factor in estimating elastic modulus reduction due to ASR. However, other factors, such as expansion rate and maximum expansion, have also significantly affected determining the amount of normalized elastic modulus. In addition, the effect of other factors, such as the proportion of fine and coarse reactive, casting direction, alkali content and geometry, were also considered in this comprehensive model. However, at lower levels, other model inputs such as temperature, the proportion of non-reactive coarse aggregates and the water-to-cement ratio also have some effects on the change in elastic modulus.

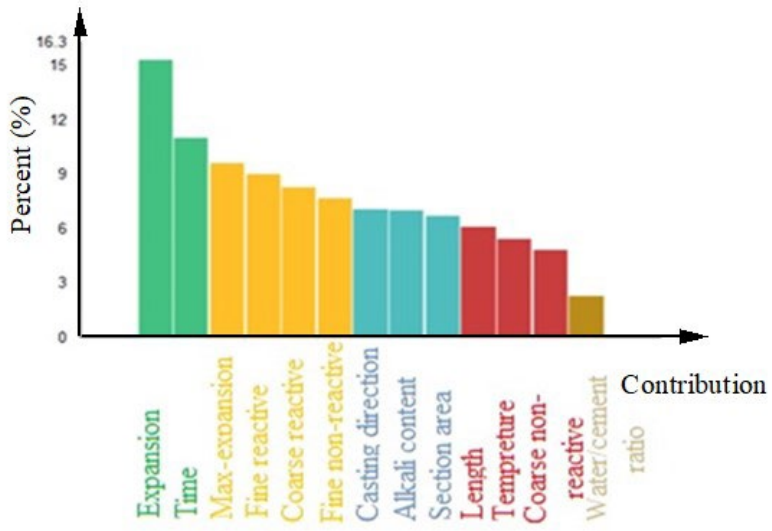

***Figure 3.11** Relative contribution of the different variables.*

The expansion, expansion rate and maximum potential expansion had the highest effectiveness percentages, with values of 15%, 11% and 10%, respectively. The proportion of aggregates, casting direction and alkali content was known as the second effective parameters, with 9%, 8% and 7%, respectively.

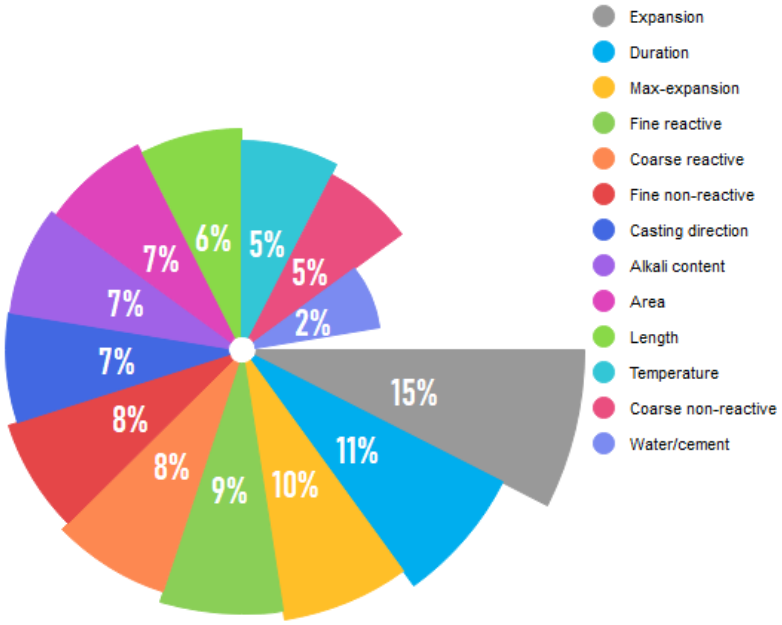

Figure 3.12 Relative importance of input variables with trainlm.

3.4.3 Comparison to Semi-Empirical Fitting Curve

Following, the elastic modulus of the collected data has been estimated and compared using existing experimental models (Esposito et al., 2016; Kawabata et al., 2017; Martin et al., 2017). Figures 3.13 to 3.15 show the ratio of measured and predicted normalized elastic modulus of all 189 concrete samples affected by ASR. The three empirical models for the lower expansion phase provide a relatively good estimate for reducing the elastic modulus. However, with the increase of expansion, the estimation error of the elastic modulus for all three models has increased

significantly. Furthermore, as shown in Figure 3.13, the predicted to actual elastic modulus reduction ratio for these models varies widely.

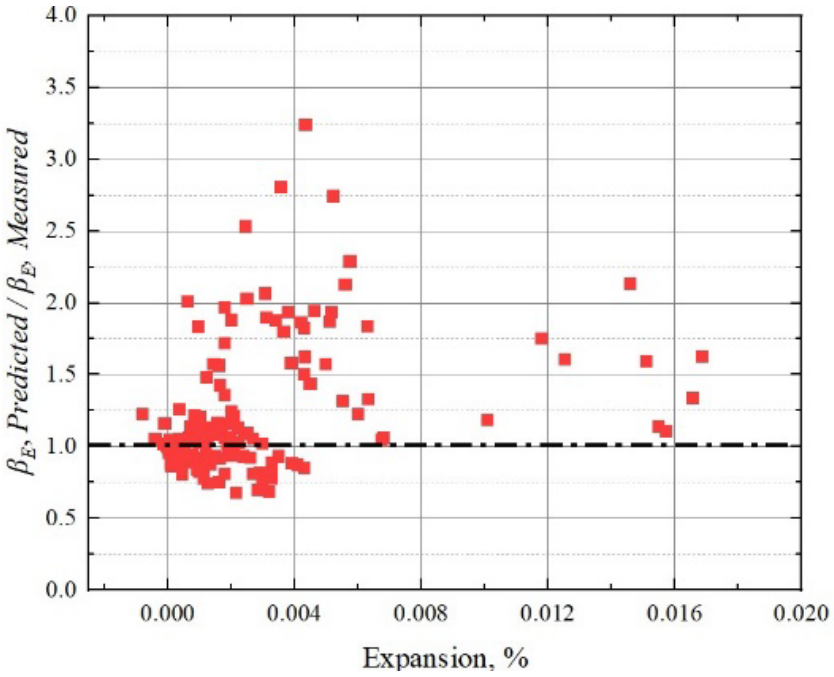

Figure 3.13 The relationship between Kawabata's model's expansion level and predicted/measured ratios.

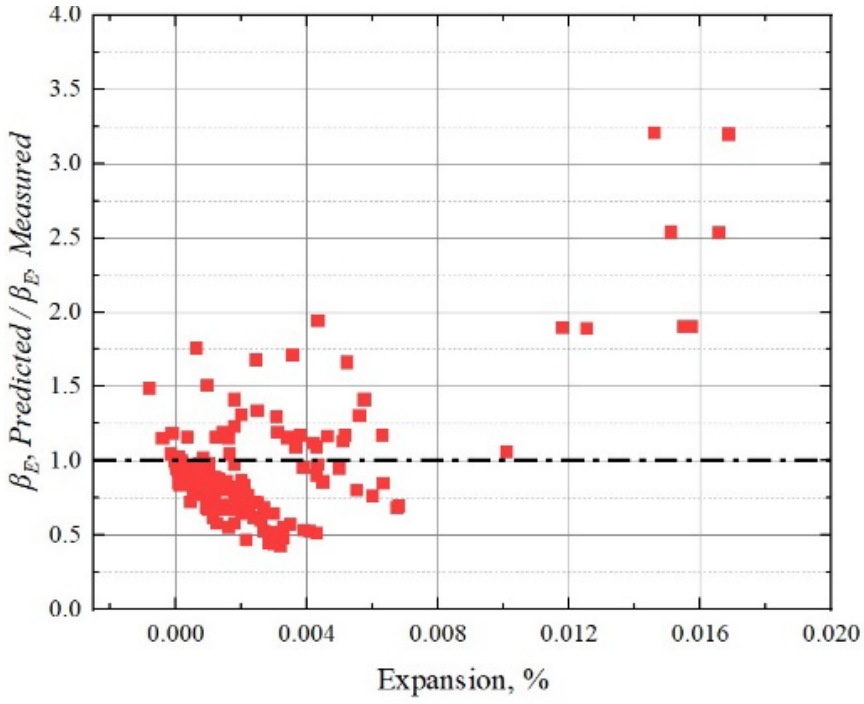

Figure 3.14 The relationship between Martin's model's expansion level and predicted/measured ratios.

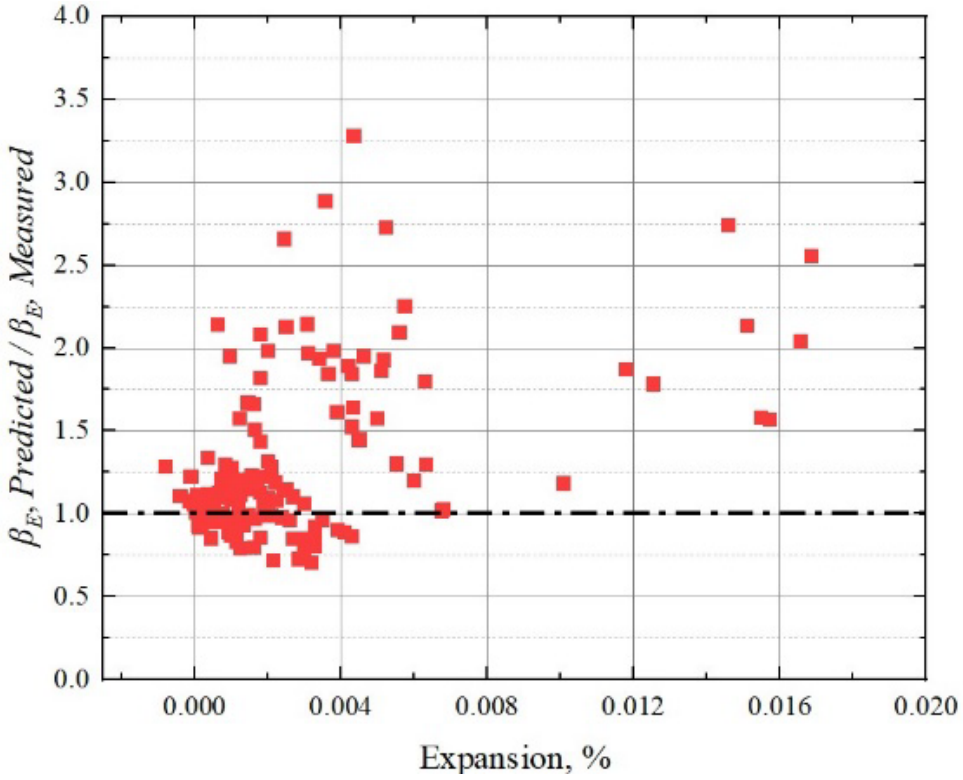

Figure 3.15 The relationship between Esposito's model's expansion level and predicted/measured ratios.

Estimated data points below the equality line in this figure imply an underestimation of the reduction in elastic modulus due to ASR. In other words, the estimated elastic modulus reduction is more significant than the actual elastic modulus reduction. The Figure 3.15 shows that the estimated elastic modulus reduction is greater than the actual reduction for most data points.

The mean square error (MSE) and coefficient of determination (R^2) for all three experimental models and the ANN model are provided in the Figure 3.16, and the results are compared in the table to assess the performance of the models. Actual and predicted values for different models are illustrated in Figure 3.16. Among the three empirical models, the coefficient of determination for the fitting curve of Esposito et al. (2017) and Martin et al. (2017) was almost the same, 0.73 and 0.72, respectively.

Among the three empirical models, the Kawabata model has the lowest accuracy with a coefficient of determination of 0.63.

In contrast, the performance of the ANN prediction model is significantly higher than the presented experimental models. The coefficient of determination for the proposed ANN model was estimated to be 0.94.

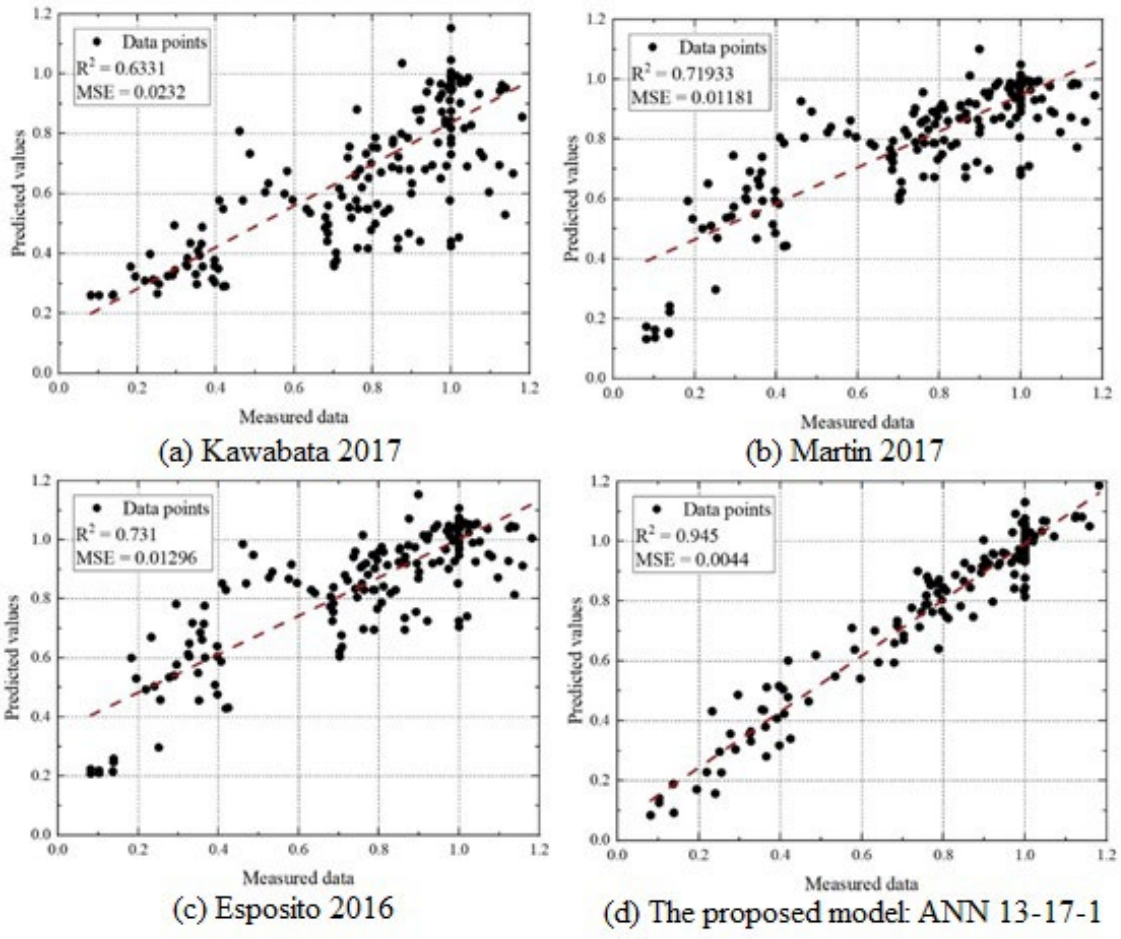

Figure 3.16 Comparison of measured and predicted outcomes from the proposed ANN model and existing empirical models.

The comparison between these observations shows the great capacity and advantage of the neural network technique in optimization and prediction problems. Methods based on fitting curves estimate the change in elastic modulus considering only the expansion level. Therefore, it is practically impossible to accurately predict the evolution of elastic modulus caused by ASR from different studies without

considering the effect of various factors on ASR in concrete, including the difference in mixture ratios, the proportion of reactive aggregates, alkali content, casting direction and exposure conditions.

Table 3.3 Comparison of experimental data and normalised elastic modulus with several empirical models and the suggested ANN model.

Model	$R^2 adjusted$	SSE	$RMSE$	MSE	R^2
Kawabata et al. (2017)	0.6311	4.3460	0.1524	0.0232	0.6331
Martin et al. (2017)	0.7179	2.2077	0.1087	0.0118	0.7193
Esposito et al. (2016)	0.7292	2.4231	0.1138	0.0130	0.7306
ANN 13-17-1	0.9431	0.6442	0.0211	0.0004	0.9445

The proposed ANN approach showed excellent predicting performance for evaluating the elastic modulus of concrete affected by ASR by considering different influencing factors. In addition, the regular residual error of existing empirical models and the proposed model are compared in Figure 3.17.

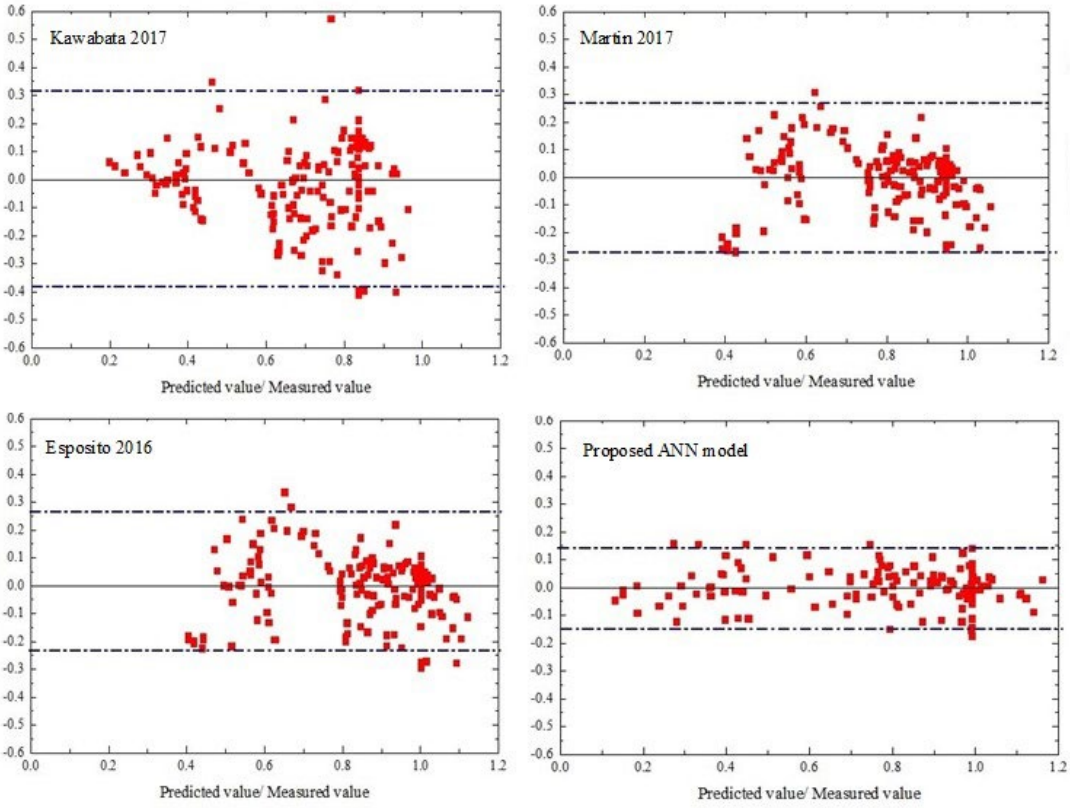

Figure 3.17 The regular residual error of existing empirical models and the proposed model.

3.5 SUMMARY

The elastic modulus change was the best indicator for identifying the progression of ASR in concrete. Therefore, several empirical models have been developed to estimate the elastic modulus reduction based on ASR expansion to assess the ASR development progress. The deterioration of concrete's mechanical properties is typically expressed in expansion and expansion rate parameters. Therefore, the results of these experiments do not directly reflect the performance of actual concrete structures.

As a result, the expansion rate should be considered for a better prediction. In addition, this component enables us to use more data, such as ultra-accelerated ASR test results that cause a rapid and significant expansion.

After collecting the experimental data from the literature, an artificial intelligence model using the artificial neural network (ANN) was developed as an accurate estimation to predict the elastic modulus of ASR-affected concrete. This novel method considers not only ASR expansion but also other influencing factors, including the expansion rate, the proportion of reactive fine and coarse aggregate, alkali content, casting direction, geometry, and maximum measured expansion. The following conclusions can be made:

By considering and weighing the contributions of various influencing factors, the optimised ANN model was able to accurately assess the change in concrete elastic modulus due to ASR.

According to the sensitivity analysis, the expansion significantly influences the modulus of elasticity of ASR-affected concrete out of the 13 input variables. Additionally, the expansion rate, maximum measured expansion, the proportion of reactive aggregates, casting direction, geometry, and the alkali content all play a significant role in the change in elastic modulus caused by ASR. Conversely, the exposure condition, the water-to-cement ratio, and the proportion of non-reactive aggregate have less impact on the elastic modulus change due to ASR.

The proposed model outperforms existing empirical models in predicting the normalized elastic modulus caused by ASR. As a result, this novel approach provides a more accurate elastic modulus prediction for evaluating ASR-damaged concrete.

It is noteworthy to mention that by providing theoretical guidance, this innovative model can help engineers analyse the mechanical properties of ASR-affected concrete structures in the field and under accelerated conditions.

In reality, engineers may be unfamiliar with the ideas and implementations of soft computing approaches. Instead, they are merely end-users for the models generated throughout this research. Therefore, user-friendly software that builds the ANNs model in a graphical user interface is developed for engineers in the field. The codes written on the MATLAB platform are compiled into an executable file that is detachable from the MATLAB environment to simplify and facilitate implementation.

Chapter 4: Numerical Constitutive Model for ASR Expansion

4.1 OVERVIEW

ASR is a deleterious chemical reaction between unstable silica found in some reactive aggregates and alkali hydroxides dissolved in cement mixtures. The gel is not harmful, but it absorbs the environment's moisture and begins to expand. As explained by Rajabipour et al. (2015), the swelling gel creates internal pressures within the concrete structure, leading to expansion, small cracks, loss of material integrity, and in most cases, compromising the structural performance. The previous chapter addressed the loss of mechanical properties based on an experimental database from the literature. This chapter is dedicated to modelling expansions induced by ASR.

The main elements that should be considered in estimating ASR expansion include the quantity and crystalline nature of reactive aggregate, alkali content, particle size, curing conditions such as temperature and humidity, and reinforcing steel ratio. Similarly, other effective parameters can be a concrete mixture, water-to-cement ratio, specimen size, and casting direction.

Multon and Toutlemonde (2010) pointed out that the higher the alkali content, the more silica will be dissolved, producing more ASR gel and, as a result, increasing the volume of ASR expansion. Although Kagimoto et al. (2014) reported this increase in volume has a pessimum limit, increasing excessive alkali content will reduce ASR expansion.

Islam and Ghafoori (2013) indicated that the type of aggregate crystal structure and the proportion of reactive aggregate also have a noticeable effect on the amount of

expansion due to ASR. In such a way that different types of materials are expected to have different expansion rates

In addition, Hobbs and Gutteridge's (1979) experimental tests revealed that the grading and size of the materials are effective in the expansion caused by ASR. Multon and Toutlemonde (2010) reported that the highest expansion was seen for materials between 0.63 and 1.25 mm, whereas zero expansion was observed for aggregates smaller than 0.08 mm.

Additionally, previous studies showed that moisture plays a very effective role in the initiation and formation of ASR gel. Some studies mentioned the minimum relative humidity required for the initiation of ASR to be 70%.

Although temperature does not affect the maximum expansion rate, Swamy's (1992) investigations showed that increasing the temperature affects the expansion rate. His report stated that the expansion rate at 50 degrees was more than twice that at 38 degrees.

Furthermore, Multon and Toutlemonde (2006) introduced the state of applied stress, which can affect the evolution of ASR expansion either externally by applying compressive and tensile stress or by using rebar (embedded reinforcement in concrete).

Although a large number of models have been developed to predict ASR expansion for ordinary concrete and reinforced concrete, there is still a lack of complete understanding of the ASR mechanism. However, relatively little study has been done regarding ASR expansion for reinforced concrete or prestressed concrete structures.

Early researchers (Hobbs, 1981, Groves & Zhang, 1990; Furusawa & Ohga et al. 1994) have provided models to estimate the expansion caused by ASR on mortar. These

models were more focused on microstructural behaviour in mortar. Some of these efforts have been partially successful.

Although these models were effective in advancing our understanding of ASR, the applicability of these models for the expansion in restraint conditions has not been evaluated. The effect of ASR expansion on reinforced and prestressed concrete structures was of greater concern. Therefore, a constitutive model has been suggested, which focuses more on ASR expansion in reinforced and prestressed concrete structures.

4.2 MODELING OF THE ASR EXPANSION

ASR has been investigated on different scales over the past few decades. Various theories have been propounded based on different modelling techniques. Some researchers (Charlwood, Solymar, et al. 1992) have developed models based on the phenomenological approach.

Over the years, several ASR models have been proposed to predict expansion and damage on both ASR-affected materials (microscopic models) and ASR-affected structures/structural elements (macroscopic models) by Multon and Sellier et al. (2009), Ulm and Coussy et al. (2000), Comby-Peyrot and Bernard et al. (2009), and Comi and Fedele et al. (2009). The first group's objective is to depict the mechanical discomfort and chemical reactions caused by ASR, or the combination of the two stages. In contrast, the second group, attempted to bridge the gap between theoretical rigour and practical applicability to actual structures by simulating the total distress of structures/structural concrete parts in a real-world scenario.

Meanwhile, to predict expansion caused by ASR in reinforced concrete structures, many approximate models in different scales have been presented, such as

the simple and semi-empirical models by Karthik and Mander et al. (2016). This model considers the amount of external compressive and tensile stress and changes in temperature and humidity. Karthik's model is a simple model that can be solved without using computational calculation, but the condition of using this model is to do an experimental test. Karthik's model is semi-empirical and requires knowing the maximum expansion value. Then, by defining the steel ratio, expansion can be estimated. This model does not consider the effect of material characteristics, size and alkali content. One of the features of this model is its simplicity, but one of the disadvantages of this model is the need to perform tests or to know the maximum expansion.

Although the ASR process has not yet been fully understood, the widely recognized theory for characterizing it states that two separate stages must be considered: gel formation and water absorption by the gel, which leads to expansion. It should be noted that this mechanism does not necessarily result in expansion. Concrete volume is constant so long as there is a sufficient void area for the gel to fill, such as pores and fractures.

Due to the lack of proper models that can account for the effects of relative humidity, alkali/silica concentration in a mixture, aggregate size, externally applied stress, and ambient temperature, a combined model was proposed. Under this constitutional model, the ASR kinetics model provided by Ulm and Coussy et al. (2000) with the moisture influence described in Léger and Côté et al. (1996) study, the effect of alkali/silica content and aggregate size provided in Multon's et al. (2006) report, and mathematical model of Saouma (2006) and Karthik (2016) to consider the influence of applied stresses, were combined. Figure 4.1 illustrates a schematic of the proposed model for ASR expansion.

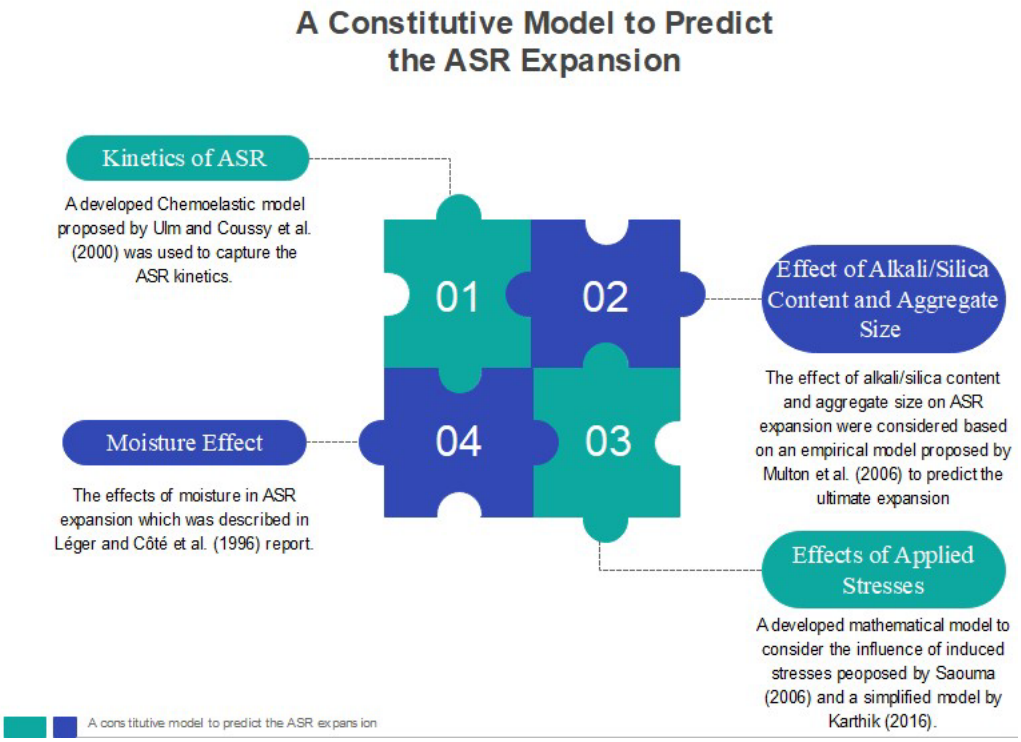

Figure 4.1 Schematic of the proposed combined model.

4.2.1 Model for ASR Kinetics

A developed chemoelastic model proposed by Ulm (1999) was used to capture the ASR kinetics. This first-order engineering model accounts for the ASR products, which impose swelling pressure on the skelton.

Based on Rajabipour et al.'s (2015) investigations, ASR damage comes from a series of reactions. Includes (1) metastable silica dissolving, (2) nano-colloidal silica sol production, (3) sol gelation, and (4) gel swelling.

$(SiO_2)_{solid} \rightarrow (SiO_2)_{aqueous} \rightarrow (SiO_2)_{sol} \rightarrow (SiO_2)_{gel} \rightarrow$ swelling of gel.

According to Multon (2003), the potential chemical differences between the solution in the gel and the concrete pore solution increase water absorption and swelling during the hydration of the ASR gel. The products expand in the pores and micro-cracks of the cementitious matrix. This swelling continues until the void pores of the

concrete are filled. After that, it leads to internal local pressure around the concrete skeleton.

A rough illustration of this mesoscopic mechanism can be seen in Figure 4.2. In stress-free conditions, the tension σ_μ in the concrete skeleton reaches a relative balance with the internal pressure caused by swelling P_g. As a result, the whole material expands.

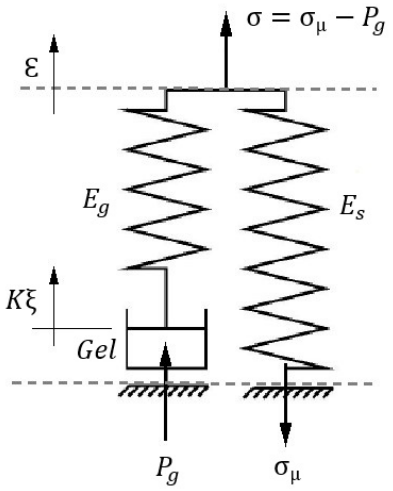

Figure 4.2 Mesoscopic Mechanism of ASR Swelling.

As Ulm and Coussy et al. (2000) reported, considering the volume increase as a function of the reaction rate (ξ), the final strain can be defined as a function of the degree of reaction. The extent of the reaction (ξ) ranges between 0 and 1, where zero indicates the initial stage, and one shows the maximum potential load.

According to the first-order engineering approach in chemoelasticity, the evolution of ξ in time is addressed as a kinetic law. As the reaction affinity $A_m = A_m(\xi)$ is defined as a function of the reaction rate, the kinetic law can be expressed as follows:

$$\sigma = 0: A_m(\xi) = K_d \frac{d\xi}{dt} \tag{4.1}$$

K_d is a positive coefficient considering the diffusion of the constituents involved in the reaction. The affinity A_m (ξ) starts from the initial value and decreases progressively over time until it reaches equilibrium, where the extent of the reaction (ξ) reaches one, at which the reaction stops.

A linear evolution of function A_m(ξ) concerning ξ is referred to as first-order reaction kinetics.

$$\sigma = 0: \qquad 1-\xi = \tau_c \frac{d\xi}{dt} \tag{4.2}$$

where $\tau_c = K_d / A_{m0}$ is the reaction's characteristic time determined by the experiment. To conclude the 3D constitutive model, the first-order reaction has been considered.

$$\forall\sigma_{ij}: 1-\xi = \tau_c (\Theta, \xi) \frac{d\xi}{dt} \tag{4.3}$$

Where τ_c is the characteristic time which depends on ASR extent (ξ) and temperature (Θ), according to Eq. (4.3), integration of the chemoelastic material law into the constitutive laws is relatively simple. Ulm provided an appropriate integration scheme. Since the kinetic law is assumed to be stress and strain-independent, only a stable time integration scheme of the ASR kinetic law is required to estimate the magnitude of the response.

Taking into account a stress-free, isothermal ASR expansion test at $\theta = \theta_0$, the results of measuring the volumetric strain ε_{ASR} as a function of time are as follows.

$$\sigma_{ij} = 0: \quad \xi(t) = \frac{\varepsilon_{ASR}(t)}{\varepsilon(\infty)} \tag{4.4}$$

Where $\varepsilon_{(\infty)}$ is an asymptotic volumetric expansion strain and ε_{ASR} (t) is a measurable function of time. Eq (4.4) demonstrates that the extent of the reaction can be experimentally estimated using macroscopic strain measurements. As a result, we

can directly examine the reaction kinetics of ASR at the macroscopic scale. Using Eq. (4.4) in Eq. (4.3) results in the following:

$$\sigma_{ij} = 0: \quad \varepsilon(\infty) - \varepsilon(t) = \tau_c(\theta_0, \xi)\frac{d\varepsilon}{dt}(t) \tag{4.5}$$

$\varepsilon(t)$ is a measurable function of time. Two timescales must be considered for the kinetics of ASR. First, the latency time, the time it takes for reactive silica to dissolve; and second, the characteristic time, which is determined by a series of stress-free expansion conditions tests at various fixed temperatures. As explained by Larive (1998), the "S" shape of the swelling curves is illustrated in Figure 4.3.

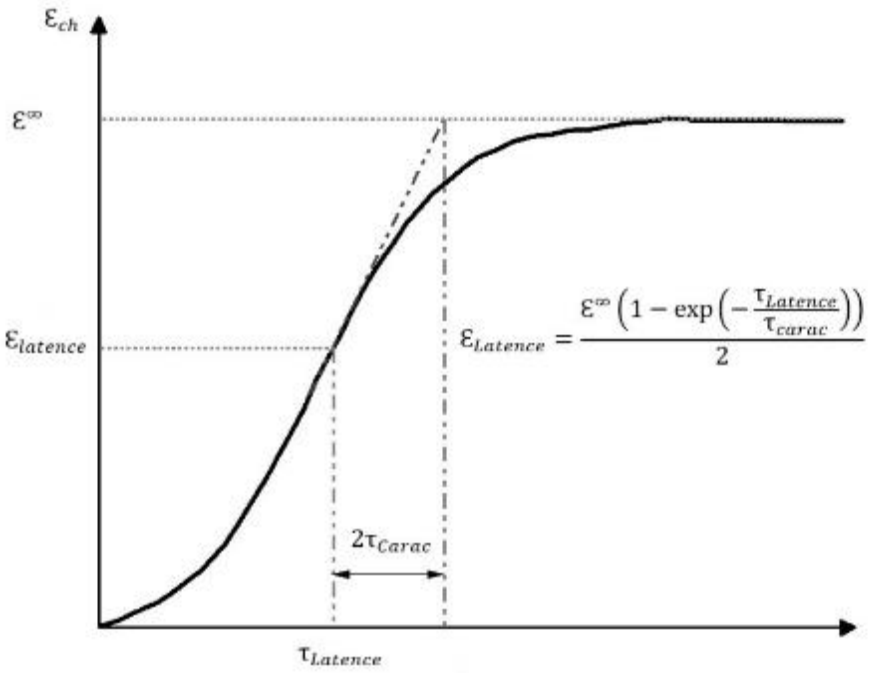

Figure 4.3 Normalized Isothermal Expansion S shape Curve.

τc is affected by temperature θ_0 as well as the extent of reaction in the form:

$$\tau c = \tau_c(\theta_0)\,\lambda(\xi, \theta_0) \tag{4.6}$$

$$\lambda(\xi, \theta) = \frac{1+\exp\left[-\frac{\tau_L(\theta_0)}{\tau_c(\theta_0)}\right]}{\xi+\exp\left[-\frac{\tau_L(\theta_0)}{\tau_c(\theta_0)}\right]} \tag{4.7}$$

Where $\tau_c(\theta_0)$ and $\tau_L(\theta_0)$ are the two constant times of the ASR kinetics in this experimentally derived kinetics function. After integration, the use of (4.7) in (4.5) yields

$$\xi(t) = \frac{1-\exp\left(-\frac{t}{\tau_C}\right)}{1+\exp\left(-\frac{t}{\tau_C}+\frac{\tau_L}{\tau_C}\right)} \tag{4.8}$$

The time constants τ_c and τ_L stand for the characteristic time and latency time of ASR swelling, respectively, and are shown in Figure 4.4.

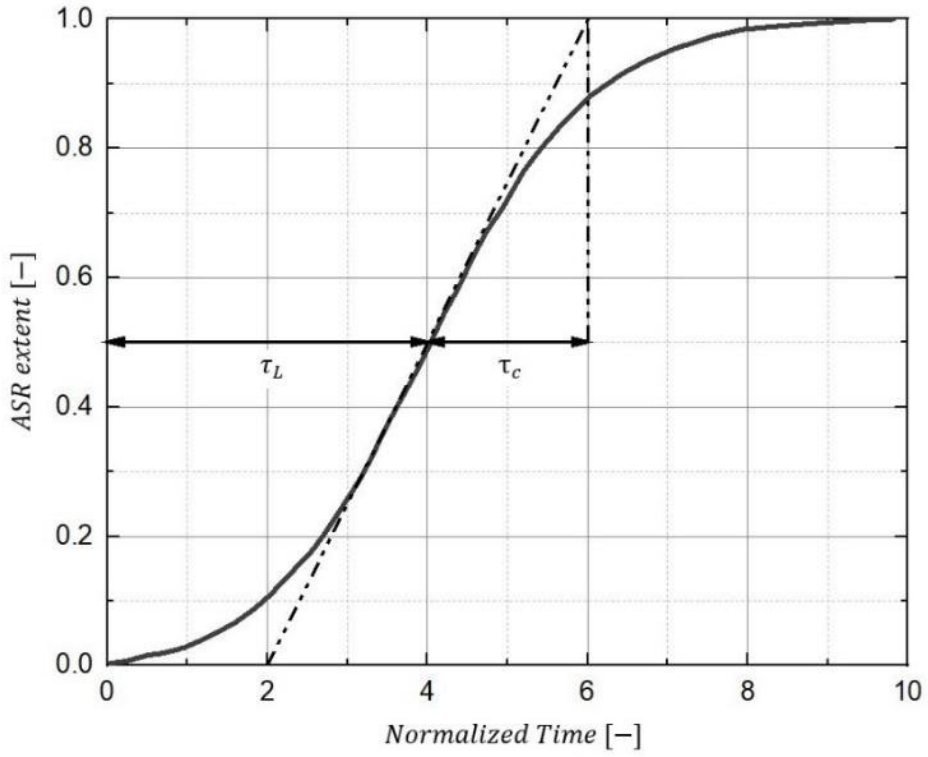

Figure 4.4 Definition of Latency Time τ_L and Characteristic Time τ_c (Ulm 1999).

By conducting stress-free expansion experiments at different constant temperatures, Larive investigated the temperature dependency of the time constants τ_c and τ_L. Figure 4.5 shows the graphs of ln (τ_c) and ln (τ_L) against 1/θ. The experimental results align (almost) along a straight line, which is consistent with the Arrhenius

concept. The slopes U_C and U_L in Figure 4.5 may be interpreted as the activation energy constants of the characteristic time and latency time, respectively, according to the Arrhenius equation.

$$U_C = 5{,}400 \pm 500 \text{ K}: U_L = 9{,}400 \pm 500 \text{ K} \tag{4.9}$$

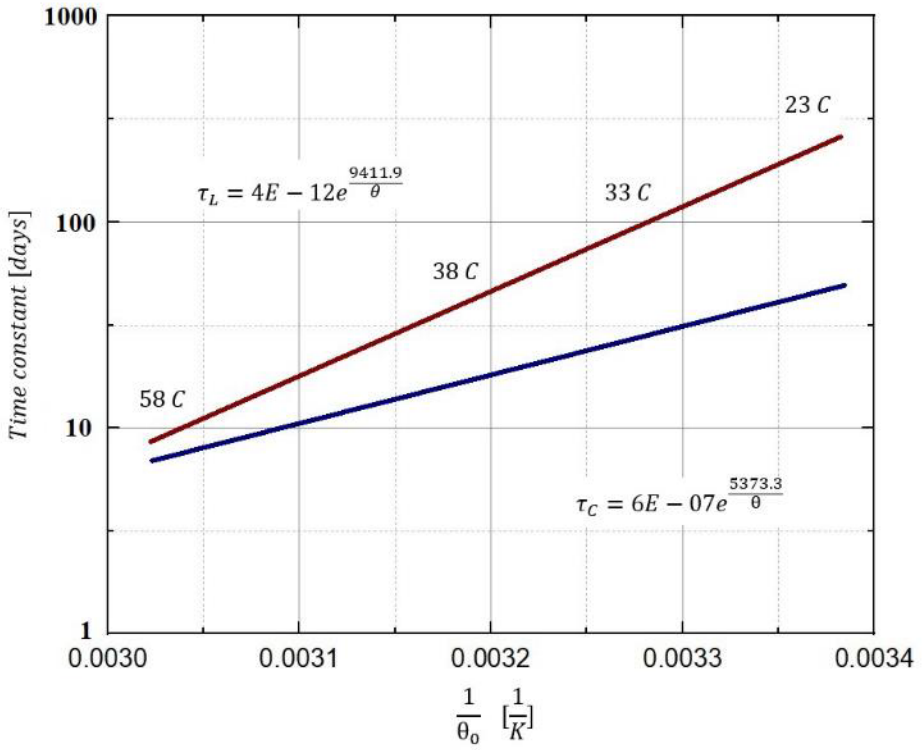

Figure 4.5 Activation Energy Constants U_C = 5,400 K and U_L = 9,700 K examined by Larive 1998.

4.2.2 Effect of Alkali Content and Aggregate Size

Regarding the alkali and silica content of the aggregates, an empirical model was presented by Multon and Cyr et al. (2008) to predict the ultimate expansion. The proposed model accounts for the alkali content in the concrete mix and aggregate size. They used total alkali content, active silica content, and active aggregate granulation as their main parameters in the development of the model. It should be noted that the kinetics of ASR are not considered in this model. Only the ultimate potential expansion can be calculated using this model.

First, the alkali content required to form ASR gel is calculated, and then the expansion is predicted based on aggregate granulation. Poyet (2003) studied the ultimate expansion in infinite time $\mathcal{E}^{\infty}$ (or ultimate potential expansion) by evaluating the reactive aggregate content, the content of reactive silica in the reactive aggregate, and the measured expansion.

$$\varepsilon_{cal}^{\infty}(t) = s.\ p.\ AC.\ \mathcal{E}_F \frac{A_C}{A_R} \tag{4.10}$$

Where $\mathcal{E}_F$ is an aggregate-dependent parameter for different materials, obtained by Poyet's empirical studies on samples with reactive particles and adequate alkali, AC is the total sand content, r is the required alkali ratio, calculated based on Poyet's results, p is the proportion of reactive aggregate of each fraction in the mortar and s is the value of dissolved silica. As Multon and Cyr et al. (2008) described, the A_C and A_R denote total aggregate consumed and total aggregate required, respectively. This model assumes that the maximum expansion occurs when there is enough alkali in the concrete mix. The required alkali can also be calculated using the following equation.

$$A_{Ri} = r.\ s_i.\ p_i.\ AC \tag{4.11}$$

It should be noted that the model assumes a constant content of alkali. (i.e., the alkali flow through structure boundaries is zero).

Figure 4.6 Summarizes the calculation steps. The model assumes that there is enough alkali in the concrete mix.

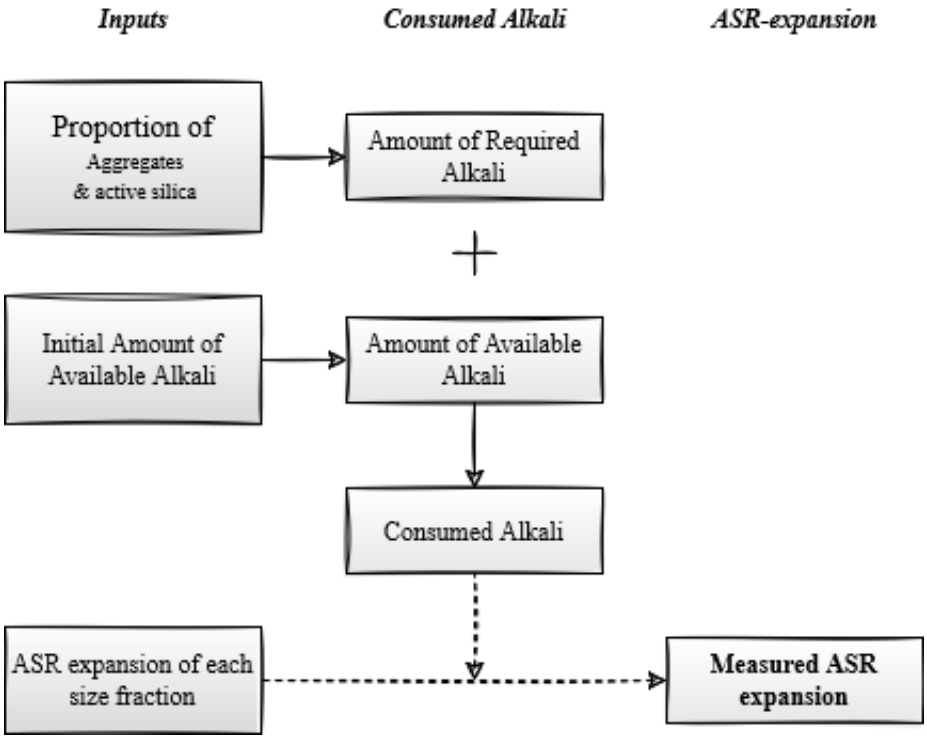

Figure 4.6 Principle of the Multon's empirical model.

The active alkali content is calculated as follows.

$$A_A = A_T - A_0 \tag{4.12}$$

A_T is the total active alkali, and A_0 is the minimum alkali content to initiate the ASR expansion, which was 3.7 kg per cubic of reactive aggregate (assuming a linear relationship between the alkali content and expansion). This proposed model assumes maximum expansion when the active alkali level exceeds the required content. Otherwise, the expansion is proportional to the available ratio to the required alkali.

This study reported a linear relationship between the extent of ASR and active coarse-aggregates. Therefore, The ASR expansion of the concrete mix was assumed to be proportional to the grain size of the active particles. Consequently, ultimate ASR expansion can be calculated by

$$\mathcal{E}_{cal} = \sum_i s_i \times p_i \times SC \times \varepsilon_i \times \frac{A_{Ci}}{A_{Ri}} \tag{4.13}$$

Where $\mathcal{E}_i$ is the maximum expansion for each aggregate particle, finally, the ASR expansion can be calculated using reactive silica content, available alkali, and size fraction expansion.

4.2.3 Effects of Applied and Induced Stresses

Two proposed models have been used to consider the effect of applied stresses on ASR expansion. The first model is a developed model by (Saouma and Perotti 2006), while the second model is a simplified model proposed by Karthik and Mander et al. (2016) that can be implemented without FEM analysis.

The first proposed model to simulate the effect of applies stresses is a developed version of Saouma and Perotti's (2006) model to account for restricted conditions. Since ASR expansion is a volume expansion, the expansion should be modelled in all directions, and no direction can be neglected. Thus, if the expansion is limited in one direction, it develops in other directions. This model defines a weight function for the three main directions to apply the expansion pressure in all directions. The general equation for estimating ASR expansion is as follows,

$$\Gamma_C = \begin{cases} 1 & if\ \sigma < o\ tension \\ 1 - \frac{e^{\beta}\sigma}{1+(e^{\beta}-1)\sigma} & if\ \sigma > 0\ compression \end{cases} \quad (4.14)$$

$$\sigma = \frac{\sigma_1+\sigma_2+\sigma_3}{3f_C'} \quad (4.15)$$

Where Γ_C is the compressive stresses induced by volume expansion introduced by Multon's (2003) precise experiments, and β is the corresponding residual fractional value.

The model assumes expansion in the three main directions regarding the defined weight functions. Although volume expansion is simple for uniaxial expansion, it is a little more complicated for bi- and tri-axial expansion.

Weight functions determine the volume expansion distribution. Weights W_i, W_j, and W_k are assigned to each main direction based on the principal stress vector.

Generally, three scenarios can be assumed. The first scenario is the uniaxial tension, where the volume expansion is equal in all three main directions. The second and third scenarios are compressive stresses. Let's assume the compressive stress is larger than the limiting on σ_u. In that case, the weight function is less than 1/3 along the corresponding direction, and the remaining weight is equally distributed between the other two. If the compressive stress is smaller than σ_u, the weight function along the direction is zero and ½ along the other two directions.

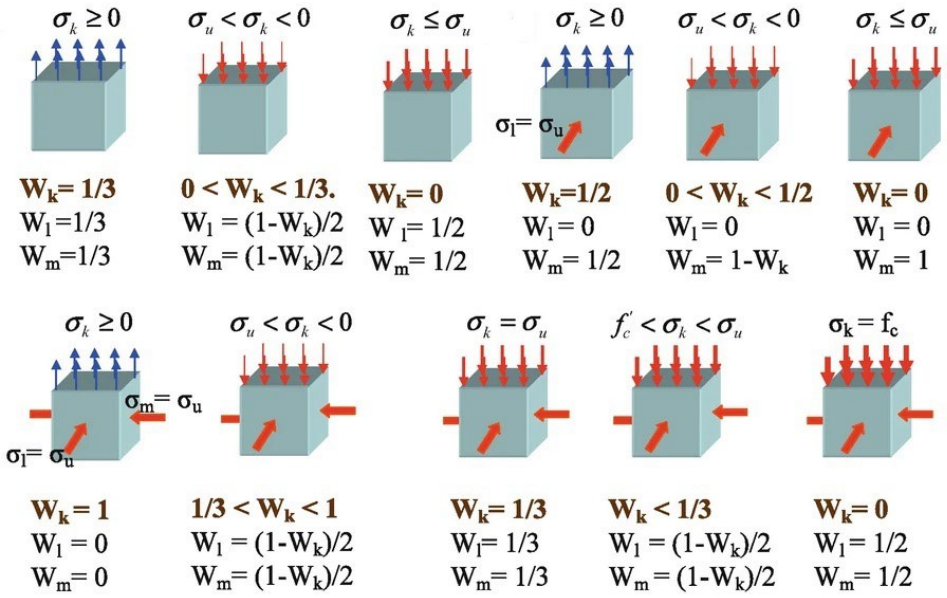

Figure 4.7 Volumetric AAR redistribution weight. Courtesy of (Sauoma, 2006).

The bi-axis stress is where the compressive stress (σ_u) is in either direction. In this case, the weight function is zero along that direction. There are three cases:

1. If tension is in one direction, the weights are equally divided.
2. If the compressive stress is larger than σ_u, the weight function is lower than ½ along the direction, and the remaining weight is assigned to the third direction.
3. If the compressive stress is lower than σ_u, the weight function is zero in that direction, i.e., the weight function in the third direction is unit.

For tri-axial stress where u is along two of the three main directions, five different cases are possible:

1. If tension is in the direction k, the weight function is a unit in that direction, and thus, the volume expansion is along the k-direction.
2. If the compression is larger than σ_u, the weight function is 1/3 along the direction with the lower value, and the remaining weight is equally assigned to the other directions.
3. If the compression is equal to σ_u, the weight function is 1/3 in all three directions, and the volume expansion is calculated based on the Γ_C coefficient.
4. If compression is lower than σ_u but larger than the compressive strength, the weight function is lower than 1/3 along the direction, and the remaining weight is equally assigned to the other directions.
5. If the compression is equal to the concrete compressive strength, the weight function is zero in that direction and ½ in the other two directions.

Therefore, the weight function along the k-direction can be generalized as follows.

$$W_i(\sigma_i) = \begin{cases} 1 - \frac{1}{\log\left(\frac{\sigma_u}{\sigma_L}\right)} \log\left(\frac{\sigma_i}{\sigma_L}\right) & for \quad \sigma_i < -0.3\ Mpa \\ 1 & for \quad \sigma_i \geq -0.3\ Mpa \end{cases} \tag{4.16}$$

It should be noted that experiments suggest that the maximum pressure of gel expansion is 11 MPa which was also proven earlier by Larive (1998).

Therefore, individual stress is defined as follows.

$$\varepsilon_i = W_i \varepsilon_V^{ASR} \tag{4.17}$$

Assuming that the principal stresses are known (i.e., σ_i, σ_{ii}, and σ_{iii}), the expansion develops in all directions based on the weight function (i.e., W_1, W_2, and W_3). As Léger and Côté et al. (1996) described, when compressive stress reaches -0.3 MPa, the weight factor is reduced until maximum stress of -10 MPa is reached in that direction. In this case, the weight coefficient becomes zero. This state is shown in Figure 4.8.

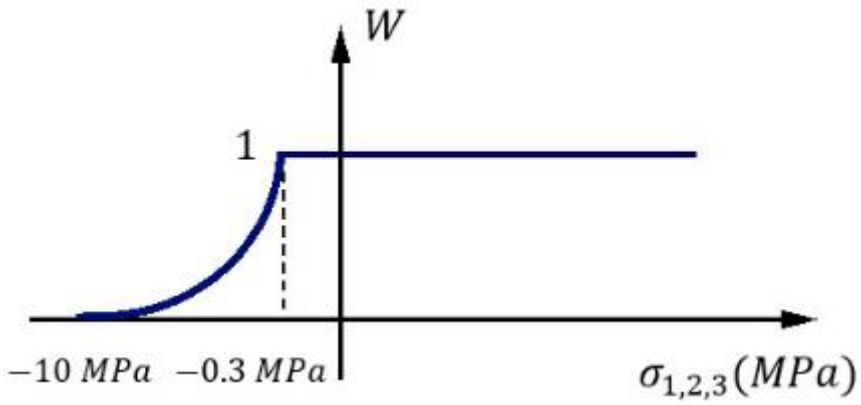

Figure 4.8 Weight factors for ASR expansion.

In this study, to simulate the expansion caused by ASR, a minimalist semi-empirical model in reinforced concrete developed by (Karthik, Mander et al. 2016) also

was employed. This new method is presented to simplify the calculations by which multiple cases were considered. This model estimates the final expansion based on the steel ratio and applied compressive and tensile stresses.

Based on extensive experimental investigations, the expansion process caused by ASR in plain and reinforced concrete is considered in Figure 4.9.

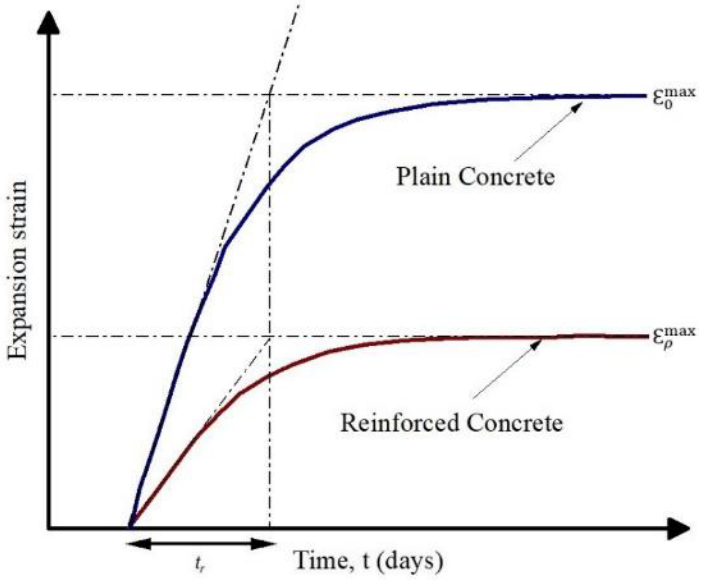

Figure 4.9 Model for ASR-induced expansion in reinforced and plain concrete.

This model determines the maximum expansion in the concrete according to the strain energy method. The following equation may be used to determine the strain energy density in a concrete prism with area A, length L, and axial stress :

$$u = \int_0^{\varepsilon} \sigma d\varepsilon \tag{4.18}$$

Where Ɛ is the strain and σ is the stress. In a simple case, the strain energy in reinforced concrete is calculated based on the strain energy in concrete (U_c) and strain energy in steel (U_s). Figures (4.10) to (4.13) provide an explanation of the mechanics of ASR-induced expansion influenced by the axial load.

This minimal semi-empirical formulation is measurable using only a few physical input parameters, such as maximum strain in plain concrete ε_0, the initiation time t_0 and the rise time t_r.

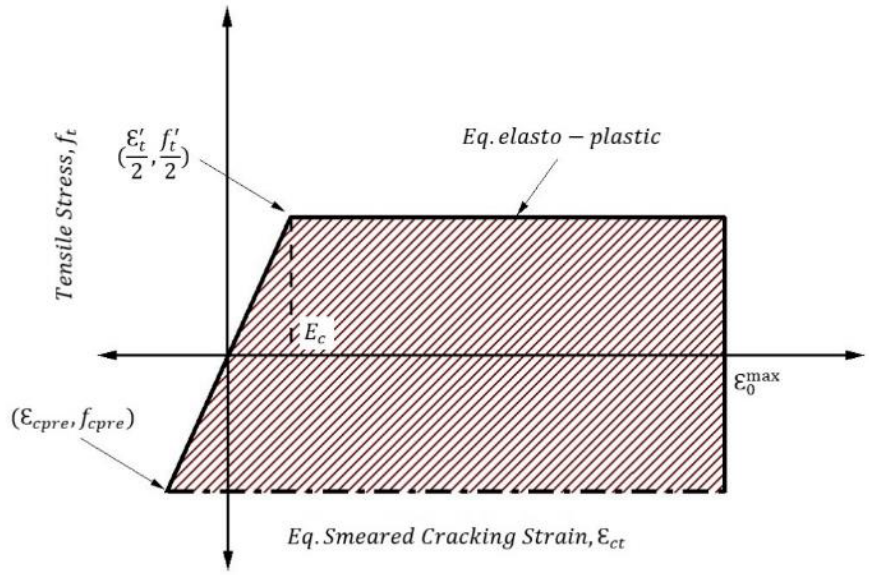

Figure 4.10 Stress-strain relation for concrete in tension.

For concrete in tension, the positive quadrant of Figure 4.10 depicts an equal elastoplastic stress relationship. Take into account the specimen of rectangular concrete in Figure 4.10 that has a longitudinal bar passing through it in the middle.

As indicated earlier, the longitudinal limitation to the longitudinal expansion of the concrete sample is larger than the transverse restriction. The expansion induced by ASR in concrete continues with time; as the expansion grows, the cover of concrete achieves its maximum tensile stress and cracks form along the longitudinal and transverse reinforcing bars. In the ultimate cracked condition, there will be no tensile tension in the cracks, but there will be some tensile stress in the concrete between the gaps. Figure 4.10 illustrates the tensile stress-average strain connection along the concrete prism using an analogous elastoplastic model.

However, concrete experiences compressive strain ε_{cpre} by applying a constant axial load, post-tensioning prestressing, or a constant compressive force P across the section. As a result of the compressive effect, concrete becomes more resistant to the expansion brought on by ASR in reinforced concrete. The region under the stress-strain curve in Figure 4.10, known as the concrete strain energy density, is represented as follows:

$$u_c = \frac{E_c}{2}\left[\left(\varepsilon_{cpre} + \varepsilon_{ct} \right)^2 - \left(\varepsilon_{ct} - \frac{\varepsilon'_t}{2} \right)^2 \right] \tag{4.19}$$

E_c is the concrete's Young's modulus; ε_{ct} refers to the tensile strain in concrete; ε'_t is the strain that corresponds to the concrete's tensile stress f'_t; and ε_{cpre} is the compressive strain that corresponds to the concrete's compressive stress $f_{cpre} = P/A_c$ where A_c is the cross-sectional area.

The elastoplastic stress-strain relationship of the reinforcing steel is shown in Figure 4.11. By applying a compressive force, the reinforcement experiences a compressive strain.

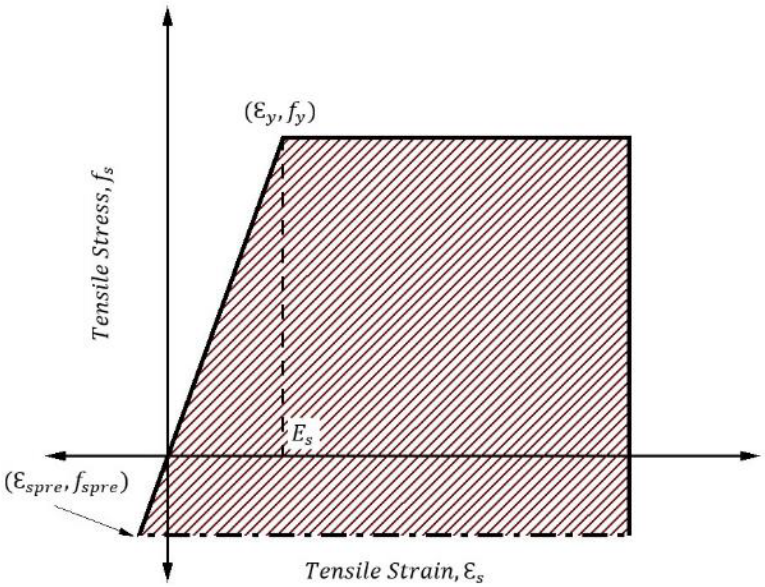

Figure 4.11 Stress-strain relation for reinforcing steel.

According to the steel ratio and the compressive load applied to the reinforced concrete structure, two states must be considered. A scenario in which the expansion strains due to the expansion of ASR exceed the yield strain of the reinforcing steel and a case in which the strains are less than the yield strain. The strain energy density of steel, shown in Figure 4.11 by the shaded region, is defined as:

$$u_s = \frac{E_s}{2}\left[\left(\varepsilon_{spre} + \varepsilon_s\right)^2 - \left(\varepsilon_s - \varepsilon_y\right)^2\right] \qquad (4.20)$$

E_s is the steel's Young's modulus; ε_s is the steel's tensile strain; ε_y is the reinforcement steel's yield strain, and ε_{spre} is the compressive strain, which corresponds to the compressive stress in steel $f_{spre} = P/A_s$ where A_s is the reinforcement steel's total cross-sectional area. Note that the term $\varepsilon_s - \varepsilon_y = 0$ applies when the strain is lower than the yield strain.

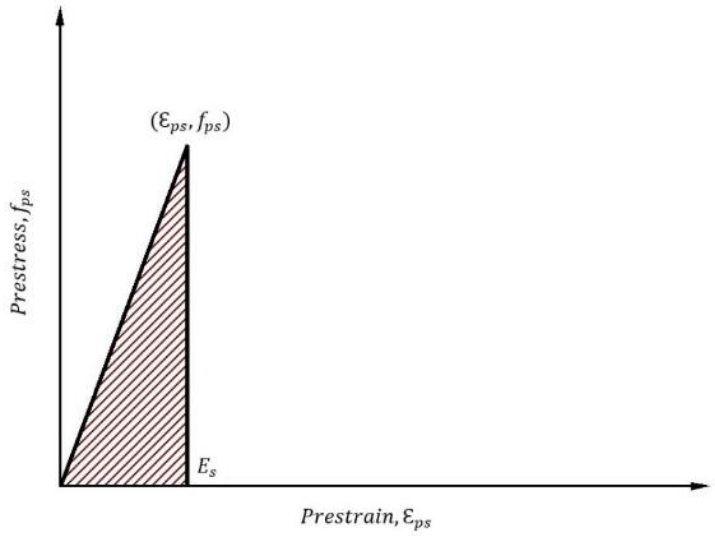

Figure 4.12 Stress-strain relation for prestressing steel.

It is also important to take into account the prestressing strands' contribution to the structure's strain energy density. Following is a calculation for the area of the highlighted region beneath the strand's stress-strain curve in Figure 4.12:

$$u_{ps} = \frac{E_s}{2}\varepsilon_{ps}^2 \tag{4.21}$$

Where A_{ps} is the area of the prestressing strands and $\varepsilon_{ps} = P/(E_s A_{ps})$ is the pre-strain in the strands.

Finally, as shown in Figure 4.13, a constant applied compressive force results in constant compressive stress ($\sigma_{const} = P/A_c$) throughout the concrete structure.

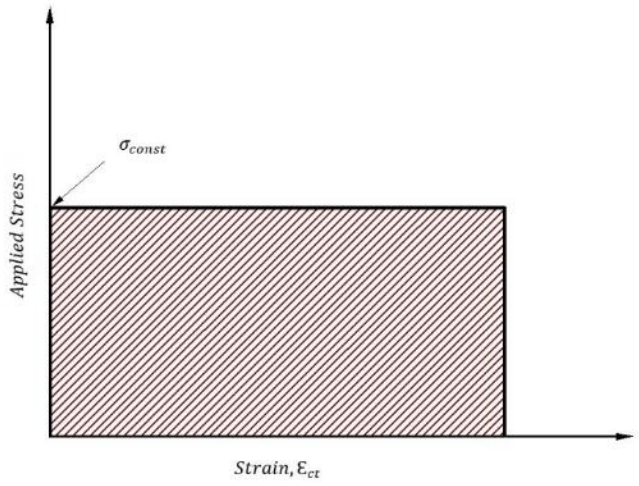

Figure 4.13 Stress-strain relation for constant applied stress.

The resulting strain energy density due to the constant applied stress can be calculated from the following equation:

$$u_{const} = \sigma_{const}\varepsilon_{ct} \tag{4.22}$$

By multiplying equations (4.19) to (4.22) and using the principle of conservation of energy:

$$U_{PC} = U_{RC} = U_c + U_s + U_{ps} + U_{const} \tag{4.23}$$

U_c is the total strain energy of concrete, U_s and U_{ps} are the total strain energy of reinforcing steel and prestressing strands, and U_{const} is the total strain energy of constant stress. Assuming the same strain in concrete and steel: ($\varepsilon_{ct} = \varepsilon_s$) and rearranging the expressions, the following conditional quadratic equation is obtained:

$$\frac{1}{2}\rho n\varepsilon_s^2\left(1-\left(1-\frac{\varepsilon_y}{\varepsilon_s}\right)^2\right)+\ \varepsilon_s\left(\frac{\varepsilon_t'}{2}-\varepsilon_{cpre}-\rho n\varepsilon_{spre}-\frac{\sigma_{const}}{E_c}\right)-\frac{\varepsilon_t'\varepsilon_0}{2}+\frac{\varepsilon_{cpre}^2}{2}+\frac{\rho n\varepsilon_{spre}^2}{2}+\frac{\rho_{ps}n\varepsilon_{ps}^2}{2}=0 \quad (4.24)$$

$\rho = A_s/A_c$ = reinforcement ratio; $\rho_{ps} = A_{ps}/A_c$ = prestressing strand ratio; and $n = E_s/E_c$ = modular ratio. The solution is defined separately for the case where the expansion strains are greater or less than the yield strain of the steel.

$$\text{For } \varepsilon_s > \varepsilon_y:\ \varepsilon_\rho = \frac{\varepsilon_0\varepsilon_t'+\rho n\left(\varepsilon_y^2-\varepsilon_{spre}^2\right)-\varepsilon_{cpre}^2-\rho_{ps}n\varepsilon_{ps}^2}{2\left(\frac{\varepsilon_t^2}{2}-\varepsilon_{cpre}+\rho n\left(\varepsilon_y-\varepsilon_{spre}\right)-\frac{\sigma_{const}}{E_c}\right)} \quad (4.25)$$

$$\text{For } \varepsilon_s < \varepsilon_y:\ \varepsilon_\rho = \frac{\frac{\varepsilon_t^2}{2}-\varepsilon_{cpre}-\rho n\varepsilon_{spre}-\frac{\sigma_{const}}{E_c}}{\rho n}\times\left(\pm\sqrt{1-\frac{\rho n\left(\varepsilon_{cpre}^2+\rho n\varepsilon_{spre}^2+\rho_{ps}n\varepsilon_{ps}^2-\varepsilon_t'\varepsilon_0\right)}{\left(\varepsilon_t'-\varepsilon_{cpre}-\rho n\varepsilon_{spre}-\frac{\sigma_{const}}{E_c}\right)^2}}-1\right) \quad (4.26)$$

Where, as previously defined, the parameters ε_{cpre}, ε_{spre}, and σ_{const} are positive for tensile strains due to tensile loads and negative for compressive strains due to compressive loads.

In the case of no prestressing strands, ρ_{ps} is equal to zero. It should also be noted that the expansion strain ε_p cannot be negative, and therefore in Eq. (4.26), it is important to consider only the positive value of its ε_ρ. If no static load or prestressing force is applied to the concrete member, the terms ε_{cpre}, ε_{spre}, ε_{ps}, and σ_{const} are zero, leading to a simplified expression for ε_ρ:

$$\text{For } \varepsilon_s > \varepsilon_y : \varepsilon_\rho = \frac{\varepsilon_0\left[1+\left(\frac{\rho n \varepsilon_y}{\varepsilon_t'}\right)\left(\frac{\varepsilon_y}{\varepsilon_0}\right)\right]}{1+\left(\frac{2\rho n \varepsilon_y}{\varepsilon_t'}\right)} \quad (4.27)$$

$$\text{For } \varepsilon_s < \varepsilon_y : \varepsilon_\rho = \frac{\varepsilon_t'}{2\rho n}\left[\sqrt{1+4\rho n\frac{\varepsilon_0}{\varepsilon_t'}}-1\right] \quad (4.28)$$

Therefore, considering the prestressing effects, as well as the applied compressive forces or the expansion strains (more or less than the yield stress of the steel), the expansion strain caused by ASR can be estimated. The reinforcement ratio (ρ and ρ_{ps}) is determined from the properties of the section and the remaining parameters, such as ε_y and ε'_t, from the properties of the reinforcing steel and concrete materials.

4.2.4 Moisture Content

Léger and Côté et al. (1996) reported for inducing major expansion, about 75% relative humidity (RH) is required, which is considered to change linearly between 75% RH and 100% RH, as illustrated in Figure 4.14.

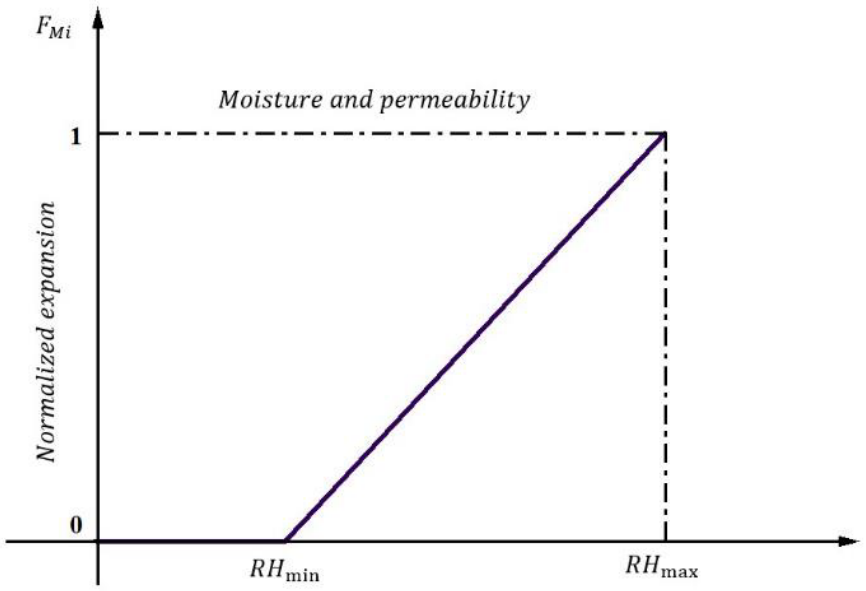

Figure 4.14 Parameter Factor of RH influencing ASR concrete expansion.

According to the ledger study on a dam, $F_M = 0$ will be applied to a dam segment with a relative humidity of less than 75%.

To rationalize the numerical simulation of concrete expansion, the concept of the F_M defined by ledger to represent the impact of moisture on the ASR expansion. From the Leger study, $F_M = 0.4$ at 85% RH and $F_M = 1$ at 100% RH, respectively. It is evident that at the upstream face of a dam, the RH is close to 100%. Therefore, the maximal expansion related to the impact of this parameter will occur around this surface. However, because of the multiple water sources and infiltration mechanisms, a comprehensive examination of the RH inside the dam's bulk is difficult, particularly if ASR affects the concrete. (Cracks, joints, drains, diffusion, capillarity, etc.).

The moisture impact is reflected in the coefficient F_M is calculated as

$$F_M(h) = \frac{1}{1-h_{min}} (h - h_{min}) \tag{4.29}$$

Given the difficulty of conducting a thorough moisture/water transport investigation, a value of $F_M = 1$ might be used as a starting point for aging hydraulic systems. Distinct F_M values may be applied to different zones with clearly defined moisture zones, for as, in a spillway pier that is partly submerged throughout its width

4.3 VALIDATION

In the case of constant temperature, the differential equations for the kinetics of ASR extent can be solved analytically. Otherwise, it must be solved numerically. Numerical calculations were performed using the Advanced Tool for Engineering Nonlinear Analysis (ATENA) finite element software.

The proposed model is validated against three experimental tests. To achieve this purpose, Clark's (1996) experimental test on cylindrical samples with dimensions of

100 mm × 200 mm with different percentages of rebar was presented and modelled. Then, the first series of Fan's experimental tests were modelled in free and restraint conditions. Finally, real-size reinforced concrete beams were modelled, and their results were compared with the experimental data. The initial parameters are shown in Table 4.1.

Table 4.1. The initial parameters employed for the numerical modelling of ASR expansion

Variable	Symbol	Value
Required alkali per reactive silica	r	*15.4%*
Proportion reactive silica	s	*21.8%*
Proportion reactive particles in sand	p	*30%*
Sand mass	AC	*833 kg/m³*
Measured ASR strain	ε_F	*0.0525%/kg*
Amount of required alkali	A_R	*8.39 kg/m³*
Total alkali in mortar	A_T	*5.4, 9 kg/m³*
Threshold alkali in concrete	A_0	*3.7 kg/m³*
Characteristic time	τ_C	*20 days*
Latency time	τ_L	*55, 45 days*
Elastic modulus of concrete	E_c	*27 GPa*
Elastic modulus of steel	E_s	*193 GPa*
Compressive strength	f_c	*26 MPa*
Yield strain	ε_y	*0.0022, 0.00145*
Tensile fracture strain	ε'_t	*0.0004, 0.00013*
Creep coefficient	C_f	*2*

4.3.1 Case Study 1

Jones and Clark (1996) conducted several experimental tests to determine the impact of ASR on concrete expansion. Experiments have been performed on cylindrical samples with different reinforcement ratios, ¼, 1/2, 1, and 2%, and the expansion has been compared with the free expansion sample. By adding sodium hydroxide to the concrete mix, the total alkali amount reached 7 kg/m^3. The samples were placed in the ASR environment at 38 degrees for approximately 250 days. The

literature has not provided all the details, so typical values are assumed for unknown parameters for the proposed model.

The following Figures (4.15 to 4.20) compare the experimental data and the proposed model results. The experimental data are in the form of points and continuous lines, representing the proposed modelling results.

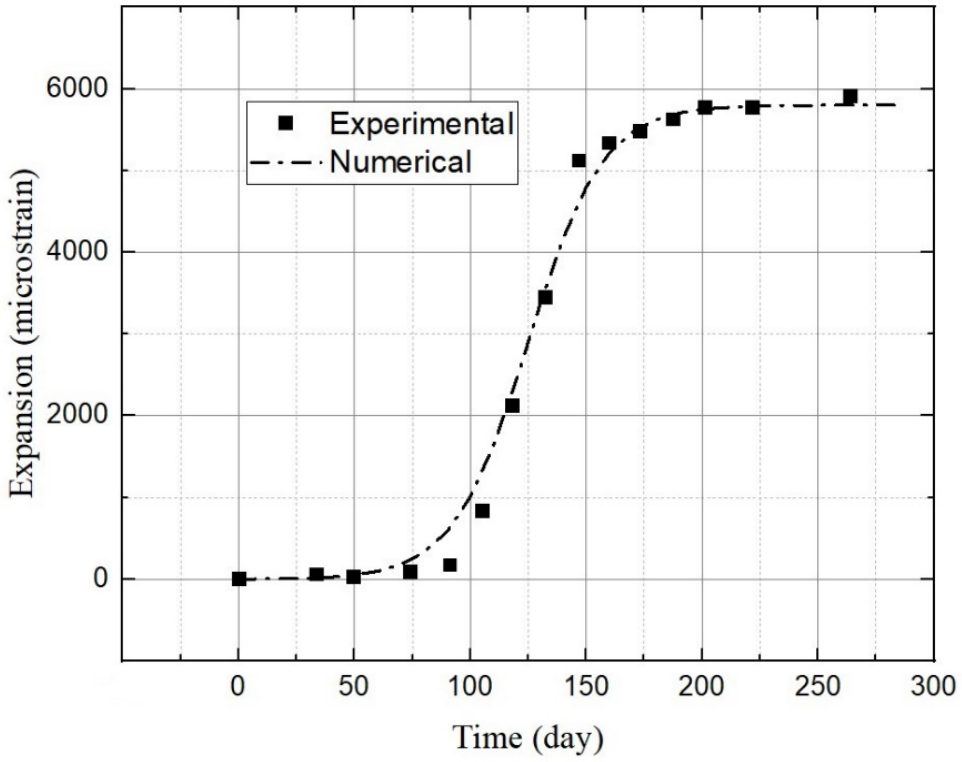

Figure 4.15 Clark's empirical values and numerical computations for free expansion are compared.

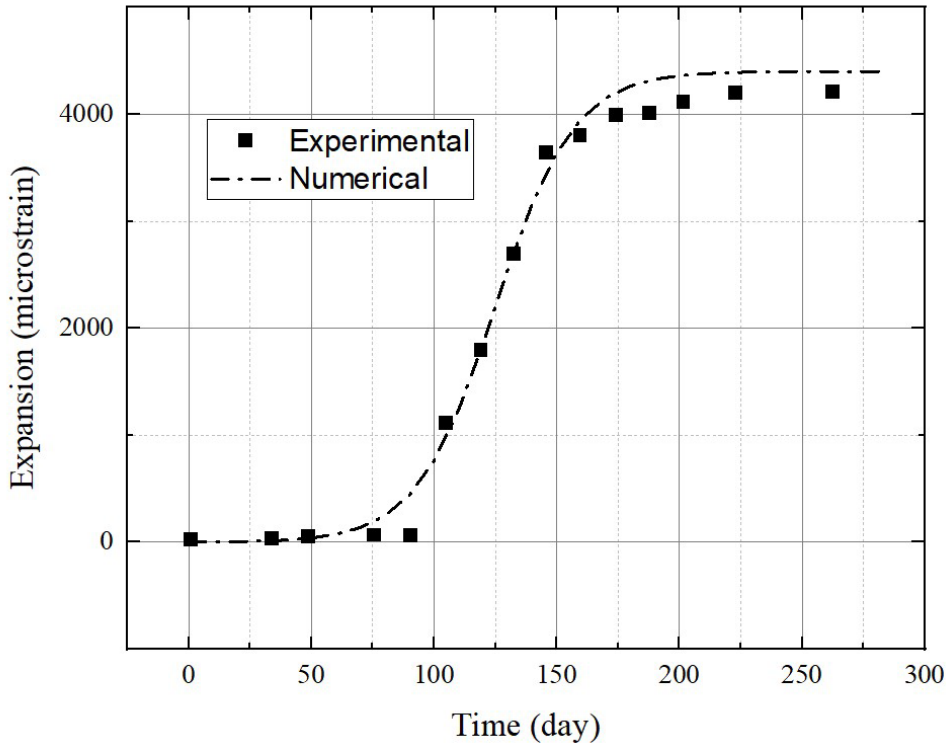

Figure 4.16 Clark's empirical values and numerical computations with 0.25% reinforcement ratios are compared.

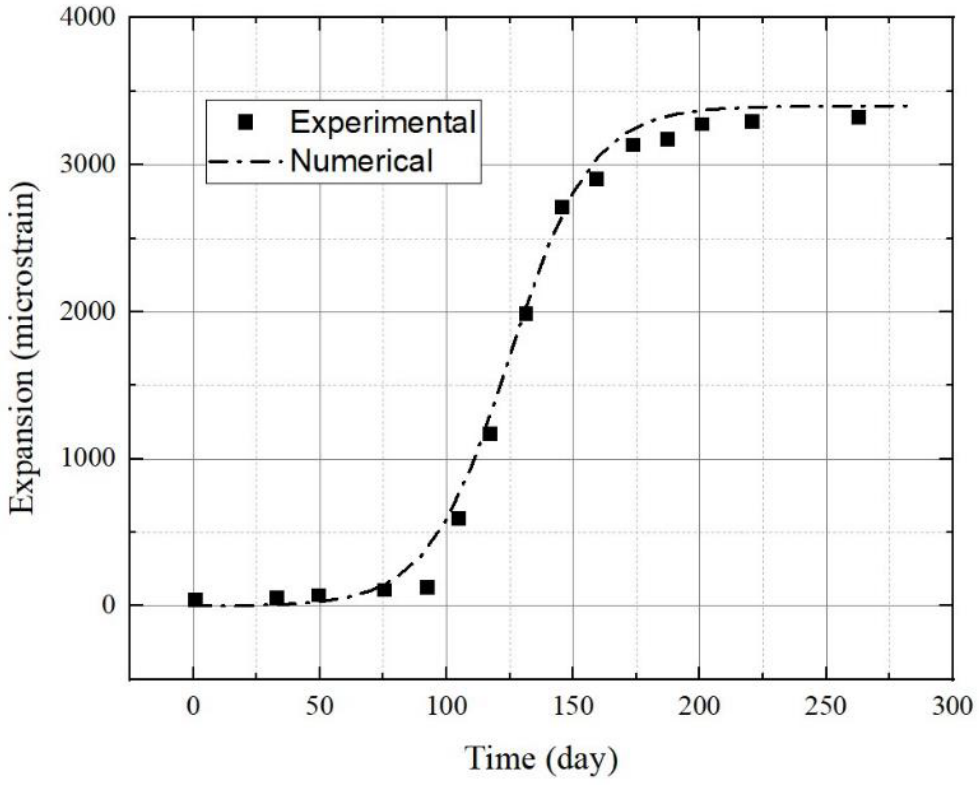

Figure 4.17 Clark's empirical values and numerical computations with 0.5% reinforcement ratios are compared.

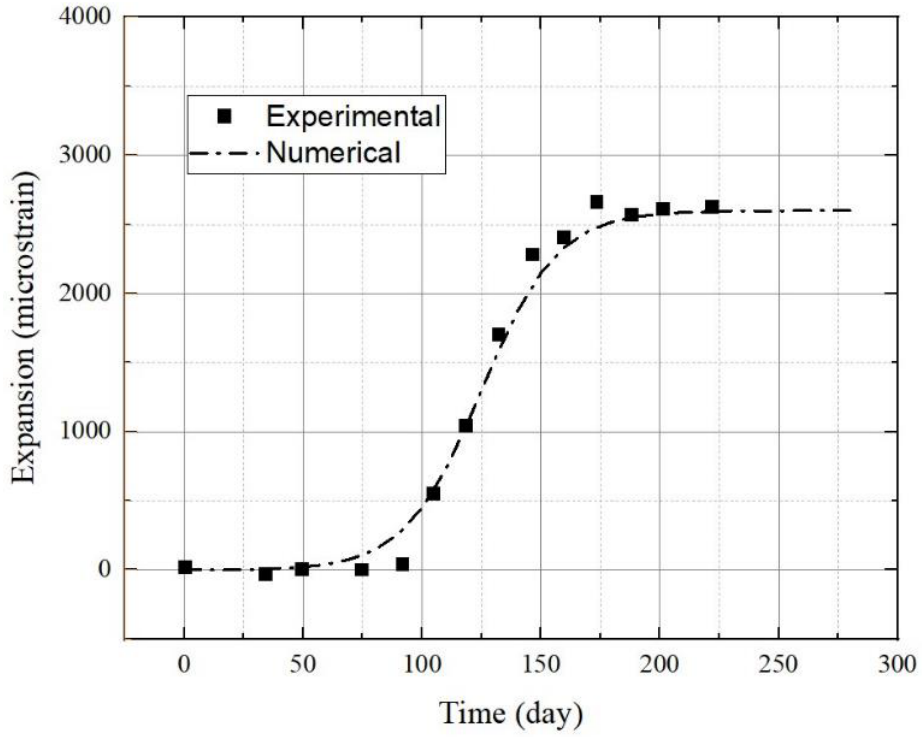

Figure 4.18 Clark's empirical values and numerical computations with 1% reinforcement ratios are compared.

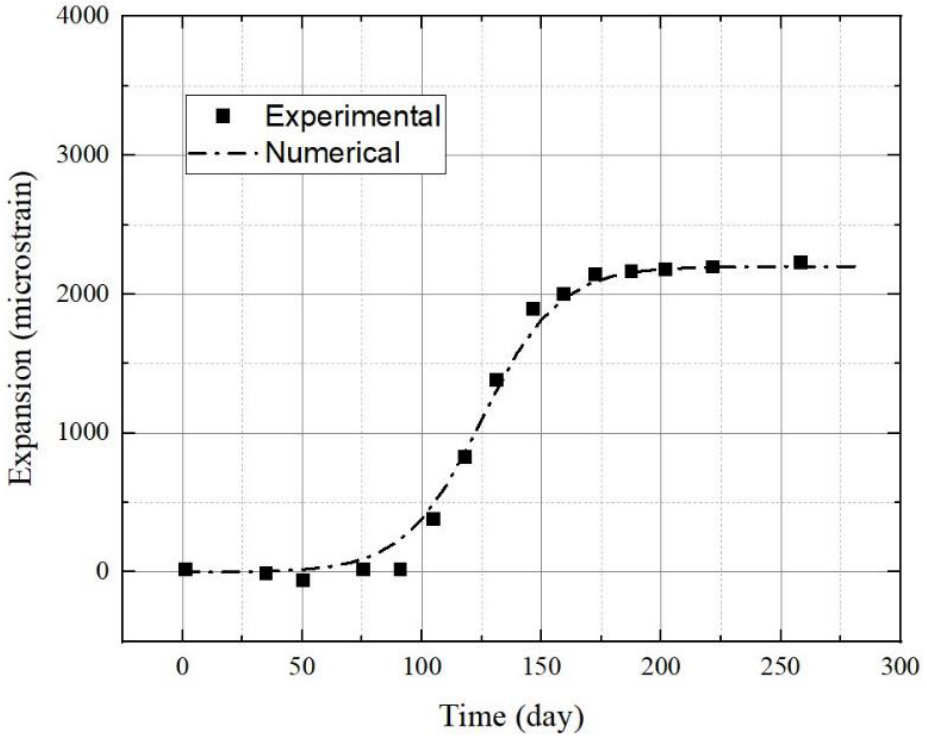

Figure 4.19 Clark's empirical values and numerical computations with 2% reinforcement ratios are compared.

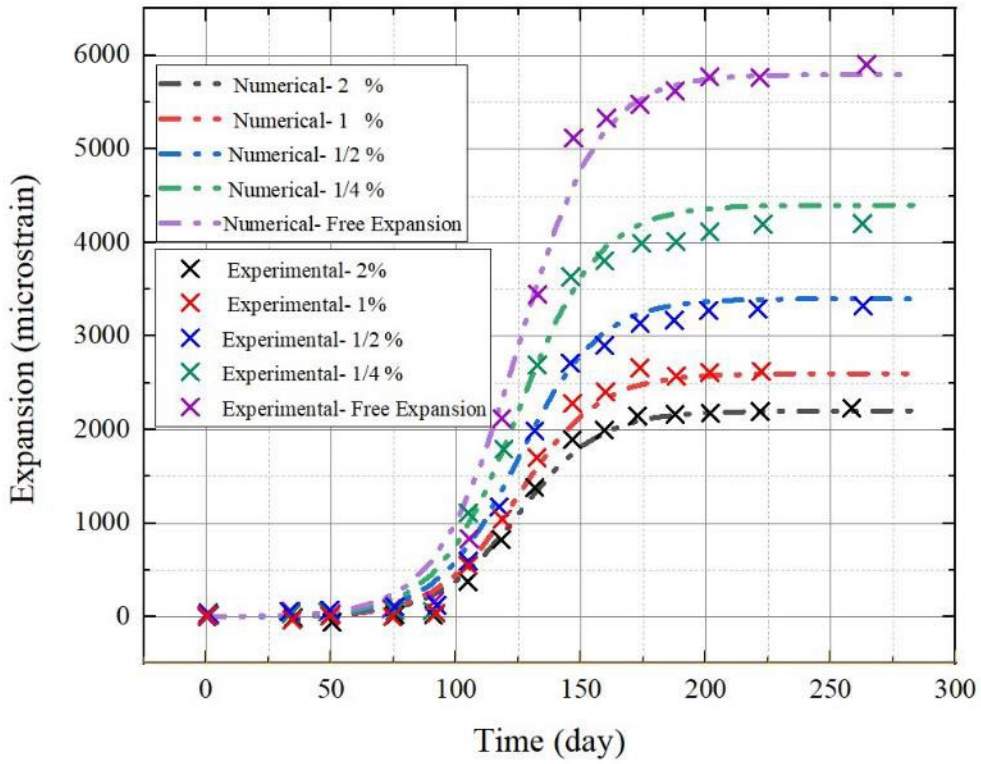

Figure 4.20 Clark's experimental findings and numerical computations are compared.

The comparison demonstrates that with plausible assumed values for a few unknown parameters required for our modelling, an accurate prediction model for ASR expansion is obtained.

4.3.2 Case Study 2

Twelve cubic samples with dimensions of 75 mm × 75 mm × 400 mm and six samples with dimensions of 225 mm×225 mm × 400 mm in free expansion condition, and three prisms in dimensions of 225 mm×225 mm×400 mm in restraint condition have been examined by Fan and Hanson (1998). In reinforced samples, four 10 mm rebars were used symmetrically in the four corners of the sample. The samples were immersed in a solution with a concentration of 0.5 M sodium hydroxide at 38 degrees. Demec gauges have been used to measure longitudinal expansion, and 6 mm electric strain gauges have been used to measure the amount of strain in rebars.

The results of these two comparisons are given in the Figures 4.21 and 4.22. Figure 4.21 shows the results of experimental data with triangle and the continuous dash line represent the results of the proposed modelling.

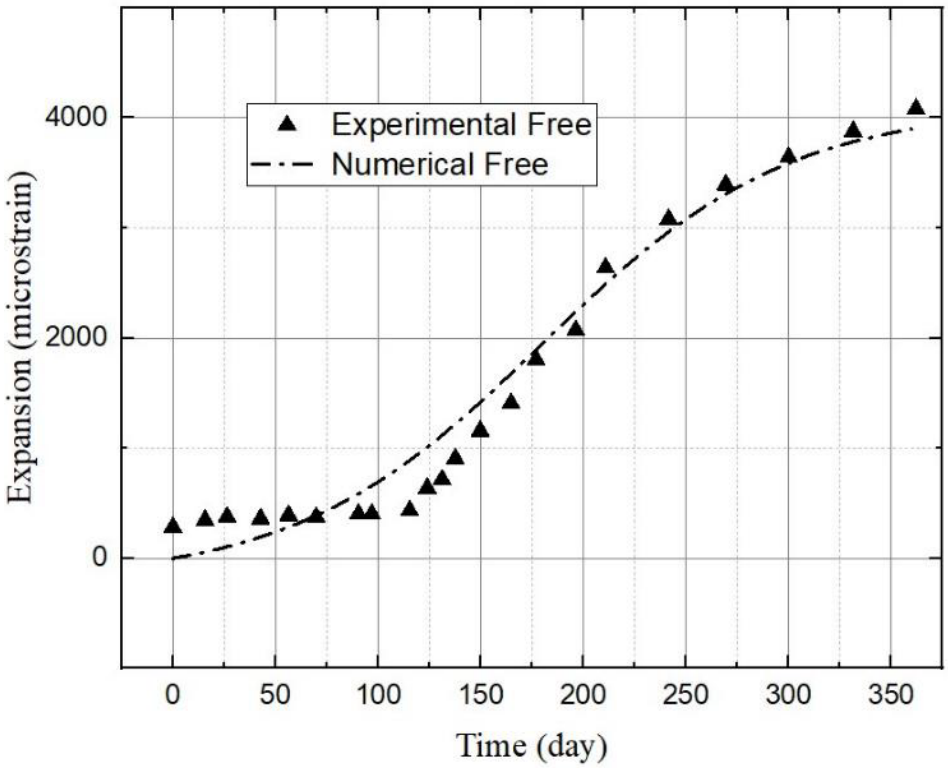

Figure 4.21 Comparative analysis of Fan's experimental and numerical results.

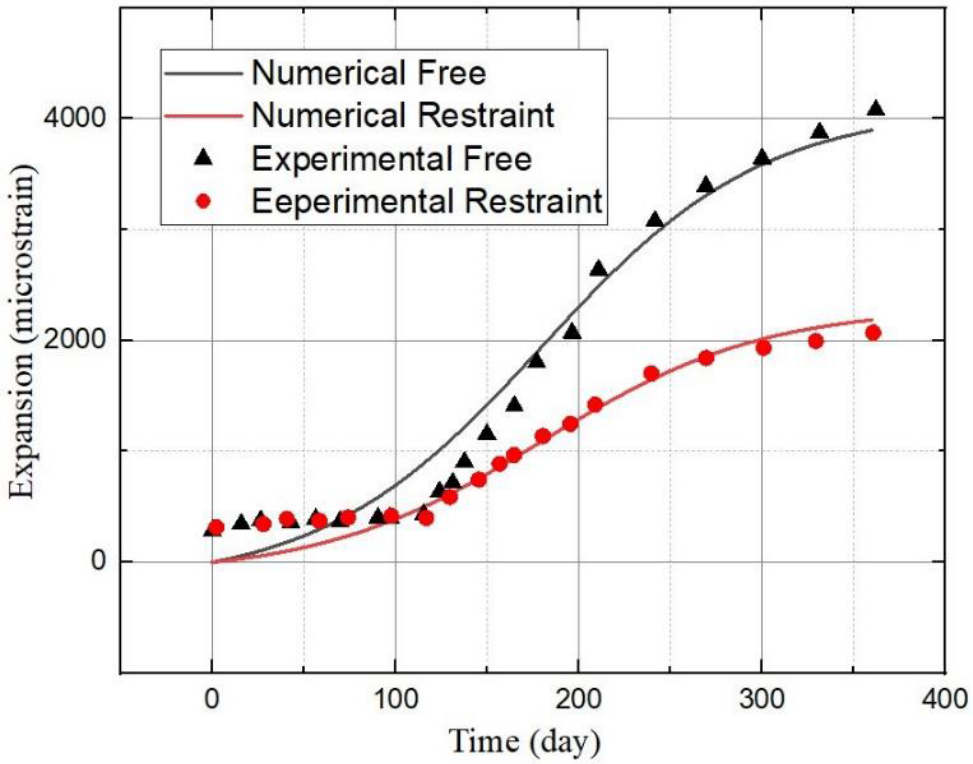

Figure 4.22 Comparative analysis of Fan's experimental and numerical results.

It is clear from Figures 4.21 and 4.22 that the proposed hybrid model can efficiently simulate the expansion due to ASR for both different modes, free and restraint expansion, in three dimensions. The literature does not include all of the necessary data for the suggested model. The unknown parameters required for modelling plain concrete expansion have been reasonably estimated. In other words, the model is calibrated in free expansion conditions. Then, the same assumptions obtained from modelling plain concrete were used in the real-size beams model.

4.3.3 Case Study 3

Four real-size beams with 150 mm × 300 mm cross-sections and 1.5 meters in length were tested by Fan and Hanson (1998). Two beams were cast normally, and the others were poured with reactive materials. The same mixture and materials were used with small samples (case study 2) and placed in the same conditions in sodium

hydroxide solution at 38 degrees. The beams of the first series were designed with two 16 mm tensile reinforcements, while the beams of the second series were designed with 10 mm tensile reinforcement.

The material used in these beams is similar to Fan's previous experiments on smaller specimens. Therefore, the same parameters obtained in the previous experiment have been used. The details of other parameters are given in this Table 4.1. Thus, no other calibration was needed for this modelling.

The strain in the upper and lower reinforcements has been monitored. The results of the comparison between the experimental data and the data obtained from the modelling are given in Figures 4.23 to 4.25. The points represent the experimental data, and the continuous lines represent the modelling results.

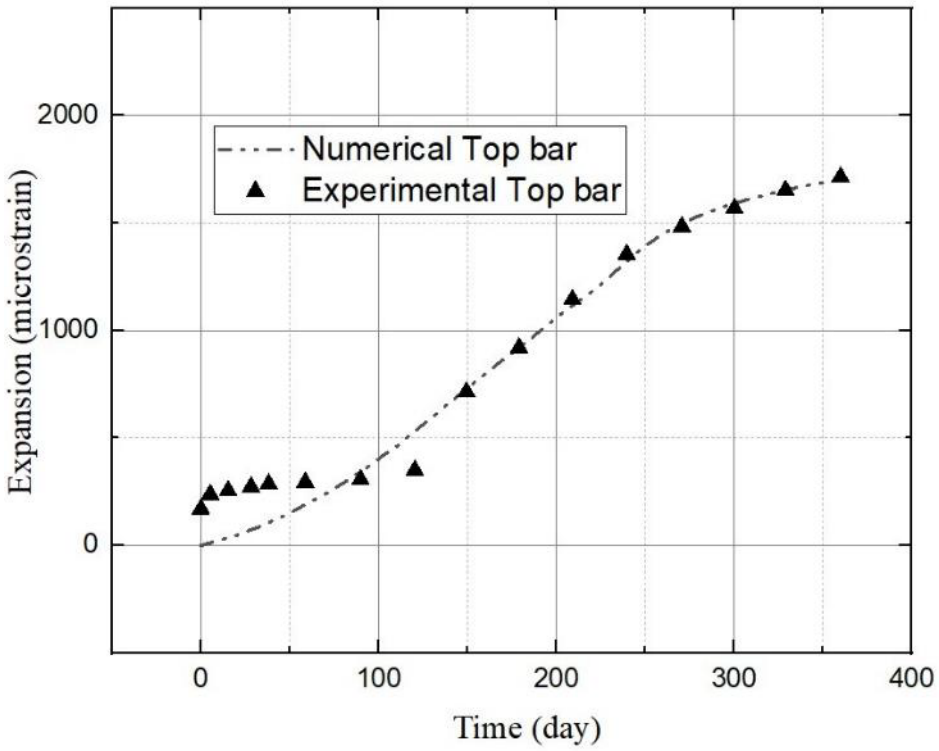

Figure 4.23 Comparative analysis of Fan's experimental and numerical results.

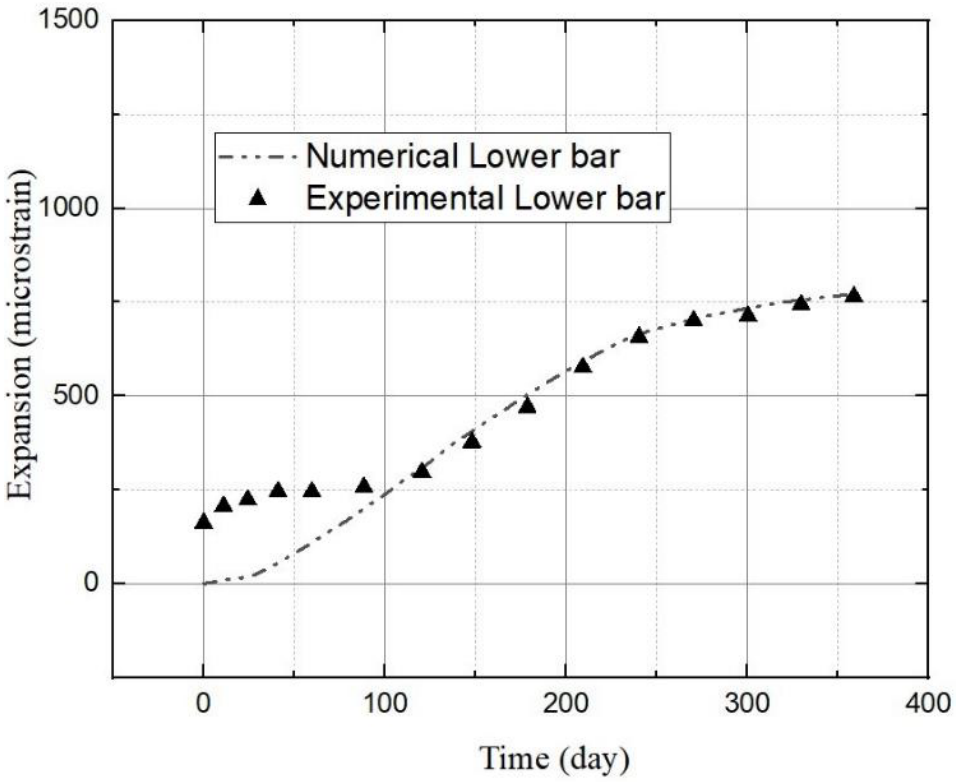

Figure 4.24 Comparative analysis of Fan's experimental and numerical results.

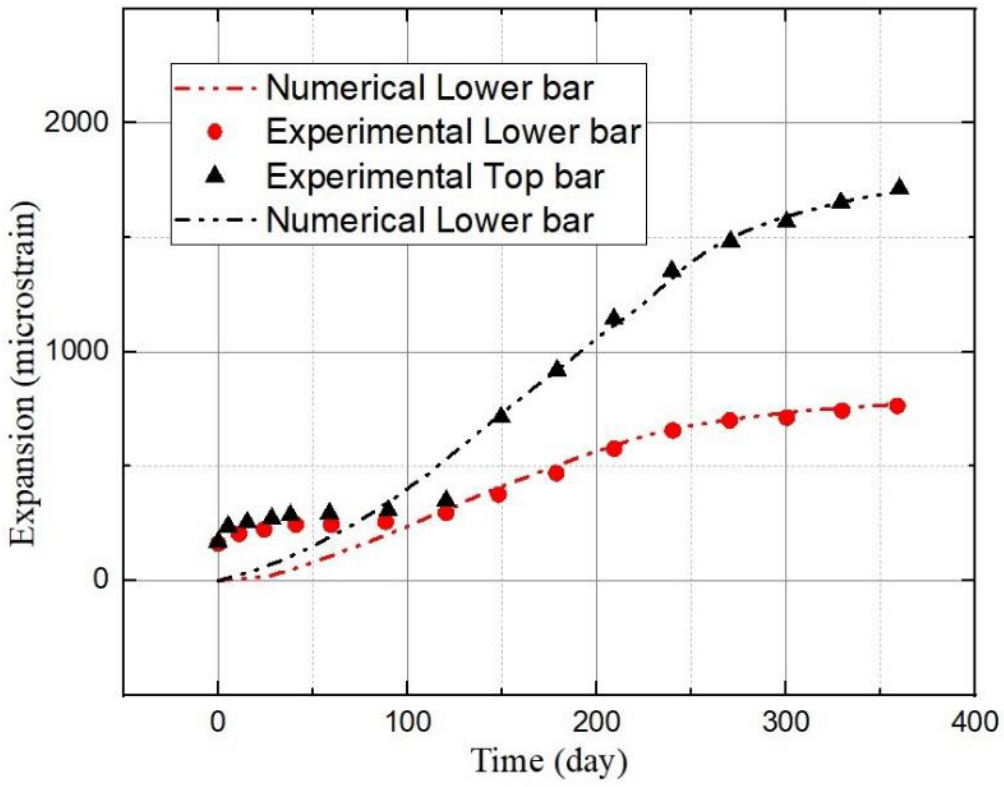

Figure 4.25 Comparative analysis of Fan's experimental and numerical results.

4.4 SUMMARY

This thermo-chemo-mechanical model is rooted in the kinetics of reaction presented by Larive (1998); despite being slightly modified, it also affects compression forces and concrete mechanics. This model assumes that the weight function distribution is based on stress sensors. In this model, stress tensors also affect the kinetics of the reaction, unlike previous models.

The validity of suggested modifications was confirmed by comparing the model's expansion predictions with experimental data from small samples and real size reinforced concrete beams. The numerical results match the experimental results well. The model calculates the expansion strain in reinforced concrete samples exposed to changing temperature and humidity in the field, taking into account the effects of post-tensioning forces.

The model can also simulate the longitudinal and transverse expansion stresses by considering reinforcement ratios, and estimating the expansion of restrained, especially prestressed, members.

In this method, modelling restraint members in both methods of using rebar or applying external stress have been considered, enabling us to model prestressed members as well.

Chapter 5: EXPERIMENTAL PROGRAM

5.1 OVERVIEW

An accurate assessment of the residual load-carrying capacity of ASR-deteriorated structures is necessary to guarantee the safety of concrete structures for strength and serviceability requirements. On the one hand, a conventional and conservative assessment of the load-carrying capacity may affect the structure's performance, and on the other hand, the structure and the public's safety may be at risk by overestimating the residual load-carrying capacity. As a result, the residual load-carrying capacity of the structures affected by ASR must be precisely assessed.

Numerous investigations and experiments on reinforced concrete members have been carried out recently by various researchers to assess the safety of concrete structures impacted by ASR (Kobayashi et al., 1988; Fan & Hanson, 1998; Deschenes et al., 2009; Monette, 1997). However, there is currently little information about the fundamental properties of ASR-damaged structures and prestressed concrete members affected by ASR.

This Chapter describes the experimental program for characterizing ASR-affected concrete samples conducted in the Laboratory, University of Technology, Sydney (Tech Lab). Eight real-size prestressed and reinforced beams and companion cylinder specimens with reactive and non-reactive aggregates were prepared. Several sets of mechanical tests were conducted, including compression, indirect tensile, and modulus of elasticity. In addition, to measure the free expansion of the concrete due to ASR, six prisms were made with reactive aggregate and measured regularly over nine

months. The design of test specimens, construction procedure, instrumentation and data collection techniques are documented.

Studies on the effect of ASR samples under field conditions sometimes last up to 10 years due to the ASR's slow reaction rate (Hamada, Otsuki, & Fukute, 1989). As a result, a quick test technique to assess the ASR-affected structures is essential. Several controlled laboratory experiments have been developed to examine the flexural and shear behaviour of reinforced concrete samples at various scales. Although the stiffness and strength of ASR-damaged concrete structures have been the subject of some experimental research in literature, a well-accepted accelerated method for estimating the residual load-carrying capacity of ASR-damaged structures is not yet available. Therefore, to achieve the ASR detrimental effect in the short term, immersion of the specimens in a heated alkali solution was used for nine months to accelerate ASR process.

After preparing the test specimens using reactive aggregates, accelerated curing was carried out, and the relationship between expansion rate, compressive strength and static elastic modulus was investigated to classify the degree of concrete deterioration. Also, the impact of detrimental ASR expansion on the structural behaviour of the reinforced and prestressed concrete beams was examined in the structural laboratory of Tech Lab.

The expansive strains and crack patterns on prestressed concrete beams affected by ASR were then reported. A free expansion was measured and recorded on prisms with embedded stainless studs at two ends of the prism. Also, the mechanical properties of ASR-affected concrete under accelerated tests were investigated. Subsequently, the destructive four-point loading tests were performed on real-size prestressed beam

samples, and the load-carrying performance was evaluated using the load-deflection curve. Finally, the strength and deformation characteristics of reactive beams were compared to non-reactive beams to assess the residual load-carrying capacity of ASR-affected beams. It should be noted that all specimens were designed and detailed to AS3600-2018.

5.2 DESIGN AND DETAILING OF PRESTRESSED BEAMS

Design of the prestressed concrete beam samples was attempted to be close to the real-size beams. As the samples had to be placed in water tanks, the size of the tank for the ASR accelerated conditions was an important parameter when designing the length of the beams.

Additionally, since the reactive concrete for the beams was made from a specific type of reactive aggregate, premix ready concrete could not be ordered from external suppliers, and mix design of the concrete had to be done at UTS Tech Lab. Therefore, it was essential to determine and control the maximum volume of concrete considering the required equipment for mixing and casting concrete for beams and companion specimens to prevent the beams from developing cold joints. In order to achieve this purpose, considering two available pan mixers, the total capacity of 140 litres of concrete for a homogeneous concrete mix was estimated.

Accordingly, considering the two factors of water tank size for the ASR conditions and the capacity of available concrete mixers in the concrete laboratory, the length of the beams was reduced to 1.5 meters.

Based on the prestress losses, in the relatively short beams, there is a significant loss due to slip in the anchorages. Therefore, using a strand for post-tensioning operations was not advised in this study.

It was critical to use an alternative technique that could apply the required effective prestressing force to the short-length concrete beam of 1.5 metres. Therefore, the Macalloy bars system were employed instead of strands for the post-tensioning procedure. Using the Macalloy bar, applying the prestress force without significant losses in the anchorages for beams with a shorter length was achievable. The minimum available diameter of Macalloy bars that could be ordered was 26.5 mm, considered suitable for the design of beams with a cross-section of 250×150 mm. As a result, the Macalloy bar was selected for post-tensioning operations in prestressed concrete beams.

According to the results of flexural tests on reinforced concrete beams affected by ASR, the ultimate strength of those affected by ASR did not change much compared to normal beams. Previous research (Fan & Hanson 1998, Abe 1989, Monette 1997, Inoue 1989) on reinforced beams showed that the ultimate strength of the beams did not change or was less than 4% in the worst case (Refer to Section 2.5.3).

Similarly, a few tests performed on prestressed concrete beams affected by ASR revealed little difference between the ultimate strength of non-reactive prestressed beam and ASR-affected prestressed beams. Clayton's studies showed that no significant change was observed in the flexural load capacity of prestressed concrete beams of typical design (Clayton & Currie et al., 1990).

In addition, based on the nature of ASR, the most impact of the alkali-silica reaction is on the concrete part of the beam. Therefore, unlike the typical design of beams, an attempt was made to design the beams so that failure occurs in the compressive surface of the concrete beam.

As a result, two pairs of prestressed beams with reactive and non-reactive concrete were designed. The first pair was designed for compression failure, and the second was designed to fail in shear.

In the first pair of prestressed beams, longitudinal rebars were used to ensure that the ductility is less than the permissible limit and failure occurs in the compressive surface of the concrete beam affected by ASR.

Stirrups have been removed in the design of second pairs of prestressed beams to make sure that the failure occurs in shear.

Six 1.5 meters beams with a cross-section of 150×250 mm were designed. The prestressing steel consists of one 26.5 mm diameter Macalloy steel bar (A_p = 572 mm^2). In order to limit the generated stresses in the concrete to 3 MPa, the effective prestress force was assumed to be 75 kN after all losses. The elastic modulus of the bar is E_p = 170×10^3 MPa, and the concrete properties are estimated as f_c'= 40 MPa and E_c = 35,000 MPa. The details of the beam design are given in Figures 5.1 and 5.2.

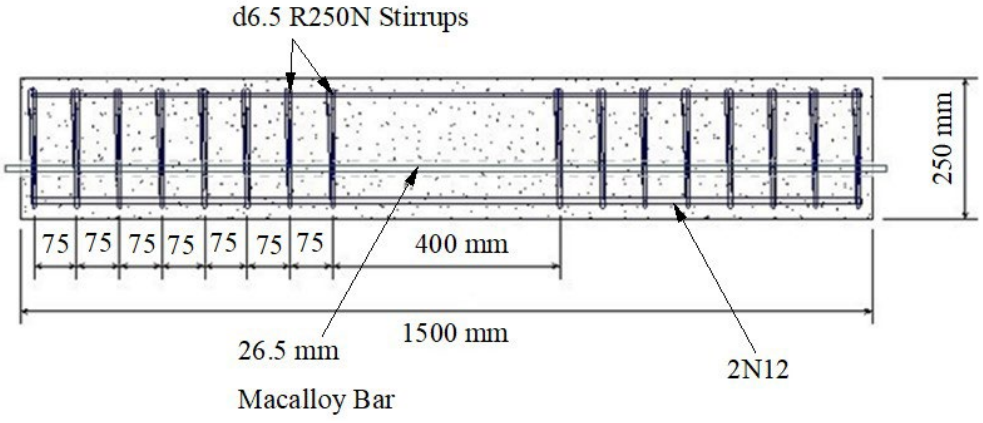

Figure 5.1 Dimensions of the beams and reinforcing details.

The details of beam design according to AS 3600 standards, reinforcement details, and effective prestress forces are given. In addition, the maximum bending moment has been estimated for the beams (Figure 5.3).

Based on AS3600-2018, α_2 = 0.79 and γ = 0.87 were calculated for f_c' = 40 MPa. The effective prestress force is P_e = 75 kN.

Therefore, the stress in the tendon is: P_e/A_p = 131 MPa.

Initial strain in the tendons because of the effective prestress is determined by:

$$\varepsilon_{pe} = \frac{P_e}{A_p \times E_p} = \frac{75 \times 1000}{572 \times 170000} = 7.713\text{e}^{-04}$$

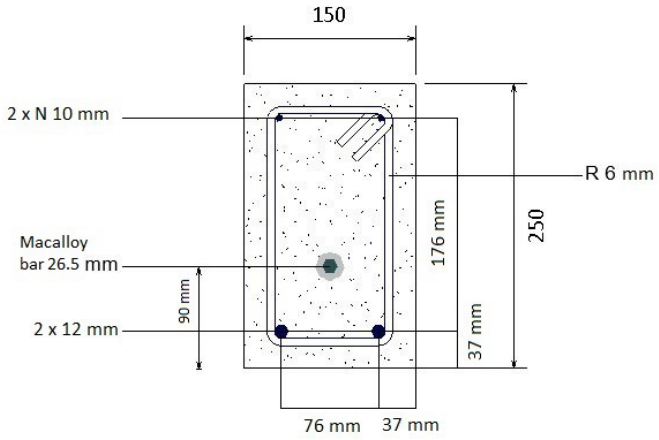

Figure 5.2 Cross section details of prestressed beams.

The concrete strain induced by the effective prestress at the level of the prestressing steel is then determined:

$$\varepsilon_{ce} = \frac{1}{E_c}\left(\frac{P_e}{A} + \frac{(P_e \times e^2)}{I}\right)$$

$$\varepsilon_{ce} = \frac{1}{35000} \times \left(\frac{75 \times 1000}{150 \times 250} + \frac{(75 \times 1000 \times 35^2)}{195312500}\right) = 7.06e^{-05}$$

The concrete strain at the level of prestressed steel at the time of failure is determined by:

$$\varepsilon_{cp} = 0.003 \times \frac{d_p - d_n}{d_n}$$

The ultimate strain in the tendons is:

$$\varepsilon_{pu} = \varepsilon_{pe} + \varepsilon_{ce} + \varepsilon_{cp}$$

$$\varepsilon_{pu} = 7.713\mathrm{e}^{-04} + 7.06e^{-05} + (0.003 \times \frac{160 - d_n}{d_n})$$

$$\sigma_{pu} = E_p \times \varepsilon_{pu}$$

$$\sigma_{pu1} = 170000 \times (8.42e^{-04} + 0.003 \times \tfrac{160 - d_n}{d_n}) \qquad (5.1)$$

$$C_c = a_2 \times f_c' \times \gamma \times b \times d_n \; ; \qquad C = 0.79 \times 40 \times 0.87 \times 150 \times d_n$$

$$T = \sigma_{pu} \times A_P + f_{sy} \times A_{st} \; ; \qquad T = \sigma_{pu} \times 572 + 500 \times 226.2$$

$$C = T \; ; \qquad \sigma_{pu2} = 7.21 d_n - 197.3 \qquad (5.2)$$

The depth of the neutral axis is d_n = 95.3 mm. The trial values of d_n have been chosen, and the corresponding values of σ_{pu} have been tabulated.

Table 5.1 Trial values of d_n and the respective values of ε_{pu} and σ_{pu}.

Trial d_n (mm)	ε_{pu} Equation	σ_{pu1} (MPa) Equation 5.1	σ_{pu2} (MPa) Equation 5.2	Error $(\sigma_{pu1} - \sigma_{pu2})$
100	0.0026	523.22	449.12	74.10
93	0.0030	472.76	510.54	37.78
95.3	0.0029	489.34	489.36	0.02

ε_{pu} = 0.0029 σ_{pu} = 489.34 MPa

Table 5.2 Geometric properties of cross section of the beams.

Geometrical Properties		
	Gross Conc.	Trans (n=8.05)
Area (mm^2) ×10^3	37.5	43.4
Inertia (mm^4) ×10^6	195.3	212.9
y_t *(mm)*	125	132
y_b *(mm)*	125	118
S_t *(mm^3) ×10^3*	1562.5	1611.1
S_b *(mm^3) ×10^3*	1562.5	1805.9

The non-prestressed steel has reached yield, that is $\varepsilon_{st} \geq \varepsilon_{sy}$ (= f_{sy}/E_s = 0.0025). The ultimate curvature is determined by the equation.:

$$k_u = \frac{\varepsilon_{cu}}{d_n} = \frac{0.003}{94.3} = 3.18e^{-05}$$

This is less than the minimum value necessary for ductility according to:

$$(k_u)\,min = \frac{0.00833}{0.8 \times 250} = 4.1652e^{-05}$$

The magnitudes of the resulting forces on the cross-section at the maximum compressive force in concrete are:

C_c = 393 kN T_p = 280 kN T_s =113.10 kN

The ultimate flexural strength M_{uo} of the rectangular section is calculated:

$$M_u = C_c \times l_c - T_p \times l_p = C_c \times \left(d_0 - \gamma \times \frac{d_n}{2}\right) - T_p \times (d_0 - d_p)$$

$$M_u = C_c \times l_c - T_p \times l_p$$

$$= 10^{-3} \times [393 \times \left(213 - 0.87 \times \frac{95.3}{2}\right) - 280 \times (213 - 160)]$$

$$\underline{M_u = 52.58 \ \ kNm}$$

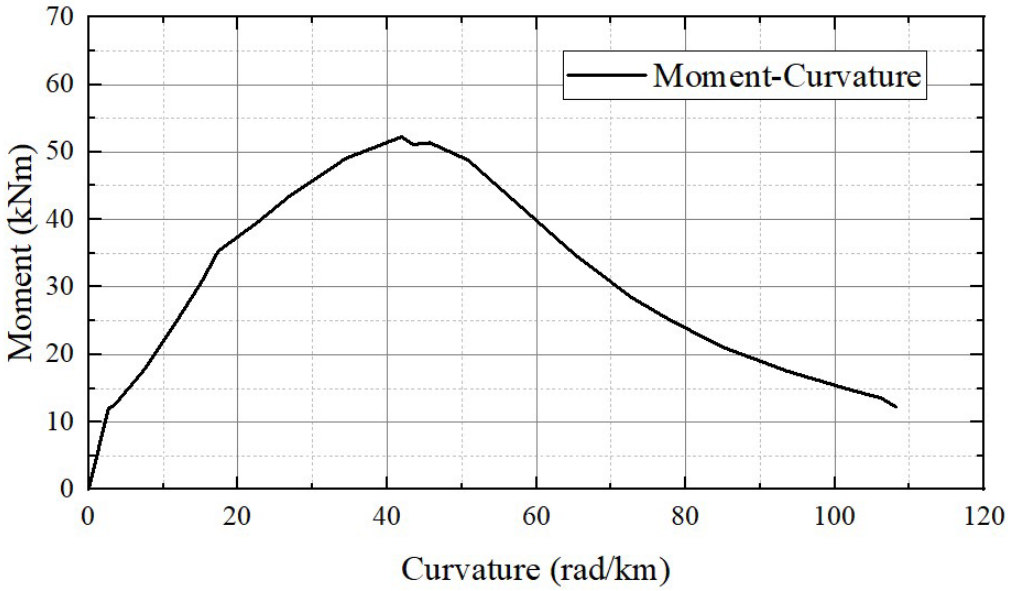

Figure 5.3 Moment-curvature diagram of prestressed beam.

5.3 MATERIAL PROPERTIES

5.3.1 Concrete Constituent Materials

The concrete mix design and materials proportions were designed considering two major goals: (I) maximise the detrimental expansion attainable within the current study's timescale, and (II) retain an accurate portrayal of current engineering practice.

Aggregate

For casting reactive and non-reactive specimens, two types of coarse aggregate were used. One was the highly reactive dacite aggregates, and another was the non-reactive limestone aggregates as a reference. Table 5.3 shows the chemical compositions of the reactive and non-reactive aggregate. 10 and 20 mm non-reactive limestone were used in the mix proportion for control specimens, while the same proportion of reactive dacite aggregates was selected for the reactive mixture. Sydney sand and non-reactive dune sand were used as fine aggregates for all mixtures. Table 5.4 illustrates the reactive and non-reactive aggregates that were used in this study. In

addition, the grading details of the Sydney sand and aggregates used in this study are shown in Figures 5.5 and 5.6.

Table 5.3 Percentile chemical composition of the aggregates.

Aggregate	CaO	SiO_2	Al_2O_3	Fe_2O_3	MgO	TiO_2	Na_2O	K_2O	LOI
Dacite aggregate	2.35	68.38	13.25	3.32	1.3	0.36	3.41	3.84	4.52
Non-reactive aggregate	9.04	43.22	14.47	12.15	8.97	2.98	4.01	1.81	1.34

As shown in Figure 5.4, all aggregates were washed, prepared, weighed, and sealed in plastic containers before casting.

Figure 5.4 Aggregates washed, weighed, and sealed in plastic containers.

Table 5.4 Different types and size of aggregates used in concrete mixture.

Aggregate	Type	Status
Limestone (20mm)	Coarse	Non-reactive
Limestone (10mm)	Coarse	Non-reactive
Dacite (20mm)	Coarse	Reactive
Dacite (10mm)	Coarse	Reactive
Crushed Dacite	Fine	Reactive
Crushed Limestone	Fine	Non-reactive
River Sand Natural (Brown)	Fine	Non-reactive
Stockton dune sand	Fine	Non-reactive

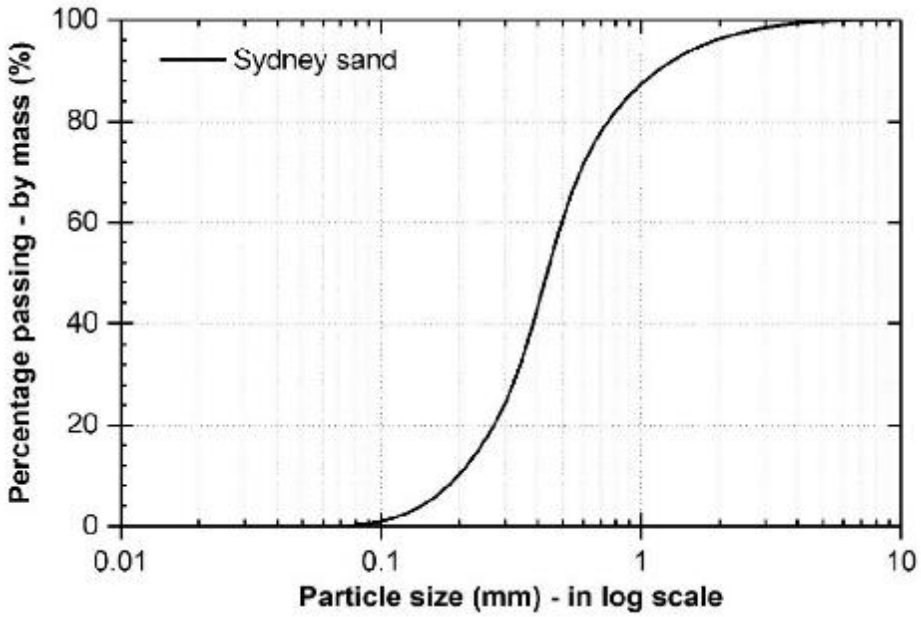

Figure 5.5 Cumulated PSD of fine aggregates (Sydney sand).

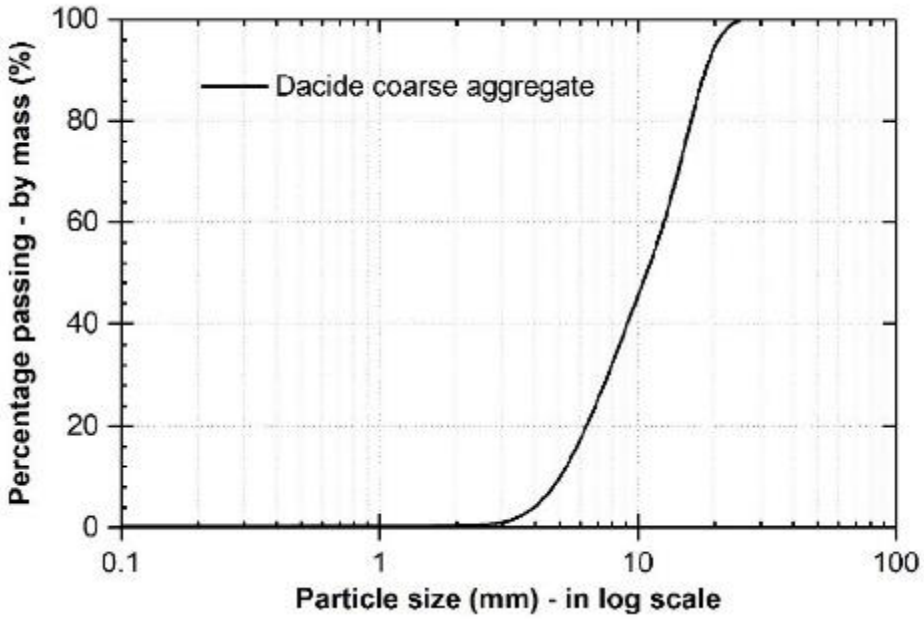

Figure 5.6 Cumulated PSD of coarse aggregates (dacite aggregate).

In order to accelerate the reaction procedure, the crushed reactive aggregate was used by 15% of the weight of the fine aggregate. However, according to prior studies on the influence of silica powder on ASR mitigation, silica powder effectively reduces ASR expansion of cementitious composites when particle sizes are smaller than 300 µm. The smaller particle size and higher silica powder concentration have a more significant impact on ASR expansion reduction. In other words, when the particle size is smaller than 300 µm, it does not accelerate the ASR and may even mitigate the ASR expansion (Guojun Ke, 2018). As a result, the crushed reactive aggregate was sieved to ensure that all crushed aggregates were larger than 300 µm, preventing the potential effect of silica powder on ASR mitigation.

Figure 5.7 Jaw crusher pulverisette 1.

The second important criterion was to use the same amount of crushed non-reactive aggregate for the non-reactive mix design to have a precisely unique mix design for all beams and specimens. Using the Jaw crusher depicted in Figure 5.7, the non-reactive fine aggregate was crushed from the non-reactive coarse aggregates, whereas the high-reactive fine aggregate was crushed from the dacite reactive coarse aggregate.

Cement

Ordinary Portland cement, supplied by Cement Australia, was used to make the concrete specimens. The cement material utilized in the mixing was a general-purpose Portland cement with an alkali content of 0.50% Na_2O_{eq} ($Na_2O + 0.658K_2O$ was used to compute cement's equivalent alkali content). Tables 5.5 and 5.6 display the chemical,

physical, and mechanical parameters of the cement used in the studies. It should be noted that cement bags were covered with plastic bags and sealed on the shelves to prevent moisture ingress (Figure 5.8).

Figure 5.8 Cement bags sealed on the shelves to prevent moisture ingress.

Table 5.5 Chemical composition of the cement.

Tested by XRF	CaO	SiO_2	Al_2O_3	Fe_2O_3	MgO	SO_3	Na_2O
Results (%)	64.5	19.5	5.0	3.0	1.2	2.5	0.5

Table 5.6 Physical, and mechanical properties of the cement.

Test	Fineness Index	Residue 45µm Sieve	Normal Consistency	Setting Initial	Setting Final	Soundness
Results	365 m^2/kg	2.6 %	26.8 %	120 Min	195 Min	2 mm
Standard	AS/NZS2350.8	AS/NZS2350.9	AS/NZS2350.3	AS/NZS2350.4	AS/NZS2350.4	AS/NZS2350.5

Admixture

Types A and F chloride-free MasterGlenium SKY 8379 complied with AS 1478.1 – 2000 were used as a superplasticizer to achieve the required slump. These admixtures were primarily designed for use in the premixed and precast concrete, where the best durability and performance, as well as enhanced workability and finishing, are required. The properties of the superplasticizer is provided in Table 5.7.

Table 5.7 Properties of superplasticizer.

Colour	*Light brown to amber*
Specific Gravity	1.047 – 1.087
pH	4.5 – 6.5

By adding a superplasticizer, cement particles have a more pronounced negative charge due to the sulphonic groups of the polymer chains, causing electrostatic repulsion and cement dispersion. MasterGlenium SKY 8379 is based on a new carboxylic ether polymer with long side chains, which significantly improves the dispersion of the cement. The steric hindrance is produced by the lateral chains connected to the polymer backbone that stabilizes the ability of the cement particles to separate and disperse. This technique generates flowable cement, while using significantly less water.

Sodium hydroxide

To increase the overall alkali content, pellets of technical grade sodium hydroxide (CS12015 sodium hydroxide) with a purity of 98% were used in the concrete mix design.

Plywood Formwork

Superior plywood manufactured from FSC-certified hardwood was used as formwork. With an A-Type Marine adhesive, this plywood withstands the rigors of moisture. In addition, the glued surface of the plywood using phenol-formaldehyde resin and a layer of resin-impregnated paper give concrete a smooth finish.

Steel Reinforcement

Reinforcement bars N12, N10 and R250 (all normal ductility) were used in specimens and were supplied by Mascotsteel. A total of six reinforcing cages have been made. The tensile reinforcement ratio of the beams was around 0.006. (Using two 12 mm bars). In addition, stirrups were made of grade R250N round reinforcing steel bars with a 6.5 mm diameter. Figure 5.9 illustrates the steel reinforcing cages.

Figure 5.9 Reinforcing cages.

The supplier of the steel rebars could not provide the exact physical specifications data on the batch of steel used in this specimen. Therefore, the reinforcing bars were prepared for pull-out testing. The pull-out test was performed in the TAFE Mechanics Laboratory. A Shimadzu UH-600kNX hydraulic universal testing machine with a 600kN maximum capacity and a 50 mm extensometer was used. Real-time auto-tuning

of control parameters was performed based on test force and strain values measured during the test. This method eliminates the need for preliminary testing and makes exact stress- or strain-controlled testing possible. According to the Australian specifications for steel reinforcing bars, the straining rate should be within the highest range of the strain rate given in AS 1391 when approaching yield stress or proof stress.

As can be seen in Figure 5.10, N12 bars were placed in the grips and pulled using a 600kN actuator. Then, the initial force was applied for the correct positioning of the rebar. After installing the highly sensitive 50 mm extensometer, the machine stretched the rebar. In the first stage of each experiment, an extensometer was used to accurately determine the elastic modulus and calibrate the actuator displacement to calculate post-yield stress/strain. Section of reinforcing bar after failure is shown in Figure 5.11.

Figure 5.10 Pull-out testing setup.

It should be noted that the extensometer was removed before yielding to avoid damage. The stress-strain curves were continuously monitored throughout the experiment, as depicted in Figure 5.12. The corresponding graphical representation is furnished in Figure 5.13, and the comprehensive test results are detailed in Table 5.8.

Figure 5.11 Section of reinforcing bar after failure.

Figure 5.12 Monitoring stress-strain curve of reinforcing bar.

The average tensile strength, upper yield point, and Young's modulus of the N12 deformed bar used in this study were 550.3 MPa, 508 MPa, and 204.5 GPa, respectively.

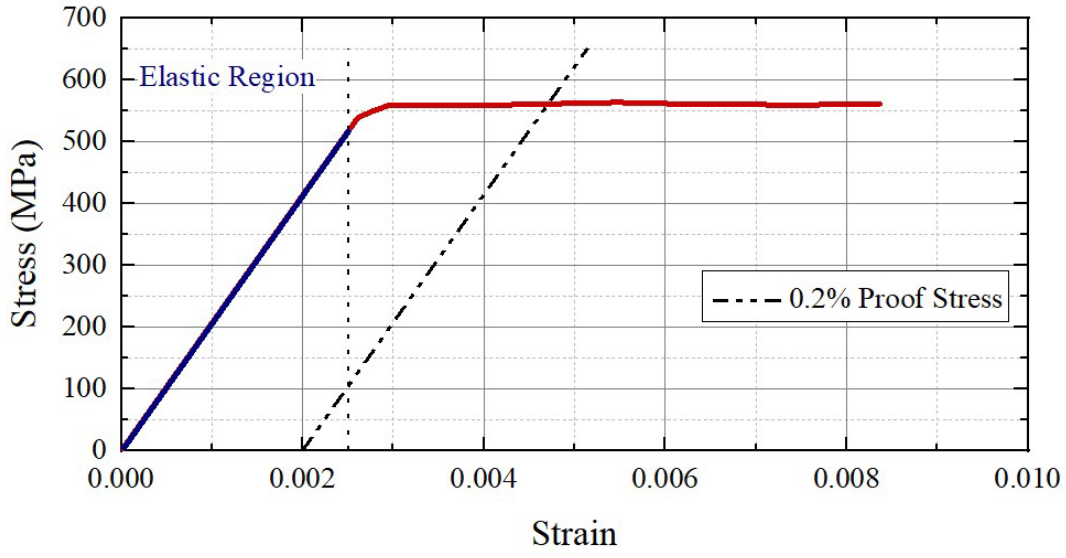

***Figure 5.13** Stress-strain curve for reinforcing steel.*

Table 5.8 Mechanical characteristic of reinforcing bars.

Bar	Nominal Yield Stress (MPa)	Ultimate Stress (MPa)	Elastic Modulus (GPa)
N12-I	510	555.6	204
N12-II	506	550.2	205

5.3.2 Post-Tensioning Bars and Accessories

The carbon-chrome steel Macalloy bars with a diameter of 26.5 mm were used in this series of tests. Macalloy post-tensioning bars are made from steel with a high tensile alloy in various diameters. Macalloy bars are offered as standard for diameters less than 40 mm up to 11.8 meters long. However, if more length is needed, it can be added by using a variety of couplers. Quenching or tempering processes are used to deliver rebars with a diameter of more than 50 mm specific properties, but for 26.5 mm Macalloy bars, the specific properties are obtained by the cold working method. The post-tensioning accessories, including ducts, plates, nuts, washers, and bars, are depicted in Figure 5.14.

Figure 5.14 post-tensioning accessories (ducts, plates, nuts, washers, and bars).

Physical parameters of the other post-tensioning accessories, including nuts, washers, end plates and ducts, are provided in Tables 5.9 to 5.12.

Table 5.9 Physical parameters of Macalloy bars.

Nominal Bar Diameter	Sectional Area	Mass / Metre	Characteristic Failing Load	Prestress at 70% Characteristic
26.5 mm	572 mm^2	4.49 kg	569 kN	398 kN

The tensile capacity and final elongation of rods are continuously estimated and measured with various tests during the production process to ensure that they meet the

BS4486[2] standards. Characteristic failure load for Macalloy steel loads is given in the Table 5.9. In addition, the failure loading on the joints is greater than on the rods. The fatigue resistance of threaded assemblies is more than two million cycles in the tensile stress range of 590 to 670 MPa, which is more than the required amount based on ETAG013[3].

Table 5.10 Physical parameters of washer and nuts

Reference	Length (mm)	Thickness (mm)	Outside diameter (mm)
Washer FSW26.5	-	5	65
Nut FN26.5	38.5	50	-

In the case of a 70% loading of the final characteristic capacity after 1000 hours at room temperature, the maximum stress loss allowed under BS4486 is 3.5%, while the relaxation rate for Macalloy bars is less than 3%. According to ETAG013, the anchorage strength is designed to be at least 95% of the main bar's failure load to ensure that the main bar, not the connections or anchorage, undergoes the final failure. The stress-strain relationship for prestressing steel is presented in Figure 5.15.

Table 5.11 Physical parameters of bearing plates.

Plate Reference	Length (mm)	Width (mm)	Thickness (mm)	Hole Diameter (mm)
FPP26.5	110	110	40	36

[2] Specification for hot rolled and hot rolled and processed high tensile alloy steel bars for the prestressing of concrete
[3] European technical approval of post-tensioning kits

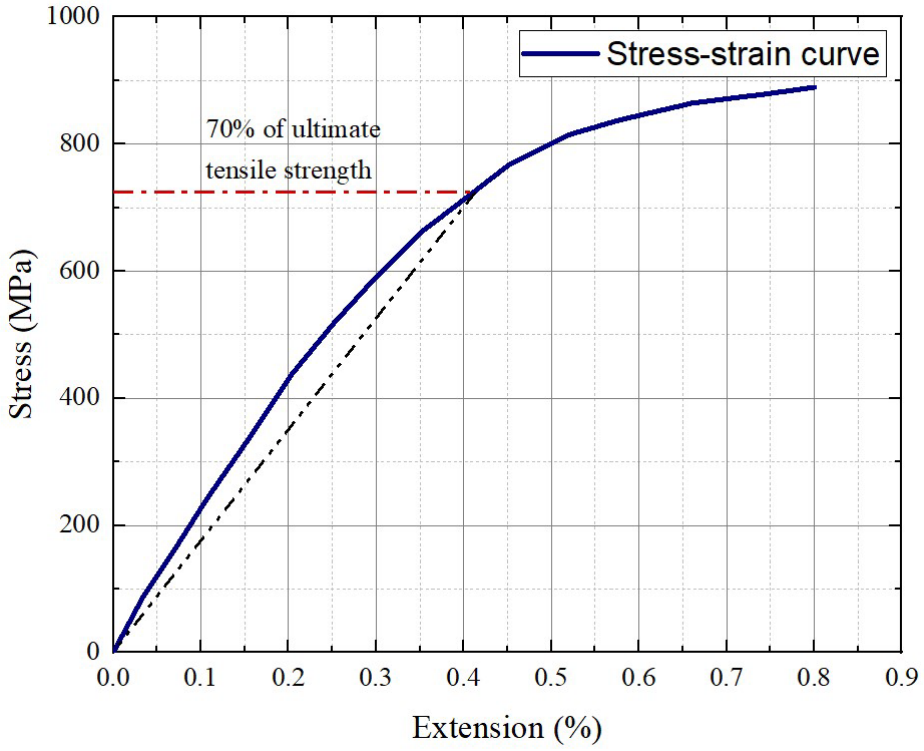

***Figure 5.15** Stress-strain curve for Post-tensioning Macalloy bar.*

Generally, a standard test called F.I.P. for high-strength steels is used to measure stress corrosion (FIP 1980, Hampejs and de la Precontrainte 1988). The results of the tests showed that none of the Macalloy rebars was repeatedly loaded, and no significant reduction in the final stresses was observed when the load was continued up to the ultimate capacity.

High-strength and fatigue-resistant Macalloy 1030 post-tensioning bar systems were used as the post-tensioning bar. This carbon-chrome steel bar has a yield strength of 1030 MPa. The benefits of using Macalloy bars can be classified as follows:

- Fatigue resistant thread.
- Ideal for prestressing concrete construction.
- Threaded to suit the requirements (End thread dimensions and specifications are presented in Figure 5.16).

- Can be cut to length on site.
- High impact resistance.
- Used for a variety of temporary and permanent constructions.
- Patented Macalloy thread allows low lock-off losses during stressing.

In addition, the Macalloy bars provide excellent relaxation characteristics and low lock-off losses, saving installation time and the need to re-stress bolts after installation. The entire rod or a portion of it can be cold threaded.

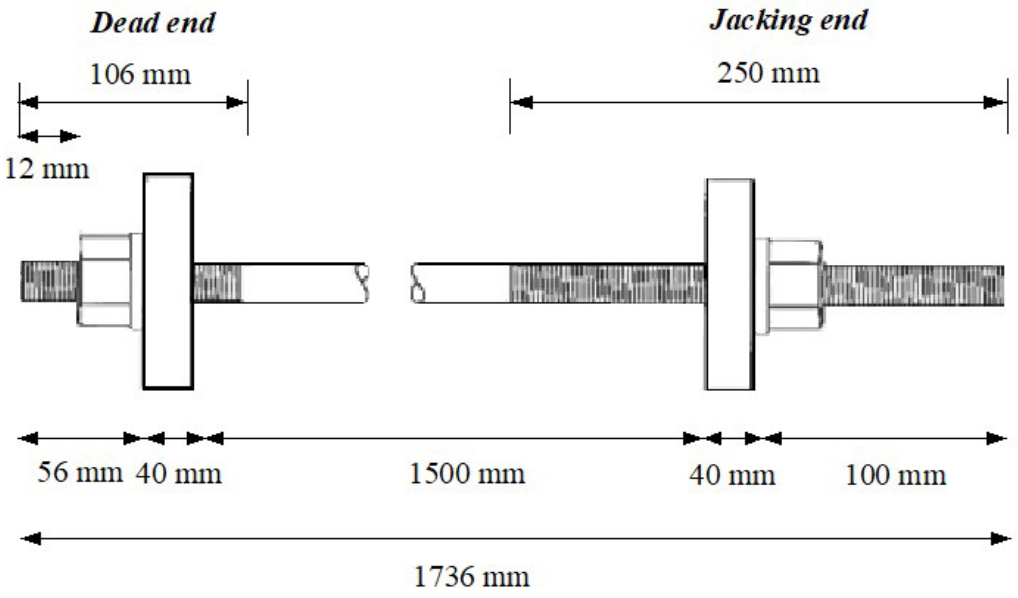

***Figure 5.16** End thread dimensions.*

Table 5.12 End thread dimensions for 26.5 mm Macalloy bars.

Jacking end S1 (mm)	Dead end S2 (mm)	X1 (mm)	X2 (mm)	X3 (mm)
250	100	100	53	12

5.4 INSTRUMENTATION AND MEASUREMENT

5.4.1 Strain Measurements

Traditional mechanical strain gauges were widely used in various laboratory experiments. Their versatility and cost-effectiveness have made them popular for measuring strain. These demountable strain gauges are an accurate and simple method for measuring strain at different points of an instrument. These gauges are commonly used to measure cracks in concrete structures in laboratory conditions. However, the optimal accuracy depends on how to use and care for the device. Using these mechanical gauges, up to 200 strains can be measured in laboratory conditions with an accuracy of 5 microstrains.

Demec strain gauge is made of metal material with a low thermal expansion coefficient as the reference bar. These strain gauges have two locating points, one fixed and the other moves along the length of the gauge. The standard gauge length varies between 100 and 500 mm.

Another important factor regarding the use of this device is the installation of reference points (discs) on the surfaces, which can significantly affect the accuracy of the test. The measurement accuracy reaches its maximum level by placing the gauge in an ideal horizontal position.

In this experiment, Demec discs were attached to the concrete beam surface. The discs were placed at a distance of 100 mm apart from each other on the surface of the beam. The placement of discs is given in Figure 5.17. Epoxy glue with high heat and moisture resistance was used to install the discs. However, the accelerated ASR environment conditions may affect the adhesion of some discs and cause them to fail and separate.

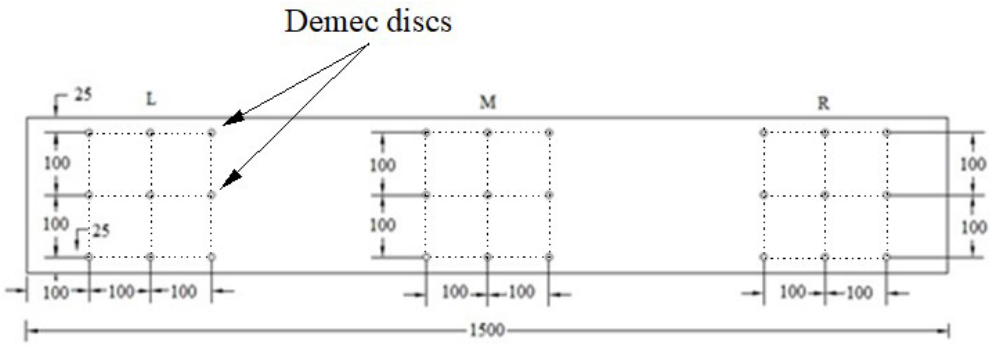

Figure 5.17 DEMEC points arrangement.

Another factor preventing the use of these traditional mechanical gauges is the maintenance conditions of the beams. They should be measured regularly in weekly or monthly periods to measure the amount of strain. Since the beams were immersed in sodium hydroxide solution, lifting the beams, and measuring them permanently and periodically is practically impossible.

In this experiment, discs were placed on the concrete beam with high precision. Expansion of the concrete surface was measured in the transverse and longitudinal directions at the end of the test.

To assess the structural behaviour of the ASR-affected concrete structures, measuring the expansion rate in the concrete core, especially around the rebars, is much more critical than the expansion rate on the concrete surface. As a result, a method for measuring the amount of strain in rebars and internal concrete parts was considered necessary.

In addition to the conventional methods described above, a data acquisition system was required for accurate and continuous measurement. Although it makes the measurement operation a bit more complicated, it has many advantages, the most important of which is persistent data storage and retrieval.

5.4.2 Electrical Strain Gauge

FLAB series strain gauges were used to measure the strain changes on the rebar. The FLA-3-11-5LT is a 3-mm length, 120 Ω resistance, and uniaxial gage for general purposes. It has a 5 m pre-attached 3-lead wire. For the concrete embedment, KM series were used. The KM type of strain transducers is designed for materials that go through a plastic-to-brittle transformation, such concrete and synthetic resin. Since they are completely waterproof and have a very low modulus, they are perfect for measuring internal strain in newly cured materials. They consider reliable for strain monitoring over the long term. Foil strain gauges were placed horizontally and vertically on the rebars in different places. Upper, lower bars and post-tensioning bars were also equipped with strain gauges. Transverse changes have also been measured by installing gauges on the stirrups. A small area was made on the bar with a grinder to accommodate the strain gauges. The placement of the strain gauges is specified in Figure 5.18.

***Figure 5.18** Installing strain gauges on bars.*

The surface of the bars was ground at the location of strain gauges by using a coarse sanding disc at a pneumatic angle. The maximum effort was made to minimize the reduction in the cross-sectional area of the rebars. Then, using fine polishing, a polished place was provided, ready for installing strain gauges. The surface of the bar was then cleaned using acetone and non-woven sponges. This process was repeated with fresh sponges and wiping in one direction until the non-woven sponge remained white after wiping. Vinyl tape to mask the region was used to prevent the glue from spreading beyond the gauge installation area. Then the gauges were installed with cyanoacrylate adhesive in the specified places. The installed strain gauges were checked for strain measurements before coating.

Due to the test conditions and environment, as well as the need to measure strain in post-tensioning bars, the use of electric strain gauges in this test was considered very necessary. However, using electrical strain gauges also had some disadvantages. The short length of gauges can record local changes in strain. In addition, some studies indicated their poor performance in reactive concrete and alkaline conditions.

Therefore, in this study, different waterproofing layers were used to protect the gauges to prevent possible failures due to the presence of moisture, temperature and reactive concrete. Figure 5.19 summarize the different steps of installing the gauges and coating procedures.

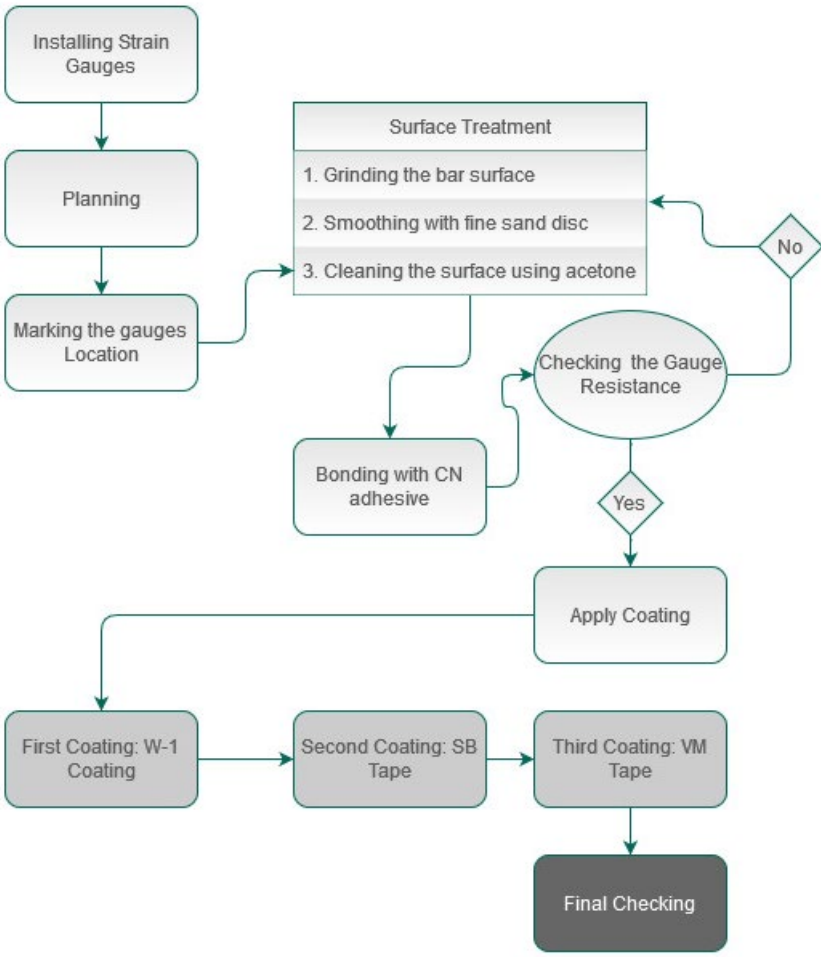

Figure 5.19 The procedure of installing gauges step by step.

Three different types of coating are presented. From left to right, the first, second, and third coatings are shown in Figure 5.20.

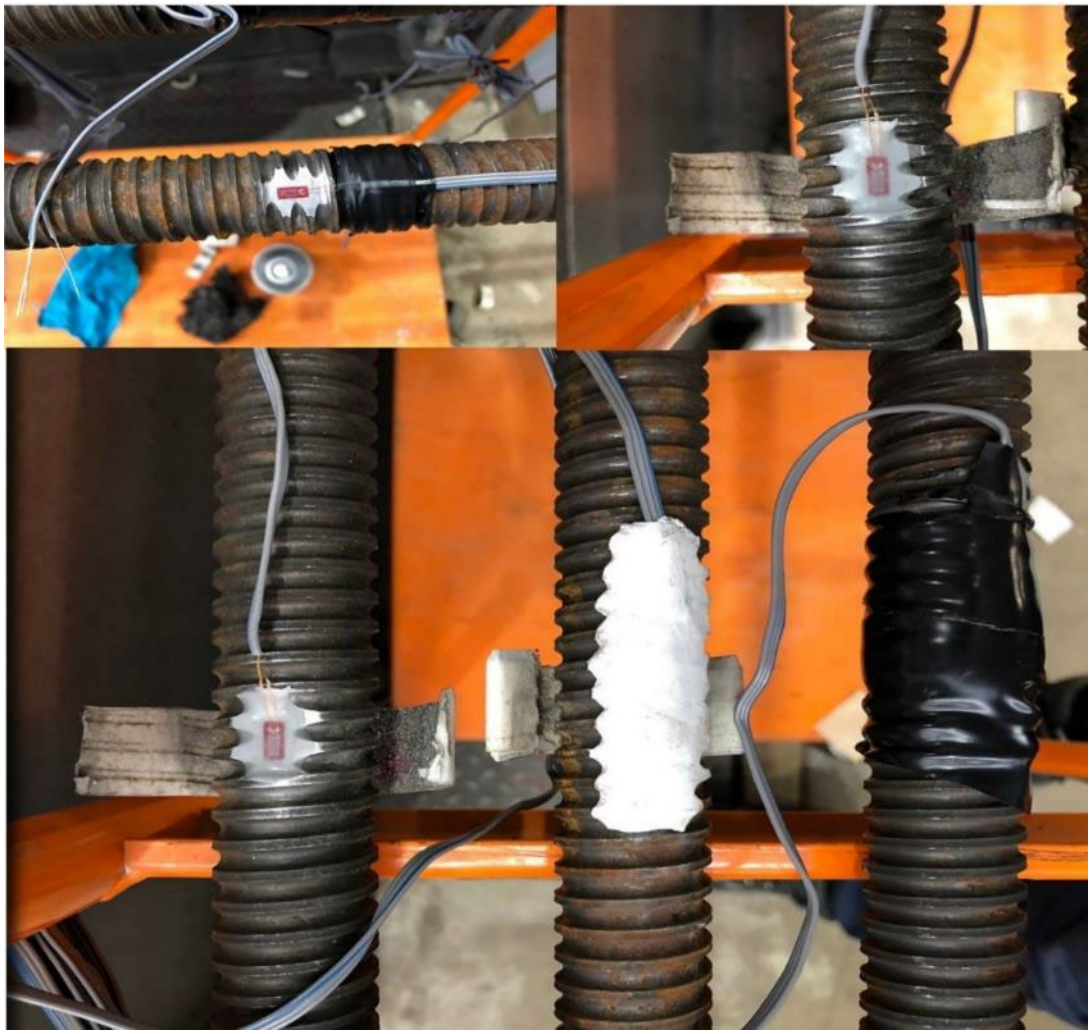

Figure 5.20 Different coating layers.

5.4.3 Data Logger

A data logger was installed to record the output data of the gauges periodically. According to the number of test samples and places required for strain measurement, a 49-channel ALMEMOR 5690-1M was used as a data acquisition system to collect the data from 49 sensors installed inside the beams. It should be mentioned that it would be possible to add a channel if needed according to the type of data logger chosen. Nine electrically separated measurement inputs with over 70 ranges are available in the

ALMEMO® 5690-1M data acquisition system, as depicted in Figure 5.21, making it ideal for use with strain gauge sensors. This model has 512 KB of EEPROM memory, which can store over 100,000 readings. By default, the system is powered by a 12V AC power supply.

Figure 5.21 ALMEMO data acquisition system.

5.5 TEST SPECIMENS

5.5.1 Cylinders for the Mechanical Properties Assessment

In order to perform concrete mechanical characteristics tests, reactive and non-reactive cylinders with a diameter of 100 mm and a height of 200 mm have been used. For each beam, using automatic compression test machine and semi-automatic MOE test machine (Figure 5.23 and 5.24), three cylindrical samples for the compressive strength test and three for the elastic modulus test were crushed in 28, 90, 180 and 270 days, respectively. The depiction of cylinders submerged within the curing tank at the concrete laboratory is presented in Figure 5.22.

***Figure 5.22** Cylinders in curing tank at the concrete lab.*

According to the statistical results provided in the literature (section 2.5.2), it was discovered that the splitting tensile strength test obtained the closest estimate for the tensile strength reduction due to ASR. Therefore, the splitting tensile strength test was employed to evaluate the tensile strength. For this purpose, cylinders with a diameter of 100 mm and a height of 200 mm were used. Three samples were tested for tensile strength for each period of 28, 90, 180 and 270 days. The specimens were covered in a climate chamber at 23 degrees Celsius for twenty-four hours till demolding. The specimens were then put in water saturated with lime at 20 degrees Celsius for 28 days. Then, all the cylindrical samples were placed in the ASR accelerated environment along with the other samples under the same conditions. Separate specimens were chosen for each test, and the surface of each specimen was polished using automatic concrete end grinding machine (Figure 5.25). The results, average and standard deviation of mechanical specifications are given in the results section of chapter six.

Figure 5.23 Automatic compression test machine.

Figure 5.24 Semi-automatic MOE test machine.

Figure 5.25 Automatic concrete end grinding machine.

5.5.2 Prisms for Free Expansion

Based on ASTM C1293 recommendation, prism samples with dimensions of 75×75×285 mm have been used to assess the free expansion of ASR-affected concrete. Six prisms were cast with reactive concrete, and three prisms were cast with non-reactive concrete (Figure 5.26). Stainless steel studs were embedded at the end of the prism during concreting to measure the expansion. After twenty-four hours in a moist room, each prism was measured and then placed in a water container. The initial expansion of the prisms was measured and recorded using a digital comparator (Figure 5.27). Also, before transferring the prisms to the accelerated ASR environment at 38 degrees, the length of the prisms was re-measured and recorded.

Figure 5.26 Prisms samples for measuring the free expansion.

Figure 5.27 Horizontal comparator for concrete.

After placing the prisms in the ASR environment, their length changes were measured and recorded in 28, 90, 180 and 270 days. Each sample was measured at least three times to ensure accurate results, and the average was calculated. All the samples

were kept under the same conditions and measured at certain time intervals. Subsequent length change of each prism was periodically measured with a comparator over a period of 9 months. The results of free expansion for different periods are given in chapter 6.

5.5.3 Reinforced and Prestressed Full scaled Beams

A total of eight concrete beams have been prepared for testing. Two conventional reinforced concrete beams and six prestressed concrete beams were cast. Attempts have been made to make the beam close to the real size. Due to space limitations and the water tank size, the beams' length was limited to 1.5 meters. It should be noted that all reactive and non-reactive beams and specimens were fabricated at the UTS Tech Lab (Figure 5.28).

Figure 5.28 Formworks for concrete beams.

The optimal capacity of each mixer pans available in the laboratory to produce homogeneous concrete is estimated to be 70 litres at most. Each concrete beam and companion specimens were made and poured simultaneously using two horizontal mixer pans to prevent cold joints. Two beams have been poured as conventional reinforced concrete, one reactive and the other with non-reactive concrete, in order to compare the expansion and load-carrying capacity of no-reactive and reactive reinforced beams due to ASR.

Reactive and non-reactive prestressed beams without transverse reinforcements were also cast to estimate the residual shear strength of prestressed beams due to ASR. Four other beams were designed with longitudinal, transverse, and prestressed rebars to calculate the flexural behaviour of prestressed beams due to ASR. One beam was poured as a reference with non-reactive concrete, and the other three beams were poured with reactive concrete. In addition, the different prestressing force has been applied to different beams to measure the effects of prestressing force on expansion and change in flexural strength.

For the beam specimens, eight formworks were constructed at UTS Tech Lab. 17 mm thick plywood was used to make the beam's moulds. Plywood was cut into specific sizes, and wooden moulds were made in the first step. Two 45 mm thick LVL plates were also utilized for each formwork's ends, with a 30 mm diameter hole for the post-tensioning bars. All bars used in the specimens were uncoated. Completed cages with the end walls before putting the sidewalls and close-ups of the reinforcing cage end detail for beams are shown in Figures 5.29 and 5.30. The name and types of each beam is summarized in Table 5.13.

Figure 5.29 Formworks without side walls.

Figure 5.30 Formworks without side walls.

As described in the previous section, the beams were equipped with Demec mechanical and electric strain gauges to measure the strain in the longitudinal, upper, lower, and shear bars and the stress changes in the prestressed bars. After placing the rebar chairs to ensure the minimum concrete cover, the reinforcement cages were placed in the moulds. A three-millimetre hole was drilled into the ducts, allowing electrical gauge connections to pass through (Figure 5.31).

Finally, the surface of the wooden moulds was oiled and transferred to the concrete laboratory for concrete pouring (Figure 5.32). The reference name of the beams is shown in Table 5.13.

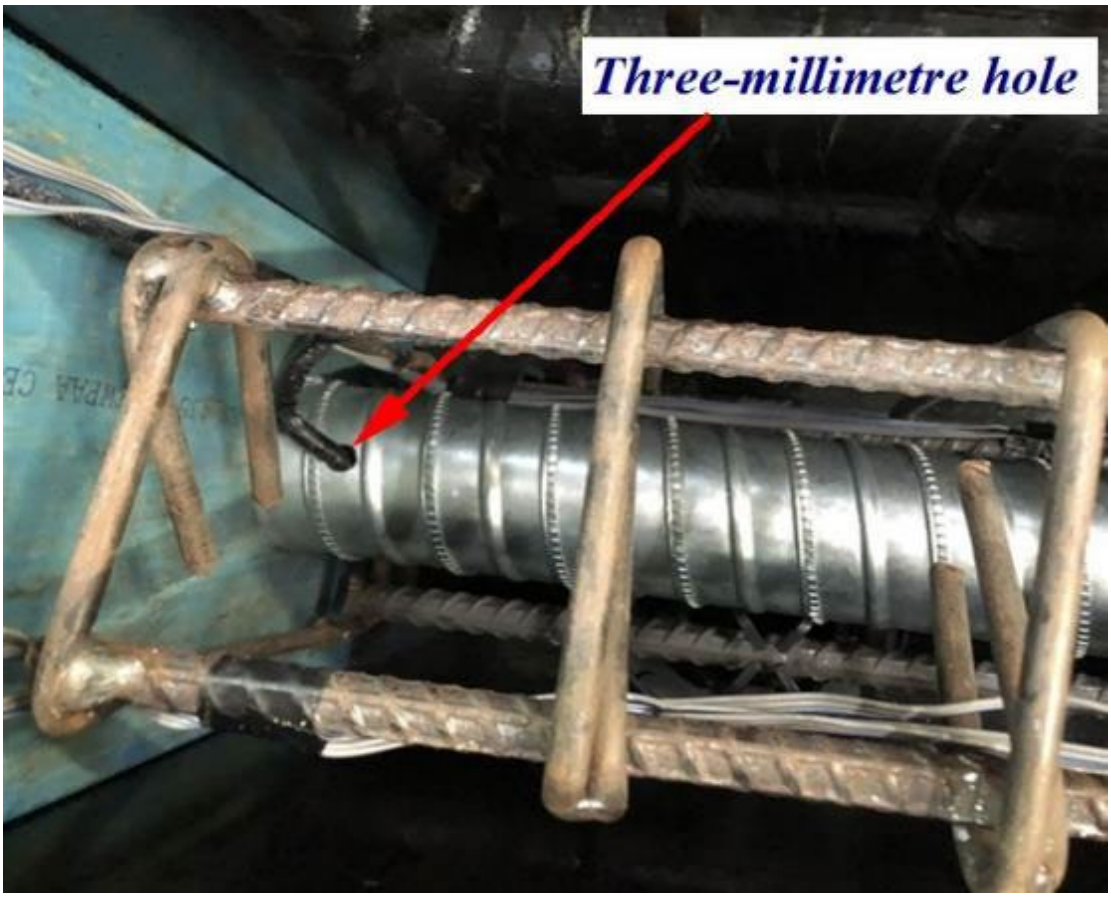

Figure 5.31 A three-millimetre hole drilled into the ducts, allowing electrical gauge connections to pass through.

Table 5.13 Name and types of beam specimens

Ref. Name of Beam	Prestressed/RC	Reactive/Non-Reactive
1-RRC	Reinforced	Reactive
2-RSH	Post-tensioned	Reactive
3-RFX	Post-tensioned	Reactive
4-RFX	Post-tensioned	Reactive
5-NFX	Post-tensioned	Non-Reactive
6-NSH	Post-tensioned	Non-Reactive
7-RFX	Post-tensioned	Reactive
8-NRC	Reinforced	Non-Reactive

Figure 5.32 Completed formworks and gauges.

It is noteworthy to mention that all plates, nuts and ends of the Macalloy bars were coated with two-layer painting spray to prevent the bars from corrosion in the water tanks (Figure 5.33).

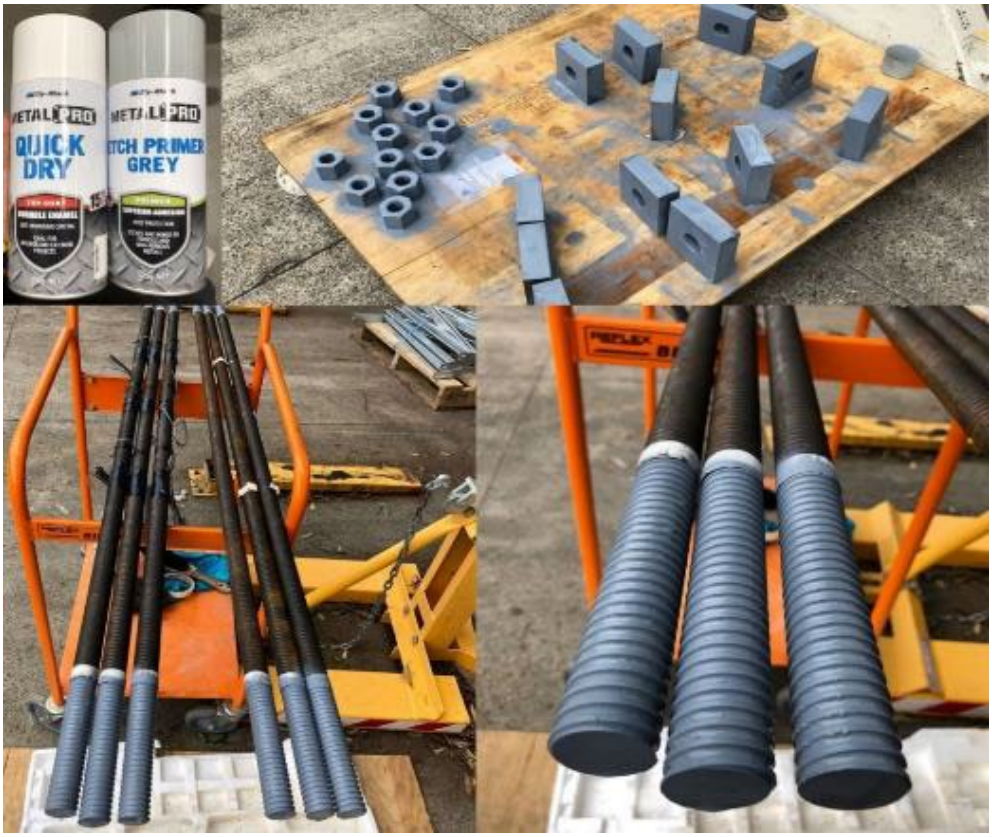

Figure 5.33 Coating the bars, plates, and nuts to prevent corrosion.

5.6 MIXTURE PROPORTION

The concrete mix had to be realistic and practical, but it also had to react in months, not years. 10 mm and 20 mm highly reactive dacite aggregate and non-reactive limestone aggregate were utilized in this experiment (Figure 5.34).

Except for the use of non-reactive limestone aggregates for non-reactive concrete and highly reactive dacite aggregates for reactive concrete, the mixing designs for reactive and non-reactive concrete were chosen similarly. As beams were designed for prestressing, the minimum target for the compressive strength of concrete was 40 MPa. By pouring different trial batches, concrete with an average compressive strength of 45 MPa was selected in the initial phase of the design. Ordinary Portland cement was used in this mixture.

Figure 5.34 Sodium hydroxide and Admixture.

In both types of reactive and non-reactive concrete, Sydney sand was used as fine aggregate. Several experimental tests were undertaken to examine the influence of sodium hydroxide solution on strength by Clayton et al. (1990). According to his findings, the dosage of Sodium hydroxide boosted the concrete's tensile strength while lowering its compressive strength. Because the consequent change in the tensile and compressive strength could have an unpredictable effect on beam performance, it was decided to dose the control and reactive mixes with Sodium hydroxide solution in equal amounts. Since sodium hydroxide (NaOH) dissolving generates heat, sodium hydroxide (NaOH) pellets with a purity of 98 per cent were supplied to the mixing water 24 hours before the mixing to enhance the Na_2O_{eq} concentration in the system. In order to get the necessary slump, Master Glenium SKY 8379 superplasticizer is utilized. Five millilitres of admixture per litre of water have been used to achieve the required strength and workability for the concrete beam. After 28 days of successful trial baches with

a minimum characteristic compressive strength of 40 MPa, the final mix design is summarized in Table 5.14.

Table 5.14 Concrete mix design.

Water/Cement (ratio)	Aggregates (kg/m^3)		Sand (kg/m^3)	P-Sand (kg/m^3)	Fine Sand (kg/m^3)	NaOH (gr/m^3)	Admix (ml)	Na_2O (gr/m^3)
	20 mm	10 mm						
0.4	793.8	340.2	466	82	61	7100	166. 7	5.5

5.7 MIXING PROCEDURE AND CURING

Two horizontal pan mixers with a capacity of 70 litres were used to mix the concrete. One beam and its companion specimens were cast using two drums. This is because one drum of fresh concrete is insufficient for casting the beam. Two separate mixing and casting processes were used to cast the beam and its companion specimens. Figures 5.35 and 5.36 depict concrete mixing and slump testing.

Figure 5.35 Mixing concrete material in horizontal pan mixer.

Figure 5.36 Mixing concrete and slump test.

The slump of each batch is provided in Table 5.15. Figure 5.37 shows the companion cylinders in the curing tanks at UTS concrete lab.

With the formwork in position, the concrete was cast around hollow ducts, which were fixed. The steel tendons were in place, unstressed in the ducts during the concrete pour. Also, the concrete is compacted with a hand-held concrete vibrator (Figure 5.38).

Concrete beams were wrapped with wet hessian cloth and plastic sheets after casting, and then stored in the laboratory at 23±2 °C for seven days before being demolded. The beams were moist cured for further 21 days after demolding by wrapping them with wet hessian cloth and plastic sheets. The hessian fabric covering the beam was checked routinely and wetted once a day to keep the moisture. After casting, the companion cylinders and prisms were demolded, and

assembled with the beams the next day. The moist curing of beams and companion specimens is shown in Figures 5.39 to 5.42.

Table 5.15 Measured slumps and number of companion cylinders for each beam.

Batch number	Slump (mm)	Number of Cylinders
#1	90/95	11
#2	85/95	12
#3	78/85	14
#4	86/94	12
#5	90/105	14
#6	87/93	12
#7	100/94	12
#8	88/90	11

Figure 5.37 Casting concrete cylinders.

Figure 5.38 Vibrating the first layer of the beam with vertical vibrator.

Figure 5.39 Placement of concrete.

Figure 5.40 Placement of concrete.

Figure 5.41 Curing concrete beams for 28 days.

Figure 5.42 Curing concrete beams for 28 days.

5.8 POST-TENSIONING OPERATION

5.8.1 Stressing the Bars

The Macalloy bar was tensioned after the desired strength of the concrete (40 MPa) had been achieved. One end of the tendon was strained while the other end was anchored. During the stressing operation, the beam was compressed, and the prestress was maintained after the tendons were secured to the concrete by the bearing of the end anchoring plates (Figure 5.43). A detailed view of the cross-section of the beam prior to the application of prestress force is provided in Figure 5.44. The schematic representation of the hydraulic jack utilized in the post-tensioning procedure is displayed in Figure 5.45.

Figure 5.43 Demolded beams after 28 days.

All post-tensioning equipment was adapted from SRG company. The stressing ram for prestressing had a capacity of 535 kN. The setup used for prestressing is shown in Figure 5.46.

Figure 5.44 Close-up view of the cross section of the beam before applying the prestress force.

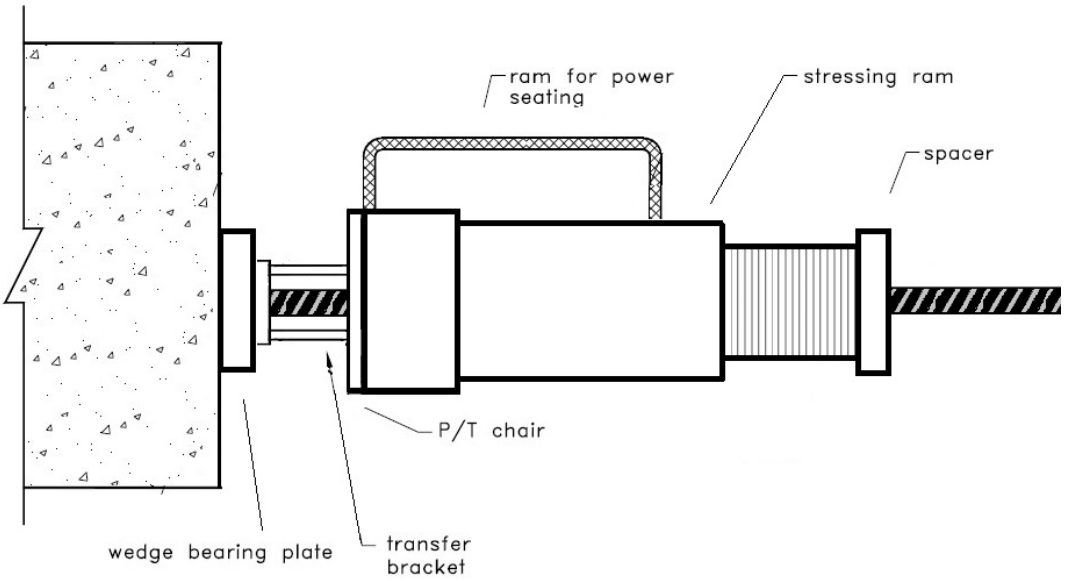

Figure 5.45 Schematic of the hydraulic jack for post-tensioning procedure.

Figure 5.46 Setting up hydraulic jack for post-tensioning operation.

The SRG company provided the hydraulic jack equipment. For this purpose, an M2 jack with calibrated gauges was used to apply the prestress force. Stressing procedures and jack details were adapted from Macalloy's Technical Department. The schematic depicting the hydraulic jack setup and the procedure for stressing the

Macalloy bars are presented in Figures 5.47 and 5.48. Furthermore, Figure 5.49 illustrates the monitoring of the applied force using a pressure gauge.

The primary stages of the procedure are as follows:

I. Each Macalloy bar was first tensioned to roughly 10% of the jacking force in order to eliminate slack.

II. After initial tensioning, the bar was given a reference mark to measure elongation.

III. Tendons were strained utilising a stepwise post-tensioning technique; the pre-tensioning force was measured using a pressure gauge on the hydraulic pump. At each step, the stressing ram stroke and bar elongation were measured to ensure force levels.

IV. Final tendon elongation was measured after all stressing stages were completed. Equipment was removed if it was deemed acceptable.

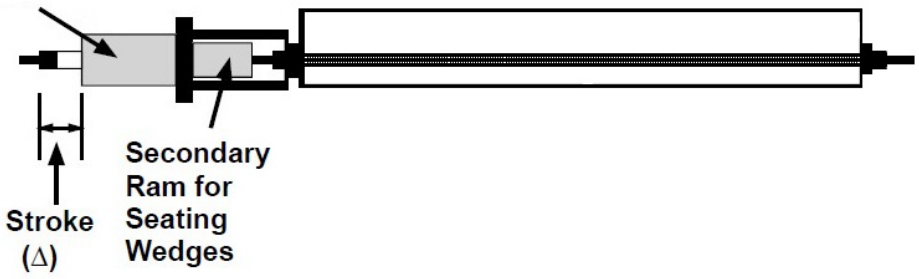

Figure 5.47 Schematic of hydraulic jack setup.

Figure 5.48 Stressing the Macalloy bars with hydraulic jack.

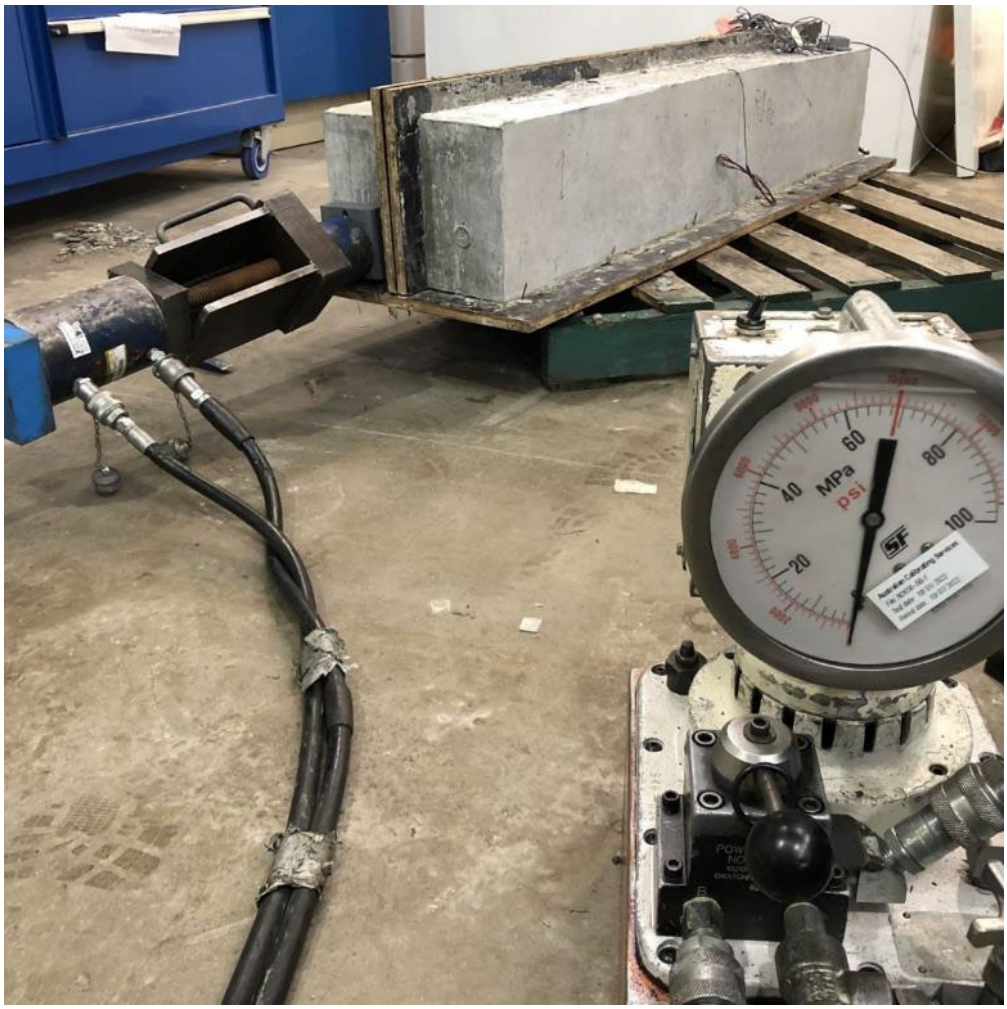

Figure 5.49 Monitoring the applied force using pressure gauge.

5.8.2 Grouting

Except for slabs on the ground, unbonded tendons are not authorised in Australian construction. The grouting operations followed the contractor's recommendations for post-tensioning.

After the bars were fixed and no additional tensioning was necessary, grout was poured into the ducts housing the tendons. By bonding the tendons to the concrete in this manner, they are more effective in controlling cracks and providing ultimate strength. Before the post-tensioning procedure, an angle hole on each plate was made at the UTS Tech Lab workshop to make a vent hole for grouting. The details of the grouting hole are shown in Figure 5.50.

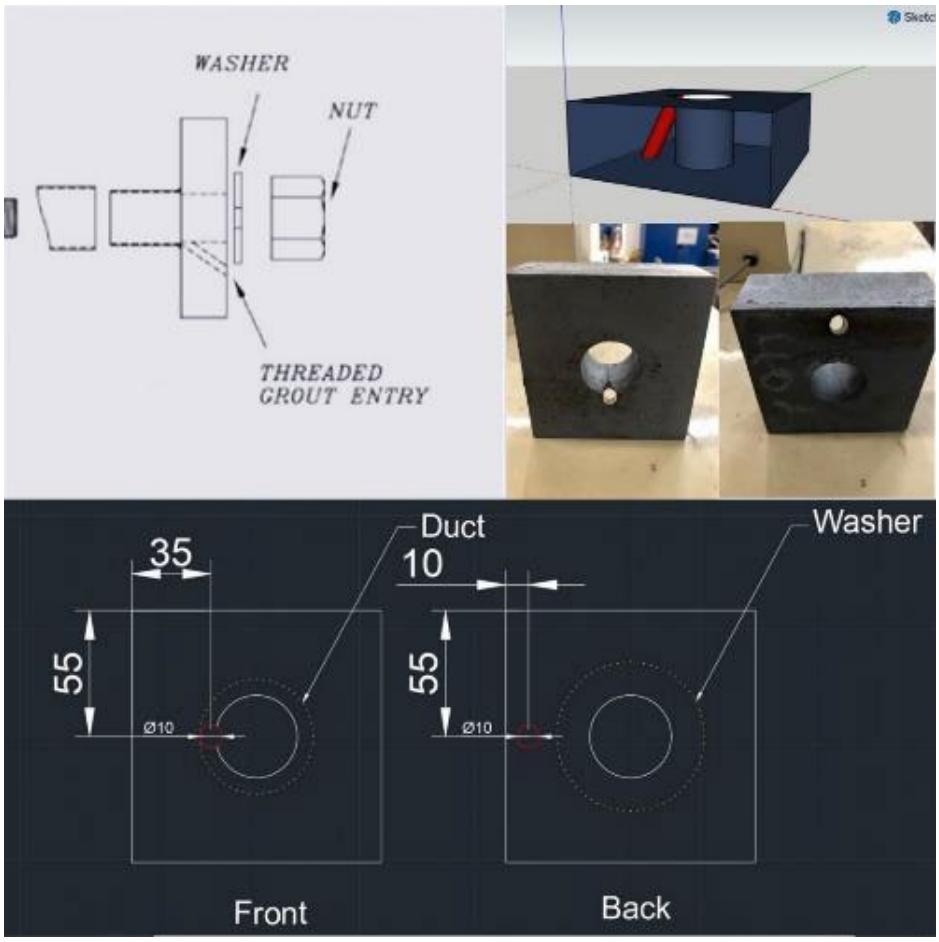

Figure 5.50 Details of angle hole for grouting vent.

Standard grout was used to grout every post-tensioned beam. At the end of the duct's, vents were built by making an angle hole on the plates. The grouting procedure is shown in Figures 5.51 and 5.52. As evident in Figure 5.53, the beams were left undisturbed for a duration of 24 hours following the injection of grout.

Figure 5.51 Mixing high-strength post-tensioning cement.

Figure 5.52 Grout injection after stressing.

Figure 5.53 Keeping beams untouched for 24 hours after grout injection.

5.9 TEST SETUP

As shown in Figure 5.54, the supports and load point used in the test setup reflected a simply supported beam in order to deliver the maximum bending moment and shear force at one-third of the span. The load was applied using a custom design Moog PID controlled servo valve system, utilising hydraulic cylinders to apply the load. The loading was applied in load control and held at various load points for monitoring crack deformations. The final step of loading to failure was carried out in stroke control at a rate similar to the rate during the initial loading period. The command loop ensured each cylinder's load was equal throughout the loading period (Figure 5.55).

A laser displacement sensor was used to measure the deflection at mid-span on the samples' upper side through failure. Loading was applied until the specimens' maximum load-carrying capacity was reached. The test setup and test loading rates were determined in a way that complies with AS3600-2018.

Figure 5.54 Test setup for load-deflection curve of 3-meter conventional reinforced beams.

In this study, the load-deflection curve based on various applied loads was created by monitoring the deflection in the centre of the beam span.

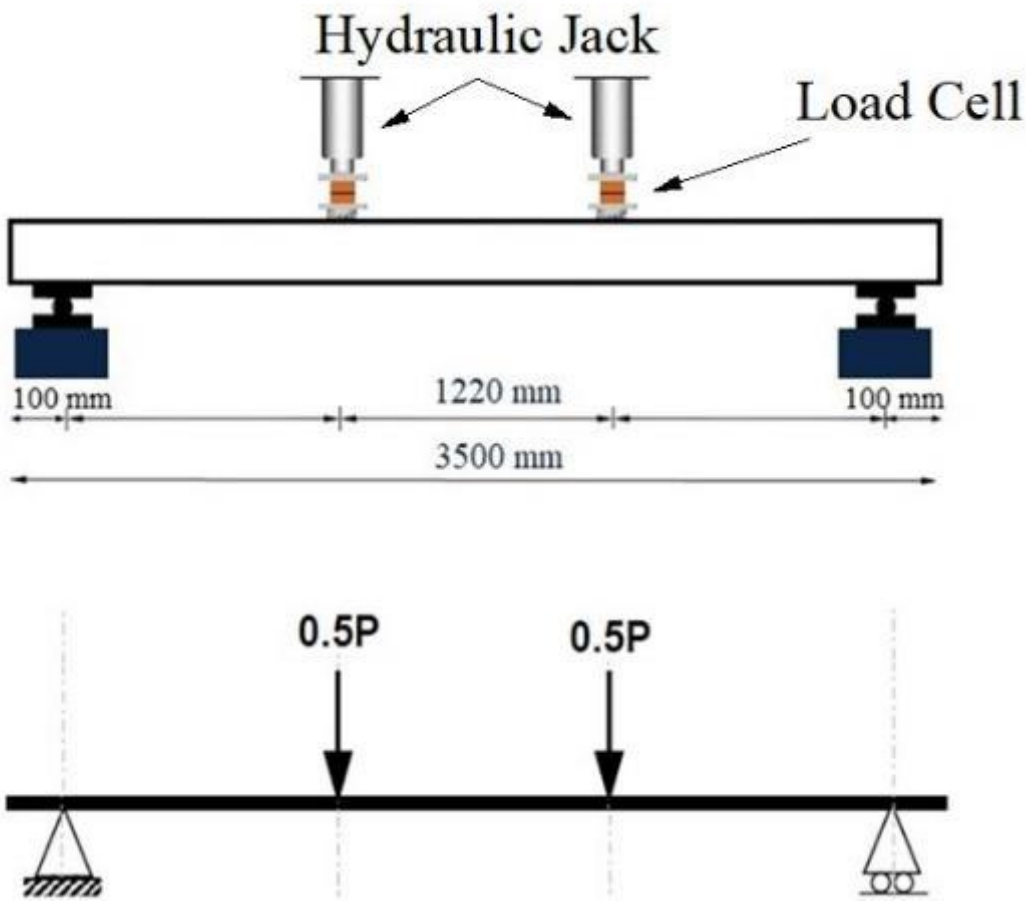

Figure 5.55 Schematic illustration of beam size and loading configuration for 3-meter conventional reinforced beams.

5.10 ASR CONDITIONING

Environmental conditions play a significant role in the degree of vulnerability of concrete due to ASR. The ASR reaction begins by combining the optimal amount of silica from reactive materials with pore solution alkalis. Nevertheless, environmental conditions are necessary for the expansion of ASR.

In ASR reaction, water is essential from two points of view. Firstly, water is vital for diffusing alkaline particles in concrete and transporting alkaline ions in the concrete pore solution. Secondly, water is influential in ASR gel's expansion rate and production. The ASR reaction alone is not vulnerable. Water absorption by ASR gel causes swelling. Then, this swelling causes pressure in the concrete skeleton, which

causes the expansion and eventually cracking of the concrete. Therefore, the water factor can be very influential as an essential effect in the ASR reaction so that it can increase, limit, or even stop the reaction rate.

In this regard, high ASR expansion is caused by the presence of reactive aggregates and an alkaline environment and significant exposure to moisture. The presence of active aggregates and alkaline without sufficient moisture only leads to no or a small expansion.

Similarly, an increase in relative humidity can significantly affect the expansion caused by ASR. In this regard, research on the relationship between the RH environment and the alkali content of concrete has been done by Thomas et al. (2006). Based on his findings, although observing the sign of ASR gel swelling in concrete even with low relative humidity is possible, a minimum relative humidity of 80% is recommended for high ASR expansion.

5.10.1 Water Tank

For the reaction to occur, the concrete must be wet. In order to stimulate the reaction in the needed time and in a regulated manner, water tanks were built to accommodate the beams. Based on the size of the beams and companion specimens, the water tanks were designed and built to the desired size. Details of the location of beams and companion specimens are specified in Figures 5.56 and 5.57. This programme commissioned two water tanks measuring 2.1 m × 1.8 m with 1 m deep as summarized in Table 5.16. Paneltim, an innovative 50 mm thick dual-skin sandwich panel, was used to construct each tank. The internal cross-rib cell structure of Paneltim construction panels is lightweight while providing excellent strength and rigidity in both length and width. These panels, composed of Polypropylene copolymer (PPCO)

or High-Density Polyethylene (HDPE), have outstanding mechanical and chemical properties.

The special features of the tanks include the following:

- excellent thermal & biosecurity properties.
- hygienic.
- chemical resistant.
- static & dynamic stability.
- shockproof and UV stabilized.

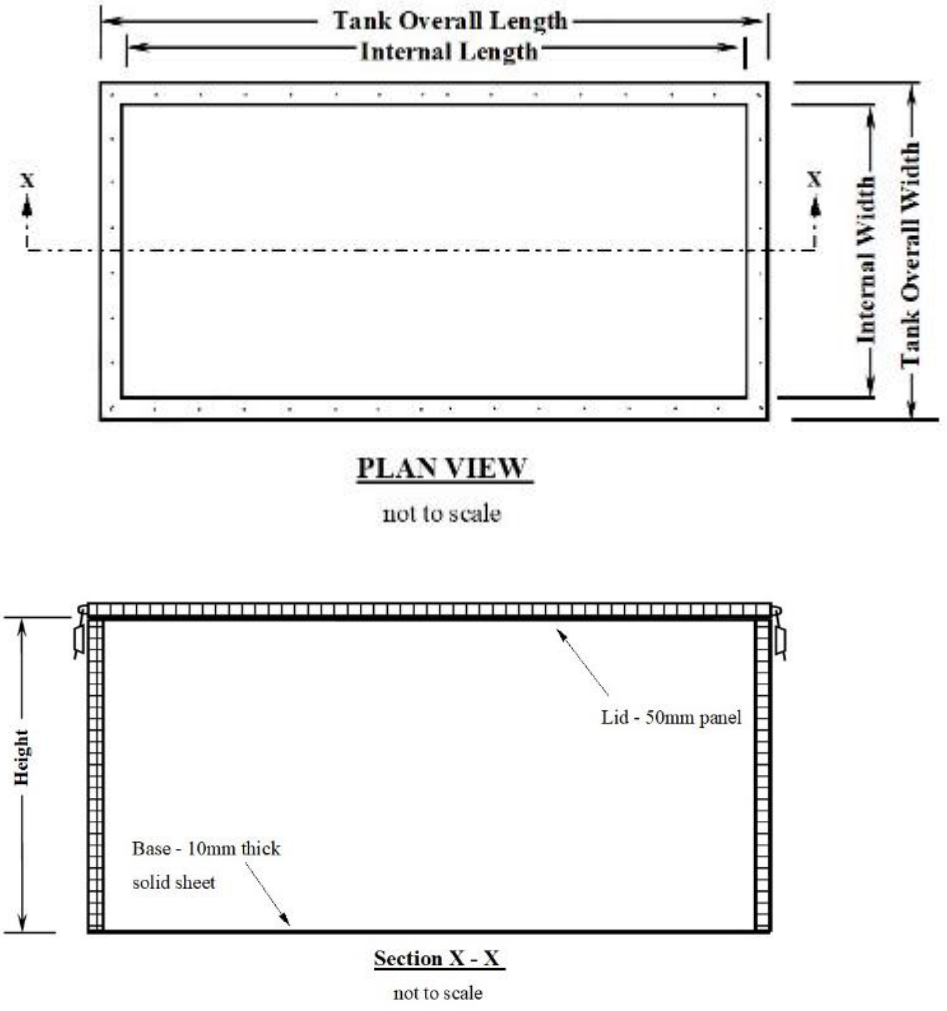

Figure 5.56 Dimensions of custom water tanks.

Figure 5.57 ASR-accelerated water tanks.

Table 5.16 Dimensions of the water tanks.

Model	*Capacity (liters)*	*Internal Dimensions (mm)*			*Overall Dimensions (mm)*		
		Length	Width	Height	Length	Width	Height
Custom	2600	2000	1650	800	2100	1750	810

The positioning of the beams, cylinders, and the heating element is depicted in Figure 5.58, while Figure 5.59 illustrates the provided roller and pin supports for the beams.

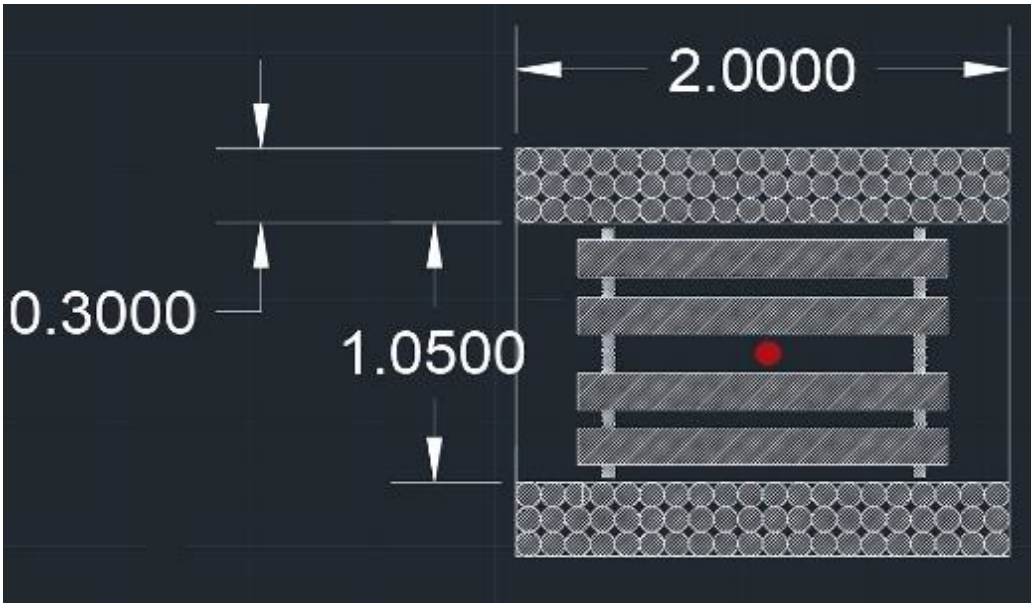

Figure 5.58 Position of the beams, cylinders, and the heating element.

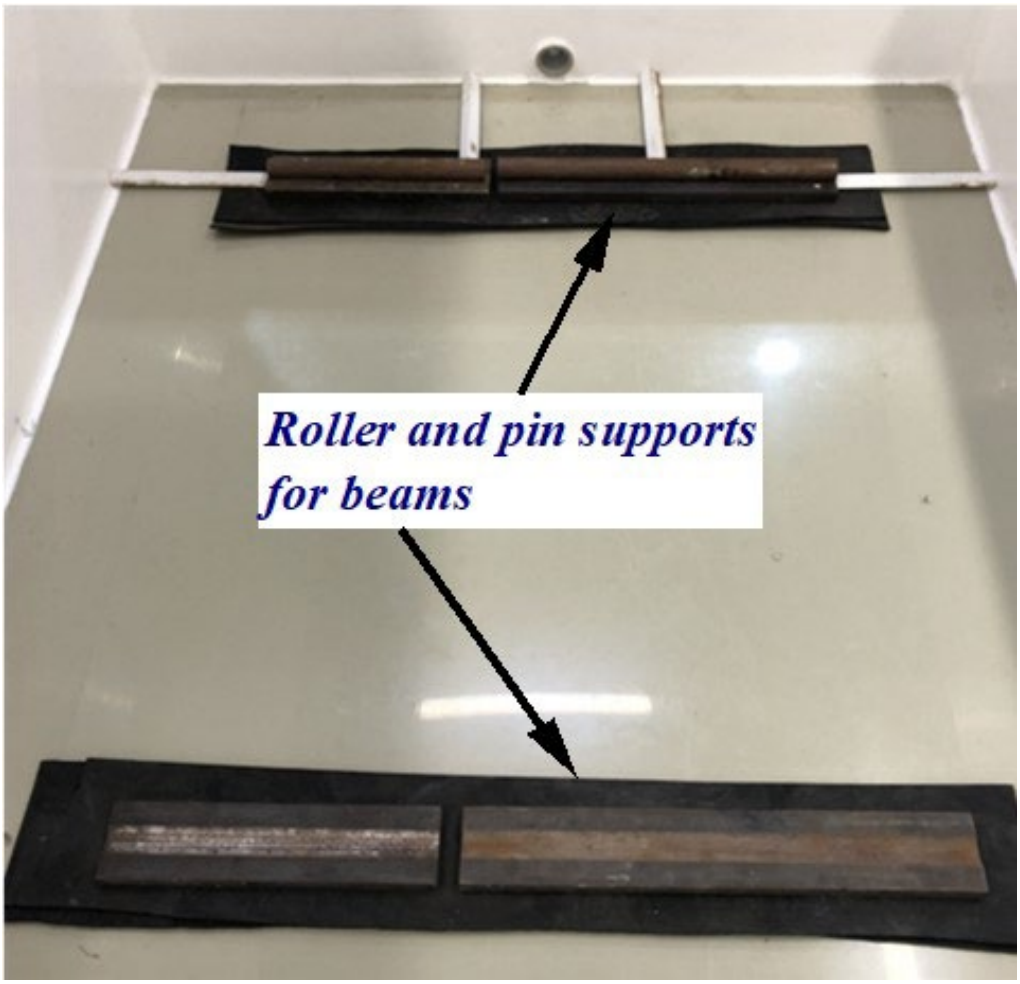

Figure 5.59 Preparing roller and pin supports for beams.

Beams were lifted and placed in the water tanks (Figure 5.60). Each water tank contains four beams. Beams are placed on two simply supported rods. Rollers and plates were used for support. Small welding points were used to fix the roller and plates for one side of the beam while the other side is a simple roller.

Figure 5.60 Lifting beams and placing them in the curing tanks.

The water tanks were filled with tap water, and the beams were maintained in an immersed state, as indicated in Figures 5.61 and 5.62.

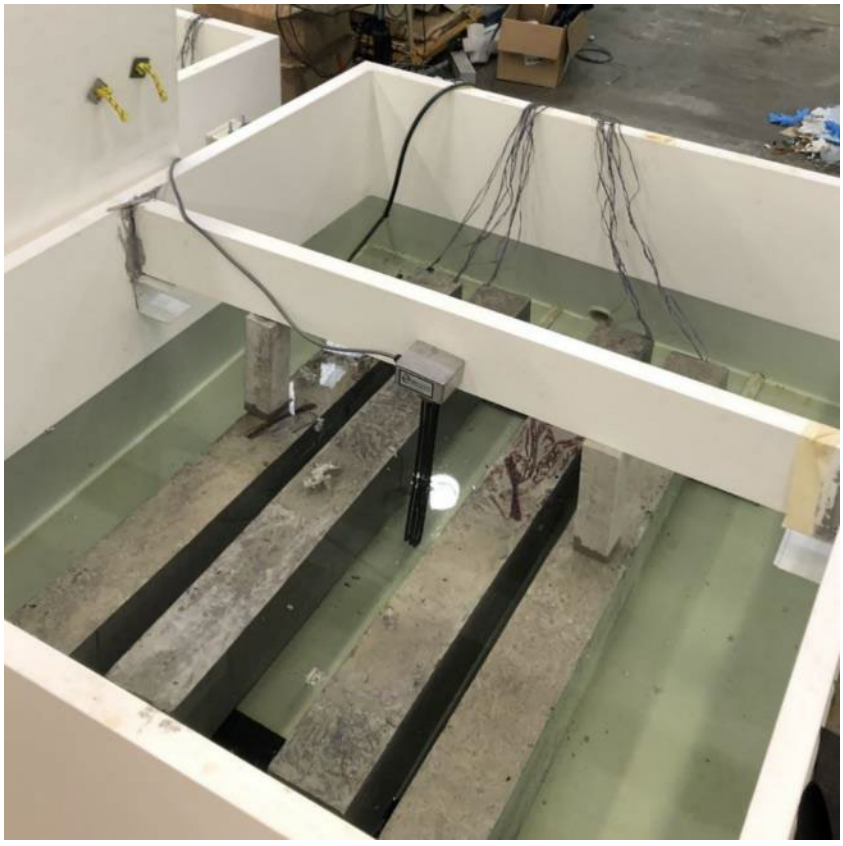

Figure 5.61 Filling the water tanks with tap water.

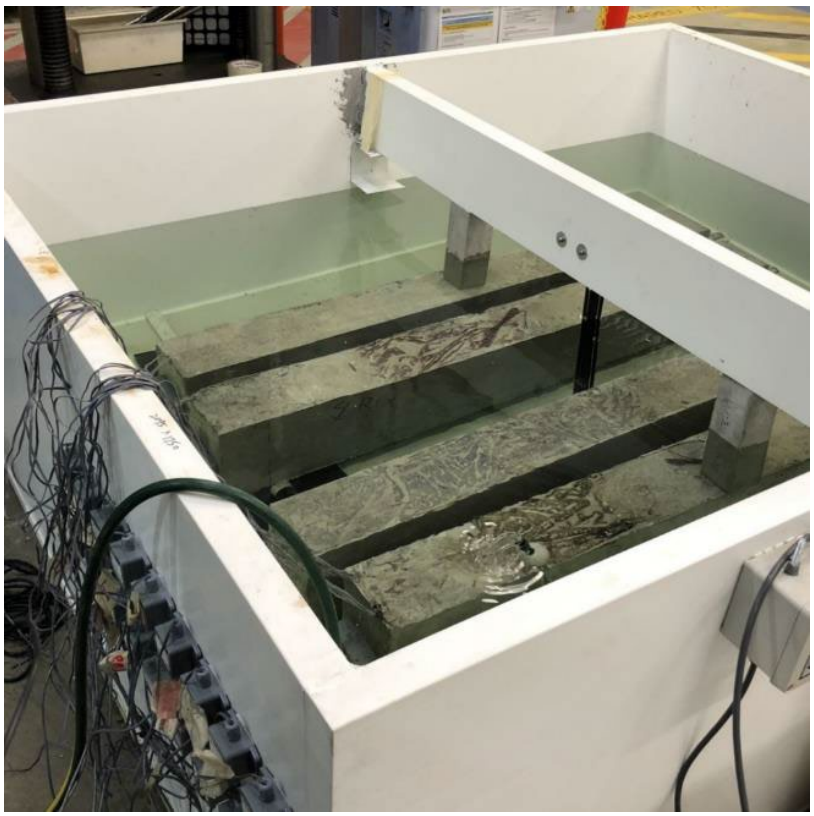

Figure 5.62 Beams immersed in water tank.

5.10.2 Immersion Heater

The ASR reaction is one of the slow chemical reactions, under normal conditions, and its damaging effects sometimes appear after tens of years. Therefore, increasing the temperature is essential to shorten the test's duration. Increasing the temperature can significantly increase the rate of the ASR reaction. According to Ulm et al., (2000), the rate of expansion roughly doubles when the temperature rises from 38 to 50 °C. Similarly, based on the formulas suggested in a different experimental study by Haha (1990), raising the temperature from 38 to 50 °C can increase the rate of reaction at roughly 1.7 times.

As the pessimum level was defined in the amount and size of reactive aggregates, an optimal level is defined for temperature. The increase in temperature, like other parameters, has an optimal amount. Although the optimal amount has not been specifically considered, based on standard tests in most sources, a temperature of 38 degrees has been considered for the ASR environment.

In two ways, the temperature of 38 degrees has been evaluated as suitable for these tests. First, many past laboratory tests have been conducted at this temperature. Therefore, choosing the same temperature can make it easier to compare the results between different experiments.

On the other hand, an excessive temperature increase can negatively affect the ASR reaction and produce false results. Research showed that increasing the temperature from 60 to 80 degrees can affect the viscosity of ASR gel and cause false results. Previously, ASR test methods, for example, AMBT, produced false results due to placing the sample in a harsh environment, which is known as one of the weak points

of that test. Therefore, increasing the temperature from 23 to 38 degrees was considered suitable for the test.

For this purpose, a vertical heating element was immersed in the water tank to increase the temperature (Figure 5.63). The heating element material is nickel, which has high resistance against an alkaline environment. A heater was attached to each tank's centre to create almost homogeneous heat water.

Also, heaters were equipped with a digital thermostat that increases the temperature to 40 degrees. Then the heater is deactivated, and two degrees are considered for changes. It will automatically turn on and raise the temperature to 40 degrees once it drops to 37 degrees. This process was repeated for the entire ASR period. In this way, the temperature remains in the range of 37 to 40 degrees for the whole time. A digital thermometer measured the water temperature in each of the tank's four corners. It was discovered that there was only a maximum three-degree temperature difference between the centre and the corners.

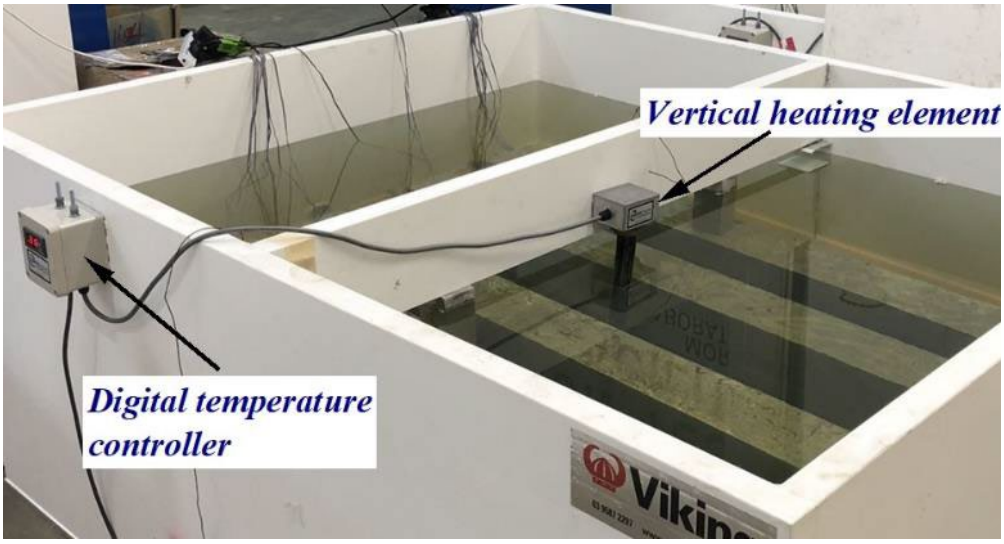

Figure 5.63 Vertical heating element and digital temperature controller.

Water was heated to 38°C by a temperature-controlled chemical-resistant heater, ensuring that the entire solution was kept at the same temperature during the acceleration period. A digital thermostat was used to monitor the temperature of the solution continuously. Both tanks were covered with plastic lids with a 5 mm honeycomb structure to prevent the solution from evaporating and keep the tanks thermal isolated during the experiments.

These heating elements are specifically designed with a low heat density ($31kW/m^2$). This means that the heater element's output is still 800W or 2400W, and the element's surface does not get as hot as other parts. This helps to keep the fluid being heated from degrading.

Each heater has an element length of 521 mm and an active length of 425 mm. The active length of an element is the portion of the element that heats up. The active length is less than the overall element length, which reduces heat transfer from the element to the mounting flange and allows the element to be positioned on the top of the tank. Regarding the safety concern, a certified electrician installed and tested heaters.

5.11 EXPANSION MONITORING

The strain has been measured and stored regularly every 6 hours. The measurement strain can be transferred directly to a PC system by connecting the data logger. For this purpose, special data logger software 'Win-control' was used to transfer information in different formats to the connected PC system. Also, an internal power source was used to reduce the risk of data loss due to power failure. The measured strain in rebars and the stress changes in post-tensioning bars in various reactive and non-reactive beams were captured to assess the expansion of concrete beams due to

ASR. In order to monitor the results of the expansion caused by ASR, the sensors are connected to the data logger and the data are transferred to the system through AMR-Wincontrol software (Figure 5.64).

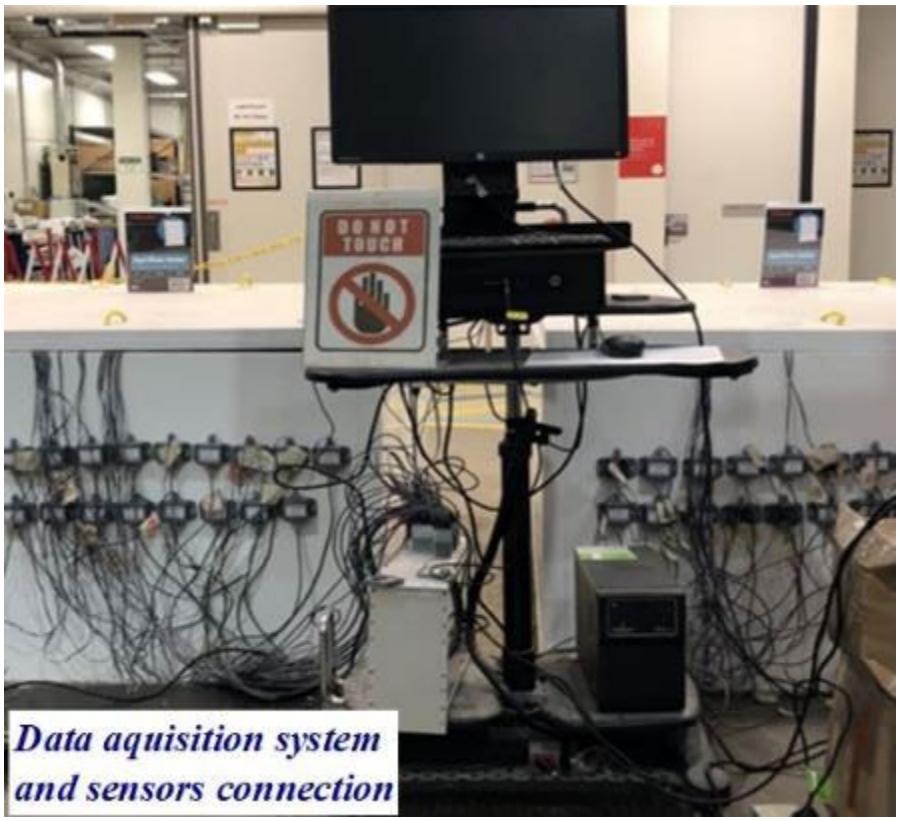

Figure 5.64 setting up data acquisition system.

After launching the application and assigning the serial interface, all configured and connected sensors are recognised and presented in the list of measurement points. Then, to manage the data, different sensors are named according to their position in the beam (Figure 5.65).

The data files can be saved in the different formats. Moreover, line diagrams may be incorporated in text documents using the OLE function.

Figure 5.65 Screenshot of AMR Win-Control Software for data acquisition.

Range, comment, limit values, and correction values were calibrated for each sensor. Figure 5.66 provides details about the current connectivity status.

AMR WinControl 8 - [Channels, Devices and Connections]

File Edit View Data Programming Settings Window Help

		Comment	Channel	Unit	Sensor	Low Lim.	Upr. Lim.	Base	Factor	Exp	Serial No.	Monitor
1		1RRC-TOP	0.20	uS	D 26	---	---	---	0.4	3		
2		3RFX-PC3	0.21	uS	D 26	---	---	---	0.4	3		
3		3RFX-RC2	0.22	uS	D 26	---	---	---	0.4	3		
4		2RSH-PC3	0.23	uS	D 26	---	---	---	0.4	3		
5		4RFX-PC3	0.24	uS	D 26	---	---	---	0.4	3		
6		4RFX-PC2	0.25	uS	D 26	---	---	---	0.4	3		
7		4RFX-PC1	0.26	uS	D 26	---	---	---	0.4	3		
8		3RFX-PC1	0.27	uS	D 26	---	---	---	0.4	3		
9		3RFX-PC2	0.28	uS	D 26	---	---	---	0.4	3		
10		4RFX-TOP	0.29	uS	D 26	---	---	---	0.4	3		
11		3RFX-RC1	0.40	uS	D 26	---	---	---	0.4	3		
12		1RRC-RB1	0.41	uS	D 26	---	---	---	0.4	3		
13		2RSH-PC1	0.42	uS	D 26	---	---	---	0.4	3		
14		4RFX-RB2	0.43	uS	D 26	---	---	---	0.4	3		
15		4RFX-RB1	0.44	uS	D 26	---	---	---	0.4	3		
16		2RSH-PC2	0.45	uS	D 26	---	---	---	0.4	3		
17		1RRC-RB2	0.46	uS	D 26	---	---	---	0.4	3		
18		8NRC-RB1	0.47	uS	D 26	---	---	---	0.4	3		
19		8NRC-RV	0.48	uS	D 26	---	---	---	0.4	3		
20		7RFX-PC3	0.49	uS	D 26	---	---	---	0.4	3		
21		5NSH-PC1	0.61	uS	D 26	---	---	---	0.4	3		
22		6NFX-PC1	0.62	uS	D 26	---	---	---	0.4	3		
23		6NFX-RC2	0.63	uS	D 26	---	---	---	0.4	3		
24		6NFX-PC3	0.64	uS	D 26	---	---	---	0.4	3		
25		5NSH-PC2	0.65	uS	D 26	---	---	---	0.4	3		
26		6NFX-PC2	0.66	uS	D 26	---	---	---	0.4	3		
27		6NFX-RC-TO	0.67	uS	D 26	---	---	---	0.4	3		
28		6NFX-RC1	0.68	uS	D 26	---	---	---	0.4	3		
29		5NSH-PC3	0.69	uS	D 26	---	---	---	0.4	3		
30		7RFX-PC1	0.80	uS	D 26	---	---	---	0.4	3		
31		8NRC-RB2	0.81	uS	D 26	---	---	---	0.4	3		
32		7RFX-PC2	0.82	uS	D 26	---	---	---	0.4	3		

Figure 5.66 Monitoring strain in reinforcing steels and post-tensioning rods.

5.12 SUMMARY

In this chapter, the process of preparing the concrete specimens for the experimental program was described. The concrete materials used along with their physical and chemical characteristics were defined.

Plain concrete prisms samples were made to evaluate the free expansion of concrete samples due to ASR. Also, real-size beams were equipped with electric strain gauges to measure the strain changes in prestressing steel due to ASR. The steps of installing and multi-step coating stages of strain gauges were presented.

To investigate the structural behaviour of the prestressed concrete beams due to ASR, a total of eight concrete beams, including six prestressed beams and two conventionally reinforced beams were cast at UTS Tech Lab. The Macalloy bar was employed for making the post-tensioned beam. The design and construction process of real-size concrete beams was presented. Also, the details and steps of post-tensioning operation and duct grouting were defined.

In addition, to evaluate the mechanical properties due to ASR, cylindrical companion samples were made with reactive and non-reactive concrete. The details of the mix design and concrete mixing procedure were described.

Finally, all real-size beams and companion concrete samples were transferred to ASR conditioning water tanks prepared for these tests and kept at 38 degrees for nine months.

During the ASR conditioning period, the expansion of the concrete samples and the changes in the strain of reinforcing and prestressing bars were regularly monitored and recorded. Tests to determine the mechanical characteristics of the cylindrical samples were also conducted at different intervals of 28, 75, 170 and 270 days.

Chapter 6: EXPERIMENAL RESULTS AND DISCUSSION

6.1 OVERVIEW

Six concrete beams, including two reinforced and four prestressed beams, were subjected to a four-point loading test after nine months of placing the concrete samples in accelerated ASR conditioning.

Three pairs of full-scale beams were studied. In the tests, two standard reinforced beams were used, one made with reactive material and one with non-reactive material. Additionally, two prestressed beams with transverse bars were tested, one made with reactive concrete and one with non-reactive concrete. Lastly, two prestressed beams without transverse bars were also tested to assess the beam's ability to resist shear with either reactive or non-reactive concrete.

The measured results of plain concrete prisms are given for free expansion evaluation. Notably, the measured values of plain concrete prisms are the average measurement of six prisms.

Additionally, the strain changes in the rebars of the main beams were regularly measured and monitored by the data acquisition system to evaluate the expansion in real-size beams.

Furthermore, mechanical tests, including compressive strength, tensile strength, and modulus of elasticity, were conducted on cylindrical samples placed in the same conditions as the original beams for different ages of 28, 75, 170, and 270 days, and the results are discussed.

6.2 ASR CRACKING AND FREE EXPANSION

6.2.1 Free Expansion of Plain Concrete Prisms

The free expansions were measured on 75×75×285 mm prisms, as shown in Figure 6.1. The expansion of six prisms was measured by horizontal length comparator in different intervals of 28, 75, 120, 170, 240 and 270 days, and the average was calculated. The expansion in each period represents the average expansion of six prisms. The details of the measured expansion of each prism, average and standard deviation are given in Table 6.1. The free expansion was measured with a horizontal length comparator using the stainless-steel studs mounted on both ends of the prisms. Before placing the samples in the ASR water tank, first readings were obtained. After temporarily removing the specimens from an alkaline solution, all further measurements were conducted promptly.

Figure 6.1 Free expansion measurement using horizontal length comparator.

After measurements were completed, the specimens were returned to the water tanks for the ASR accelerated conditioning to proceed.

Table 6.1 Measured free expansion of prisms.

	Expansion of prisms (mm)					
Day	28	75	120	170	240	270
Prism-1	0.1010	0.2580	0.4276	0.6045	0.8728	0.9600
Prism-2	0.0987	0.2690	0.4200	0.6267	0.8684	0.9583
Prism-3	0.1087	0.2530	0.4190	0.5970	0.8803	0.9436
Prism-4	0.0967	0.2627	0.3998	0.5854	0.8582	0.9629
Prism-5	0.0963	0.2715	0.4038	0.5673	0.8725	0.9562
Prism-6	0.1063	0.2877	0.4200	0.5737	0.8564	0.9682
Mean	0.1013	0.2670	0.4150	0.5924	0.8681	0.9582
SD	0.0052	0.0122	0.0108	0.0218	0.0092	0.0083

In addition, the specimens were regularly inspected for cracks. As illustrated in Figure 6.2, ASR cracks are apparent on the surface of the prism's samples. Cracking development and growth are shown in Figure 6.4.

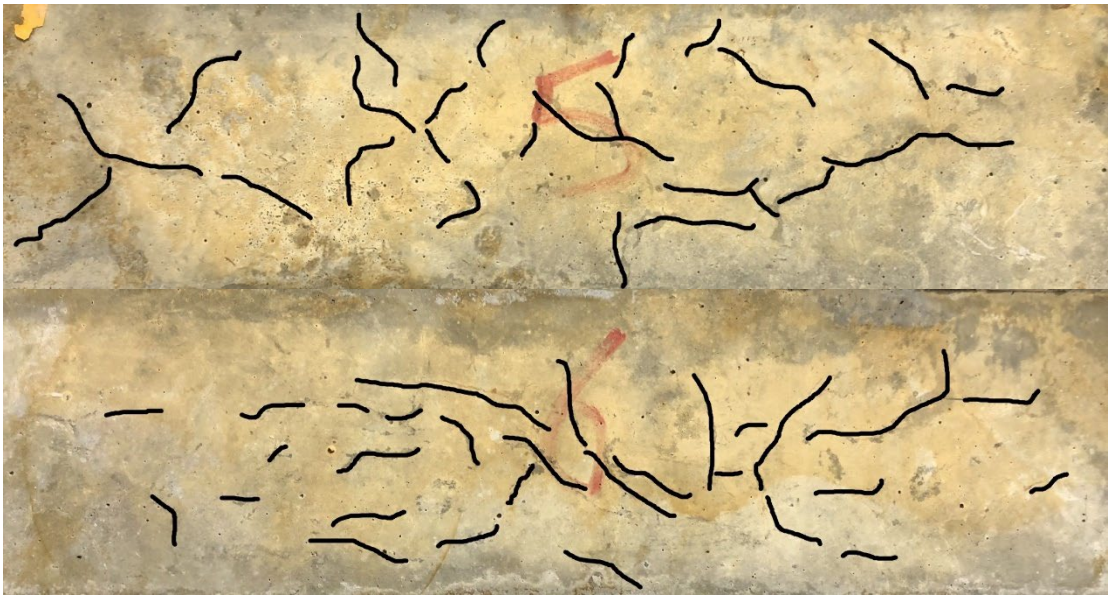

Figure 6.2 Surface map cracks in concrete prisms due to ASR.

The measured expansion of prisms samples has reached 3362 microstrains after nine months. The free expansion was estimated at 936, 1456, 2078 and 3050 microstrains for 75, 120, 170 and 240 days, respectively. Figure 6.3 shows the prisms length expansion.

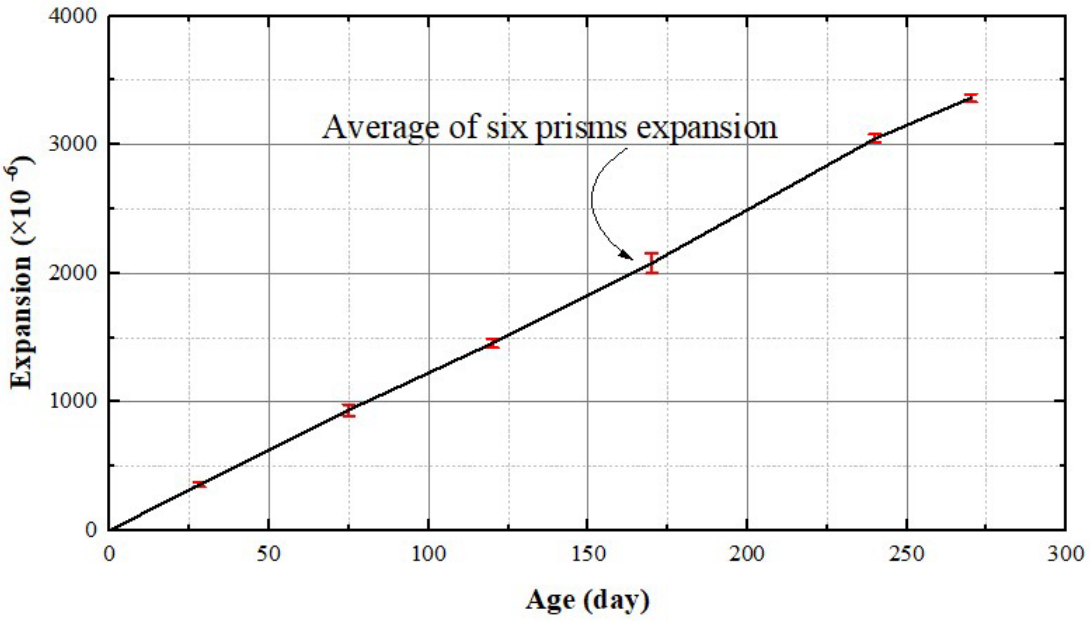

Figure 6.3 Length expansion of plain concrete prisms.

Figure 6.4 ASR cracking development and growth on the surface of prisms.

6.2.2 Changes in Steel Strains

Table 6.2 lists the measured steel strains following the specified accelerated cure intervals. The longitudinal expansion of beams was measured on the Macalloy bars, top and bottom steel reinforcing bars. The expansion of all beams was monitored for 270 days. From the findings of expansion monitoring, the following important conclusions were drawn:

ASR cracking initially emerged on the longitudinal top surface of the beams. During the first several days, beams expanded because of rising temperatures and concrete saturation. The cracks spread and interconnected, generating major longitudinal cracks.

Initially, during the first few days after immersion, the strain on the top bars was between 100 and 150 microstrains, regardless of whether they were reactive or non-reactive beams. This may be mostly due to a 15°C temperature differential, since the first zero values of strains were recorded at 23°C, while subsequent measurements were conducted at 38°C. For the non-reactive beams, subsequent expansion was negligible. The expansive strain of about 158 microstrains was found to occur finally in the upper longitudinal and 77 microstrains in the stirrup of non-reactive beams.

About a month after immersion in the ASR-curing water tank, the following swelling of the reactive beams due to ASR commenced. At nine months, the peak longitudinal expansion of beams 1RRC and 3RPC was about 1832 and 1820 microstrains, respectively (Figures 6.5 and 6.6). As depicted in Figure 6.7, the longitudinal expansion at the level of the reinforcement was drastically decreased due to the reinforcement's constraining effect.

Table 6.2 Measured strain in steel reinforcing bars in different beam specimens.

Specimen	Measured Strain ($\times 10^{-6}$)		
	Lower bar	Stirrup	Upper bar
8NRC	77	50	138
1RRC	458	610	1832
6NPC	70	77	158
3RPC	235	835	1820
4RPC	188	897	1934
7RPC	140	865	1950

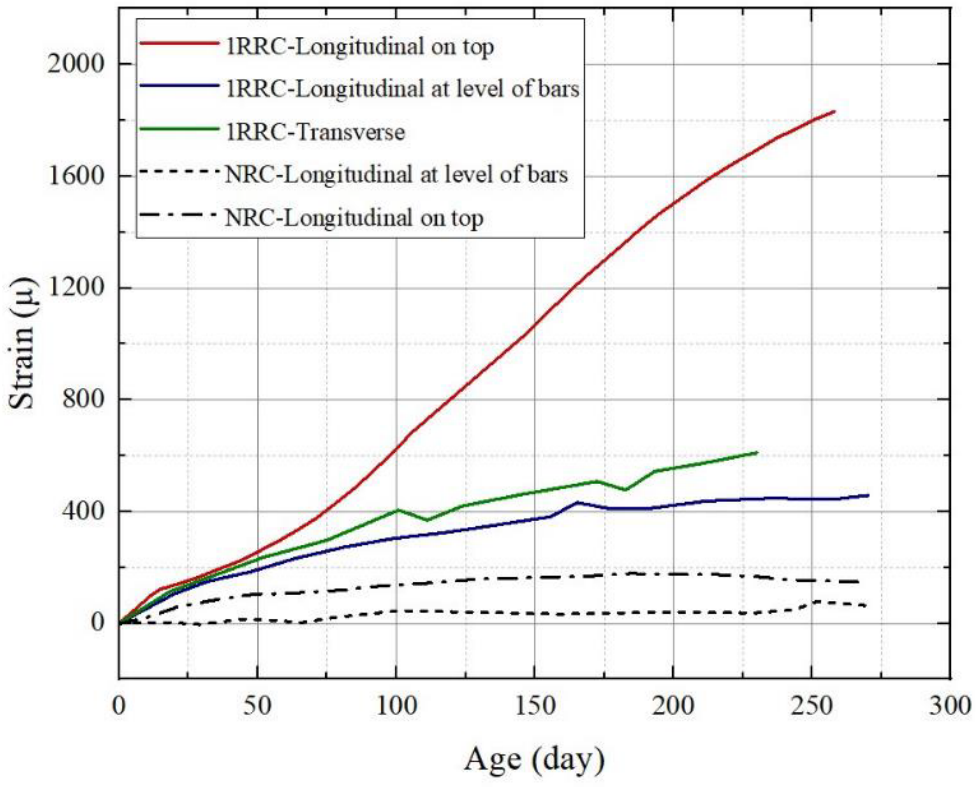

Figure 6.5 Strain of steel reinforcement in reinforced beam 1RRC.

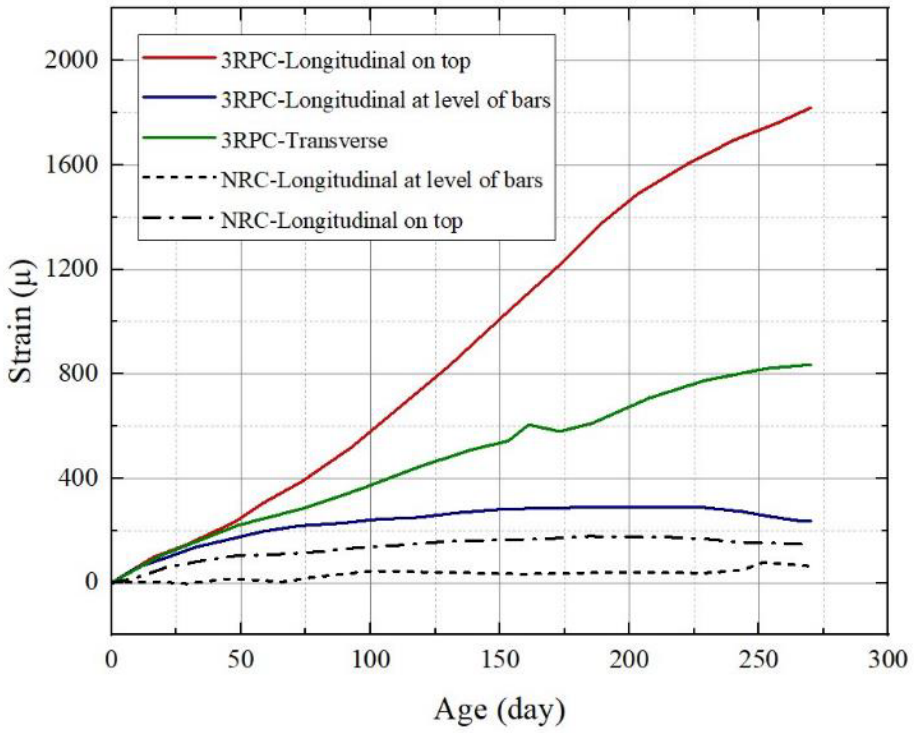

Figure 6.6 Strain of steel reinforcement in prestressed beam 3RPC.

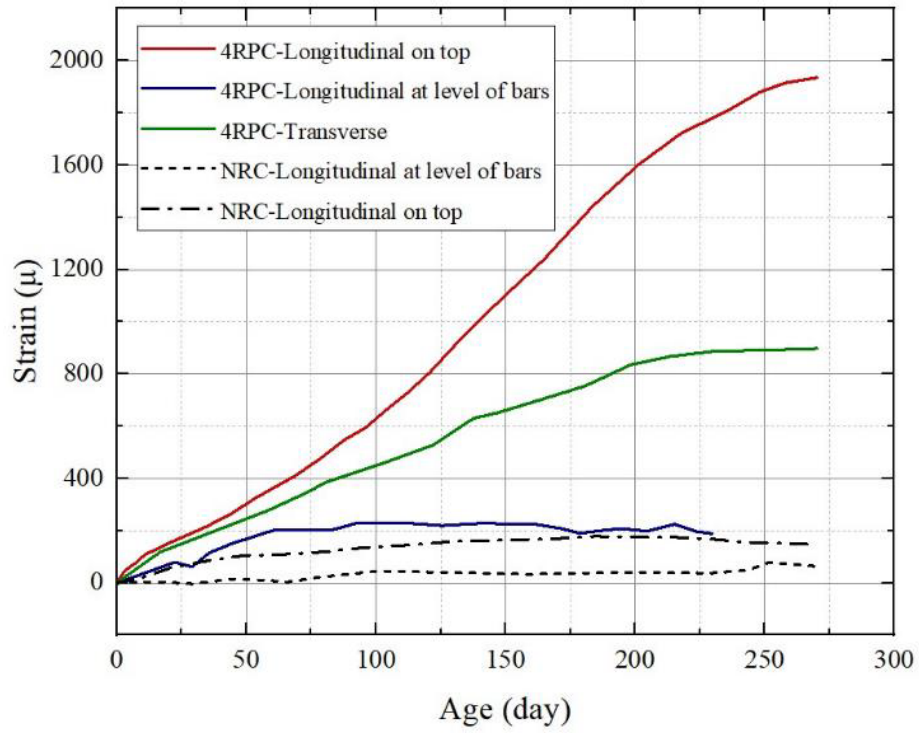

Figure 6.7 Strain of steel reinforcement in prestressed beam 4RRC.

Beam length expansions were greater than beam depth expansions because the volumetric reinforcement ratio was higher in the longitudinal direction than the minimum volumetric shear reinforcement ratio in the span. The stirrup tensile strain in prestressed ASR beams was higher by approximately 225 microstrains than in reinforced beams. Similarly, this relative increase in the stirrup tensile strain of the 7RPC beam reached around 865 microstrains, resulting in several longitudinal cracks (Figures 6.8 and 6.9).

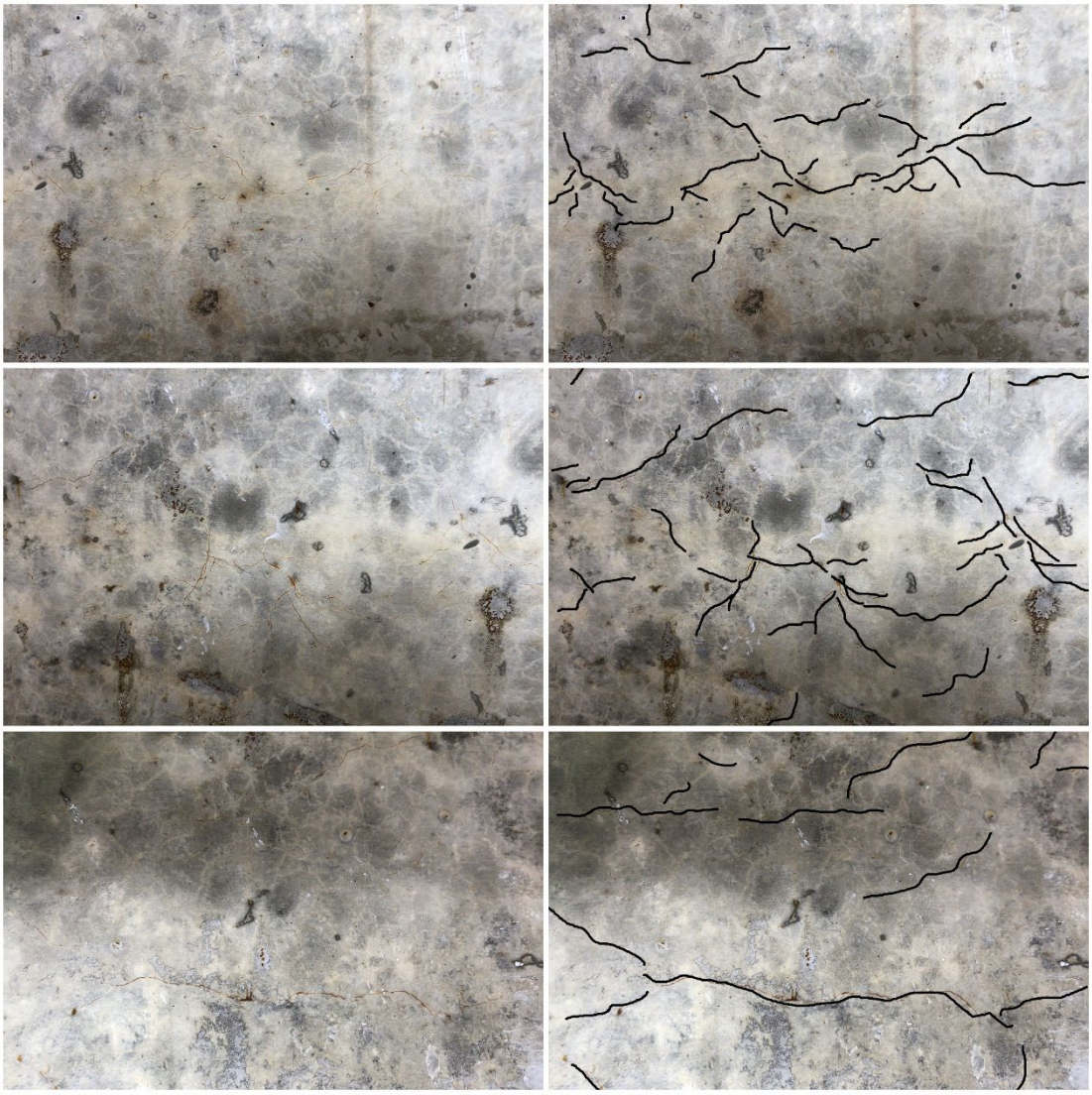

Figure 6.8 ASR cracks on the surface of reactive prestressed beams.

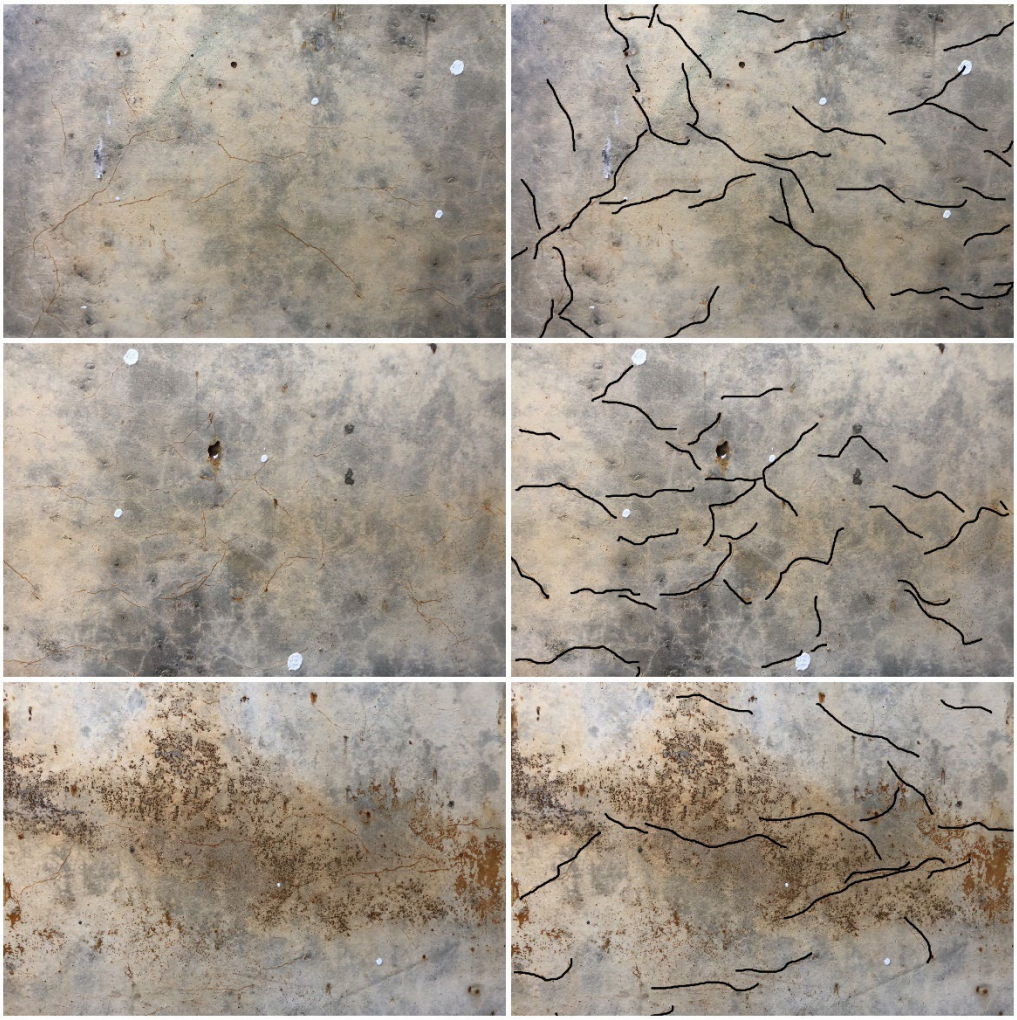

Figure 6.9 ASR cracks on the surface of reactive prestressed beams.

The change over time in the strain of the prestressing steel bars in the representative specimen are shown in Figures 6.10 to 6.12.

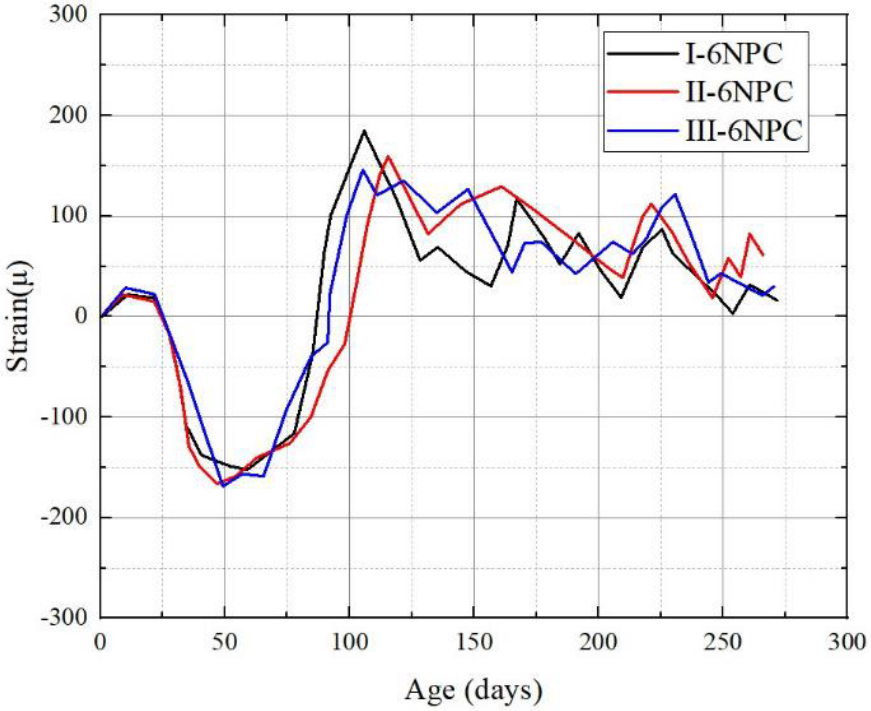

Figure 6.10 Strain of prestressing-steel bar in beam 6NPC.

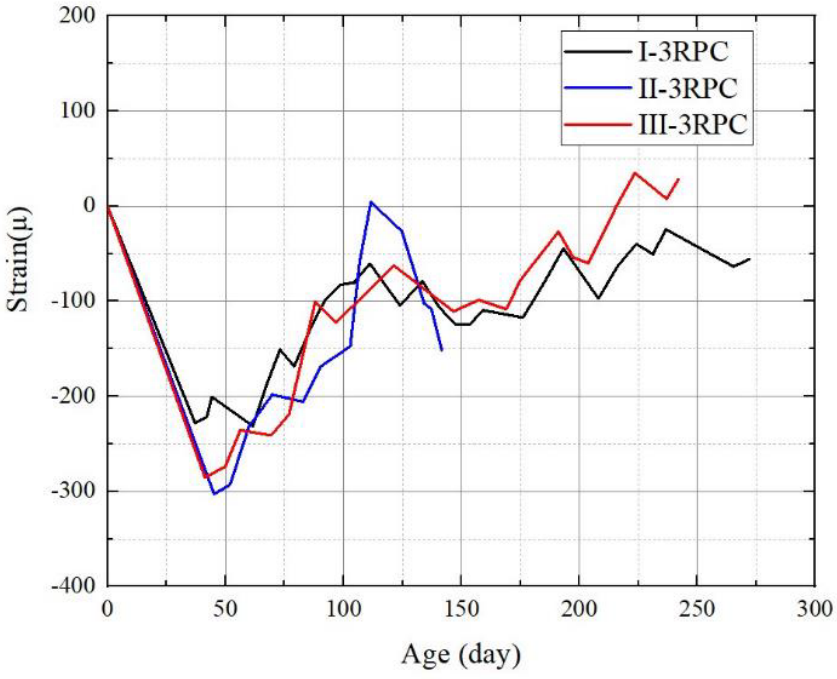

Figure 6.11 Strain of prestressed steel bar in beam 3RPC.

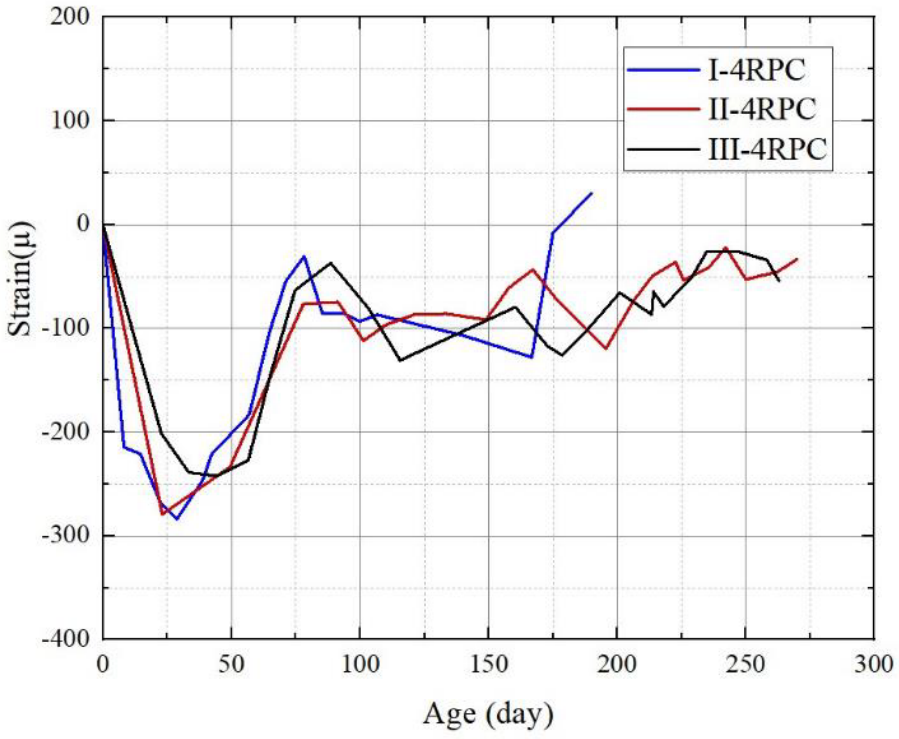

Figure 6.12 Strain of prestressed steel bar in beam 4RPC.

By comparing the samples of each series, after the first month, the strain in the prestressing steel bar decreased to a maximum of about 300μ on the pressure side. However, it changed to the tensile side by about 150μ. A tendency to recover to the strain level at the initial tension was observed.

6.3 MECHANICAL PROPERTIES

The evolution of compressive strength, tensile strength and modulus of elasticity were calculated from each mixture's average of three cylinders. To estimate changes in mechanical properties, 100×200 mm cylinders with reactive and non-reactive materials were used for comparison (Figure 6.13). Also, all concrete samples were kept in the same ASR accelerated conditions. The figure shows an ASR-affected cylinder and a normal cylinder sample.

Figure 6.13 Companion cylinders. (a) left cylinder cast with non-reactive concrete (b) right cylinder cast with reactive concrete.

The compressive strength of ASR-affected samples has been compared with the 28-day value. At first, the compressive strength increased slightly. After 75 days, the compressive strength increased by 10%. After that, no significant change in compressive strength was observed. At 170 and 270 days, 46 MPa and 47 MPa compressive strength was measured at 170 and 20 days, respectively (Figure 6.14). Table 6.3 shows the change in compressive strength in different periods.

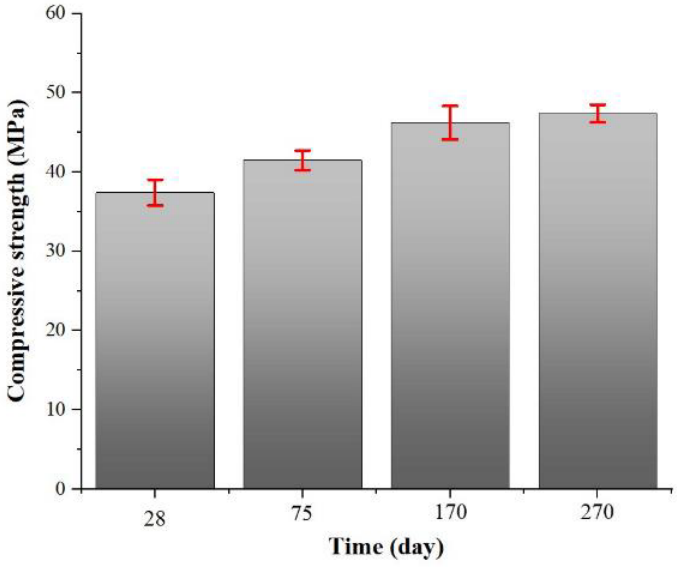

Figure 6.14 Change in compressive strength of ASR-affected cylinders standard deviations.

Although the trend of compressive strength of ASR-affected samples is upward, the slope of this increase is lower than that of normal samples (Figure 6.15). The comparison of the compressive strength measured for the normal sample and the damaged sample shows that the compressive strength of damaged samples was experienced 20% and 24% lower than the measured value from the non-reactive samples in 170 and 270 days, respectively.

Table 6.3 Compressive strength of cylindrical concrete specimens

	28 days (MPa)	75 days (MPa)	170 days (MPa)	270 days (MPa)
Sample 1	37.32	39.83	45.64	48.59
Sample 2	35.85	41.38	44.47	46.41
Sample 3	39.12	42.25	48.55	47.13
f'_c	37.43	41.15	46.22	47.38
COV %	4.37	2.98	4.55	2.34

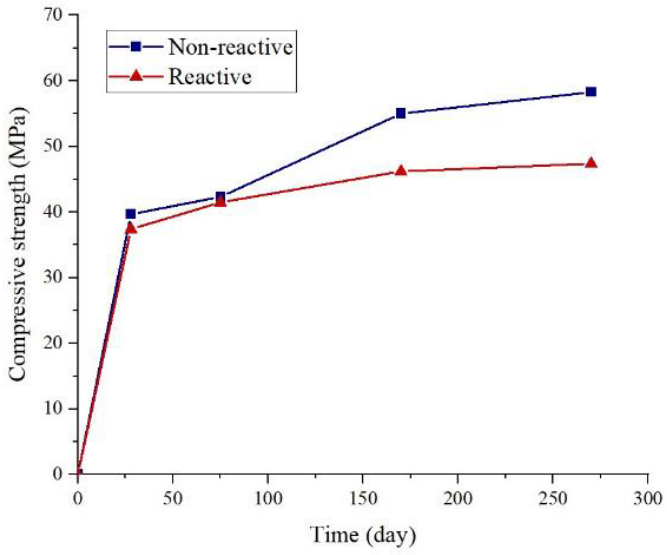

Figure 6.15 Evolution of the compressive strength of companion cylinders.

Similar to compressive strength, as illustrated in Figure 6.16, a slight increase was observed in the results of the tensile strength of the cylindrical samples of the ASR-damaged samples. But after that, the trend shifted downward. The tensile strength of the reactive sample shows 8% and 21% loss in 170 and 270 days, respectively. The results obtained from the splitting tensile strength tests are given in Table 6.4.

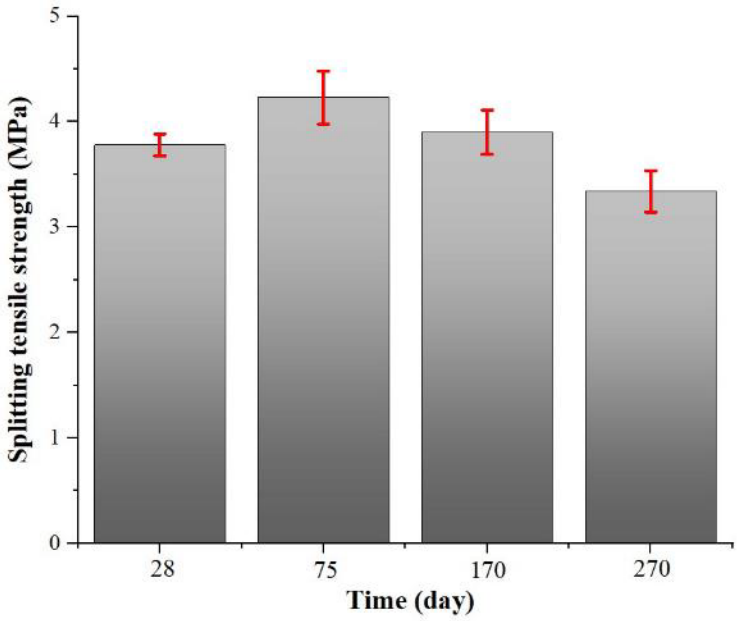

Figure 6.16 Change in splitting tensile strength of ASR-affected cylinders standard deviations.

Table 6.4 Splitting tensile strength of cylindrical concrete specimens.

	28 days (MPa)	75 days (MPa)	170 days (MPa)	270 days (MPa)
Sample 1	3.9	4.5	3.9	3.4
Sample 2	3.7	4	3.7	3.5
Sample 3	3.75	4.2	4.12	3.15
f'_t	3.78	4.23	3.90	3.35
COV %	2.75	5.94	5.37	5.38

In addition, as summarized in Figure 6.17, the comparison between the reactive and non-reactive samples indicates that the ASR-affected samples' tensile strength was about 15 and 36% lower than the measured value for the non-reactive samples at 170 and 270 days, respectively.

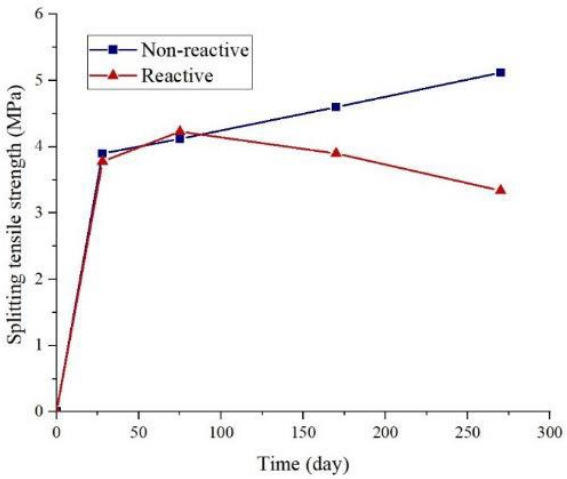

Figure 6.17 Evolution of the splitting tensile strength of companion cylinders.

As depicted in Figure 6.18, the elastic modulus reduction of samples affected by ASR has been compared with the 28-day value. The material's microcracking because of accelerated ASR could be attributed to the decrease in modulus of elasticity. The elastic modulus decreases by 15 and 28% in 170 and 270 days, respectively.

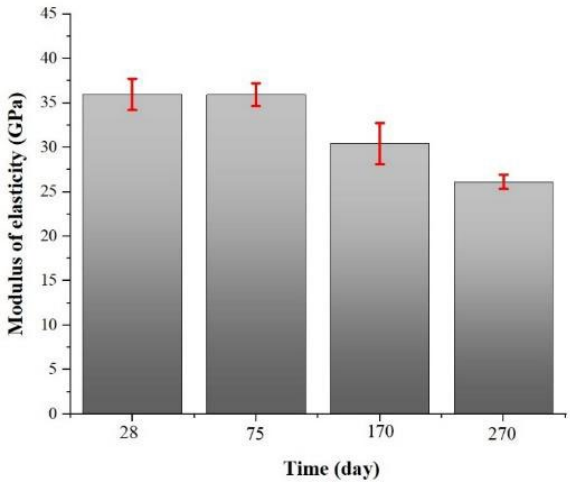

Figure 6.18 Change in modulus of elasticity of ASR-affected cylinders and standard deviations.

The changes in the modulus of elasticity in different time intervals are given in Table 6.5.

Table 6.5 Modulus of elasticity of concrete specimens.

	28 days (GPa)	75 days (GPa)	170 days (GPa)	270 days (GPa)
Sample 1	36.5	36	31.5	25.4
Sample 2	34	34.6	27.8	27
Sample 3	37.4	37.2	32	26
E_c	35.97	35.94	30.43	26.13
COV %	4.89	3.62	7.54	3.09

Figure 6.19 shows the comparison results between the elastic modulus of the normal sample and the sample damaged by ASR. The elastic modulus decreases by 24% and 40% in 75, 170 and 270 days, respectively.

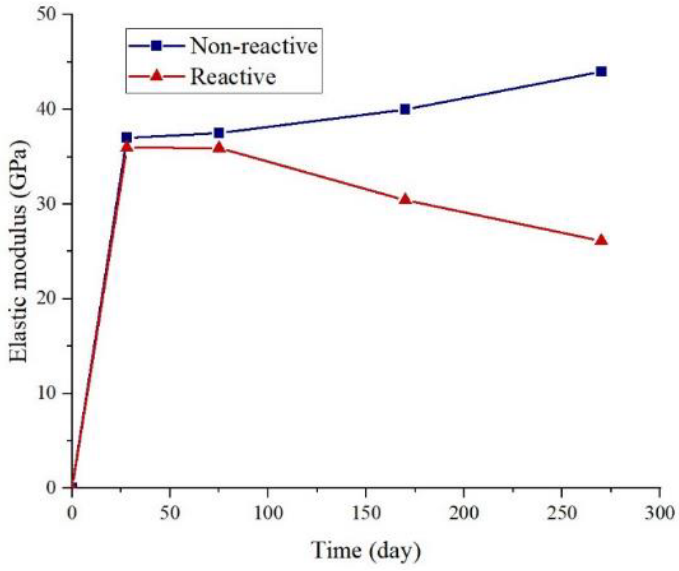

Figure 6.19 Evolution of the static modulus of elasticity of ASR-affected companion cylinders.

6.4 STRUCTURAL BEHAVIOUR

Several tests were conducted on both reactive and non-reactive beams to compare the residual load-carrying capacity of normal and ASR-affected beams to ascertain the repeatability and better understand the flexural and shear behaviour of the ASR-affected reinforced and prestressed beams.

Three conventional reinforced concrete beams with non-reactive concrete were experimentally evaluated for compression, tensile, and shear failure modes at UTS structural lab to validate the non-linear finite element modelling.

The beams were transferred from the accelerated ASR water tanks to the structural laboratory to perform a 4-point loading test to study the structural behaviour of the beams after nine months of accelerated ASR curing. Before lifting the beams from the ASR accelerated water tank, the alkalinity level of the solution was measured first to estimate the risk of an alkaline environment. For this purpose, a pH meter has been used (Figure 6.20).

Figure 6.20 pH meter used for measuring the pH level of solution after the ASR accelerating period.

Using a forklift, the beams were carefully relocated to the structural laboratory. As shown in Figure 6.21, the loading places were marked, and capping was done using dental plaster.

Figure 6.21 Capping the location of loading points.

Flexural and shear behaviour of large-scale reinforced and prestressed beams were investigated. In this context, three pairs of full-scale beams were studied. Two conventional reinforced beams with reactive and non-reactive materials, two prestressed beams with transverse bars with reactive and non-reactive concrete, and two prestressed beams without transverse bars to evaluate the beam's performance in shear with reactive and non-reactive concrete were tested.

The reinforced beams were tested to measure their ability in flexure, the first pair of prestressed beams were evaluated for their performance in compression failure, and the second pair of prestressed beams were designed to test for shear failure. Figure 6.22 presents the loading information.

Figure 6.22 Four-point loading test setup.

Both beams with reactive materials were constructed using similar concrete mixtures that included highly reactive coarse aggregate and a cement equivalent alkali concentration of 1.75%.

Compressive strength, tensile strength, and elastic modulus of ASR concrete, which were measured on the 100×200 mm cylinder specimens, were reduced to approximately 76%, 72%, and 60% of that of normal concrete, respectively, at the time of loading tests (nine months). This indicates that when no restraint against expansion exists, the strength and elastic modulus of ASR concrete deteriorates significantly.

6.4.1 Reactive and Non-reactive Conventional Reinforced Beams

At the early elastic stages, the behaviour of the ASR-affected and unaffected beams remained unchanged. Thereafter, the ASR-affected beam's stiffness was higher than that of the unaffected beam. In addition, the cracking moment of the reinforced ASR beam was greater than that of the normal concrete beam, even though the tensile strength obtained from cylinder specimens of ASR concrete decreased to about 70% of that of normal concrete. This could be attributed to the chemical prestress due to the pressure of ASR expansion in the bottom fibre of the reinforced concrete section in ASR beams. The bottom surface of the beam was the first location of the crack, followed by the top surface. The majority of the beam's cracks were vertical and centered in the middle third. The cracks which had occurred at the previous loading grew as the load increased, and the tension failure occurred. Figure 6.23 shows flexural crack patterns of the reinforced concrete beam after failure.

Figure 6.23 Crack patterns of the reinforced beam after flexural failure.

A comparison of the load-deflection relationship of normal reinforced concrete beam and ASR-affected reinforced concrete beam is shown in Figure 6.24.

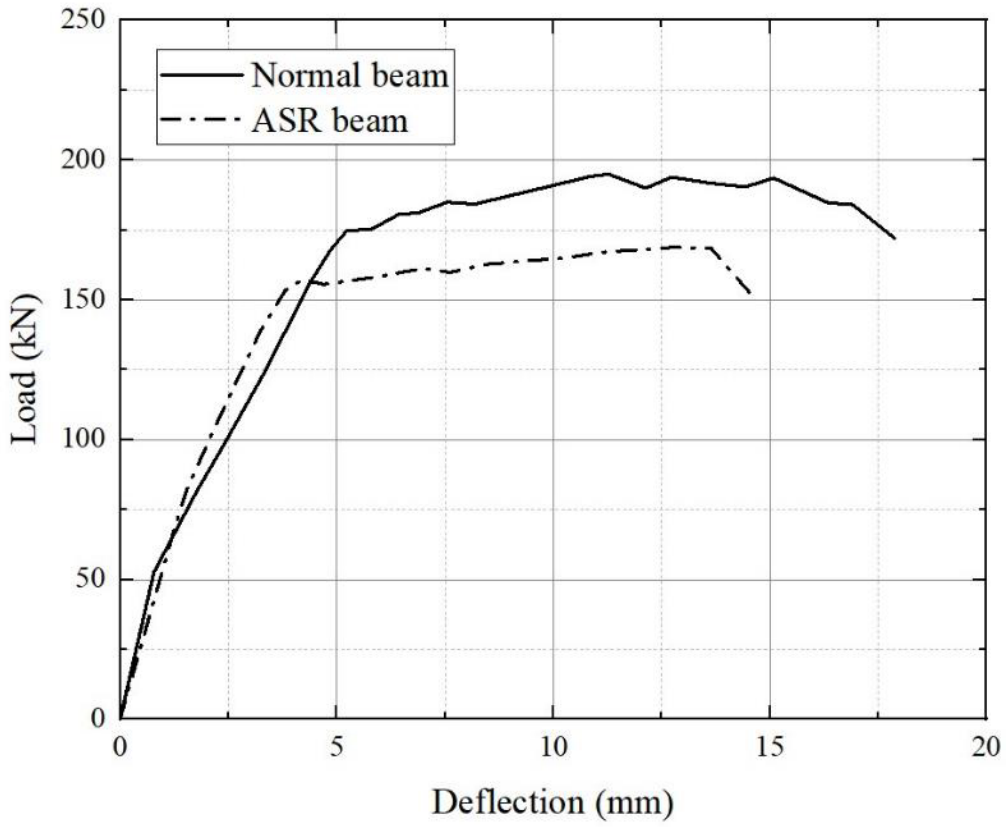

Figure 6.24 Deflection at the centre versus an applied load of reactive and non-reactive reinforced beams in flexural.

Although ASR expansion may have caused a significant tensile strain to be induced in the longitudinal steels, the yield strength and ultimate flexural strength of the ASR beam were reduced by less than 14% in comprising each corresponding normal beam.

6.4.2 Reactive and Non-reactive Prestressed Beams in Shear

The results of the shear tests revealed that the beam made of non-reactive concrete had a 3% higher shear capacity compared to the beam affected by ASR (Figure 6.26). The ASR affected the concrete tensile strength, causing a slight decrease in it, which did not impact its resistance to shear failure. The shear strength and stiffness of both the normal and ASR-affected prestressed beams were comparable. Tests on shear

failure revealed only a slight change in the shear behaviour of prestressed concrete beams due to ASR expansion (Figure 6.25).

Figure 6.25 Crack patterns of the prestressed beam after shear failure.

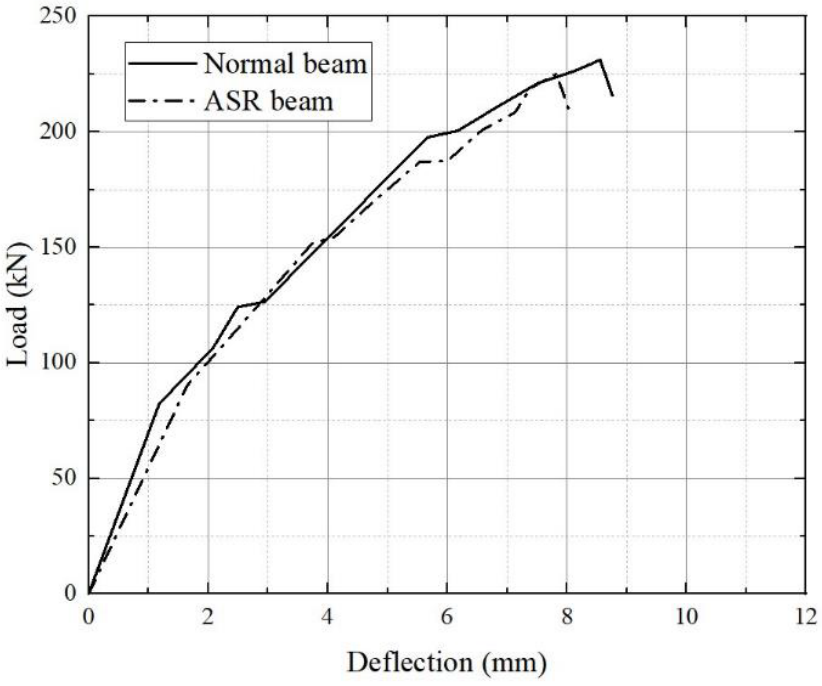

Figure 6.26 Deflection at the centre versus an applied load of reactive and non-reactive prestressed beams in shear.

6.4.3 Reactive and Non-reactive Prestressed Beams in Compression

The compressive failure in the test started with crushing the concrete on the top surface, followed by yielding the steel on the tension side, while prestressing bar was not yielded. The failure occurred when the compressive strength of the concrete was exceeded, with the top of the beam near the mid-span being the first to fail, where the bending moment was highest (Figure 6.27).

The ultimate strength of the ASR prestressed beam was reduced by less than 10% compared to each corresponding normal beam. A similarity was also observed between the stiffness of the ASR-affected and normal beams.

Figure 6.27 Crack patterns of the prestressed beam after flexural compression failure.

As illustrated in Figure 6.28, there were no significant changes in the flexural capacity or stiffness of prestressed beams subjected to ASR. This indicates that neither a significant change in concrete compressive strength nor a significant reduction in prestressing occurred due to ASR.

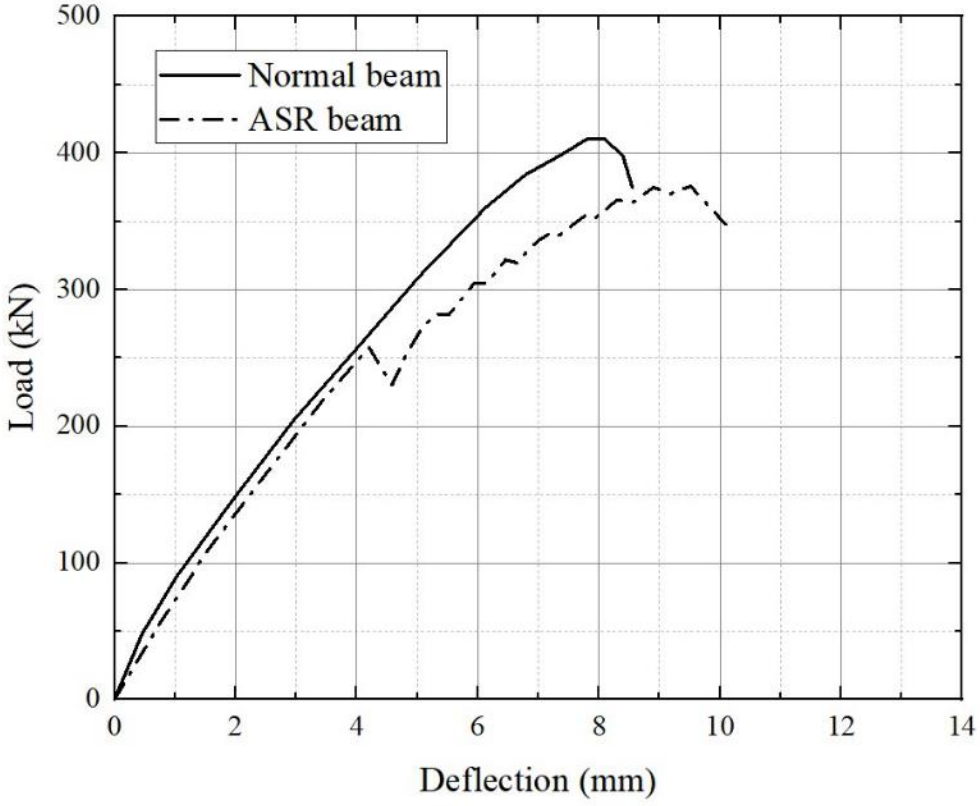

Figure 6.28 Deflection at the centre versus an applied load of reactive and non-reactive prestressed beams in compression.

The location of the failure crack, which occurred exactly where the ASR crack was present, is the notable aspect of the failure of the ASR-affected beam, which can underscore the importance of the ASR crack pattern on the concrete beam's failure (Figures 6.29 and 6.30).

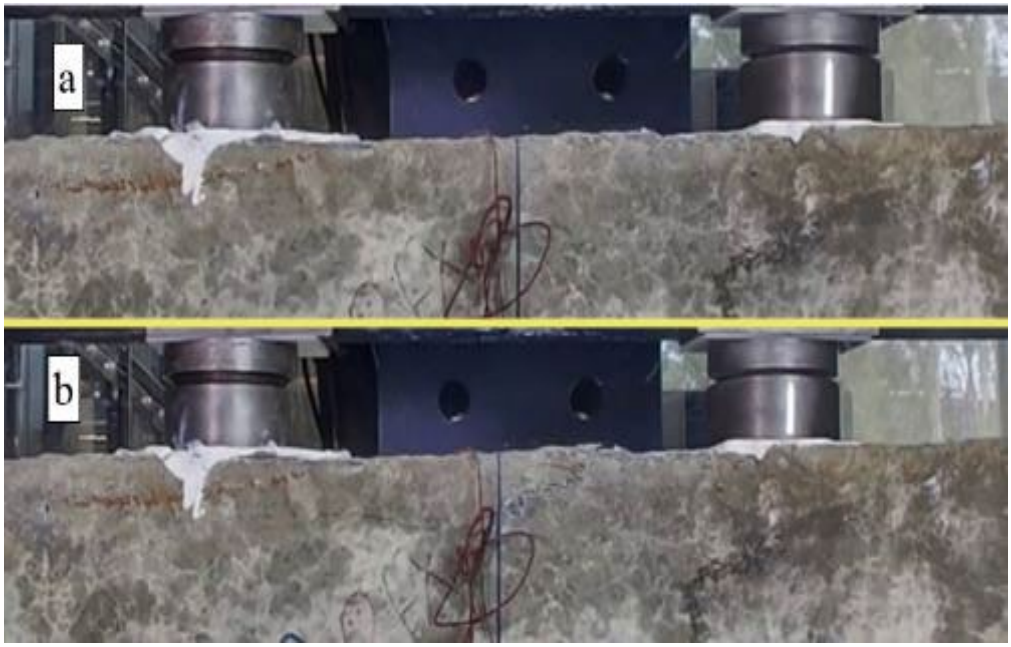

Figure 6.29 Prestressed beam (a) before failure (b) after flexural compression failure.

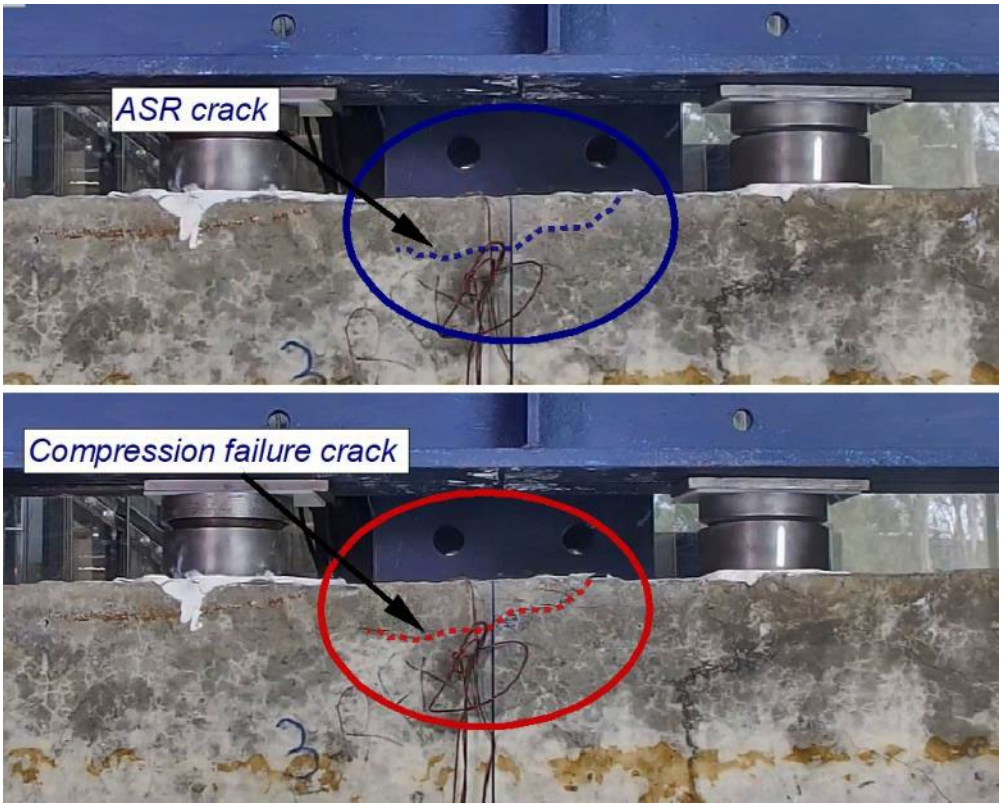

Figure 6.30 Compression failure crack happened along the ASR crack.

6.5 SUMMARY

Results of the experimental program (Including specimen conditioning and expansion monitoring, conducting mechanical tests, and flexural and shear testing) were reviewed within this chapter.

According to the findings, concrete samples experienced up to $0.33e^{-4}$ expansion over nine months in ASR accelerated conditions. The strain changes caused by ASR in the steel reinforcing bars and ASR crack patterns of concrete samples were discussed.

Strains in reinforcing bars were monitored on a regular basis. The results of changes in strains of steel showed that the upper bar of the beam experienced the highest expansion. In addition, the transverse strain in the prestressed beams, which were restrained more in the longitudinal direction, was observed to be slightly higher than the transverse strain in the reinforced beams. The strain changes were more significant in the upper area, whereas the strain changes of reinforcing steel in prestressed beams were slightly less at the lower bars.

The strain in the upper reinforcing bars reached $0.195e^{-4}$, while the strain changes for the lower bars were significantly less ($0.014e^{-4}$). The strain in lower bars for prestressed beams was evaluated to be almost equal to reinforced beams, thus indicating that the use of reinforcing bars alone greatly reduces the expansion due to ASR and applying more external force, such as prestressing force, does not result in much difference in strain changes.

No significant difference was observed in strain changes in prestressing bars for reactive and non-reactive beams.

Regarding the structural behaviour of the beams, the cracking moment increased slightly in the reinforced beams. This can be attributed to the chemical prestress

generated by ASR expansion. The reinforced beam's ultimate flexural load was measured to be 14% less than the ultimate load-carrying capacity of the non-reactive beam.

The failure mode for both prestressed, reactive, and non-reactive beams without transverse bars was a shear failure. The ultimate load capacity of the prestressed beam in shear decreased by less than 5%. The decrease in shear capacity was considered reasonable since the tensile strength of reactive cylindrical concrete samples due to ASR was 30% lower than non-reactive samples.

The ultimate load capacity of the prestressed beam witnessed a slight reduction in compression failure. The cracks continued diagonally at the support to the loading points, but the final failure occurred in the compressive area of the beam. The failure of the beam took place in the compressive zone, precisely at the location of the ASR cracks. This can indicate the significant associated with the ASR cracking pattern. The compression concrete failure that happened along the ASR crack was clearly confirmed.

Not much change was observed from comparing the results of prestressing steel strains in reactive and non-reactive beams. This may imply that ASR did not impact the prestress force and cause any loss of prestressing force.

Chapter 7: FINITE ELEMENT MODELLING OF ASR-AFFECTED PRESTRESSED CONCRETE BEAMS

7.1 OVERVIEW

To predict the ultimate strength of reinforced and prestressed concrete beams with Non-linear materials and geometry, a three-dimensional finite element model has been developed in this Chapter. Numerical modelling was presented to predict the bending behaviour of prestressed concrete beams using Non-linear finite element analysis. First, the application of this model was verified by accurate simulation of reinforced concrete beams with different failure modes. Three reinforced concrete beams were experimentally evaluated for compression, tensile, and shear failure modes at UTS structural lab. Then all the beams were modelled using Non-linear finite element software, and experimental and numerical findings were compared.

Using ATENA Non-linear finite element software version 5.7, the ultimate strength of reinforced and prestressed concrete beams tested in the lab were compared and analyzed to validate the numerical modelling. Next, reinforced concrete beams were tested under a four-point loading test method to facilitate the comparison of experimental and numerical results. Then, the load-deflection curves obtained from different failure modes of experimental tests were compared with numerical modelling. Similarly, prestressed concrete beams were modelled by applying the ASR volume strain and considering material properties reduction due to ASR. For this purpose, beams were loaded under uniform self-weight load in the first step. Then the prestress force was applied as an initial strain to the post-tensioning bars. Thereafter, ASR

volume strain was applied to the beams as an internal strain (based on the proposed hybrid model described in Chapter four). Finally, the beams were subjected to a four-point loading test to determine and predict the flexural and shear behaviour of ASR-affected prestressed beams.

In addition, to better understand the behaviour of prestressed structures caused by ASR, a series of precast prestressed concrete rectangular bridge beams have been selected for modelling. There are approximately 1100 of these bridges on the VicRoads arterial road network and a similar number on the local road network (Taplin, Al-Mahaidi et al. 2000).

In this model, the tensile behaviour of concrete was modelled using fracture mechanics, and the compressive behaviour of concrete was modelled using plasticity. For concrete under tension, the stress-strain law considers the two phases prior to and after cracking. Smeared crack formulation and the crack band model were used to develop the fracturing model. Strength and stiffness degradation can be considered by either employing a novel proposed numerical model, as described in chapter three, or by using the measured properties from companion samples. The measured values of companion samples were used as an input for compressive and tensile strength, while the elastic modulus was calculated based on the proposed numerical model in chapter 3.

Based on the constitutive model discussed in chapter four, the effects of relative humidity, alkali/silica mixture concentration, aggregates size, externally applied stress, and ambient temperature were considered in applying the ASR expansion.

This chapter outlines the numerical modelling approach, and the constitutive material law used to model concrete and rebars.

7.2 NON-LINEAR CONCRETE

The fracture-plastic model was used for this analysis. The behaviour of concrete was modelled as plastic in compression and fracture in tension. Concrete nonlinear material was defined using the fracture-plastic model. In this model, the tensile behaviour of concrete was modelled based on fracture mechanics, and the compressive behaviour of concrete was modelled with plasticity. Based on the smeared crack formulation and the crack band model, the fracturing model was developed. Before and after cracking, the stress-strain law for tension has two phases. Before cracking, the behaviour of concrete was termed linear elastic. Moreover, concrete experiences exponential softening, which is dependent on the crack opening law and fracture energy. The behaviour of concrete under compression was modelled using a plastic model based on the work of William Mentrey. (1995, Menetrey and Willam)

Two components comprise the stress-strain relationship for the plastic model in concrete: hardening and softening. In the phase of hardening, the formulation is based on strain, as recommended by CEB-FIB (Béton, 1993). Softening is formulated based on plastic displacement.

Material axes of concrete cracks can be defined as fixed or rotating cracks. In the case of fixed cracks, the direction of the cracks is considered fixed geometrically, and the transfer of normal and shear stress is modelled directly. Therefore, the crack model is more accurate geometrically. In the rotating crack model, the orientation of the cracks corresponds to the direction of the primary stress. When the direction of the crack opening changes, so does the direction of the crack. This approach makes computations easier. In this investigation, the smeared fixed crack model was used. The role of the opening of the crack was determined using the model provided by Hordjik in 1991. (Hordijk 1993). Based on the FIB model, this model contains the nonlinear

tensile and compressive behaviour of concrete. From the cubic compressive stress f cu are calculated the cylinder compressive strength f c' and tensile strength f t. Following are the formulae that may be used to determine these parameters.

$$f_c' = -0.85\, f_{cu} \tag{7.1}$$

$$f_t = 0.24\, f_{cu}^{\frac{2}{3}} \tag{7.2}$$

$$E_c = (6000 - 15.5 f_{cu})\sqrt{f_{cu}} \tag{7.3}$$

The parameter G_f presents the fracture energy, which may be computed as follows.

$$G_f = G_{f0}\left(\frac{f_c'}{10}\right)^{0.7} \tag{7.4}$$

Where G_{f0} was considered equal to 0.03 N/mm for 16 mm aggregates. The reduction of compressive strength due to cracks was considered 0.8, and the plastic strain of concrete under pressure was obtained from the following equation.

$$\varepsilon_{cp} = \frac{f_c'}{E_c} \tag{7.5}$$

7.2.1 Tension Prior to Crack

In this state, the behaviour of concrete in tension was presumed linear elastic, so stress and strain follow Hooke's law.

$$\sigma = E_c \varepsilon \tag{7.6}$$

Where σ is the concrete's tensile stress, ε is its strain, and E_c is the modulus of elasticity of concrete.

7.2.2 Stress Reduction After Cracking

Following is a hypothetical model for the tensile stress of concrete after causing a crack in the concrete, which combines the crack opening law and fracture energy model with the crack band theory. Stress-strain curve for concrete in tension is provided in Figure 7.1.

$$\frac{\sigma}{f_t} = \left\{1 + \left(c_1 \frac{w}{w_c}\right)^3\right\} \exp\left(-c_2 \frac{w}{w_c}\right) - \frac{w}{w_c}(1 + c_1^3)\exp\left(-c_2\right) \tag{7.7}$$

Crack openings is denoted by w. Also, w_c is the stress release crack opening, c_1=3, c_2= 6.93, and $w_c = 5.14\frac{G_f}{f_t}$

In this computational model, the fracture energy G_f is the energy needed to create a unit area of the stress-free crack and is assumed to be 0.03 N/mm for this model.

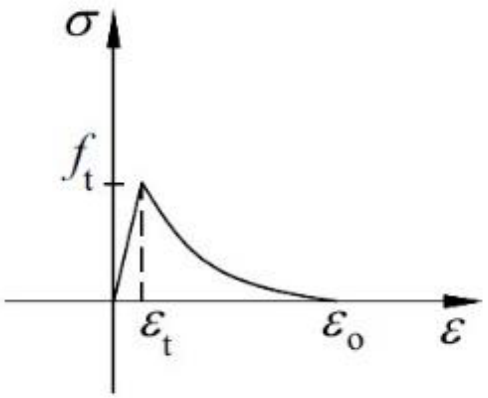

Figure 7.1 Stress-strain curve for concrete in tension.

7.2.3 Compression Before Peak Stress

In this state, the curve shown in Figure 7.2 represents the stress-strain curve for concrete in compression.

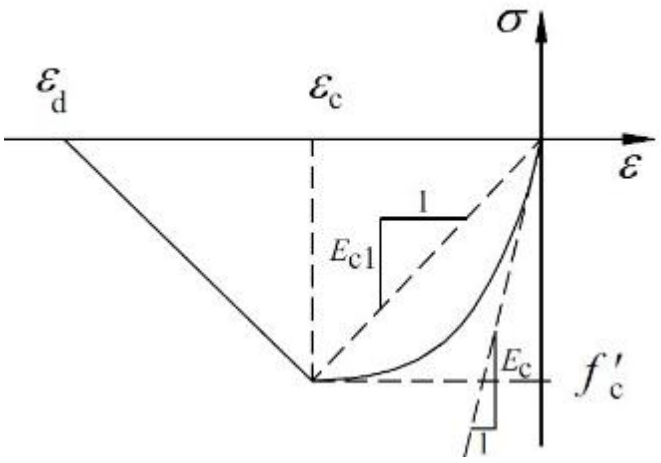

Figure 7.2 Compressive stress-strain curve for concrete.

The link between stress and concrete strain in compression was stated in the following formula, which is suggested by the CEB-FIP Model Code 1990 (Comite Euro-International du Beton 1993).

$$\sigma = f_c' \frac{kx - x^2}{(1+(k-2)x)} \ , \ x = \frac{\varepsilon}{\varepsilon_c} \ , \ k = \frac{E_c}{E_{c1}} \tag{7.8}$$

7.2.4 Compression Behaviour After Peak

After the peak, it is asumed that the softening law for concrete under compression is linearly downward. In this investigation, a theoretical compression model based on dissipated energy was used. According to Van Mier's (1986) hypothesis, this model assumes that compression failure is localised in a plane normal to the direction of principal compressive stress. Additionally, displacement is considered to be independent of the structure's size. As a result, the strain can be estimated as below.

$$\varepsilon_d = \varepsilon_c + \frac{w_d}{L_d'}, \tag{7.9}$$

where w_d is the plastic displacement at the end of the softening curve, assumed to be 0.5 mm, ε_d is the compressive strain limit, and L_d' is the band width, respectively.

7.3 FEM MODEL AND SOFTWARE

The behaviour of prestressed concrete structures, such as concrete cracking, concrete crushing, and reinforcement yielding, was simulated using the ATENA finite element programme, which was developed particularly for 3D nonlinear finite element analysis of solids based on constitutive law. The characterization of the stress-strain relationship for concrete and tensile softening function and the crack band used in ATENA are provided in Figures 7.3 and 7.4, respectively. Additionally, input data, model geometry, and material requirements have all been pre-processed using GiD software. This research used ATENA version 5.7 finite element software for modelling.

GiD is software with an interactive graphical user interface that creates input data for analysis in the ATENA environment. ATENA software receives GiD output for processing and analysis. GiD is often used to specify components, prepare data, and display the result of numerical simulations.

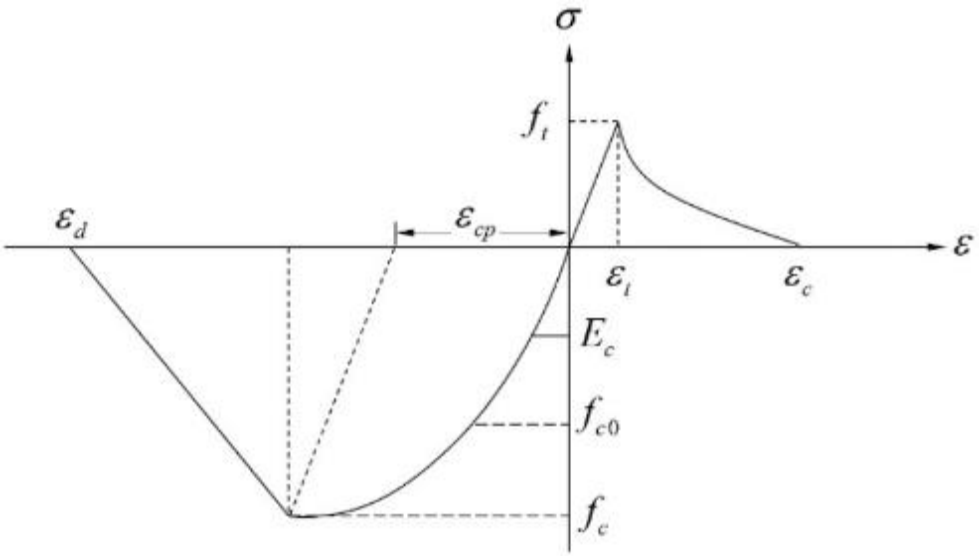

Figure 7.3 Stress-strain relationship for concrete in ATENA-3D.

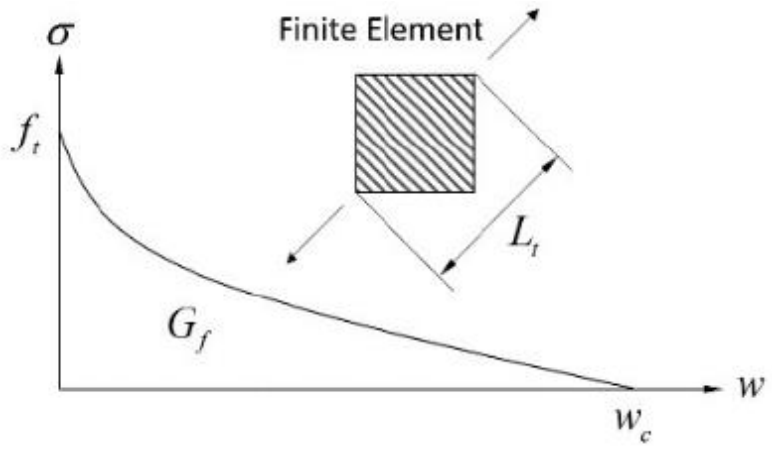

Figure 7.4 Tensile softening function and the crack band used in ATENA-3D.

It is worth mentioning that the combined fracture-plastic model in CC3DNonLinCementitious2 is included in ATENA. In addition, smeared or discrete bar element modelling rebars are possible in the ATENA environment. Thus, it is an easy-to-adopt model.

Figures 7.5 to 7.8 provide a concise overview of the Elasticity-Based Material Model (SBETA), the Fracture-Plastic Material Model, and the algorithm employed for creep and shrinkage analysis as incorporated within ATENA 3D.

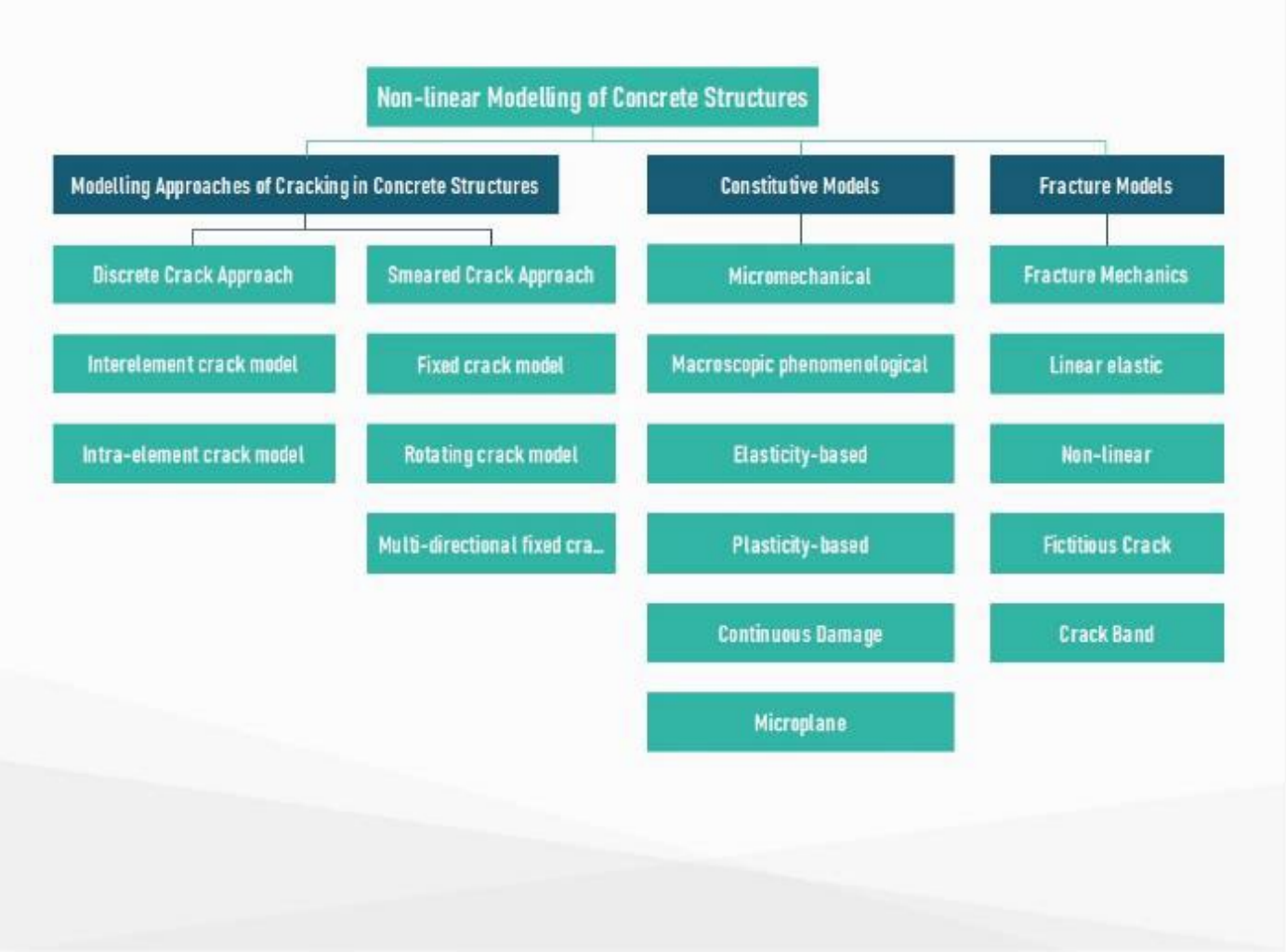

Figure 7.5 Cracking techniques, constitutive models, and fracture models for nonlinear modelling of concrete structures (Chong, 2004).

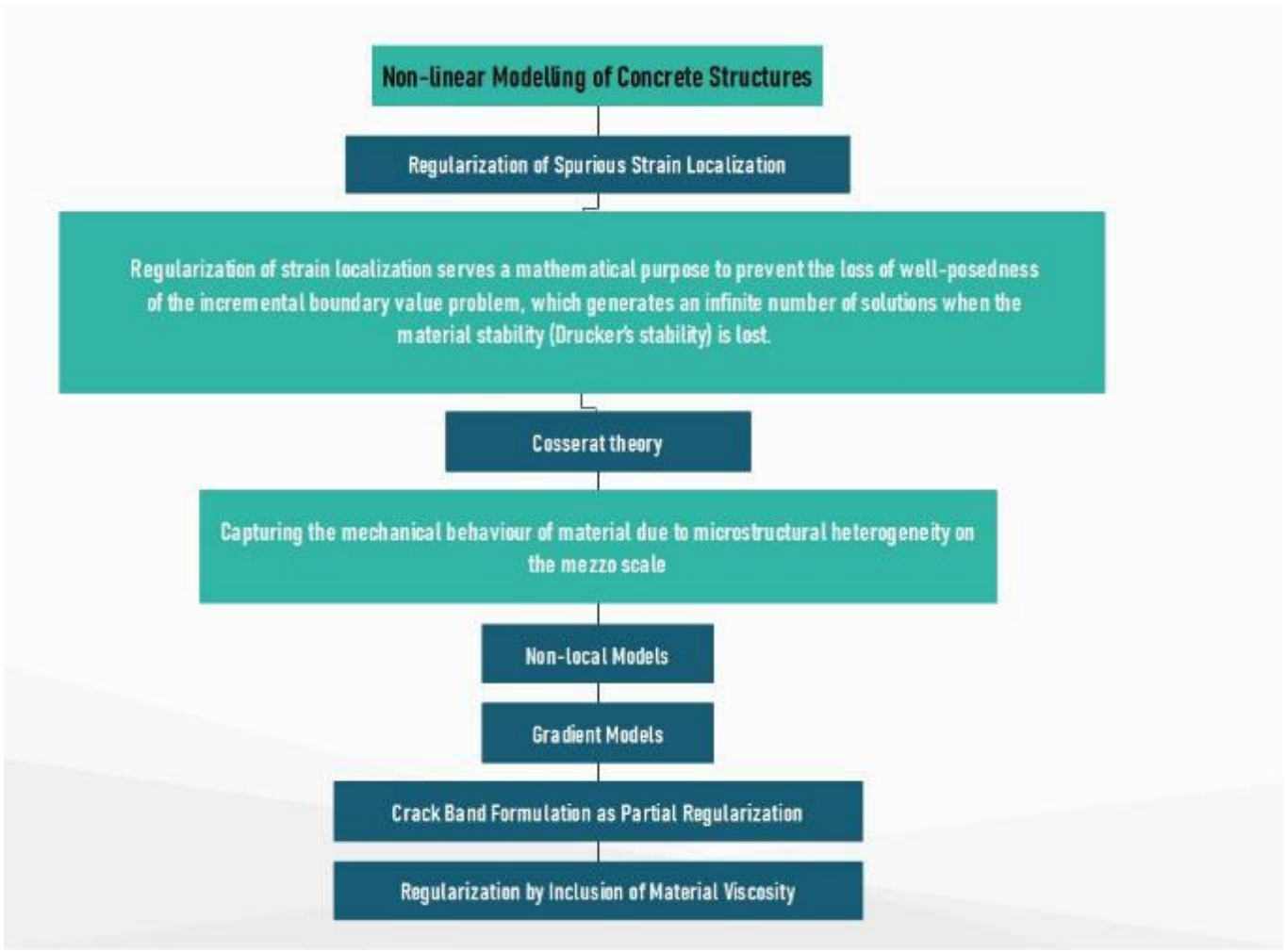

Figure 7.6 Regularization of spurious strain localisation inside nonlinear models of concrete structures (Chong, 2004).

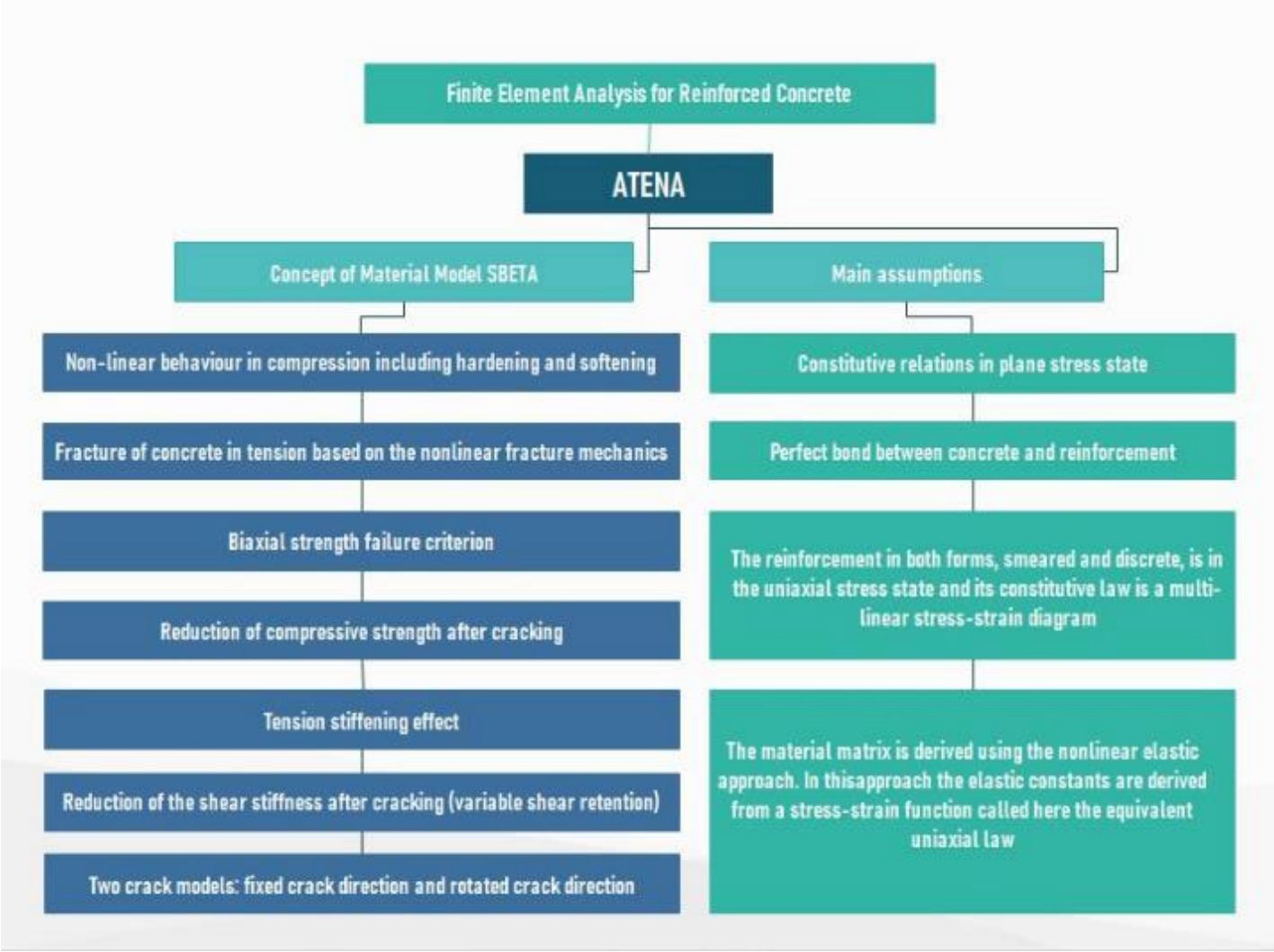

Figure 7.7 Constitutive model in ATENA (ATENA, 2012).

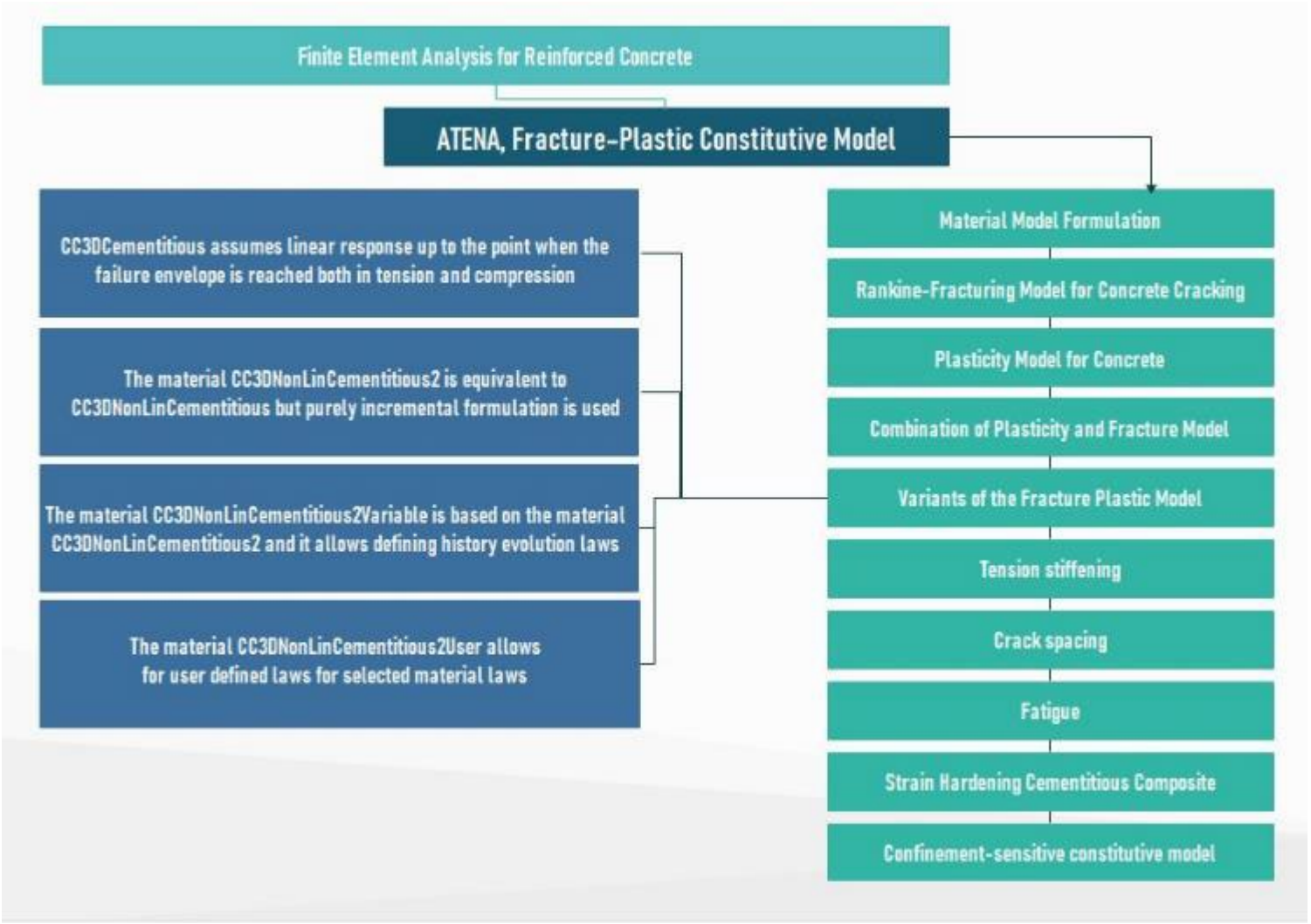

Figure 7.8 Fracture–Plastic Constitutive Model in ATENA 3D (ATENA, 2012).

7.4 VERIFICATION STUDIES

Analyses were conducted on three conventional reinforced concrete beams to verify the finite element model and evaluate the accuracy of the FEM model. As part of the structural level investigation, analyses were performed on three reinforced concrete beams with different failure modes, which were made and cast at UTS Tech Lab. The numerical model details the constitutive model for concrete and steel bars, as well as the simulation-based modelling technique. The experimental protocol outlines the fabrication and testing of a beam specimen.

7.4.1 Geometry and Materials

Three reinforced concrete beams with normal strength concrete were fabricated at Tech Lab of UTS University. The first beam was designed with three 12 mm longitudinal tensile bars to fail in flexural. To avoid the formation of localised diagonal splitting cracks across the shear span, stirrups were placed along the span, beyond the support, at a constant distance of 240 mm.

The second beam was designed to fail in compression. Two rows of 16 mm rebar were used in tension to ensure failure occurs in compression. Stirrups were also placed at a distance of 80 mm along the loading span. The third beam was made of three 16 mm tensile bars without stirrups to express the beam's performance in shear failure. The span of beams one and two is 3500 mm, while it was reduced to 3200 mm for the third beam. The schematic of the beam geometry is shown in Figure 7.9. Also, the cross-sectional details and steel bar details are provided.

Table 7.1 lists the concrete mix design. Three 150 × 300 mm cylinders were cast for each beam to determine the mean compressive strength f_c. Table 7.1 summarises the concrete's 28-day mean compressive strength results. The reinforced beams used

for this test were designed with the specifications shown in Figure 7.9 in accordance with AS 3600.

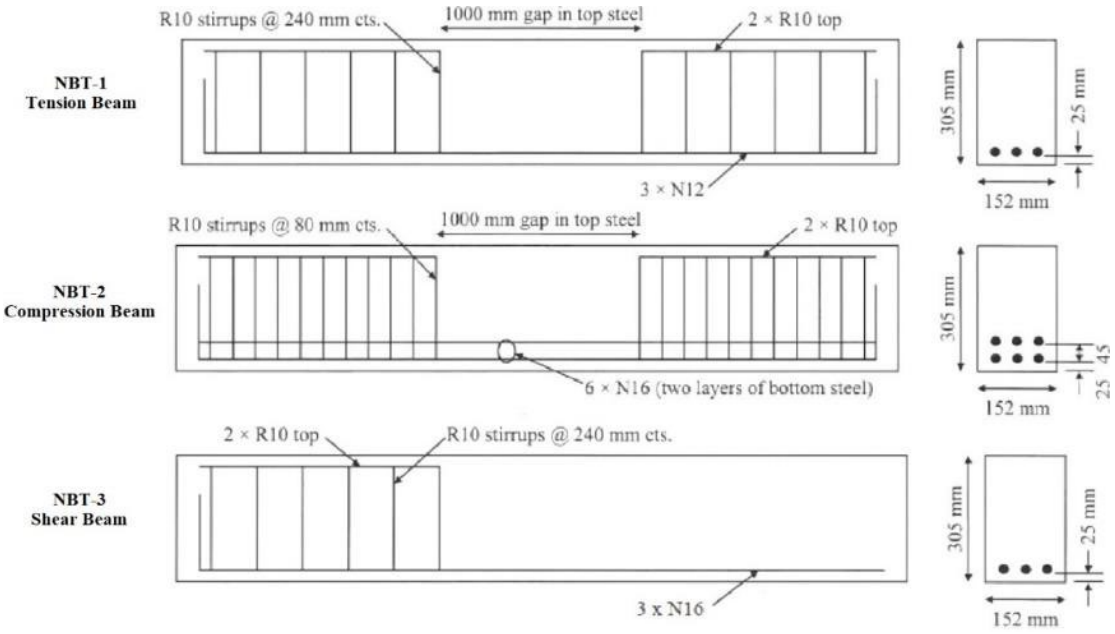

Figure 7.9 Structural details of beams.

Table 7.1 Summary of concrete mixture and compressive strength at 28 days

Water	***Cement***	***Aggregate***	***Sand***	f'_c
(Litre)	*(kg/m³)*	*(kg/m³)*	*(kg/m³)*	*(MPa)*
167	380	1130	549	38

7.4.2 General Structural Modelling

The beams were subjected to non-linear analysis using the finite element software ATENA-GID. The material properties and boundary conditions were assigned, and a geometrical model was made (Figure 7.10). The models were developed to be as close to the testing as possible. In GID, the reinforcement was modelled as a line, and volumes represent the three-dimensional regions. After the geometry was created, each volume was given a set of material properties, and boundary conditions were used to

specify supports and loads. Modulus of elasticity, Poisson's ratio, strength in direct tension f_t, and compressive strength f_c were defined as the basic concrete parameters.

Reinforcement bars and tendons were defined as 1D line elements. In order to prevent the initial post-tensioning stress from being focused at one node, bearing plates were assigned to both ends of the post-tensioned bars. Defining monitoring points is a crucial step in this analysis. During the analysis, the monitoring points were used to measure the evolution of load and deflection. Displacement in the middle of beams and the applied load at the top of the beam were monitored by defining monitor points. Initial loads resulting from gravitational forces and post-tensioning were manually inputted in different load stages. To maintain stability throughout analysis and limit the number of iterations required to solve each step, a minor displacement was used.

The analytical solver utilised the Newton-Raphson iterative solution with tangent stiffness and 1.0% residual force error. One monitoring point was defined in the centre of the beam to regulate deflection, and two monitoring points were represented at the location of the force application to measure the load reaction. The lower level of the beam has designated deflection monitoring points, while the higher level has designated force monitoring points. The computed load-deflection curve was compared with the experimental results.

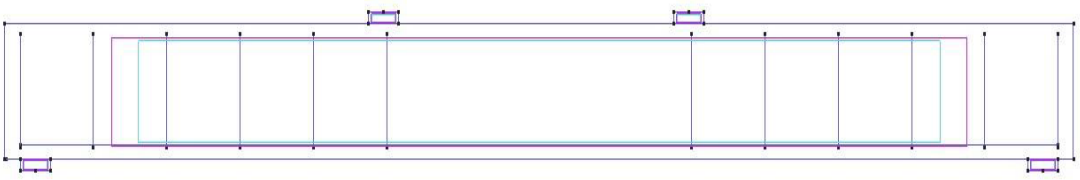

Figure 7.10 Geometrical model.

7.4.3 Material Modelling

Concrete

For the beam's concrete, CC3DNonLinCementitious2 material has been used to consider crushing, cracking, and plastic behaviour. Diverse stress states result in different material characteristics. CC3Dnonlinear, fracture-plastic material was used for concrete (Figure 7.11).

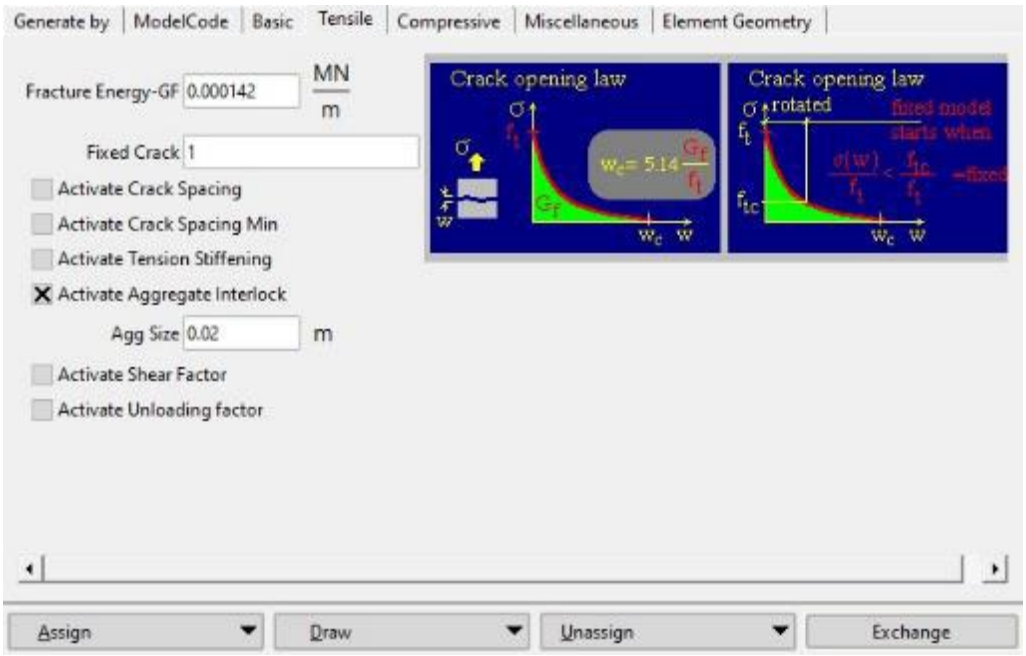

Figure 7.11 Material properties for CC3DNonLinCementitious2 (ATENA, 2012).

Steel plates

In experimental tests, steel profiles have been employed in the places of force application to prevent the development of excessive strains in the loading regions. The linear material "CC3DElastIsotropic" with an elasticity modulus of 200 GPa was used to represent the steel plates at the loading sites and supports. Support and loading steel plates were modelled with elastic isotropic materials and in three dimensions on the presumption that steel plates were rigid. They are represented identically by steel plates with dimensions of 75 mm in width and 40 mm in thickness in FE modelling. The steel

plates in the loading areas and supports are assumed to be rigid and defined in 3D with isotropic elastic material (Figure 7.12).

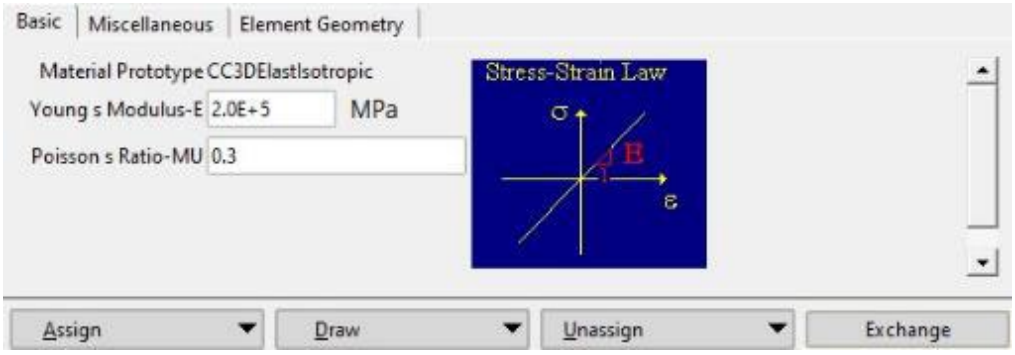

Figure 7.12 Material properties for CC3DNonLinCementitious2 (ATENA, 2012).

Reinforcing bars

Rebars were defined one-dimensionally in concrete as a discrete bar element modelling. Without considering strain hardening, 'CCReinforcement' elastic fully plastic bar was utilized as reinforcing bar material. Figure 7.13 depicts a multi-linear plastic stress-strain relationship for reinforcement bars.

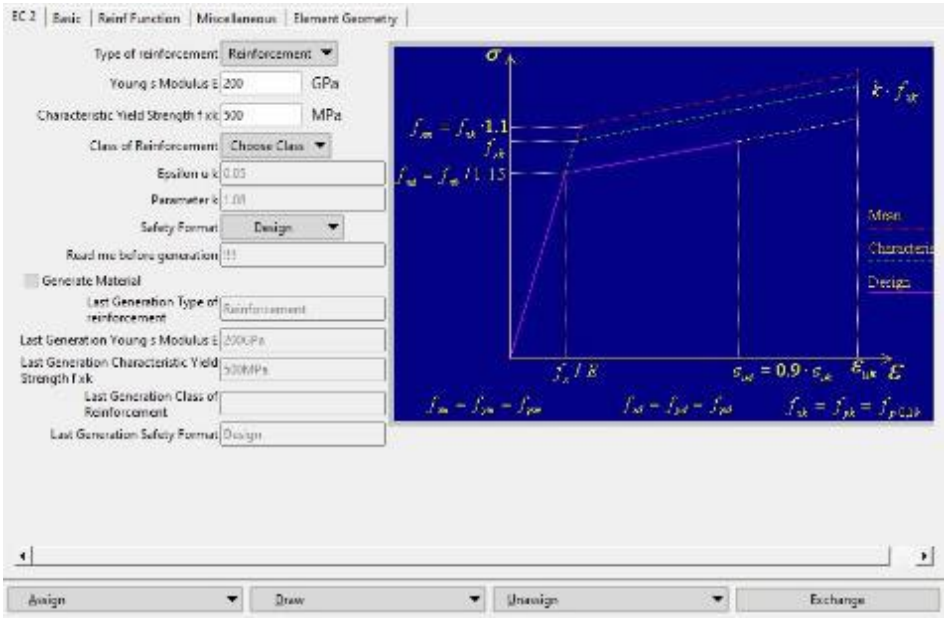

Figure 7.13 Material properties for CC3DNonLinCementitious2 (ATENA, 2012)

7.4.4 Meshing Properties

Three-dimensional solid linear tetrahedral components with three degrees of freedom per node modelled the concrete slab and steel plates. In beam modelling, 8-node hexahedral elements were used, and 50 mm meshes were chosen for the beam. The plates were meshed by default, and tetrahedral elements were employed. The number of numerical calculations was drastically decreased by using four-point linear tetrahedral components rather than 10-point quadratic elements, and as a consequence, processing performance was increased. The element's size in this modelling can only be a maximum of 60 mm. Boundary conditions and beam meshing are shown in Figures 7.14 and 7.15.

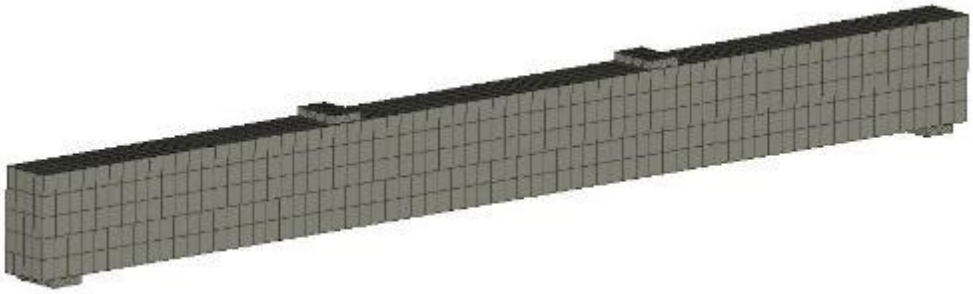

Figure 7.14 Generation of mesh.

7.4.5 Boundary Conditions

The bond-slip connection between the contact surface of the rebar and the surrounding concrete can be defined manually. In this modelling, it was assumed that the rebar and the concrete connection were perfect. Therefore, the bond-slip was not taken into account. In this analysis, longitudinal rebars were accounted for compressive and tensile only.

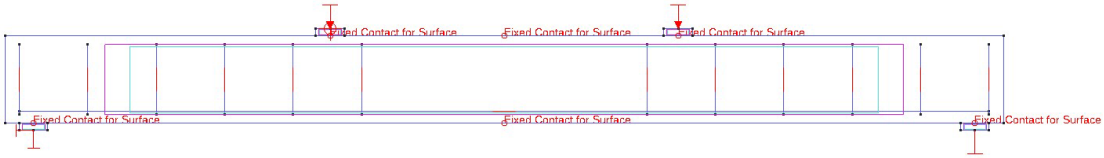

Figure 7.15 Support conditions and boundary conditions of reinforced concrete beam.

7.4.6 Loading Intervals

In modelling, the force has been delivered to the beam using a displacement control mechanism, similar to loading in actual experiments. At each displacement increment, the two-point applied loads on the beam's top surface, and the beam's deflection in the centre of the span have been observed. The force has been applied to the beam in the form of a one-millimetre displacement in each step.

7.4.7 Comparison of Simulation and Test Results

Flexural failure occurred in beam NBT-1. Near the beam's midsection, a major flexural fracture propagated virtually straight from the tensile portion to the compression chord. Low-reinforcement beams are characterised by yielding and tensile failure of the reinforcing bars, which caused the eventual collapse.

The failure of the NBT-2 beam occurred in crushing failure mode. The crack occurred at the top chord of the beam. The collapse in this mode is more similar to failure in the shear mode. The NBT-2 beam showed much higher stiffness than the NBT-1 beam. The ultimate load in this beam was the highest among all three beams.

As seen in Figure 7.19, the third concrete beam, NBT-3, collapsed due to shear fractures without reinforcing yielding. A shear fracture proceeded from the bottom to the top of the beam, dividing it into two blocks that were only linked by the longitudinal reinforcement, which was in the elastic regime. The geometry of the crucial fracture

precluded the use of any other load-bearing device. After the peak load, a vertical decline in load-carrying capacity was found.

Figure 7.16 depicts the reaction of the NBT-3 beam's midspan deflection to a load. Bilinear behaviour was seen until the ultimate load of 128 kN, after which shear fractures appeared in the area between the external support and the applied load, causing a dramatic decline in load capacity. NBT-3 was much more rigid than NBT-1. As a result, the mid-span deflection of NBT-1 at the ultimate load was less than the values obtained for NBT-1 and NBT-2.

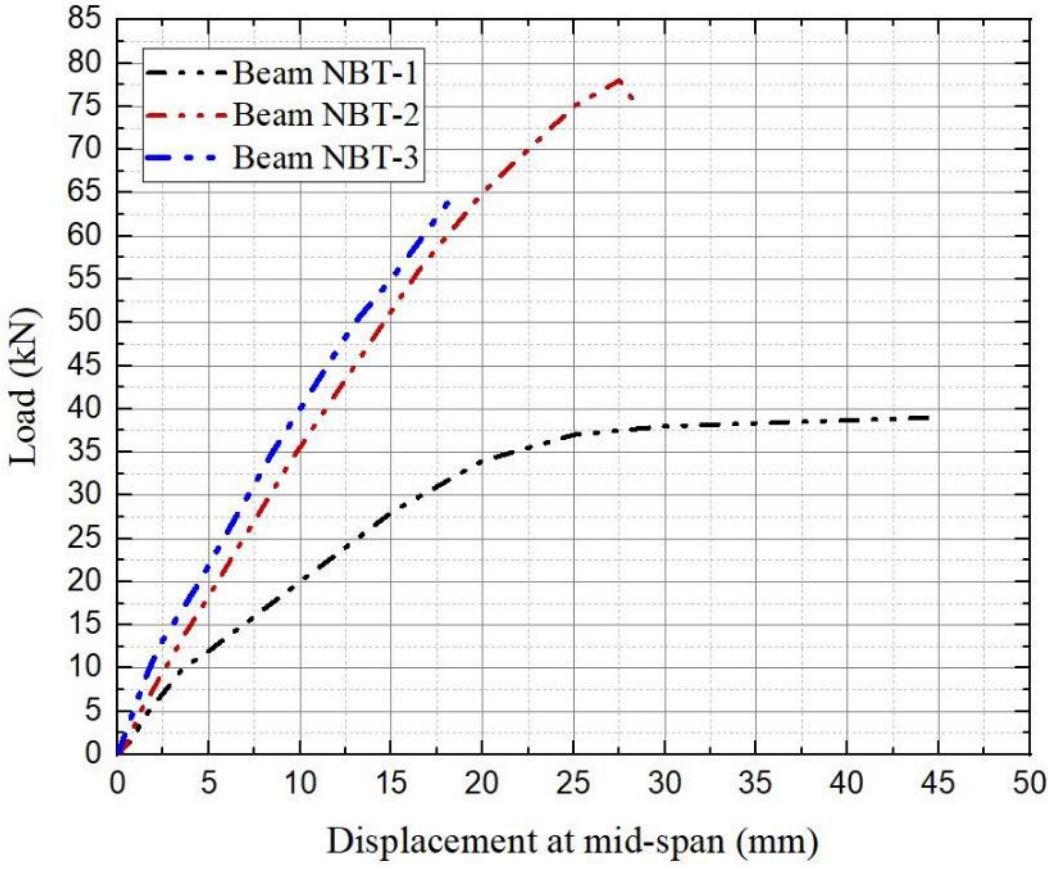

Figure 7.16 Load-deflection curves for different concrete beams conducted experimentally.

Table 7.2 provides a summary of the computational and experimental findings for reinforced beams. The outcomes comprised the experimental ultimate load ($P_{u,Exp}$) and the associated mid-span deflection ($\Delta_{u,Exp}$), the numerically calculated ultimate

load ($P_{u,FE}$) and the corresponding mid-span deflection ($\Delta_{u,FE}$), the failure mode, and the accuracy of the numerical results. Using Equation (7.10) as specified, the ductility index (Δ) was calculated (Akbarzadeh and Maghsoudi 2010). In addition, the stiffness (K) was estimated in line with (Park, 1989) using the equation (7.11).

$$\Delta = \frac{\Delta_f}{\Delta_y} \tag{7.10}$$

$$K = \frac{P_{0.75}}{\Delta_{0.75}} \tag{7.11}$$

Where Δ_y and Δ_f are the mid-span deflection at yield and failure, respectively.

The load level at 75% of the ultimate loads is $P_{0.75}$, and the mid-span deflection is $\Delta_{0.75}$.

The crack pattern for specimen NBT-1 and the stress distribution in the rebar members are depicted in Figures 7.17 and 7.18, respectively.

Table 7.2 Experimental versus finite element results for reinforced beams with different failure modes

Specimen ID	*Experimental*		*Finite element*		*Failure mode*	$\frac{P_{u,Exp}}{P_{u,FE}}$	$\frac{\Delta_{u,Exp}}{\Delta_{u,FE}}$	$\frac{P_{0.75}}{\Delta_{0.75}}$
	$P_{u,Exp}\ (kN)$	$\Delta_{u,Exp}\ (mm)$	$P_{u,FE}\ (kN)$	$\Delta_{u,FE}\ (mm)$				
NBT-1	38.96	44.87	38.25	47.43	Tension	1.02	0.95	2.28
NBT-2	78.05	27.38	78.68	25.93	Compression	1.00	1.06	3.35
NBT-3	65.12	18.42	65.24	18.69	Shear	1.00	0.99	3.90

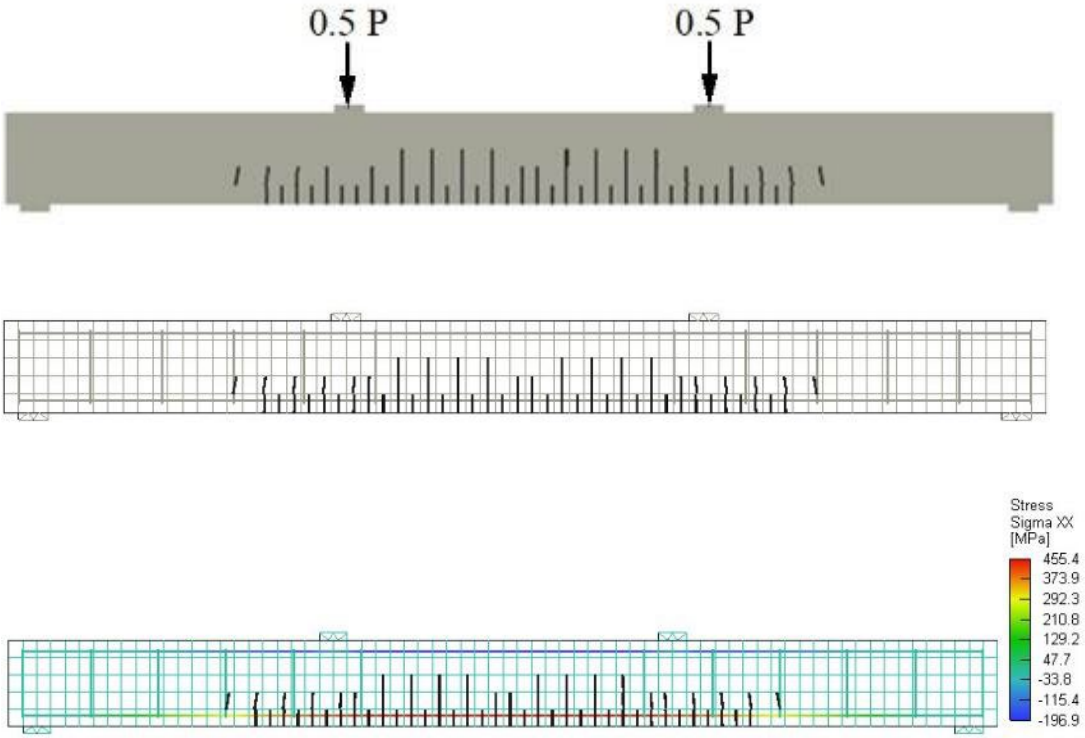

Figure 7.17 Crack pattern for specimen NBT-1.

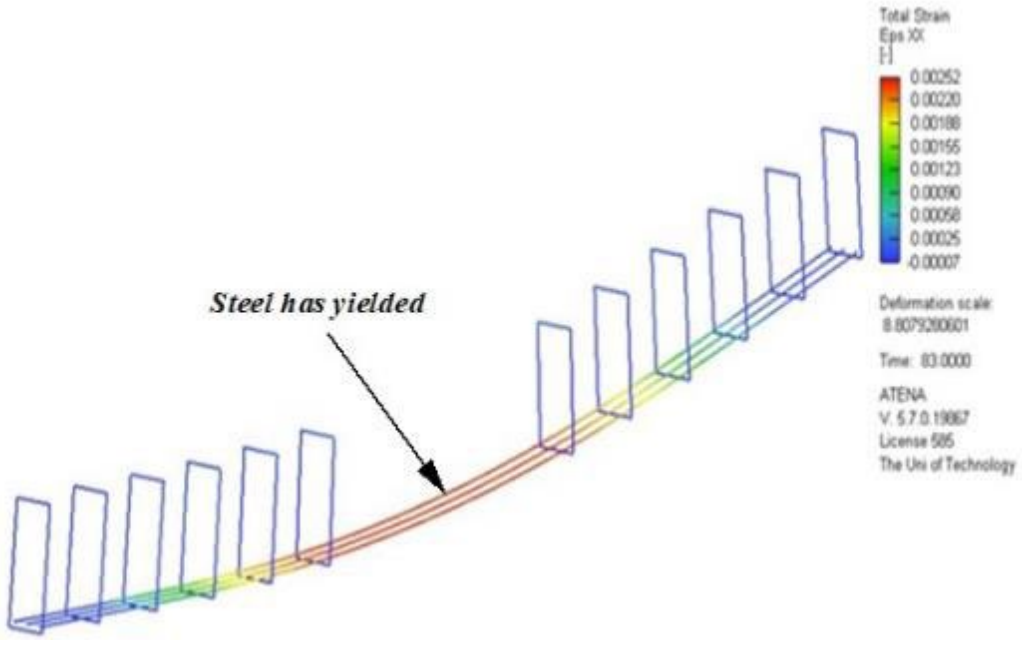

Figure 7.18 Principal stress of rebar members at their maximum.

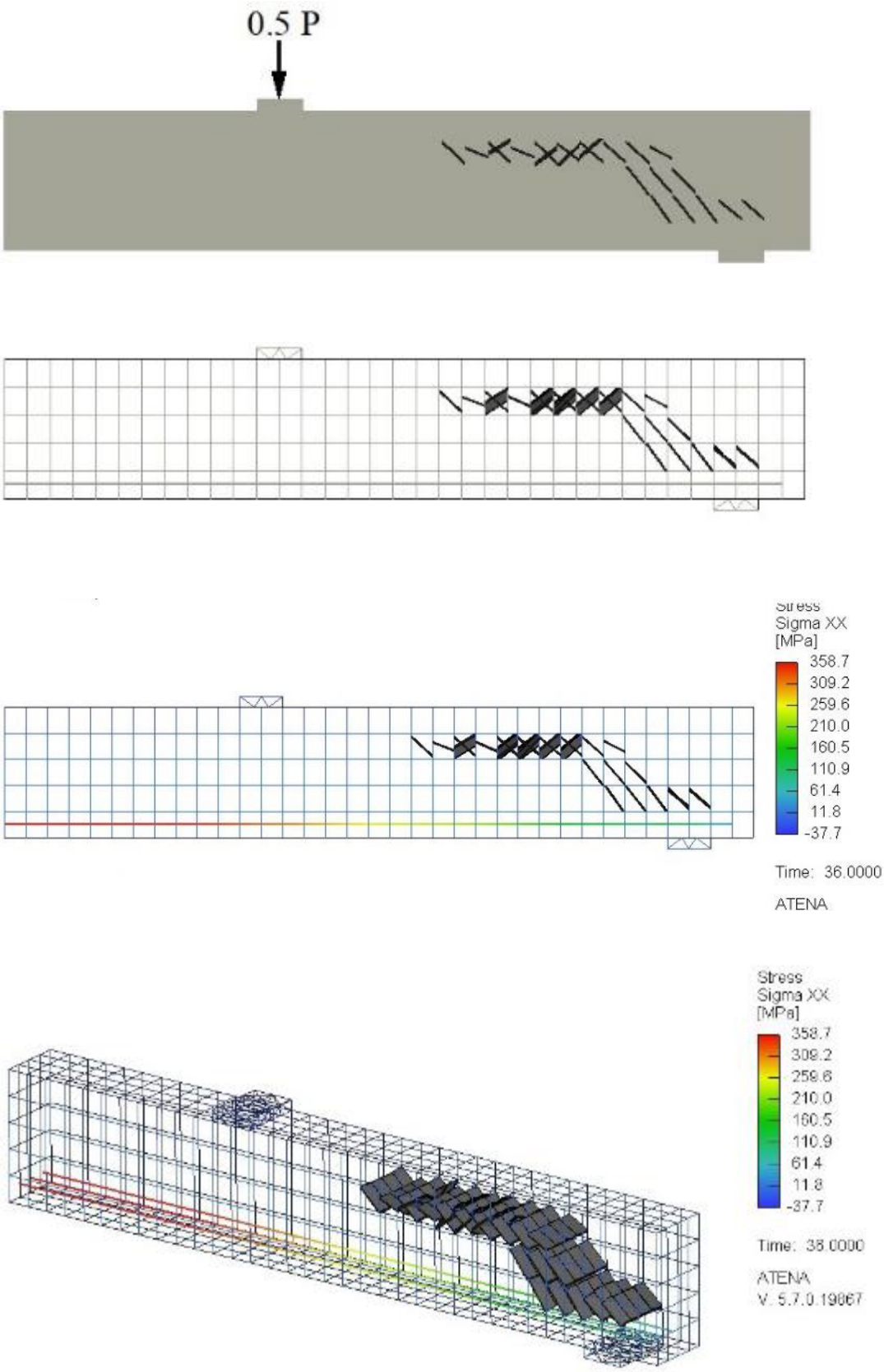

Figure 7.19 Crack pattern for specimen NBT-3.

A comparison is made between the experimental load and deflection curve and the ATENA load and deflection curve. Three critical points have been chosen for comparison: ultimate load, yielding load, and cracking load. The numerical/experimental ratios were analysed and shown in Table 7.3 in order to verify the precision of the numerical model. According to the table, the ratios of numerical to experimental load values range between 0.95 and 1.06 for the maximum load. It implies that the numerical model accurately predicts the experimental values, which are in excellent agreement with them.

In the NBT-1 beam, the tensile steel reached the yield stress at the moment $M_{y,}$ which was somewhat less than the ultimate moment M_u. In this case, tensile steel yield occurs before the compressive capacity of the concrete is reached (Figure 7.20). In contrast, the failure mode for NBT-3 was shear. The failure occurred suddenly. As shown in Figure 7.21, the failure happened before the steel reached the yield point.

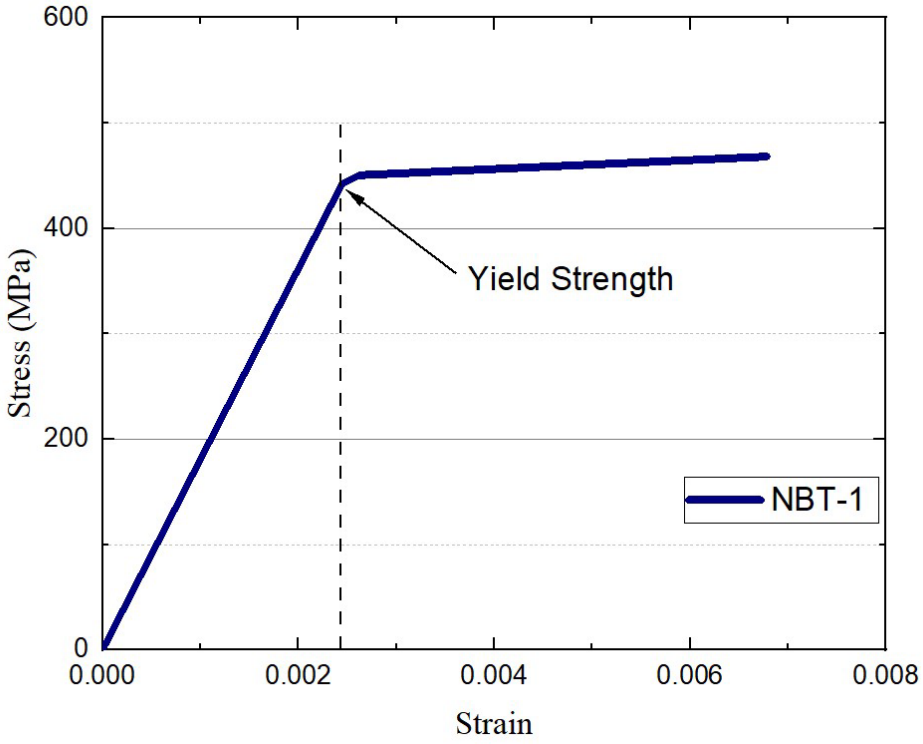

Figure 7.20 Stress-strain curve for reinforcement bar of NBT-1.

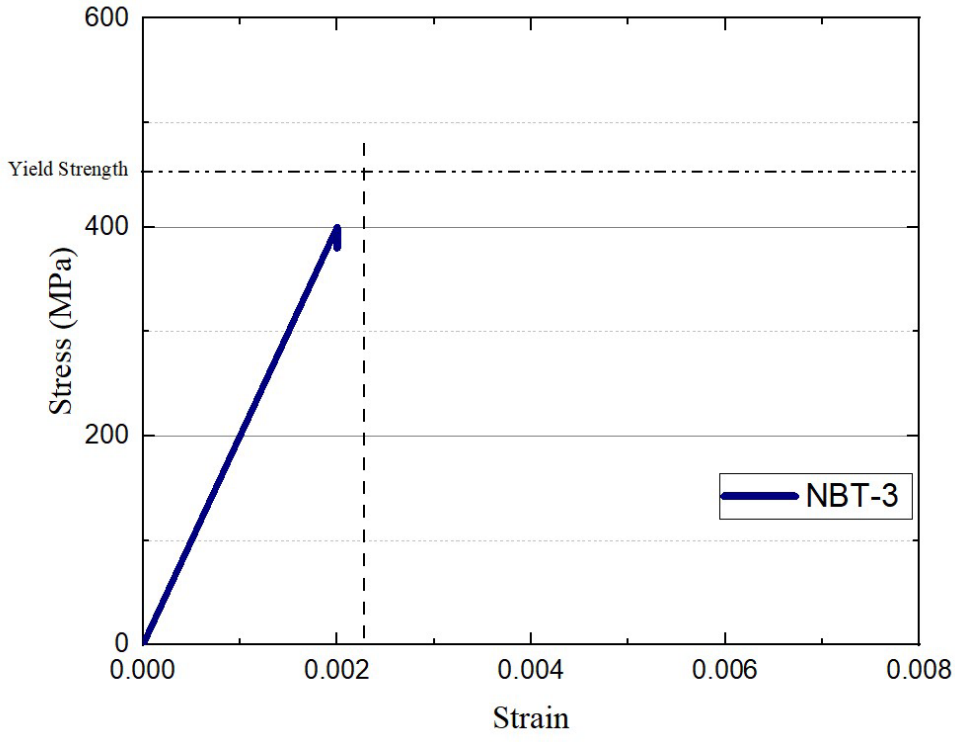

Figure 7.21 Stress-strain curve for reinforcement bar of NBT-3.

The comparison of FEM data reveals that the similarity between simulation and experimental results in terms of load and deflection curve is more than 90%. The comparison of load-deflection curves derived by the ATENA 3D application validates the accuracy of the 3D finite element modelling. Figures 7.22 to 7.24 compare all specimens' simulated load-deflection curves to experimental load-deflection curves.

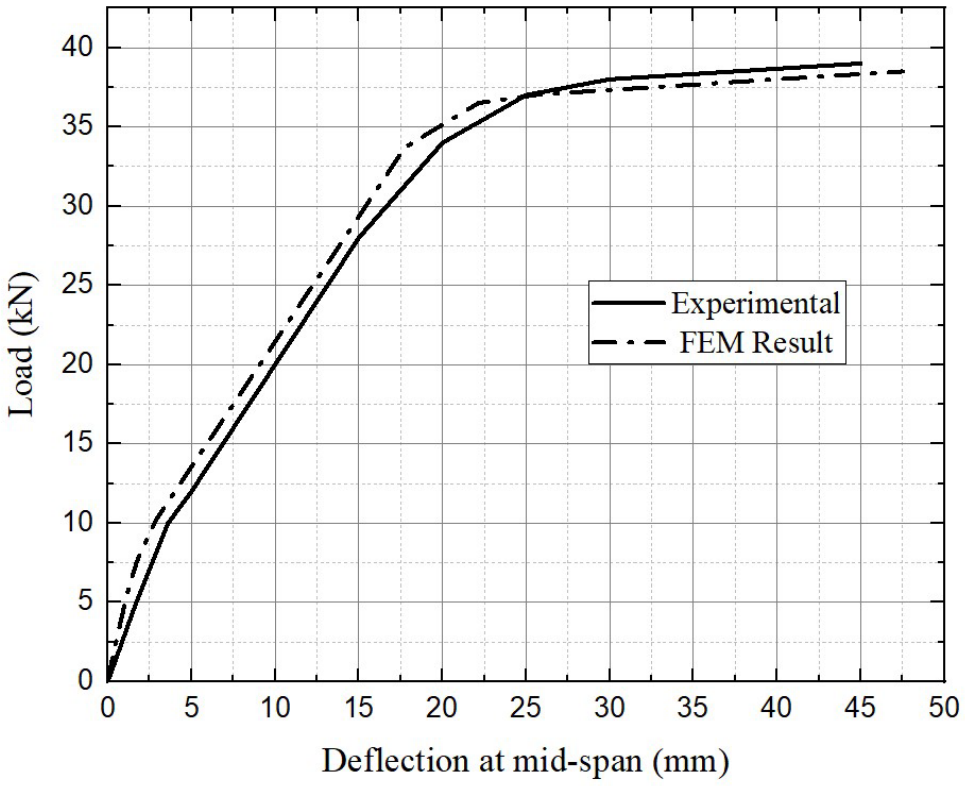

Figure 7.22 Comparison of experimental and numerical results of mid-span deflection versus applied load of NBT-1.

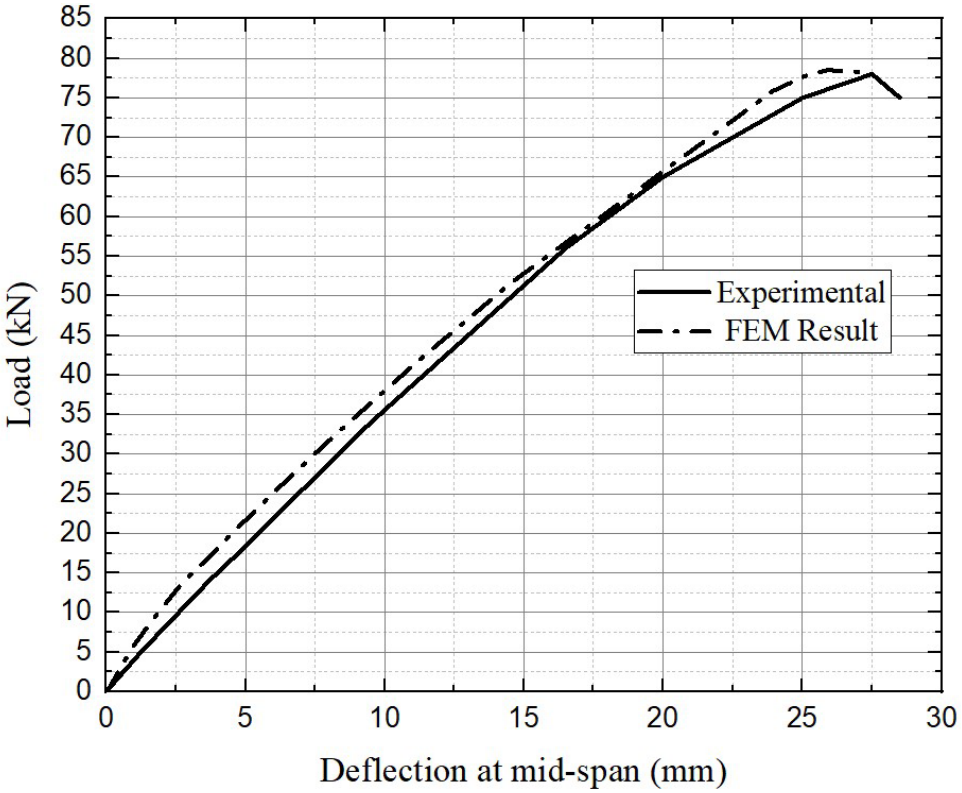

Figure 7.23 Comparison of experimental and numerical results of mid-span deflection versus applied load of NBT-2.

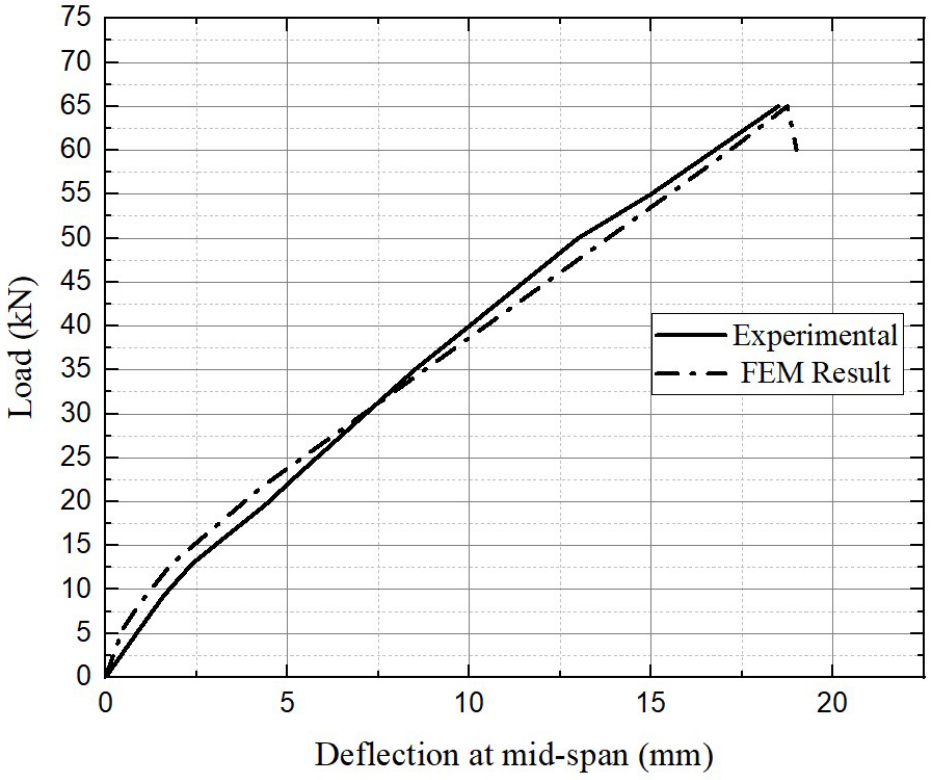

Figure 7.24 Comparison of experimental and numerical results of mid-span deflection versus the applied load of NBT-3.

In general, the numerical findings of all beams' fracture patterns were somewhat comparable to the experimental data. In addition, the relationship between load and deflection closely matches experimental data.

The FE model crack patterns of specimens represent three failure modes (Tension, compression and shear failure, respectively). They were compared with the experimental observations of the different failure modes in Figures 7.25 to 7.27.

Table 7.3 Parameters for constitutive concrete model in ATENA

Parameters	Value
Young's Modulus, E (MPa)	32,338
Poisson's ratio, v	0.2
Cylinder compressive strength, fc (MPa)	-41.4
Tensile strength	4.0
Fracture energy	7.02×10^{-5}
Critical compression displacement	-0.0005
Plastic strain at compressive strength	-0.002
Smeared crack model	Fixed
Shear factor	20
Reduction of concrete strength due to cracking	0.8
Tension stiffening multiplier	0.25
Aggregate interlock	0.02

Figure 7.25 provides a comparison of crack patterns for the experimental and modelling of beam NBT-1.

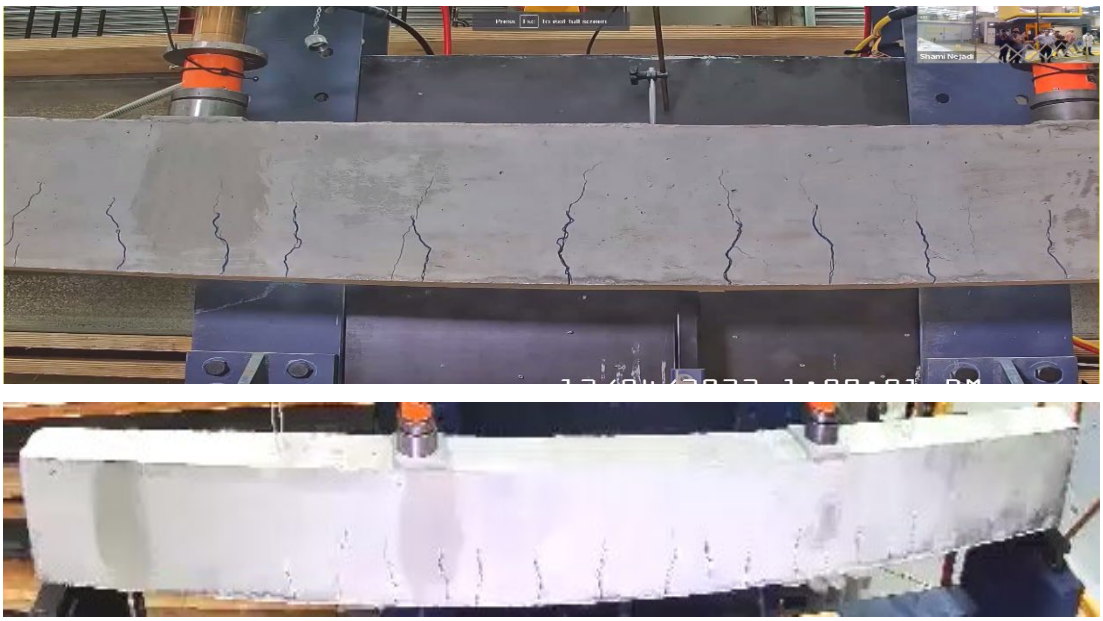

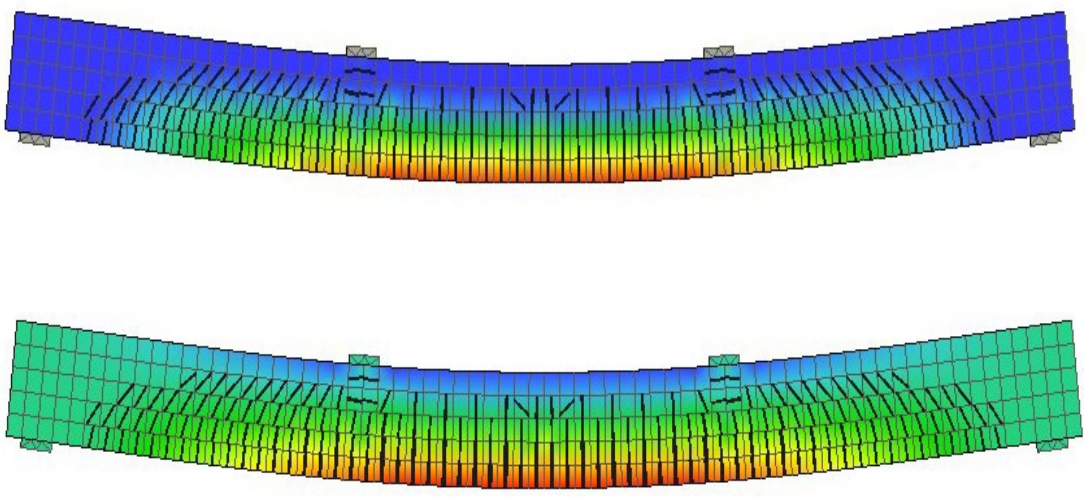

Figure 7.25 Maximum principal strain and crack patterns of beam NBT-1.

Figure 7.26 compares crack patterns for the experimental and numerical compression failure of the NBT-2 beam.

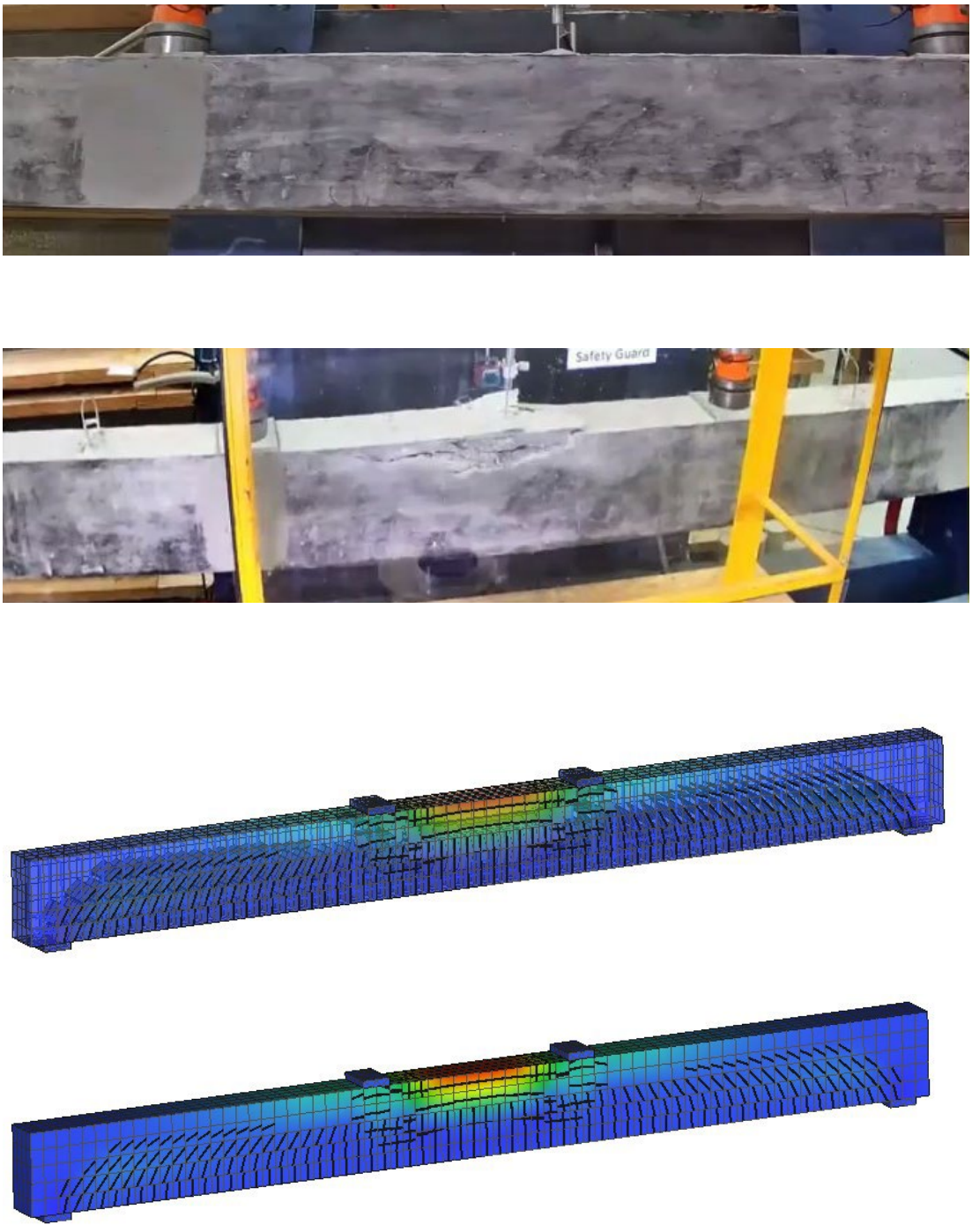

Figure 7.26 Maximum principal strain and crack patterns of beam NBT-2.

Figure 7.27 compares crack patterns for the experimental and modelled shear failure in the NBT-3 beam.

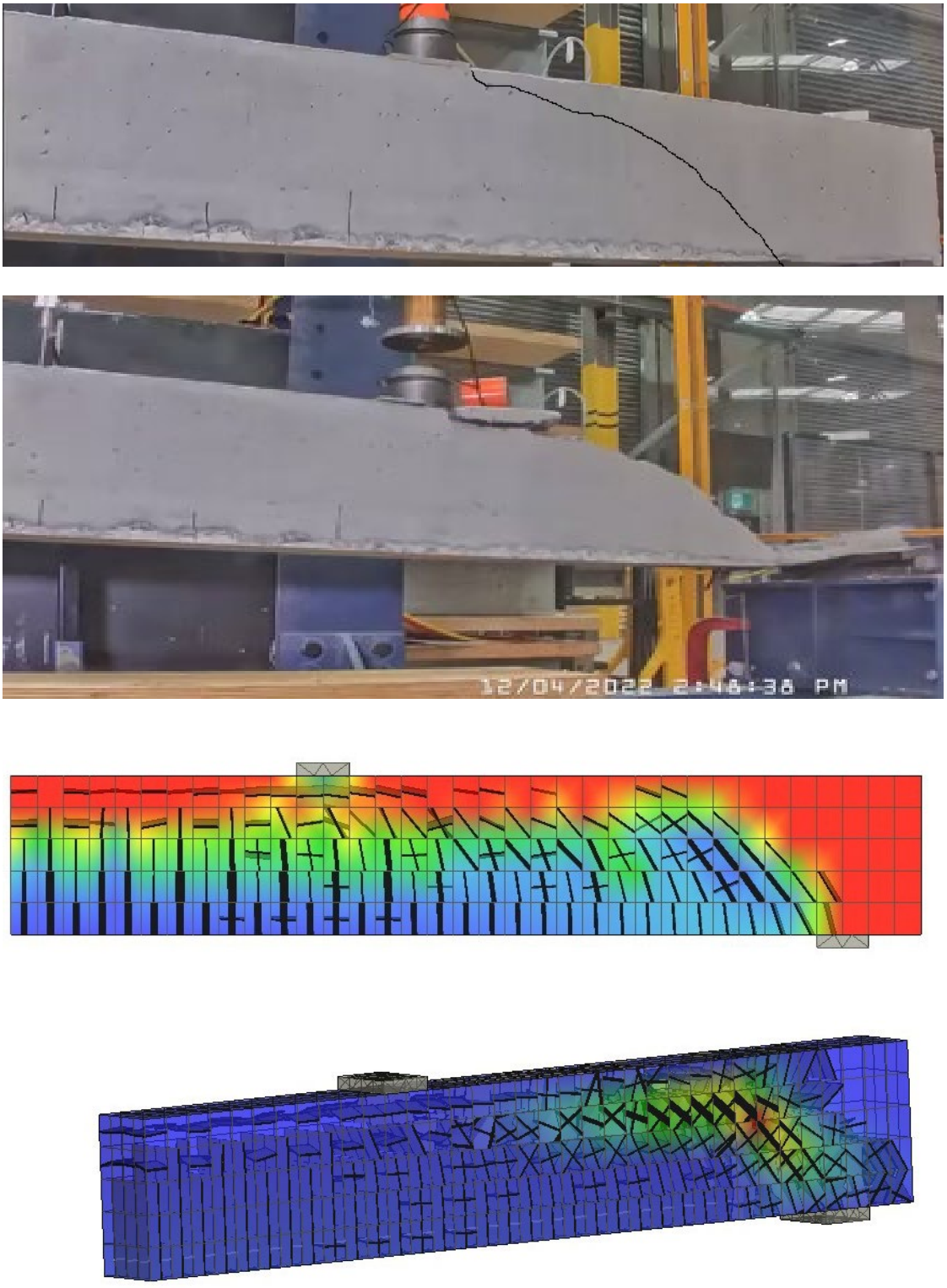

Figure 7.27 Maximum principal strain and crack patterns of beam NBT-3.

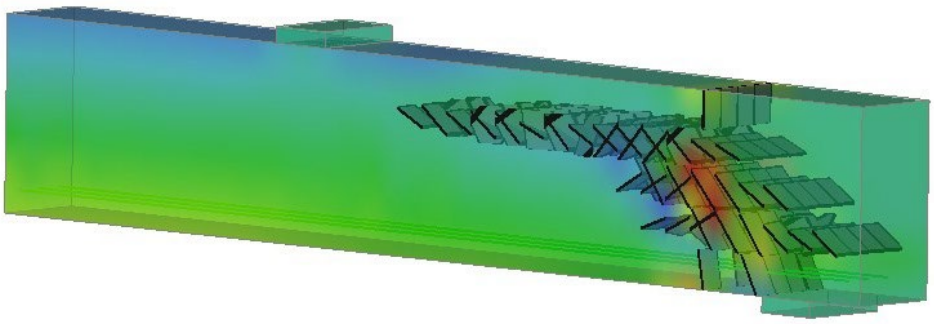

Figure 7.28 Crack patterns of beam NBT-3.

In general, the numerical findings of fracture patterns in all beams were comparable to the experimental data. In addition, the load versus deflection relationship closely matches experimental findings.

7.5 FE SIMULATION OF ASR-AFFECTED PRESTRESSED CONCRETE BEAM

Material properties of companion specimens were used as the input parameters for concrete properties. Smeared cracking was the fundamental concept used in the current finite element modelling (Červenka, Jendele et al. 2000). The 8-node basic built-in solid element CC3DNonLinCementitious2 was used to model the concrete. Concrete's fracture theory was based on Figure 7.3's illustration of the uni-axial stress-strain law. Before cracking, it is assumed that the behaviour of the concrete under tension is linear elastic, and a fictional crack model based on a crack-opening law and fracture energy is used to characterise tension after cracking. The CEB-FIP Model Code 2010 (Code 2010) formula for the ascending branch of the concrete stress versus strain equation in compression was accepted.

The constitutive model for steel bars in ATENA was a multilinear curve, as seen in Figure 7.13. Therefore, modelling takes into account several steel behaviour phases, such as the elastic phase, yielding, and final fracture. The longitudinal steel and vertical

stirrups were modelled using the 'CCReinforcement' built-in truss element. It was supposed that steel bars and concrete were completely bonded. The investigation also modelled steel plates at the support and loading sites using a linear-elastic method.

The standard Newton-Raphson solver was used to complete the study, and a 50 mm finite element mesh size was determined to be optimal.

7.5.1 Self-weight Loading

In the first interval, the weight of concrete and steel bars was manually calculated and uniformly applied through the span.

7.5.2 Prestressing Load

As shown in Figure 7.29, the finite element analysis results show an upward deflection of the prestressed concrete beams after post-tensioning Macalloy bars.

The stress in the post-tensioning bar after prestressing load is reached 130.1 MPa. At the Post-tensioning stage, the stress in the concrete due to prestress load at the end of the beam was estimated between 0.03 and 3.80 MPa in tension and compression, respectively. The generated stress for the beam's section due to prestress load was between 0.63 and 3.4 MPa in compression.

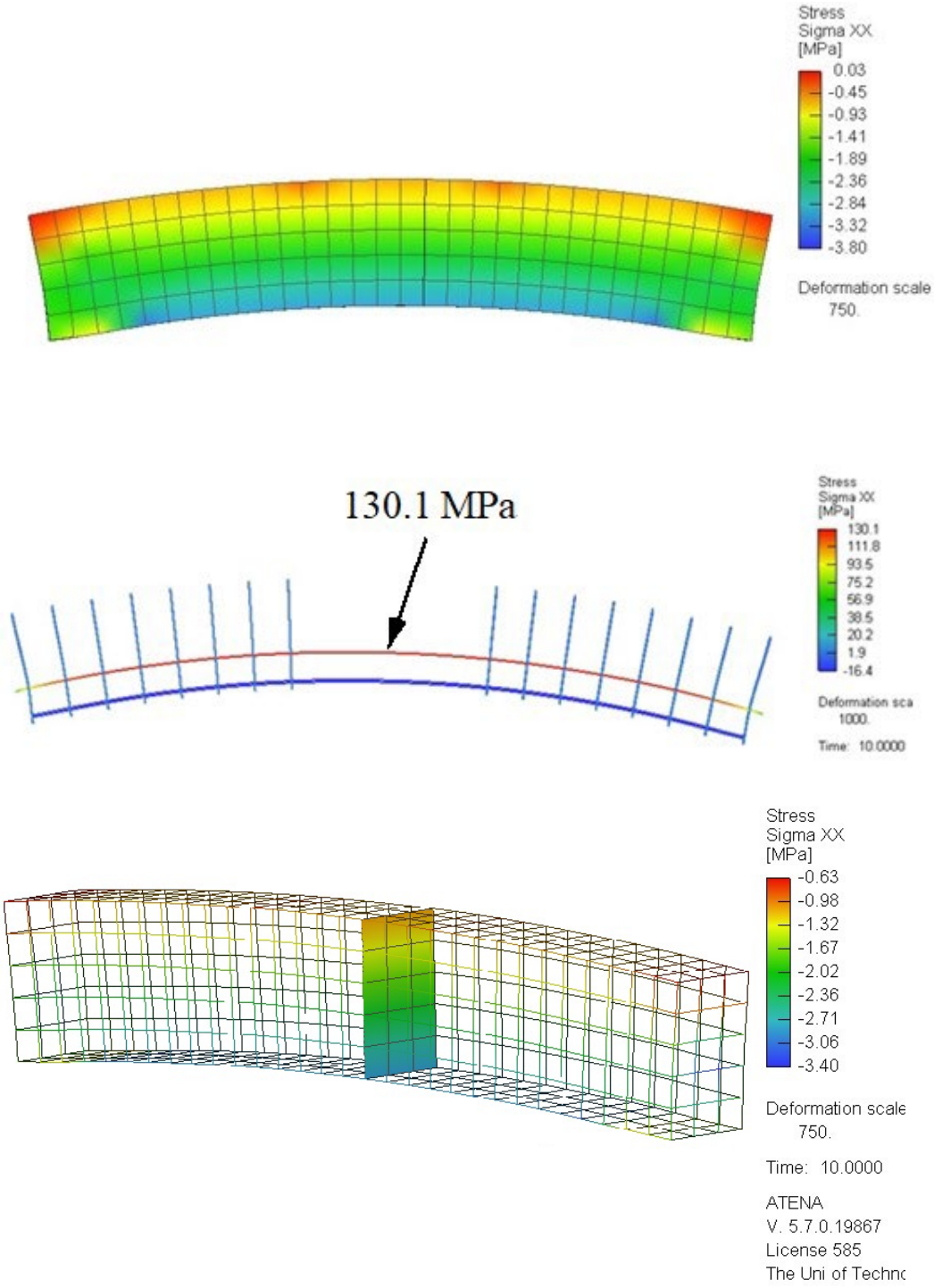

Figure 7.29 3D Modelling of the beam due to prestress only.

7.5.3 Applying ASR Volume Strain

According to the constitutive model discussed in chapter 4, ASR volume expansion was applied considering different factors including, kinetics of reaction, the effects of relative humidity, alkali/silica mixture concentration, aggregate size and

type, externally applied stress, and ambient temperature. By using element initial strains, the ASR strains were implemented (Figure 7.30).

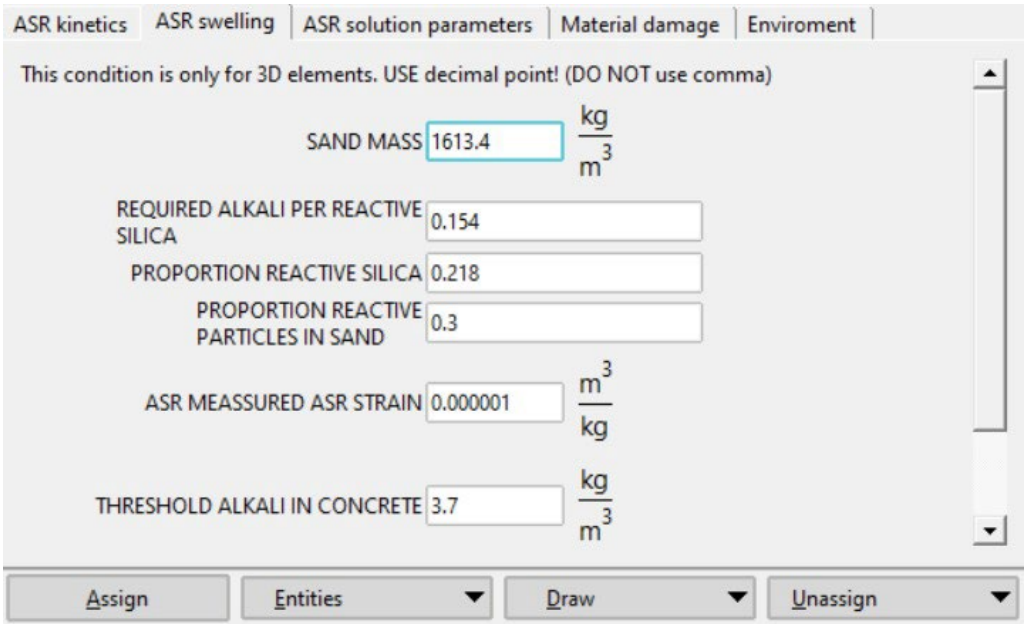

Figure 7.30 ASR volume expansion in ATENA 3D.

7.5.4 Under Four-point Load Test

In the next interval, two-point loads are applied to measure the flexural capacity of the beam (Figure 7.31). In this analysis, displacement has been carried out progressively to failure at a rate of 0.1 mm at every step.

The high strength bar was reached to 762 MPa stress at the ultimate load. Also, two reinforcing bars were yielded. The maximum calculated load was 205 kN for each point which is equal to 91 kN-m ultimate moments. The cracking patterns and deformation are provided in Figures 7.32 and 7.33.

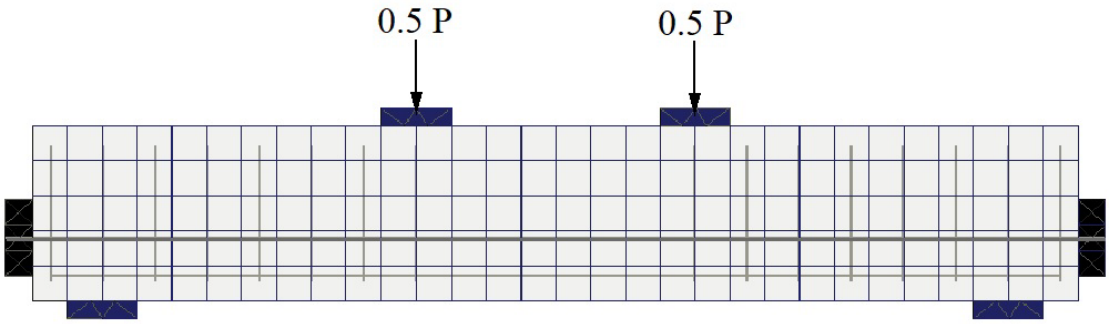

Figure 7.31 Four-point loading beam modelling.

The supports and load point used in the test setup reflected a simply supported beam with the maximum bending moment and shear force at one-third of the span. The loading was applied in load control and held at various load points for monitoring crack deformations. The final step of loading to failure was carried out in stroke control at a rate similar to the rate during the initial loading period. The command loop ensured each cylinder's load was equal throughout the loading period.

The force has been delivered to the beam using a displacement control mechanism, similar to loading in actual experiments. At each displacement increment, the two-point applied loads on the beam's top surface, and the beam's deflection in the centre of the span have been observed. The force has been applied to the beam in the form of a one-millimetre displacement in each step. Loading was applied until the specimens' maximum load-carrying capacity was reached.

Figure 7.33 depicts beam characteristics including deformation, failure pattern, and propagation of fractures inside the beam under stress.

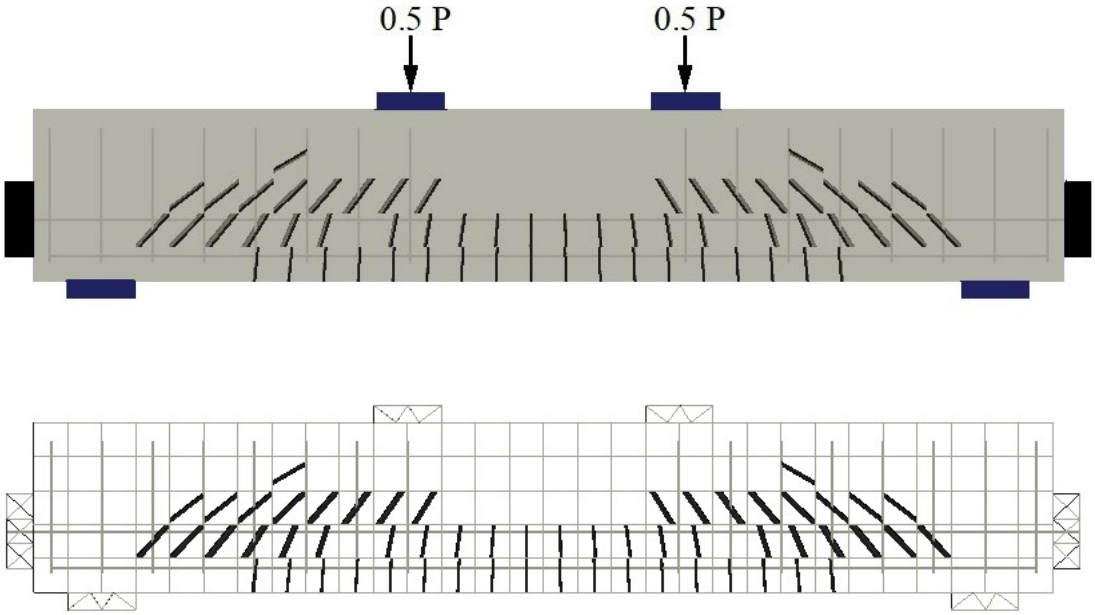

Figure 7.32 Crack patterns at yielding and maximum load.

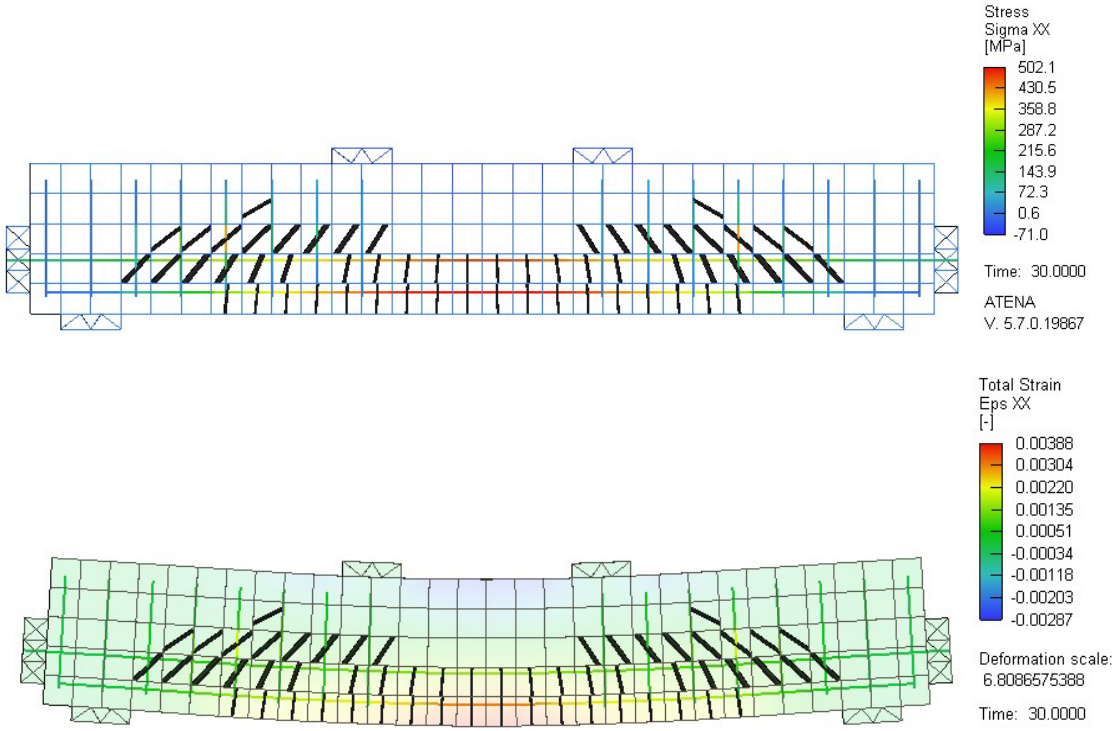

Figure 7.33 Deformation, stress and strain of beam at failure.

7.6 FE SIMULATION OF ASR-AFFECTED PRESTRESSED CONCRETE BRIDGES IN VICROAD

To help determine the effect of ASR on the flexural capacity of the beams, analysis was conducted on rectangular prestressed concrete bridge girders. A prestressed bridge beam was modelled as part of the load-carrying capacity assessment of ASR-affected prestressed structures (Figure 7.34). This was one of the initial standard precast prestressed concrete bridge beam components used in Victoria. The bridge's length is 4.5 metres, and the material properties is provided in Table 7.4 and depicted in Figure 7.35.

Table 7.4 Concrete core compressive strength and elastic modulus

Compressive strength (MPa)	Elastic modulus (MPa)
48	29000

Assuming the beams are exposed to ASR, the beams are modelled for different stages of damage due to ASR. In this modelling, after applying the ASR effect, the beams have been subjected to 4-point loading tests. The ultimate strength, ductility, and deflection of the damaged beams at different ages have been investigated in this analysis.

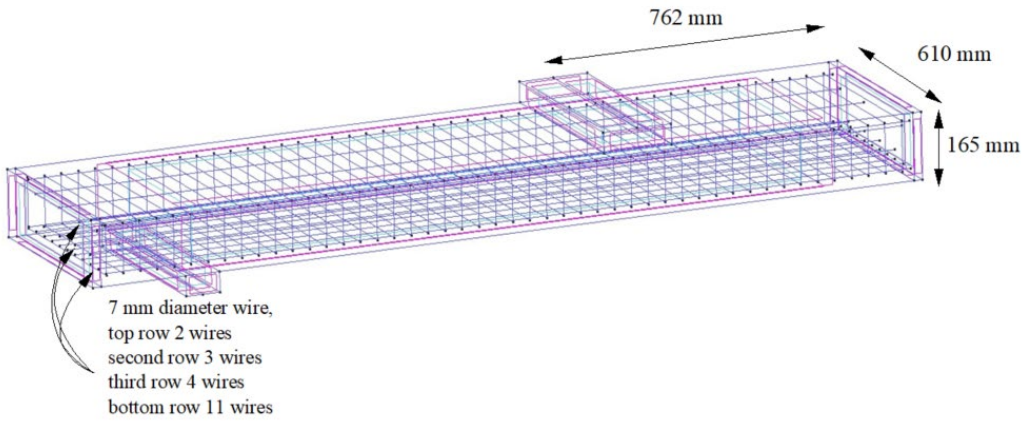

Figure 7.34 Geometry and details of the prestressing wire and loading point.

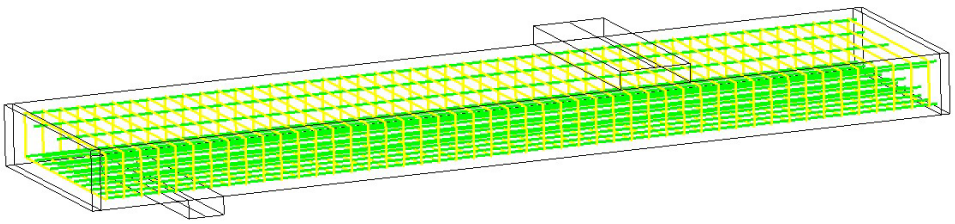

Figure 7.35 3D modelling half of the prestressed bridge beam.

7.7 RESULTS AND DISCUSSION

7.7.1 Tested Prestressed Beams Affected by ASR at Tech Lab

The present investigation used finite element modelling to estimate the structural performance of prestressed and reinforced concrete beams impacted by ASR. Concerning the standard reinforced beam. The first fractures appeared in the beam when the applied force reached 52 kN. Figure 7.36 displays the load-displacement curves for normal beam (8NRC) and ASR-affected beam (2RRC) derived from experiment and FEM analysis. Notably, the yielding deflection of beams was computed by using the lowest cross-sectional stiffness at midspan as the average value for the whole beam. This simplification overestimates the yielding deflection, but because it is less than 10%, it was deemed acceptable (Guo and Shi, 2003).

The FEM numerical results showed satisfactory agreement with the experimental result which strongly proved the reliability of the proposed methodology. From both numerical and experimental results (Figures 7.36 to 7.38), the ASR-damaged beam performed smaller yielding load.

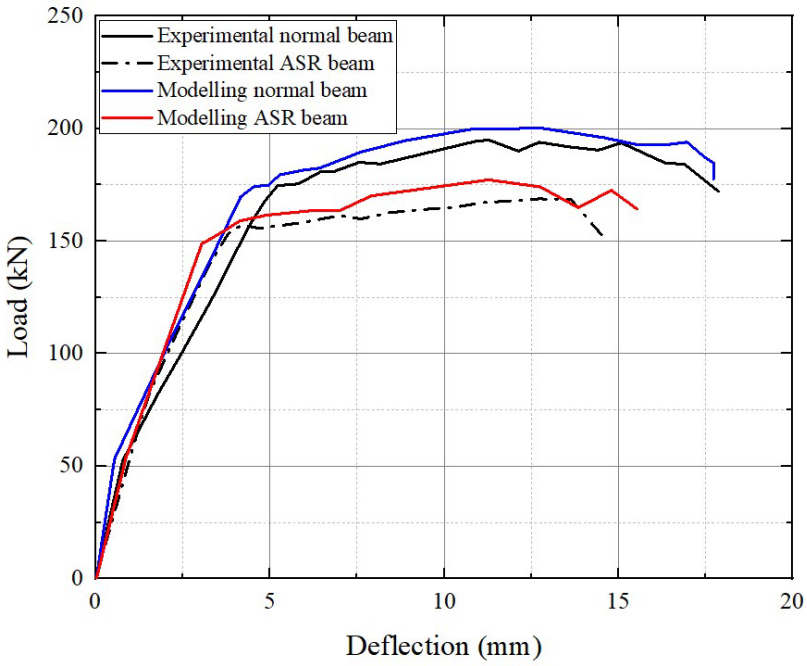

Figure 7.36 The load-displacement curves for non-reactive prestressed beam.

The FEM numerical results indicated that the cracking load (52 kN) took place at deflection of 0.51 mm. After cracking, the tensile strength was mainly carried by tensile bars. As a result, several cracks can be seen on the surface of the beam. In addition, yielding load was 169.35 kN at 4.17 mm. However, the experimental results showed larger deflection at yielding load (5.2 mm) compared with numerical result, see Figure 7.38. For ASR-affected reinforced beam, the FEM numerical results demonstrated that the cracking load (58 kN) and yielding load (148.16 kN) took place at deflection of 0.96 mm and 2.97 mm. At this stage, the rebars have reached yielding at their critical surface. With a small force increase, the deflection increases significantly, indicating the stiffness reduction in the beam. In accordance with the measured strain values, as detailed in Chapter Three, the reduction in the elastic modulus attributed to Alkali-Silica Reaction (ASR) is estimated at 35 percent. Furthermore, the extent of expansion due to ASR, as assessed utilizing the approach expounded in Chapter Four, has been taken into consideration. Given the prestressed

nature of this bridge's design, it is anticipated that the minimum expansion will occur in the tensile region of the beam, where longitudinal reinforcing bars and tension strands are situated. For this specific scenario, the maximum estimated expansion in the longitudinal reinforcing bars is 820 microstrain, and this value has been integrated into the modeling process.

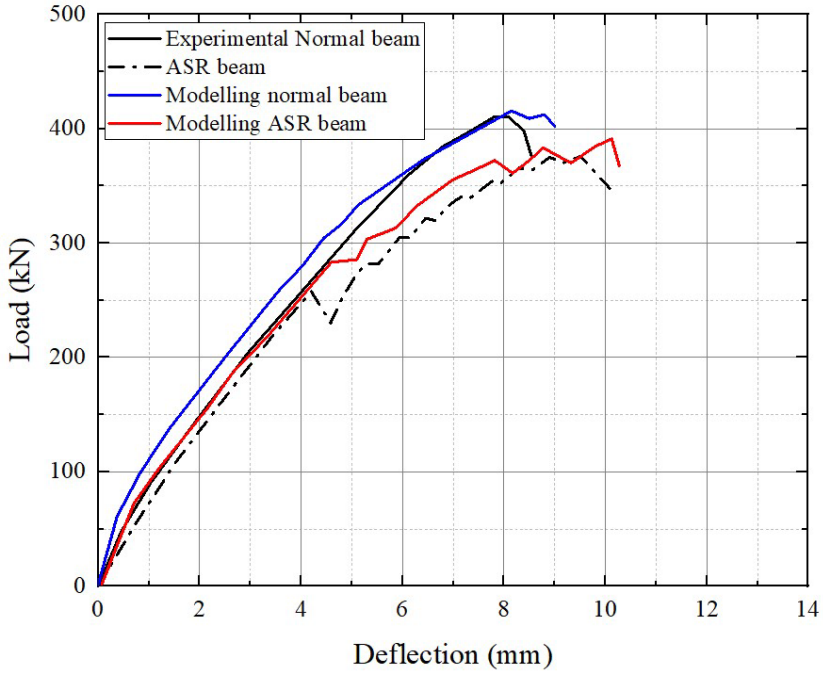

Figure 7.37 The load-displacement curves for non-reactive prestressed beam.

The load-displacement curves for non-reactive prestressed beam (6NPC) and ASR-affected prestressed beam (3RPC) by both experiment and FEM analysis were given in Figure 7.37. Similar to the experimental test, beams failed in flexural compression. The ultimate load for non-reactive prestressed beam in compression was 417.31 kN at 8.14 mm. However, the experimental results showed slightly lower deflection at ultimate load (8 mm) compared with numerical result, see Figure 7.37. For ASR-affected prestressed beam, the FEM numerical results demonstrated that the ultimate load (391 kN) took place at deflection of 10.12 mm.

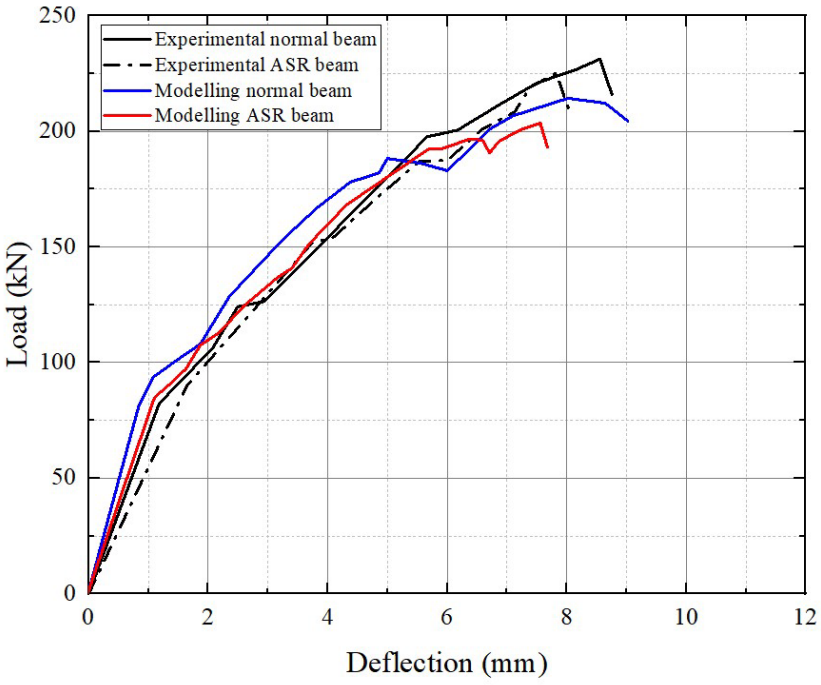

Figure 7.38 The load-displacement curves for non-reactive prestressed beam.

The load-displacement curves for non-reactive prestressed beam (8NPC) and ASR-affected prestressed beam (2RPC) by both experiment and FEM analysis were given in Figure 7.38. Similar to the experimental test, these prestressed beams without stirrups failed in shear. The ultimate load for ASR-affected prestressed beam in shear failure was 204 kN at 7.60 mm. Similarly, the experimental results showed the same deflection at ultimate load (7.81 mm) compared with numerical result, see Figure 7.38. For non-reactive prestressed beam, the FEM numerical results demonstrated that the ultimate load (214 kN) took place at deflection of 8 mm.

7.7.2 ASR-AFFECTED PRESTRESSED CONCRETE BRIDGES IN VICROAD

Firstly, the normal prestressed beam was modelled, and its load-deflection diagram was provided as a reference for comparison with ASR-damaged beams. Then the prestressed beam was modelled with different damage degrees due to ASR.

For the second model, it was assumed 0.25% expansion due to ASR. In this case, the yield strength and ultimate strength are estimated as 134.8 kN and 162 kN, respectively. Results showed that the yield strength and ultimate strength have decreased by 7.3% and 8.5% compared to the control prestressed beam, respectively. Similarly, in the third case, the beam was modelled by applying the effect of ASR, assuming that the expansion is more than 0.25% and limited to 0.30% due to ASR (Figure 7.39). The beam's strength reduction compared to the control beam was calculated as 10.8% and 9.6%.

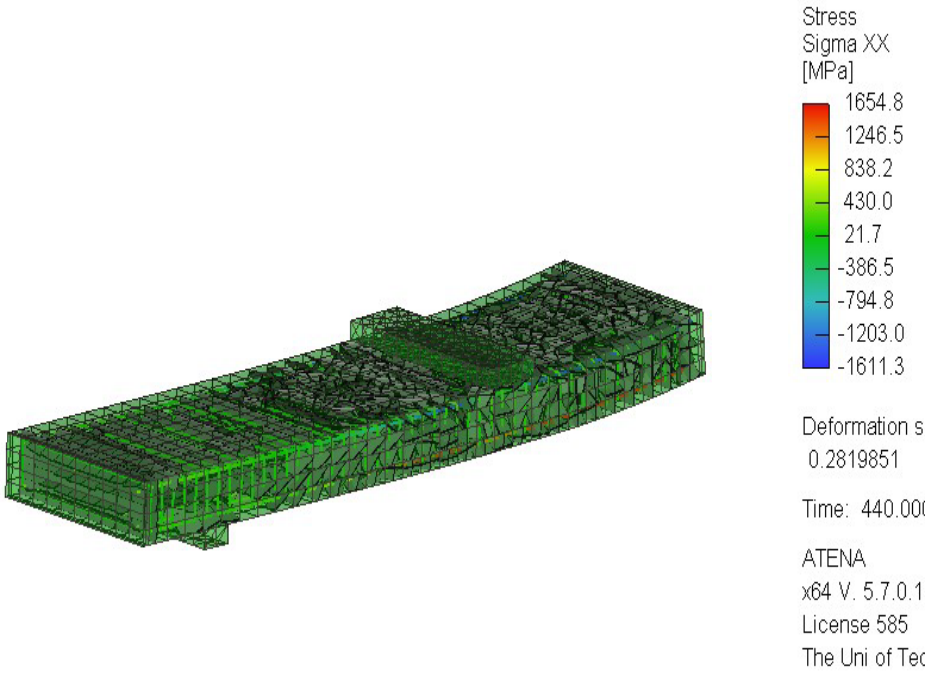

Figure 7.39 Deformation and stress of ASR-affected prestressed bridge beam at failure.

Finally, as illustrated in Figure 7.40, the flexural load capacity of the damaged beam due to ASR, for expansion of more than 0.35% and less than 0.4%, was estimated to be 132 kN and 156 kN, respectively. The results indicated that the carrying capacity has decreased by 12% compared to the control prestressed beam. Figure 7.41 demonstrates deformation and stress of ASR-affected prestressed bridge beam at failure.

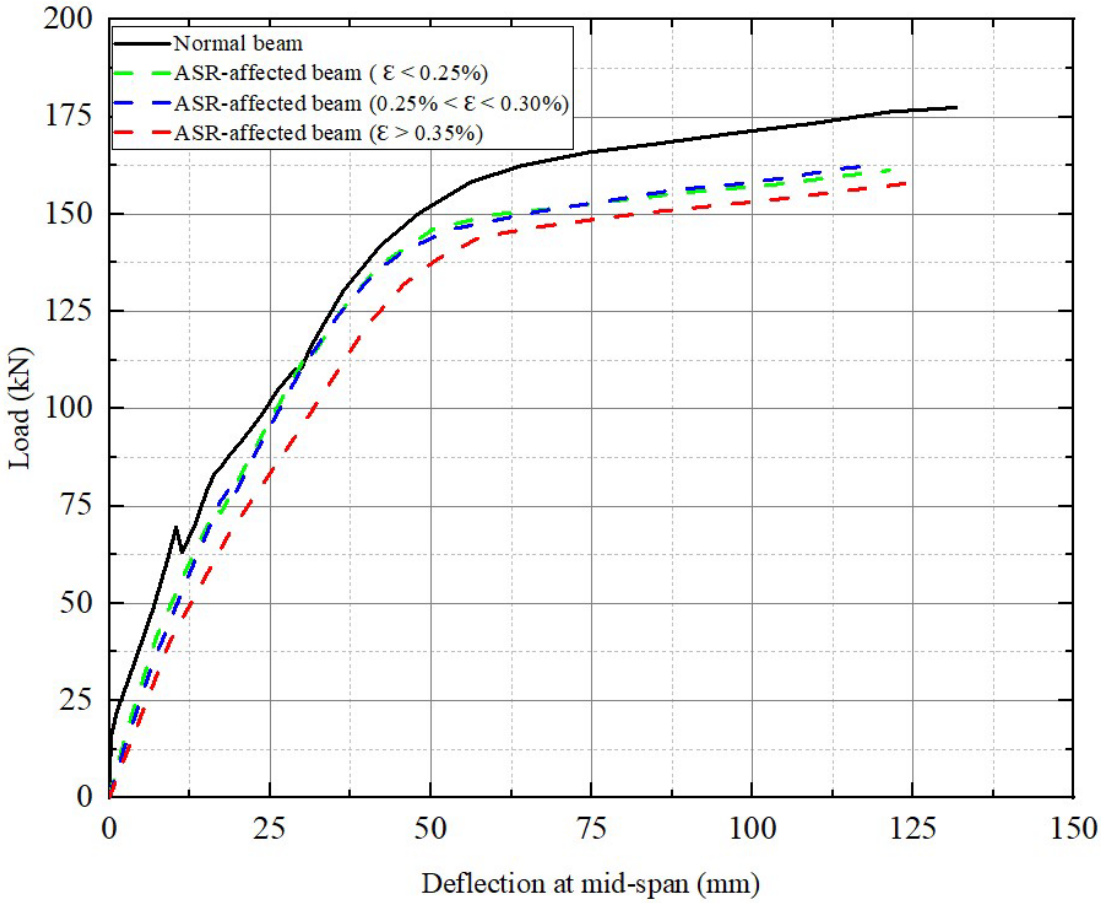

Figure 7.40 The load-displacement curves for non-reactive prestressed beam.

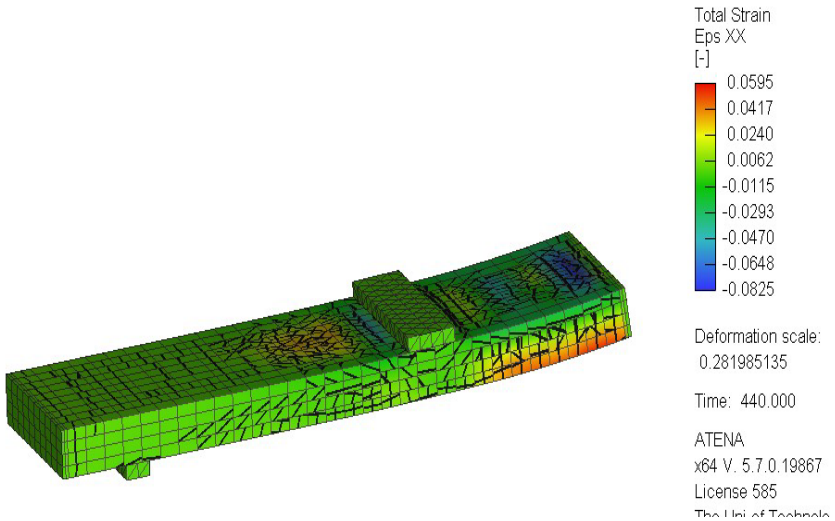

Figure 7.41 Deformation and stress of ASR-affected prestressed bridge beam at failure.

7.8 SUMMARY

According to SA HB 79:2015 (Australian standard, 2015), typical approaches for analysing the behaviour of ASR-affected structures are no longer relevant due to the generated anisotropy and changes in the mechanical properties of concrete. An alternative procedure for nonlinear analysis of prestressed concrete structures affected by ASR was presented and implemented within the developed finite element software to analyse three-dimensional concrete structures to address this requirement .

An attempt was made to model the ASR strain's impact on the prestressed concrete members' structural performance. A realistic ASR strain model was generated to simulate the behaviour of prestressed concrete beams affected by ASR.

Firstly, the results of the tests on ASR-affected real-size prestressed and reinforced members conducted in the laboratory were used to validate the numerical model. Thereafter, the proposed numerical model evaluated the effects of ASR on the flexural and shear performance of the tested prestressed concrete beams at the UTS Tech Lab.

Consequently, the residual strength simulation was presented and analysed. The beam load-carrying capacity of the reinforced and prestressed beams was predicted by numerical modelling. The load-deflection curve was numerically calculated and then compared with the experimental results.

Finally, a real prestressed bridge beam was modelled, assuming different degrees of damage and expansion due to ASR. The load-deflection curves were plotted. The Strength reduction due to ASR for different expansion values was compared to the normal beam. The results of the bridge beam modelling showed that the yield strength experienced a decrease of 7.3%, 10.8%, and 9.25% for expansion less than 0.25%,

between 0.25% and 0.30%, and between 0.35% and 0.4%, respectively. In addition, the ultimate strength of the beams was estimated to be 8.47%, 9.6%, and 12% for expansion less than 0.25%, between 0.25% and 0.30%, and between 0.35% and 0.4%, respectively. It should be noted failure modes were flexural for all prestressed bridge beams, and no change was observed in the failure mode of the ASR-damaged beams. These modelling results can provide a better understanding of the effect of ASR on prestressed concrete structures.

In this study, there was a strong correlation between the numerical modelling laboratory findings. The findings demonstrate that the suggested numerical model is able to accurately assess and predict the behaviour of concrete structures, mainly prestressed concrete beams.

Chapter 8: SUMMARY AND CONCLUSIONS

8.1 SUMMARY

ASR is considered as a prolonged chemical reaction; hence, it requires a longer period to determine the degradation rate in field conditions. In addition, providing accelerated ASR conditions, such as water tanks and temperature control, for real-size concrete structures is challenging, costly, and practically impossible in most cases. In this study, eight real-size beams, including two conventionally reinforced concrete beams and six prestressed concrete beams, were mixed and cast with companion cylindrical samples and concrete prisms. The design and construction process of real-size concrete beams was presented. The process of preparing the concrete specimens and fabrication for the experimental plan was elucidated. The concrete materials used, and their physical and chemical characteristics were defined. Plain concrete prisms samples were made to evaluate the free expansion of concrete samples due to ASR. All samples were kept in accelerated ASR conditions in water tanks designed and built for this series of tests at 40 degrees for nine months. During the ASR conditioning period, strain changes in the rebars of the beams were monitored and recorded regularly using electric strain gauges.

Furthermore, using various proposed models, a precise model was presented that enables us to analyse and estimate the flexural capacity of concrete structures, especially prestressed concrete structures, damaged by ASR.

According to a comprehensive reviewing of the literature, a numerical model was presented in the first step to predict the changes in the mechanical properties of ASR-

damaged concrete. Since the most significant impact of ASR is on the elastic modulus of concrete, a numerical model was developed using an artificial neural network (ANN) model to predict the evaluation of the elastic modulus of ASR-affected concrete based on 13 crucial input factors.

A constitutive model was then proposed in the next step. This combined model was developed to predict the expansion due to ASR by considering the kinetics of ASR, applied stresses, alkali content, and the effect of relative humidity.

In the third step, both the estimated reductions in elastic modulus due to ASR (calculated using the proposed ANN model in the first step) and the calculated ASR-induced expansion (calculated using the proposed constitutive model in the second step) were applied as input data in the FEM model.

After that, the FEM modelling results were compared and verified with those obtained from the experimental tests conducted at the UTS Tech Lab.

Finally, an existing Country Roads Board prestressed bridge beam at VicRoads was modelled, assuming exposure to alkali-silica reactions at different ages. The structure's bearing capacity against varying degrees of damage due to ASR was analysed and investigated.

Moreover, three conventionally reinforced concrete beams with three different failure modes were designed with normal concrete to validate the selected fracture-plastic model in FEM software. After testing the beams at the UTS Tech Lab, the obtained results were compared and evaluated with the FEM modelling results.

8.2 CONCLUSIONS

The results of mechanical properties tests on ASR-affected concrete samples revealed that the compressive strength of concrete affected by ASR initially showed a slight increase, before declining gradually to about 76% of its original value.

The splitting test effectively showed the impact of ASR on the tensile behaviour of plain concrete, with a final tensile strength that was about 36% lower than its initial value.

Among different mechanical properties, elastic modulus showed the most sensitivity to ASR, indicating the corresponding degradation even at small expansion values. Reduction up to 60% was observed for the elastic modulus of concrete affected by ASR.

Moreover, a comparison of the degradation behaviour of compressive and splitting tensile strengths with the elastic modulus denoted a nonlinear relationship, as a result, it is not possible to apply the known stiffness-strength formulation developed for unaffected concrete.

The proposed artificial neural network (ANN) model outperforms existing empirical models for predicting the normalised elastic modulus produced by ASR. This model provides a more accurate prediction of the elastic modulus of ASR-damaged concrete.

The innovative proposed ANN method considers ASR expansion and other influencing variables, such as expansion rate, reactive fine and coarse aggregate proportion, alkali content, casting orientation, geometry, and maximum observed expansion.

In addition, these components allow us to utilise more data, such as the results of ultra-accelerated ASR tests, which, in turn, leads to a high rate and considerable expansion.

The sensitivity analysis of the 13 input factors showed that the expansion has the most significant effect on the modulus of elasticity of ASR-affected concrete. After that, the expansion rate, maximum expansion, the proportion of reactive aggregates, casting orientation, geometry, and alkali content substantially affect the modulus change caused by ASR.

In contrast, the exposure situation, the water-to-cement ratio, and the proportion of non-reactive aggregate have a negligible effect on the change in elastic modulus due to ASR.

The proposed constitutive model combines the kinetic of the reaction with the influence of moisture, the effect of alkali/silica concentration, and the influence of applied stresses. The validity of this constitutive model was evaluated by comparing predictions of expansion with experimental data from several specimens and real scale reinforced concrete beams. The computational results and experimental test results were in excellent agreement.

Moreover, the comparison of the measured expansion and modelling results for restraint member with reinforcing bars or applied stress, revealed that the capability of this combined method for predicting the ASR induced expansion in prestressed members.

A total of eight concrete beams, including six prestressed beams and two conventionally reinforced beams, were tested at UTS Tech Lab. After nine months of exposure to ASR-enhanced conditions, the concrete samples exhibited an expansion of

$0.33e^{-04}$. The results of the strain changes in the reinforcing steel bars of the ASR-affected conventional reinforced beams showed that the expansion rate was the highest for the upper bars, reaching about 0.196%. The strain changes for the lower bars were found to be almost negligible. Similarly, the strain changes caused by ASR for the lower rebars of prestressed beams were measured to be almost negligible (0.022%).

At the same time, while strain changes caused by ASR at the level of steel bars were lower in the prestressed beam, the strain changes in upper bars and stirrups were slightly higher in the prestressed beam compared to the ASR-affected conventional reinforced beam.

The strain changes in prestressing bars of prestressed beams with reactive and non-reactive concrete were almost similar. The strain in the prestressing bars decreased slightly at first and then tended to zero.

In terms of the structural behaviour of the beams affected by ASR, the ultimate strength of the ASR-damaged conventional reinforced beam decreased by 14% in comparison to the normal conventional reinforced beam. In contrast, the cracking moment in the ASR-damaged beam increased slightly, which can be attributed to the induced ASR expansion pressure.

Compared to the normal prestressed beam, the reduction in the ultimate strength of the prestressed beam damaged by ASR was almost negligible (3%).

The reduction in the ultimate strength of the prestressed beam damaged by ASR in compression failure was measured as less than 10%. The location of the concrete crush in compression was the noticeable point in this type of failure. The failure occurred exactly along the ASR cracks, which can emphasize the importance of the ASR crack pattern.

Finally, the novel method for nonlinear analysis of concrete structures impacted by ASR which was proposed to predict the behaviour of prestressed concrete beams suffering from ASR was validated using results from laboratory tests conducted on real-size prestressed and reinforced concrete beams affected by ASR.

The concrete's tensile behaviour was modelled using fracture mechanics while the compressive behaviour was modelled using plasticity. The stress-strain law for concrete under tension incorporated two phases, pre-, and post-cracking, and fracture models were developed using smeared crack formulation and the crack band model.

The comparison of the experimental and numerical results showed that the fracture-plastic model accurately modelled the stiffness of both reactive and non-reactive beams. Numerical modelling also depicts that ASR little impacts the rigidity of the prestressed beams due to anisotropic damage induced by the presence of the prestress force.

A real prestressed bridge beam was modelled and analysed for different degrees of damage due to ASR. The analysis of the prestressed bridge beam damage caused by ASR revealed that the ultimate strength reduction of the ASR-affected prestressed beam was less than 10% for expansion up to 0.3% and a maximum of 12% for expansion up to 0.4%.

As found in the laboratory tests, the appearance of initial flexural cracks in ASR-impacted reinforced beams model occurred at a higher load compared to non-reactive beams, due to the chemical prestress caused by the restrained expansion in the restraint direction.

As with the experimental results, no significant change was observed in the flexural capacity of the modelled prestressed beams.

It should be noted that the bond behaviour in modelling was assumed to be a perfect connection as no evidence of substantial loss of bond due to ASR was observed from the experimental test results.

This research has shown a high level of agreement between the numerical modelling results and the experimental results. The proposed method can effectively evaluate and predict the behaviour of concrete structures due to ASR, particularly prestressed concrete beams.

8.3 RECOMMENDATIONS FOR FUTURE RESEARCH

- The beam's failure took place in the compressive zone and precisely at the location of the ASR cracks. This can indicate the importance of the ASR cracking pattern. Therefore, researchers should perform additional studies on the ASR crack patterns.
- The analytical and experimental results presented in this thesis are aimed to investigate the residual load-carrying capacity of ASR-affected concrete beams. Due to the accelerated ASR conditions, samples were immersed in the water, therefore the long-term behaviour of the samples including prestress losses due to creep and shrinkage are not taken into account. However, these losses play an important role in prestressed concrete structures.
- Since in this study we have utilized Macalloy bars, an extensive experimental program may be conducted on longer beams to investigate the effect of ASR on the tendons and strands.
- An experimental program could be conducted to study the effect of ASR on the structural behaviour of pre-tensioned concrete structures.

- An experimental program could be conducted to study the effect of ASR on the bond behavior of prestressing bars.

References

Abe, M., S. Kikuta, Y. Masuda and F. Tomozawa (1989) "8th Internationl Conference on Alkali-Aggregate Reaction."

Ahmed, T., E. Burley, S. Rigden and A. I. Abu-Tair (2003). "The effect of alkali reactivity on the mechanical properties of concrete." Construction and Building Materials **17**(2): 123-144.

Akbarzadeh, H. and A. A. Maghsoudi (2010). "Experimental and analytical investigation of reinforced high strength concrete continuous beams strengthened with fiber reinforced polymer." Materials & Design **31**(3): 1130-1147.

ASTM (2003). Standard guide for petrographic examination of aggregates for concrete.

ASTM, C. "289. 2007. Standard test method for potential alkali–silica reactivity of aggregates (Chemical method)." The American Society for Testing and Materials Philadelphia, USA.

ASTM, C. (2018). "227, Standard Test Method for Potential Alkali Reactivity of Cement-Aggregate Combinations (Mortar-Bar Method)." ASTM International: West Conshohocken, PA, USA.

Australia, S. (2015). Alkali aggregate reaction—Guidelines on minimising the risk of damage to concrete structures in Australia.

Bažant, Z. P. and A. Steffens (2000). "Mathematical model for kinetics of alkali–silica reaction in concrete." Cement and Concrete Research **30**(3): 419-428.

Bazant, Z. P., G. Zi and C. Meyer (2000). "Fracture mechanics of ASR in concretes with waste glass particles of different sizes." Journal of engineering mechanics **126**(3): 226-232.

Beaver, J., L. Jiang and M. Sherman (2013). "Inspection and monitoring of ASR-affected structures at Seabrook Station, NH."

Beeby, A. (1983). "Cracking, cover, and corrostion of reinforcement." Concrete international **5**(2): 35-40.

Ben Haha, M. (2006). Mechanical effects of alkali silica reaction in concrete studied by SEM-image analysis, EPFL.

Bérubé, M.-A., J. Duchesne, J. F. Dorion and M. Rivest (2002). "Laboratory assessment of alkali contribution by aggregates to concrete and application to concrete structures affected by alkali–silica reactivity." Cement and Concrete Research **32**(8): 1215-1227.

Bérubé, M.-A. and B. Fournier (1993). "Canadian experience with testing for alkali-aggregate reactivity in concrete." Cement and Concrete Composites **15**(1): 27-47.

Béton, C. E.-I. d. (1993). CEB-FIP model code 1990: Design code, Thomas Telford Publishing.

Blight, G. E. and M. G. Alexander (2011). Alkali-aggregate reaction and structural damage to concrete: engineering assessment, repair and management, CRC Press.

Broekmans, M. A. T. M. (2004). "Structural properties of quartz and their potential role for ASR." Materials Characterization **53**(2): 129-140.

Červenka, V., L. Jendele and J. Červenka (2000). "ATENA Program Documentation–Part 1." Cervenka Consulting sro.

Charlwood, R., S. Solymar and D. Curtis (1992). A review of alkali aggregate reactions in hydroelectric plants and dams. Proceedings of the international conference of alkali-aggregate reactions in hydroelectric plants and dams.

Chatterji, S., N. Thaulow and A. D. Jensen (1988). "Studies of alkali-silica reaction, part 6. Practical implications of a proposed reaction mechanism." Cement and Concrete Research **18**(3): 363-366.

Cherry, B. and W. Green (2021). Corrosion and protection of reinforced concrete, CRC Press.

Clayton, N., R. Currie and R. Moss (1990). "Effects of alkali-silica reaction on the strength of prestressed concrete beams." Structural Engineer **68**: 287-292.

Comby-Peyrot, I., F. Bernard, P.-O. Bouchard, F. Bay and E. Garcia-Diaz (2009). "Development and validation of a 3D computational tool to describe concrete behaviour at mesoscale. Application to the alkali-silica reaction." Computational Materials Science **46**(4): 1163-1177.

Comi, C., R. Fedele and U. Perego (2009). "A chemo-thermo-damage model for the analysis of concrete dams affected by alkali-silica reaction." Mechanics of materials **41**(3): 210-230.

Diamond, S. (1975). "A review of alkali-silica reaction and expansion mechanisms 1. Alkalies in cements and in concrete pore solutions." Cement and Concrete Research **5**(4): 329-345.

Diamond, S. (1976). "A review of alkali-silica reaction and expansion mechanisms 2. Reactive aggregates." Cement and Concrete Research **6**(4): 549-560.

Diamond, S. (1983). "Effect of Microsilica on Pore Solution Chemistry of Cement Pastes." J. of American Concrete Institute **66**(5).

Diamond, S. (1983). "Effects of Microsilica (Silica Fume) on Pore-Solution Chemistry of Cement Pastes." Journal of the American Ceramic Society **66**(5): C-82-C-84.

Diamond, S. (2000). Chemistry and 0ther characteristics of ASR gels. Proc. of the 11th International Conference on Alkali-Aggregate Reaction in Concrete.

Dron, R. and F. Brivot (1992). "Thermodynamic and kinetic approach to the alkali-silica reaction. Part 1: Concepts." Cement and Concrete Research **22**(5): 941-948.

Du, H. and K. H. Tan (2014). "Effect of particle size on alkali–silica reaction in recycled glass mortars." Construction and Building Materials **66**: 275-285.

Dunant, C. F. and K. L. Scrivener (2012). "Effects of aggregate size on alkali–silica-reaction induced expansion." Cement and Concrete Research **42**(6): 745-751.

Esposito, R., C. Anaç, M. A. Hendriks and O. Copuroglu (2016). "Influence of the alkali-silica reaction on the mechanical degradation of concrete." J. Mater. Civ. Eng **28**(6).

FAN, H. (1998). "EFFECT OF ALKALI SILICA REACTION EXPANSION AND CRACKING ON STRUCTURAL BEHAVIOR OF REINFORCED CONCRETE BEAMS." ACI Structural Journal **95**(5): 498-505.

Fan, S. and J. M. Hanson (1998). "Length expansion and cracking of plain and reinforced concrete prisms due to alkali-silica reaction." Materials Journal **95**(4): 480-487.

Farny, J. A. and S. H. Kosmatka (1997). Diagnosis and control of alkali-aggregate reactions in concrete, Portland Cement Association Skokie, IL.

Figueira, R. B., R. Sousa, L. Coelho, M. Azenha, J. M. de Almeida, P. A. S. Jorge and C. J. R. Silva (2019). "Alkali-silica reaction in concrete: Mechanisms, mitigation and test methods." Construction and Building Materials **222**: 903-931.

FIP, W. (1980). Report on Prestressing Steel: 5. Stress Corrosion Cracking Resistance Test for Prestressing Tendons, Technical Report, FIP, Paris.

Fournier, B., R. Chevrier, M. DeGrosbois, R. Lisella, K. Folliard, J. Ideker, M. Shehata, M. Thomas and S. Baxter (2004). The accelerated concrete prism test (60 C): variability of the test method and proposed expansion limits. Proc. of the 12th Int. Conf. on AAR in Concrete, Beijing (China).

Furusawa, Y., H. Ohga and T. Uomoto (1994). "Analytical study concerning prediction of concrete expansion due to alkali-silica reaction." Special Publication **145**: 757-780.

Ganz, H.-R. (2008). "Prestressed structural concrete: New developments and applications." Encontro Nacional Betão Estrutural **2008**: 3-20.

Gao, X. X., S. Multon, M. Cyr and A. Sellier (2013). "Alkali–silica reaction (ASR) expansion: Pessimum effect versus scale effect." Cement and Concrete Research **44**: 25-33.

Garcia-Diaz, E., D. Bulteel, Y. Monnin, P. Degrugilliers and P. Fasseu (2010). "ASR pessimum behaviour of siliceous limestone aggregates." Cement and Concrete Research **40**(4): 546-549.

Garcia-Diaz, E., J. Riche, D. Bulteel and C. Vernet (2006). "Mechanism of damage for the alkali–silica reaction." Cement and Concrete Research **36**(2): 395-400.

Giaccio, G., R. Zerbino, J. M. Ponce and O. R. Batic (2008). "Mechanical behavior of concretes damaged by alkali-silica reaction." Cement and Concrete Research **38**(7): 993-1004.

Giannini, E. and K. Folliard (2012). Stiffness damage and mechanical testing of core specimens for the evaluation of structures affected by ASR. Proceedings of the 14th International Conference on Alkali–Aggregate Reaction in Concrete.

Giorla, A. B., K. L. Scrivener and C. F. Dunant (2015). "Influence of visco-elasticity on the stress development induced by alkali–silica reaction." Cement and Concrete Research **70**: 1-8.

Guo, Z.-H. and X.-D. Shi (2003). "Reinforced concrete theory and analyse." Press of Tsinghua University: Beijing, China.

Godart, B., M. R. de Rooij and J. G. Wood (2013). Guide to diagnosis and appraisal of AAR damage to concrete in structures, Springer.

Goguel, R. (1995). "Alkali release by volcanic aggregates in concrete." Cement and Concrete Research **25**(4): 841-852.

Groves, G. W. and X. Zhang (1990). "A dilatation model for the expansion of silica glass/OPC mortars." Cement and Concrete Research **20**(3): 453-460.

Haha, M. B. Mechanical Effects of Alkali Silica Reaction in Concrete Studied by SEM-Image Analysis, 2006, DOI.

Haha, M. B., E. Gallucci, A. Guidoum and K. L. Scrivener (2007). "Relation of expansion due to alkali silica reaction to the degree of reaction measured by SEM image analysis." Cement and Concrete Research **37**(8): 1206-1214.

Hampejs, G. and F. F. I. de la Precontrainte (1988). The FIP stress corrosion test with ammonium thiocyanate, FIP.

Hayman, S. (2010). Preventing Alkali Silica Reaction in the Mactaquac Dam Using High Volume Fly Ash Concrete, University of New Brunswick, Department of Civil Engineering.

Hobbs, D. and W. Gutteridge (1979). "Particle size of aggregate and its influence upon the expansion caused by the alkali–silica reaction." Magazine of Concrete research **31**(109): 235-242.

Hobbs, D. W. (1981). "Discussion: The alkali2–silica reaction2—a model for predicting expansion m mortar." Magazine of Concrete Research **33**(117): 208-220.

Hobbs, D. W. (1988). Alkali-silica reaction in concrete, Thomas Telford Publishing.

Hooton, R. (1991). "New aggregate alkali-reactivity test methods."

Hordijk, D. A. (1993). "Local approach to fatigue of concrete."

Ichikawa, T. (2009). "Alkali–silica reaction, pessimum effects and pozzolanic effect." Cement and Concrete Research **39**(8): 716-726.

Ichikawa, T. and M. Miura (2007). "Modified model of alkali-silica reaction." Cement and Concrete Research **37**(9): 1291-1297.

Ideker, J. H., B. L. East, K. J. Folliard, M. D. A. Thomas and B. Fournier (2010). "The current state of the accelerated concrete prism test." Cement and Concrete Research **40**(4): 550-555.

Islam, M. S. and N. Ghafoori (2013). "Evaluation of Alkali-Silica Reactivity Using Aggregate Geology, Expansion Limits of Mortar Bars and Concrete Prisms, and Kinetic Model." Journal of Materials Science Research **2**(2): 103.

Jones, A. and L. Clark (1996). "The effect of restrained expansion on the assessment of structures with ASR." TRL REPORT 161.

Kagimoto, H., Y. Yasuda and M. Kawamura (2014). "ASR expansion, expansive pressure and cracking in concrete prisms under various degrees of restraint." Cement and concrete research **59**: 1-15.

Karthik, M. M., J. B. Mander and S. Hurlebaus (2016). "ASR/DEF related expansion in structural concrete: Model development and validation." Construction and Building Materials **128**: 238-247.

Kleib, J., G. Aouad, G. Louis, M. Zakhour, M. Boulos, A. Rousselet and D. Bulteel (2018). "The use of calcium sulfoaluminate cement to mitigate the alkali silica reaction in mortars." Construction and Building Materials **184**: 295-303.

Kobayashi, K., S. Inoue, T. Yamasaki and K.-i. Nakano (1988). "Alkali aggregate reaction in prestressed concrete beams." International Journal of Cement Composites and Lightweight Concrete **10**(4): 233-240.

Kurtis, K. E. and P. J. M. Monteiro (2003). "Chemical additives to control expansion of alkali-silica reaction gel: proposed mechanisms of control." Journal of Materials Science **38**(9): 2027-2036.

Kyoto (1986). COMMITTEE ON AAR OF THE HANSHIN EXPRESSWAY CO**:** 339.

Lane, D. S. (1994). Alkali-silica reactivity in Virginia, Virginia Transportation Research Council.

Larive, C. (1997). Apports combinés de l'expérimentation et de la modélisation à la compréhension de l'alcali-réaction et de ses effets mécaniques, Ecole nationale des ponts et chaussees.

Latifee, E. R. and P. R. Rangaraju (2015). "Miniature Concrete Prism Test: Rapid Test Method for Evaluating Alkali-Silica Reactivity of Aggregates." Journal of Materials in Civil Engineering **27**(7): 04014215.

Léger, P., P. Côté and R. Tinawi (1996). "Finite element analysis of concrete swelling due to alkali-aggregate reactions in dams." Computers & structures **60**(4): 601-611.

Li, P., N. Tan, X. An, K. Maekawa and Z. Jiang (2020). "Restraint Effect of Reinforcing Bar on ASR Expansion and Deterioration Characteristic of the Bond Behavior." Journal of Advanced Concrete Technology **18**(4): 192-210.

Lindgård, J. (2013). "Alkali-silica reaction (ASR)–Performancetesting."

Lindgård, J., Ö. Andiç-Çakır, I. Fernandes, T. F. Rønning and M. D. Thomas (2012). "Alkali–silica reactions (ASR): Literature review on parameters influencing laboratory performance testing." Cement and concrete research **42**(2): 223-243.

Lindgård, J., Ö. Andiç-Çakır, I. Fernandes, T. F. Rønning and M. D. A. Thomas (2012). "Alkali–silica reactions (ASR): Literature review on parameters influencing laboratory performance testing." Cement and Concrete Research **42**(2): 223-243.

Liu, H., J. Yang and X. Wang (2017). "Bond behavior between BFRP bar and recycled aggregate concrete reinforced with basalt fiber." Construction and Building Materials **135**: 477-483.

Locati, F., S. Marfil and E. Baldo (2010). "Effect of ductile deformation of quartz-bearing rocks on the alkali-silica reaction." Engineering Geology **116**(1): 117-128.

Lu, D., B. Fournier, P. E. Grattan-Bellew, Z. Xu and M. Tang (2008). "Development of a universal accelerated test for alkali-silica and alkali-carbonate reactivity of concrete aggregates." Materials and Structures **41**(2): 235-246.

Maraghechi, H., F. Rajabipour, C. G. Pantano and W. D. Burgos (2016). "Effect of calcium on dissolution and precipitation reactions of amorphous silica at high alkalinity." Cement and Concrete Research **87**: 1-13.

Mather, K. and B. Mather (1950). Method of petrographic examination of aggregates for concrete. PROCEEDINGS-AMERICAN SOCIETY FOR TESTING AND MATERIALS, AMER SOC TESTING MATERIALS 100 BARR HARBOR DR, W CONSHOHOCKEN, PA 19428-2959.

Menetrey, P. and K. Willam (1995). "Triaxial failure criterion for concrete and its generalization." Structural Journal **92**(3): 311-318.

Mohammed, T. U., H. Hamada and T. Yamaji (2003). "Alkali-silica reaction-induced strains over concrete surface and steel bars in concrete." Materials Journal **100**(2): 133-142.

Monette, L., Gardner, J. Grattan-Bellew (2000). Structural effects of the alkali-silica reaction on non-loaded and laded reinforced concrete beams. 11th ICAAR, Quebec, Canada.

Monette, L. J.-G. (1998). Effects of the alkali-silica reaction on unloaded, statically loaded and dynamically loaded reinforced concrete beams, University of Ottawa (Canada).

Mukhopadhyay, A. and X. Shi (2019). Microstructural characterization of portland cement concrete containing reclaimed asphalt pavement aggregates using conventional and advanced petrographic techniques. Advances in cement analysis and concrete petrography, ASTM International.

Multon, S. (2003). Evaluation expérimentale et théorique des effets mécaniques de l'alcali-réaction sur des structures modèles, Marne-la-Vallée.

Multon, S. (2003). Évaluation expérimentale et théorique des effets mécaniques de l'alcali-réaction sur des structures modèles.

Multon, S., M. Cyr, A. Sellier, N. Leklou and L. Petit (2008). "Coupled effects of aggregate size and alkali content on ASR expansion." Cement and Concrete Research **38**(3): 350-359.

Multon, S., J. F. Seignol and F. Toutlemonde (2005). "Structural behavior of concrete beams affected by alkali-silica reaction." ACI Materials Journal **102**(2): 67-76.

Multon, S., A. Sellier and M. Cyr (2009). "Chemo–mechanical modeling for prediction of alkali silica reaction (ASR) expansion." Cement and Concrete Research **39**(6): 490-500.

Multon, S. and F. Toutlemonde (2006). "Effect of applied stresses on alkali–silica reaction-induced expansions." Cement and Concrete Research **36**(5): 912-920.

Multon, S. and F. Toutlemonde (2010). "Effect of moisture conditions and transfers on alkali silica reaction damaged structures." Cement and Concrete Research **40**(6): 924-934.

Okelo, R. and R. L. Yuan (2005). "Bond strength of fiber reinforced polymer rebars in normal strength concrete." Journal of composites for construction **9**(3): 203-213.

Pan, J., Y. Feng, J. Wang, Q. Sun, C. Zhang and D. Owen (2012). "Modeling of alkali-silica reaction in concrete: a review." Frontiers of Structural and Civil Engineering **6**(1): 1-18.

Pan, J. W., Y. T. Feng, J. T. Wang, Q. C. Sun, C. H. Zhang and D. R. J. Owen (2012). "Modeling of alkali-silica reaction in concrete: a review." Frontiers of Structural and Civil Engineering **6**(1): 1-18.

Park, R. (1989). "Evaluation of ductility of structures and structural assemblages from laboratory testing." Bulletin of the New Zealand Society for Earthquake Engineering **22**(3): 155-166.

Piersanti, M. (2015). "Testing Recycled Concrete Aggregate Suffering Different Levels of Alkali-Silica Reaction for Use in New Structures of Alkali-Silica Reaction for Use in New Structures." Master of Applied Science, Ryerson University.

Poyet, S. (2003). Etude de la dégradation des ouvrages en béton atteints par la réaction alcali-silice: Approche expérimentale et modélisation numérique multi-échelles des dégradations dans un environnement hydro-chemo-mécanique variable, Marne-la-Vallée.

Poyet, S., A. Sellier, B. Capra, G. Foray, J. M. Torrenti, H. Cognon and E. Bourdarot (2006). "Chemical modelling of Alkali Silica reaction: Influence of the reactive aggregate size distribution." Materials and Structures **40**(2): 229.

Rajabipour, F., E. Giannini, C. Dunant, J. H. Ideker and M. D. A. Thomas (2015). "Alkali–silica reaction: Current understanding of the reaction mechanisms and the knowledge gaps." Cement and Concrete Research **76**: 130-146.

Rajabipour, F., H. Maraghechi and S. Shafaatian (2012). ASR and its mitigation in mortars containing recycled soda-lime glass aggregates. 14th international conference on concrete alkali aggregate reactions (ICAAR), Austin.

Ramyar, K., A. Topal and Ö. Andiç (2005). "Effects of aggregate size and angularity on alkali–silica reaction." Cement and Concrete Research **35**(11): 2165-2169.

Ranc, R. and L. Debray (1992). Reference test methods and a performance criterion for concrete structures. Proceedings of the 9th International Conference on AAR in concrete.

Rivard, P., M.-A. Bérubé, J.-P. Ollivier and G. Ballivy (2003). "Alkali mass balance during the accelerated concrete prism test for alkali–aggregate reactivity." Cement and Concrete Research **33**(8): 1147-1153.

Rivard, P., M. A. Bérubé, J. P. Ollivier and G. Ballivy (2007). "Decrease of pore solution alkalinity in concrete tested for alkali-silica reaction." Materials and Structures **40**(9): 909-921.

S. Ohno, Y. Y. I., Y. Sh.mozakl, T. MOr.ikawa (1989). THE MECHANICAL BEHAVIOUR OF BEAMS COATED AFTER ALKALI SILICA REACTION DAMAGE. 8th Internationl Conference on Alkali-Aggregate Reaction.

Šachlová, Š., A. Kuchařová, Z. Pertold, R. Přikryl and M. Fridrichová (2017). "Quantitative assessment of alkali silica reaction potential of quartz-rich aggregates: comparison of chemical test and accelerated mortar bar test improved by SEM-PIA." Bulletin of Engineering Geology and the Environment **76**(1): 133-144.

Sanchez, L., B. Fournier, M. Jolin and J. Bastien (2014). "Evaluation of the stiffness damage test (SDT) as a tool for assessing damage in concrete due to ASR: Test loading and output responses for concretes incorporating fine or coarse reactive aggregates." Cement and concrete research **56**: 213-229.

Santos, M. and J. Brito (2008). "O panorama nacional das reacções álcalis-sílica em betões." Revista Engenharia Civil da UM **32**: 57-71.

Saouma, V. and L. Perotti (2006). "Constitutive model for alkali-aggregate reactions." ACI materials journal **103**(3): 194.

Sargolzahi, M., S. A. Kodjo, P. Rivard and J. Rhazi (2010). "Effectiveness of nondestructive testing for the evaluation of alkali–silica reaction in concrete." Construction and Building Materials **24**(8): 1398-1403.

Shakoorioskooie, M., M. Griffa, A. Leemann, R. Zboray and P. Lura (2021). "Alkali-silica reaction products and cracks: X-ray micro-tomography-based analysis of their spatial-temporal evolution at a mesoscale." Cement and Concrete Research **150**: 106593.

Sirivivatnanon, V., J. Mohammadi and W. South (2016). "Reliability of new Australian test methods in predicting alkali silica reaction of field concrete." Construction and Building Materials **126**: 868-874.

Smaoui, N., M.-A. Bérubé, B. Fournier and B. Bissonnette (2004). "Influence of specimen geometry, orientation of casting plane, and mode of concrete consolidation on expansion due to ASR." Cement, concrete and aggregates **26**(2): 1-13.

Society, C. (2010). Non-structural cracks in concrete: A concrete society report, Concrete Society London.

Standard, A. (2011). C1567. Standard Test Method for Determining the Potential Alkali-Silica Reactivity of Combinations of Cementitious Materials and Aggregate (Accelerated Mortar-Bar Method), West Conshohocken, PA: ASTM International.

Stanton, T. E. (2008). Expansion of concrete through reaction between cement and aggregate.

Swamy, R. and M. Al-Asali (1988). "Engineering properties of concrete affected by alkali-silica reaction." Materials Journal **85**(5): 367-374.

Swamy, R. N. (1992). The alkali-silica reaction in concrete, Blackie Glasgow.

Swamy, R. N. and M. Al-Asali (1988). "Expansion of concrete due to alkali-silica reaction." Materials Journal **85**(1): 33-40.

TAKENAKA (1987). TECHNICAL RESEARCH LABORATORY. Private Communication.

Taplin, G. R., R. S. H. Al-Mahaidi, G. Boully and S. Kwei (2000). Strength assessment of prestressed concrete rectangular beams. Austroads 4th Bridge Conference, Austroads.

Thomas, M., B. Fournier, K. Folliard, J. Ideker and M. Shehata (2006). "Test methods for evaluating preventive measures for controlling expansion due to alkali–silica reaction in concrete." Cement and Concrete Research **36**(10): 1842-1856.

Thomas, M., B. Fournier and K. J. Folliard (2012). Selecting measures to prevent deleterious alkali-silica reaction in concrete: rationale for the AASHTO PP65 prescriptive approach, United States. Federal Highway Administration.

Thomas, M. D., B. Fournier and K. J. Folliard (2013). Alkali-aggregate reactivity (AAR) facts book, United States. Federal Highway Administration. Office of Pavement Technology.

Thomas, M. D., B. Fournier, K. J. Folliard, J. H. Ideker and Y. Resendez (2007). The use of lithium to prevent or mitigate alkali-silica reaction in concrete pavements and structures, Turner-Fairbank Highway Research Center.

Thomas, M. D., B. Fournier, K. J. Folliard and Y. Resendez (2011). Alkali-silica reactivity field identification handbook, United States. Federal Highway Administration. Office of Pavement Technology.

Touma, W., D. W. Fowler and R. L. Carrasquillo (2001). Alkali-silica reaction in portland cement concrete: testing methods and mitigation alternatives.

Ulm, F.-J., O. Coussy, L. Kefei and C. Larive (2000). "Thermo-chemo-mechanics of ASR expansion in concrete structures." Journal of engineering mechanics **126**(3): 233-242.

Vivian, H. (1950). "The effect of amount of added alkalis on mortar expansion." Part XII In Studies in Cement-Aggregate Reaction, Bulletin(256): 31-47.

Vo, D., S. Multon, P. Morenon, A. Sellier, E. Grimal, B. Masson and P. Kolmayer (2021). "Evaluation of structures affected by Alkali-Silica reaction (ASR) using homogenized modelling of reinforced concrete." Engineering Structures **246**: 112845.

Zapała-Sławeta, J. and Z. Owsiak (2016). "The role of lithium compounds in mitigating alkali-gravel aggregate reaction." Construction and Building Materials **115**: 299-303.